Tidal Stream Resource Assessment of the Anglesey Skerries and the Bristol Channel

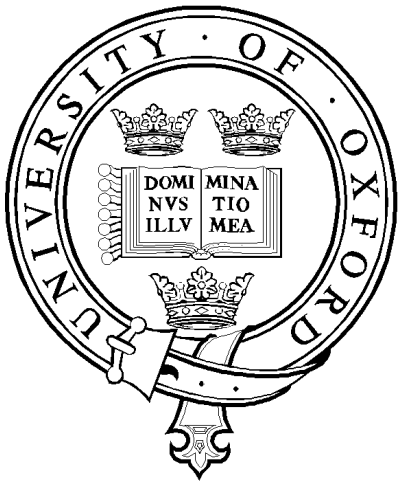

Sena Serhadlıoğlu

St. Edmund Hall

Department of Engineering Science
University of Oxford

A thesis submitted for the degree of
Doctor of Philosophy

Hilary 2014

Abstract

Tidal Stream Resource Assessment of the Anglesey Skerries and the Bristol Channel

A thesis submitted for the degree of Doctor of Philosophy
Sena Serhadlıoğlu
St. Edmund Hall, Oxford
Hilary Term 2014

Utilising tidal currents as a renewable energy resource is presently under consideration to meet the requirements of increasing worldwide energy demand and the need to reduce carbon emissions. In this respect, in-stream tidal devices are proposed to convert the kinetic energy of currents into useful extractable power. In order to extract a useful amount of energy from tidal currents, the proposed devices need to be deployed in an array or farm-like format. Due to the thrust exerted by the devices within an array, the natural flow regime will inevitably be changed. In light of this, this study aims to estimate the maximum power that can be extracted by tidal turbine arrays and assess the far-field effects of energy extraction in the designated areas around the UK for various array configurations.

In this thesis, the ocean tides are modelled using the long wave equations, commonly referred as the shallow water equations (SWEs). A numerical solver based on a Runge-Kutta discontinuous Galerkin finite element method is employed to solve the SWEs. One main advantage of the discontinuous Galerkin method is that it approximates the solution individually at each element, which allows for discontinuities within the solution system while ensuring mass conservation locally and globally. The selected numerical solver has been verified against several benchmark tests. It is then modified to include a line discontinuity to represent the effect of tidal turbine array(s) in a coastal basin. The algorithm implemented in the numerical solver involves a sub-grid model, which is based on Linear Momentum Actuator Disk Theory (LMADT) to approximate the local flow-field in the presence of the turbines. This near-field approach allows the flow velocity at the turbine to be estimated with a greater accuracy. As the power available to the turbines is related to the velocity at the turbine blades, the characterisation of the designated tidal site as a resource using LMADT may be more accurate than previously proposed methods. An additional advantage of using LMADT is that it provides a distinction between the power extracted by the turbines and the total amount of power that is removed from the tidal stream, including the wake mixing losses. The methodology employed in this thesis has been applied to two tidal basins around the UK; the Anglesey Skerries (a headland) and the Bristol Channel (an oscillating bay). A comprehensive unstructured triangular finite element model has been constructed to simulate the naturally occurring tides at these regions. The constructed model has then been validated against field measurement.

The validated model is used to conduct parametric studies, which evaluate the importance of tidal array locations, configurations and operating conditions on the available power at the Anglesey Skerries and the Bristol Channel sites. The parametric study aims to evaluate a realistic upper limit of available power at each site considered. This study also provides a unique analysis to examine the potential tidal farm interactions by deploying several tidal arrays at both Anglesey Skerries and the Bristol Channel.

Acknowledgements

I would first like to express my gratitude to my supervisors, Prof. Guy T. Houlsby and Prof. Alistair G.L. Borthwick for their guidance, encouragement and patience throughout this project. Despite his busy schedule with departmental obligations, Guy has always found the time to help and advise me on how to proceed with my work. His skills in programming have been very helpful getting my head around coding complex routines in the numerical solver. This thesis would not have been possible without his continuing support, motivation, and trust in me, for which I am most grateful. I feel immensely privileged to have had the chance to work with him in this research. Although Alistair has moved away from Oxford in 2011, he also has been a great support and help throughout this DPhil project. His enthusiasm and experience have helped to overcome many technical difficulties within this work. His bright ideas, encouragement and kindness have been the inspiration for me to apply for a degree at Oxford. In this respect, I owe him a great debt of gratitude. Throughout this project, I have also worked with Dr. Thomas A.A. Adcock, who has been an excellent mentor and a great friend. I am grateful to him for all the interesting discussions we had about tidal hydrodynamics as well as his support and encouragement. Together with Guy and Alistair, Tom has always been there for me, for which I am truly thankful.

I owe many thanks to colleagues and friends in the Civil Engineering Group for their support and advice. Special thanks to Conor Fleming, Christopher Vogel, Justine Schluntz, Clarissa Belloni, and Ignacio Lamada Martinez for all the technical support they have provided in accordance with many fruitful discussions we had throughout this DPhil. I would also like to thank Dr. Scott Draper, who has spent so many hours both in person and also over the phone, to establish the basis of the momentum sink approach within the discontinuous Galerkin method. His patience with me was remarkable and has been highly appreciated. Regarding the numerical techniques, support provided by Dr. Esteban Ferrer has been of great help. On the technical side, I must thank Dr. Ross McAdam for sharing his knowledge on tidal physics, which has contributed in shaping my work. I would like to acknowledge Dr. Ethan Kubatko of the Ohio State University here, for making the DG-ADCIRC numerical solver available to us and for his assistance in getting used to the code. In carrying out this project, I have received remarkable help from ECSG team. In particular, I would like to thank them for letting me use the computer labs during the first half of this project. However, without the services of the Advanced Research Computing of the University of Oxford, this project would have never been completed.

I would like to acknowledge the Energy Technologies Institute, which has been the funding body of the work presented in this thesis throughout the PerAWaT project.

I would also thank all my friends both in Oxford and abroad, for making my life a pleasure. Thank you all for finding the time to share a laugh or two when needed.

The last words belong to my family. To my parents, Sibel and Müjdat, I love you so much! I am most thankful to your trust, support and endurance. Without your endless love, prayers and encouragement, I would never have acknowledged my abilities and found the courage to follow my dreams. To my brother, Serdar, I love you! Thank you for basically being the best brother ever and for taking care of me all my life. You have planted the seeds of scientific curiosity in me, which has paved the way to where I am right now, thank you! With all those great people in my life, I feel most blessed.

CONTENTS

Nomenclature

Chapter 1

c	Wave celerity ($c = \sqrt{gH}$)
T	Period
λ	Wavelength ($\lambda = cT$)
g	Gravitational acceleration
H	Total water depth
u	Tidal current speed
ζ	Free surface water elevation
L	Distance between the open boundary and the reflecting boundary
ρ	Fluid density
A	Total swept area of the turbines within an array
SIF	Significant Impact Factor
α_4	Wake induction factor
P_{MAX}	Maximum undisturbed kinetic power density
B	Blockage ratio

Chapter 2

Section 2.1

δ	Ratio of length scales
H	Vertical scale of water column
L	Characteristic horizontal scale of the flow

Section 2.2

ζ	Free surface water elevation
h	Bathymetric depth of the water column below the geoid
H	Total depth of the water column (i.e. $H = \zeta + h$)
u,v	Depth-averaged velocity components in x- and y- directions
c_f	Bed friction coefficient
f	Coriolis parameter
F_x, F_y	Additional forces in the system in x- and y- directions (e.g. wind stress, tidal potential forces)
C	Chézy friction coefficient
n_M	Manning friction coefficient
Ω	Angular velocity of the Earth's rotation (2π rad/day)

θ_o	Latitude of the location of interest
β	Beta plane approximation parameter
δ	Incremental coefficient
R	Radius of the Earth
y	Coordinate positive northwards between latitudes θ_o+$\delta\theta$
$\mathbf{u}$	Vector of conserved variables
$\mathbf{F}$	Flux vector
$\mathbf{s}$	Source (sink) term vector
Section 2.3	
u	Conserved variable
Γ	Domain boundary
L_D, L_N	Value of the conserved variable defined by Dirichlet and Neumann boundary conditions respectively
∂_n	Gradient normal to the boundary
Section 2.6	
Ω	Flow domain
N_e	Number of non-overlapping elements
e	An element
Ω_e	Element domain
$\partial\Omega_e$	Element boundary
ϕ_h	Test function
V_h	Discrete space of piecewise polynomial functions
$\left(f,g\right)$	Inner product of functions f and g taken over the element domain Ω_e
$\langle f,g\rangle$	Inner product of functions f and g taken over the element boundary $\partial\Omega_e$
P^k	Space of polynomials of order k
$\mathbf{u}$	Exact solution
$\mathbf{u}_h$	Approximate solution
$\mathbf{n}$	Normal vector ($\mathbf{n} = \left[n_x, n_y\right]^T$)
$\widehat{\mathbf{F}}(\cdot,\cdot)$	Numerical flux
E1,E2	Arbitrary neighbouring elements in Figure 2.1
i	Common edge between elements E1 and E2 in Figure 2.1
u^{int}, u^{ext}	Solution on edge i when approaching the element from inside and outside of element E1 in Figure 2.1
Section 2.6.1	
ℓ	Single edge on an element e
Γ	Total number of edges in the flow domain
Ω	Element domain

$\partial\Omega$	Element boundary
Γ^{int}, Γ^{ext}	Set of interior and exterior edges
s^{int}, s^{ext}	Estimate wave speeds internal and external to the edge
s^*	Contact wave speed
$\overline{u}$, $\overline{v}$	Velocity components normal to the edge in *x*- and *y*- directions
q	Correction factor in HLLC numerical flux calculations
H_*	Water depth at the contact wave
Section 2.6.2	
$P_K^{\alpha,\beta}$	K^{th} order Jacobi polynomial of weighs α and β
ε_1, ε_2	Coordinates of the master triangle
η_1, η_2	Coordinates of the quadrilateral element
$\tilde{\mathbf{u}}_{pq}$	Model degrees of freedom
$\psi_{pq}(\varepsilon_1, \varepsilon_2)$	Trial (test) function described in Equation 2.30
Section 2.6.3	
L_h	Operator
c	Characteristic wave speed ($c = u \mp \sqrt{gH}$)
p	Polynomial degree
Δx	Smallest grid space
Δt	Time step
Section 2.6.4	
$\Lambda\Pi_h$	Slope limiter operant
Section 2.7	
(x, y)	Grid dimensions
u	Depth-averaged velocity in *x*- direction
R	Hydraulic radius
S_o	Bed slope
Re	Reynolds number
U_c	Characteristic velocity
L_c	Characteristic length
ν	Kinematic viscosity coefficient
U_{inlet}	Average upstream velocity across the inlet section
h	Half of the distance across the upstream channel
n	Polynomial order used in discontinuous Galerkin solution
E	Lamb parameter
R	Radius of the Earth
Ω	Angular velocity of the Earth's rotation (2π rad/day)
h_o	Mean depth (m)
(x', y')	Non-dimensional computational domain dimensions

r	Mesh resolution
$b(x)$	Bed profile

Chapter 3

Common to Chapters 4 to 8 and Appendix 1

H,u,v	Primitive variables of: total water depth, depth-averaged velocities in x- and y- directions
$\overline{(\ )}$	Normal to a computational element interface
$(\ )^{int,ext}$	Value of a variable on a Gaussian point along an edge when approaching the edge from the interior or exterior of it.
$(\ )_*$	Solution of a one-dimensional local Riemann problem
ΔH	Depth change across a turbine
Fr	Froude number
$\Delta H/H$	Relative head difference across a turbine
B	Blockage ratio
α_4	Wake velocity coefficient
α_2	Turbine velocity coefficient
β_4	Bypass flow velocity coefficient
T	Thrust applied to the flow by the turbine(s)
C_T	Thrust coefficient
C_{TL}	Local thrust coefficient
C_P	Power coefficient
D	Axial flow turbine diameter
b	Lateral spacing between tidal turbines in an array (in Section 3.2) The width of the open channel (in Section 3.2.1)
Θ	Ratio between the downstream and upstream total water column heights
c	Celerity
$P_{available}$	Available power to the turbines
P_{wake}	Power lost to mixing
P_{total}	Total power extracted from the stream
η	Turbine efficiency

Chapter 4

N	Total number of tidal elevation recording stations
n	Index for observation stations
(x_n, y_n)	Coordinates for each station
ζ_{M2}^{grid}	M_2 elevation amplitude for a given grid
H_n	Amplitude of a tidal constituent
σ_n	Angular speed (frequency) of a tidal constituent

φ_n	Phase lag of a tidal constituent (°)
t	Time
c_f	Bed friction coefficient
$u_{surface}$	Surface velocity of the fluid
$\bar{u}_{mean}$	Depth-averaged velocity
z	Distance vertically above the seabed
h	Local water depth

Chapter 5

u	Current velocity
P_a	Power available to the turbines
P_e	Power extracted from the stream

Chapter 6

φ_ζ	Tidal elevation phase (°)
φ_c	Tidal current phase (°)
$\Delta\varphi$	Phase difference between the tidal levels and tidal currents (°)
ω	Model forcing frequency
ω_{M2}	M_2 frequency
ω/ω_{M2}	Ratio of the model forcing frequency and the M_2 frequency

Chapter 7

ΣP_{avail}	Arithmetic sum of the available power outputs

Appendix 1

Also see Chapter 3 nomenclature

u_{t2}	Flow velocity at the turbine
u_{t4}	Wake velocity downstream of the turbine
u_{b4}	Bypass flow velocity
ρ	Fluid density
Fr	Upstream Froude number

Chapter 1

Introduction and Literature Review

Utilising the tides as a major renewable energy resource is presently under consideration in the context of increasing worldwide energy demand and the need to reduce carbon emissions to mitigate against global warming. In comparison to other sorts of renewable energy technologies, tidal energy is a highly predictable and robust energy resource (O'Rourke *et al.*, 2010). Conventionally, tides have been exploited by constructing a barrage across a tidal estuary to extract the potential power of the tides. Recently, exploiting tidal currents has been proposed as an alternative to utilising the rise and fall of the tides. This thesis considers utilising this latter technology and evaluates the maximum available tidal power at selected sites around the UK.

Exploitation of tidal currents requires the installation of in-stream tidal energy devices that act in a similar way to wind turbines (Draper, 2011). In order to extract a useful amount of energy, the proposed tidal turbines need to be deployed in an array (or farm-like) format (Vogel et al., 2013; Divett *et al.*, 2013; Vennell, 2012; Draper, 2011). The tidal flow is fundamentally different to the less constrained atmospheric flow, due to the presence of the free surface, and so deployment of tidal stream devices in an array will inevitably have a significant impact on the flow regime, even at basin-scale. Changes to the flow would in turn affect the efficiency of the tidal devices, limiting the amount of power available to the turbines. Thus, it is important to understand the natural tidal response of basins for resource assessment.

Section 1.1 summarises the physical description of naturally occurring tides, and tidal patterns. Section 1.2 provides an introduction to presently available technologies for extracting power from the tides. Section 1.3 reviews the literature on different methodologies employed to assess tidal stream power resource. Section 1.4 introduces the UK tidal basins selected for the resource assessment study. Section 1.5 lists the aims and objectives of this thesis. Section 1.6 provides a brief outline of the thesis.

1.1. Naturally Occurring Tides

Naturally occurring tides can be simply explained by Newton's law of gravitation, which states that any particle in the universe attracts another particle with a force directly proportional to the masses of the bodies, but inversely proportional to the square of the distance between them (Pugh, 1987). In this respect, tides occur as a result of the dynamic response of the oceans to the gravitational forces applied primarily by the Moon and the Sun, with a minor contribution made by other celestial bodies (Draper, 2011; Pugh, 1987). The response of the oceans can be observed by means of the rise and fall of the mean water level (Cartwright, 1993). The amplitude of this change in the water level is dependent on many factors in addition to the gravitational attraction applied by the Moon and the Sun. Pugh (1987) explains that if the Earth were a perfect sphere covered with water that is deep enough, and would not be affected by its rotation (i.e. the Coriolis acceleration), the tides would occur instantaneously due to the applied gravitational force. This results in the so-called equilibrium tide. In this case, the amplitude of the tidal range would be much smaller than the actual ocean tides. However, the presence of the continents, the Coriolis force, bed friction, and the variable ocean bathymetry have an important influence on the response of the oceans to tidal forcing (Draper, 2011). Consequently, the natural modes of oscillation of the oceans, which have periods close to the semidiurnal tidal period, lead to substantial differences between the observed tidal ranges around the world (Garrett and Maas, 1993; Platzman *et al.*, 1981).

Although the tidal response of the oceans is highly complicated due to the different mechanisms involved, it is possible to explain several features of the oceanic tides in general terms (Webb, 1976). The following sections aim to summarise these common features.

1.1.1. Tidal Patterns

The observed common patterns in the oceanic tides are related to the motions of the celestial bodies relative to the Earth, which have an influence on large diurnal tides as well as the spring-neap cycles (Pugh, 1987). Diurnal tides occur once a day due to the relative declination of the Sun and the Moon with respect to the Earth, with the declination determining the variation of the tidal range (Pugh, 1987). For instance, the solar declination varies seasonally, and is at its highest in June and December. The contribution of the solar declination along with that of the major lunar declination results in large diurnal tidal ranges

during these months. Over a nodal period of 18.6 years, the lunar declination reaches a maximum, which contributes to the overall diurnal tidal ranges (Lisitzin, 1957).

Semidiurnal tides occur twice a day, and are, in amplitude, considerably greater than the diurnal tides (Pugh, 1987). The frequency band of the semidiurnal tides (12.41 hours) is close to the near resonant period (~14 hours) of some oceans (Pugh, 1987; Platzman *et al.*, 1981). One of the largest semidiurnal tides observed in the UK is the M_2, which is the principal lunar tidal constituent. Figure 1.1 shows the principal lunar semidiurnal tidal constituent (M_2) range around the world. The M_2 tidal constituent has average amplitude of about 0 - 50 cm in the deep ocean and exceeds 130 cm around the UK coasts. The white lines on the figure indicate the co-tidal lines, which join locations where the high waters occur simultaneously. The contour plot shows the amplitudes of the observed M_2 tidal constituent. Similarly, the tidal harmonic maps can be presented by superimposing the co-tidal lines onto the co-amplitude lines, which delineate locations with the same tidal amplitudes.

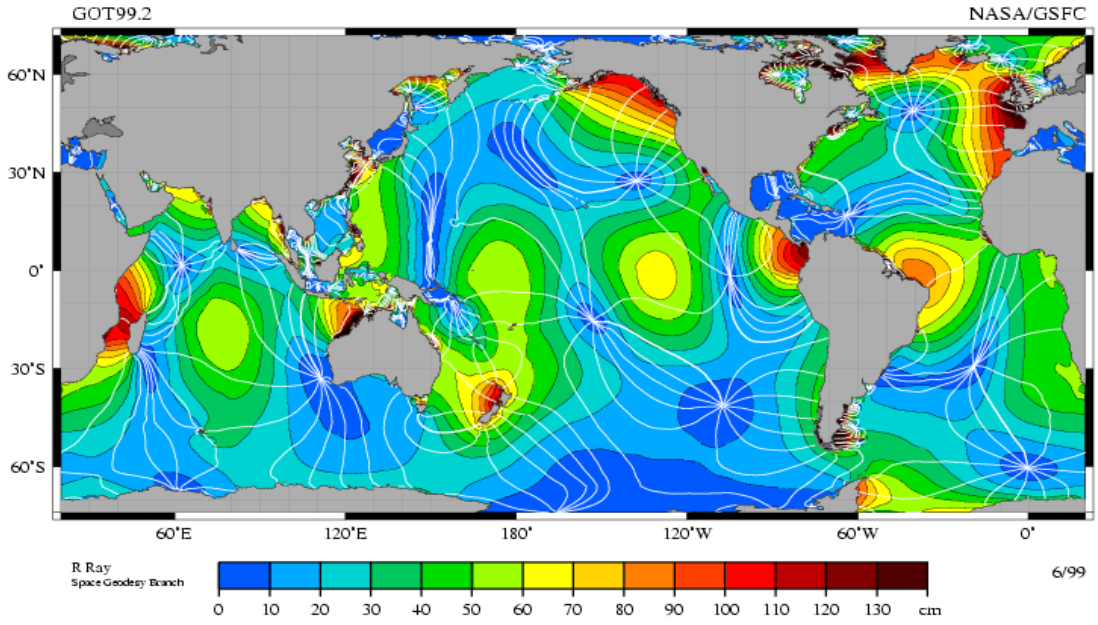

Figure 1.1 M_2 tidal ranges around the world. The white lines indicate the co-tidal lines where high tides occur at the same time (NASA, 2006).

Figure 1.1 shows a number of amphidromes, defined as positions where the amplitude of a harmonic constituent tends to zero, implying no change in water level over the tidal cycle. The co-tidal lines emanate from these amphidromic points about which the tidal wave rotates. These amphidromic systems behave in a similar manner as a Kelvin wave in terms of

propagation, where the rotation of the propagation is anticlockwise in the northern hemisphere and clockwise in the southern hemisphere (Pugh, 1987).

Due to the time-dependent relative alignments of the Sun and the Moon with respect to the Earth, the amplitudes of the semidiurnal tidal constituents vary with a period of 14.8 days. Within this period, spring tides occur when the solar and lunar tide-raising forces are in-phase and have a magnifying effect on the amplitudes of the semidiurnal tides (Pugh, 1987). Neap tides occur when the solar and lunar tide-raising forces are at quadrature, resulting in low tidal ranges. Pugh (1987) notes that the amplitudes of two successive spring tides are usually different due to the varying distance between the Moon and the Earth. The tidal amplitudes at a lunar perigee (when the Moon is closest to the Earth) are 15% greater than when the Moon is at an average distance and are 15% lower during an apogee, when the distance between the Moon and the Earth is at greatest (Pugh, 1987).

1.1.2. Long Wave Characteristics

The semidiurnal tides and diurnal tides are long waves with periods of 12.41 hours and 24.83 hours, respectively, and wavelengths (several hundreds of km) that are much larger than the ocean bathymetric depths (Pugh, 1987).

Considering a non-rotating system, as an ocean gravity wave propagates away from a fixed point, high and low water levels will be observed respectively, which are a one-half a wavelength distance away from each other (Pugh, 1987). If the wave propagates with celerity c and period T, the wavelength is,

$$\lambda = cT. \qquad 1.1$$

Assuming that the wave amplitude is much smaller than the total water depth and that the water depth is considerably smaller than the tidal wavelength, the wave celerity can be written as (Lamb, 1932; Proudman, 1953),

$$c = \sqrt{gH}. \qquad 1.2$$

Equation 1.2 implies that the wave celerity, c, depends on the gravitational acceleration (g) and the total water depth (H). From classical long wave theory (Pugh, 1987) it may be shown that the tidal current speed, u, is related to the free surface elevation (ζ) at a fixed point by,

$$u = \zeta\sqrt{\frac{g}{H}}. \qquad 1.3$$

At times of local high water, the maximum current is in the same direction as that of the propagating wave. However, at times of low water, the current is in the opposite direction to that of the propagating wave (Pugh, 1987).

When a tidal wave reaches the continental shelf, it undergoes reflection due to the relatively sudden change in depth. The observed tide is thus a combination of the propagating and reflected waves (Defant, 1961; Redfield, 1980; Pugh, 1987). Pugh (1987) uses an idealised case of a sinusoidal flow in a long, frictionless channel of constant depth to explain the characteristics of a tidal wave. The absence of friction in the system means that energy is conserved, so that the amplitude of the reflected wave is the same as that of the incident wave when the wave reaches the barrier at the head of the channel. A standing wave occurs as the incident wave interferes with the reflected wave. A standing wave system consists of 'nodes', where the amplitude is equal to zero with maximum currents, and 'antinodes', where amplitude is a maximum and the current is zero. For a tide with wavelength λ, the distance between these nodes and antinodes is $\lambda/4$ (Pugh, 1987). The first node is located a quarter-wavelength away from the barrier; the first antinode is half a wavelength away from the barrier. The time required for a wave to propagate from the entry to the channel and then return to the same point after reflection is the natural period of oscillation, and is given by (Proudman, 1953),

$$\frac{2L}{\sqrt{gH}}, \qquad 1.4$$

where L is the distance between the open boundary to the reflecting barrier.

The amplitude of the observed tides is also affected by the natural oscillation periods of the oceans and seas (Pugh, 1987). The response of an ocean or sea to tidal forcing is amplified when the period of the forcing oscillations is close to the natural period of the ocean and sea.

In real oceans, the reflected waves are smaller in amplitude due to the frictional forces applied at the seabed decaying the wave amplitude along the channel. This in turn results in weaker reflected waves, corresponding to superposition of a progressive wave on a standing wave (Pugh, 1987). In such a system, the progressive wave carries the tidal energy to the

upper reaches of the basin. An example for this kind of system is the Irish Sea, which will be discussed in detail in Chapter 5.

One of the primary objectives of this thesis is to understand the change in the tidal system due to the operation of tidal turbine arrays. This implies that the energy of the incoming waves will be extracted, which in turn results in decreased tidal ranges in the immediate vicinity of the turbine arrays. This change in the tidal range will inevitably affect the partially progressive wave structure observed in many coastal areas. Chapter 7 presents a discussion on how the local tidal regime is affected when large tidal farms are deployed at selected sites around the UK.

1.2. Tidal Energy Resource

The global energy demand is presently primarily met by the fossil fuel resources (O'Rourke *et al.*, 2010). According to the International Energy Agency (2007), 88% of the global energy share is provided by fossil fuel, consisting of oil, natural gas, and coal. However, these resources are finite, and an alternative needs to be provided to address the growing global energy demand. Moreover, the environmental impact of using fossil fuels is a problem in its own right (O'Rourke *et al.*, 2010). The release of greenhouse gases has resulted in an on-going global rise in temperature and corresponding rise in the mean sea water levels (US NREL, 2005). In this respect, development of renewable energy technologies could play an important role in decreasing the exploitation of conventional energy resources while having a neutral impact on the climate.

The European Union has set renewable energy targets to be achieved by 2020 for EU countries to reduce the climate change impact of carbon dioxide emissions (DECC, 2010). Within the scope of the EU Renewable Energy Directive (2009), EU countries are each required to prepare an action plan designed according to the available renewable energy resources (in the country concerned), specifying how and by how much they aim to utilise such resources to meet the EU standards for energy production (DECC, 2010).

This EU directive requires the United Kingdom to ensure that 15% of its total energy consumption must be met by means of renewable energy resources by 2020 (EU Renewable Energy Directive, 2009). In this context, the UK is focusing on the following renewable energy resources: offshore wind, biomass, geothermal energy, wave and tidal energy (DECC,

2010). Of these resources, tidal energy is of significant importance as tides are predictable and there are several sites around the UK where the tidal current speed exceeds 2 m/s, the critical speed for viable power production (ABPmer *et al.*, 2004). In the Atlas of UK Marine Renewable Energy Resources published by DTI (2008), the main sites that are found to be appropriate for tidal energy utilization are listed such as the Pentland Firth, Anglesey, the Isle of Wight, the Bristol Channel, Alderney, Islay and Campbeltown.

Two main approaches are taken to extract energy from tides. The first approach focuses on utilising the tidal range by constructing barrages or lagoons in bay areas, using turbines as in wind energy industry. The second approach is to install turbines at locations where the tidal current velocities are within sensible limits (Black and Veatch, 2005). The following sections summarise the status of tidal energy technologies, with particular emphasis on the UK.

1.2.1. Tidal Barrages

Tidal barrages utilise the rise and fall of the tides. Typically tidal barrages are operated in ebb generation mode, which involves filling the basin with water during flood tide and releasing the trapped water through the turbines when there is a sufficient hydrostatic head difference across the barrage (O'Rourke *et al.*, 2010; Baker, 1991; Prandle, 1984). Tidal barrages can also be operated in flood generation or a two-way generation mode (O'Rourke *et al.*, 2010).

Around the world, there are four tidal barrages operating (O'Rourke *et al.*, 2010). The oldest of these tidal barrages is located in France. La Rance tidal barrage has been operating since 1967 and has a capacity of 240 MW with a net power output of approximately 480 GWh/y (Boyle, 2004). Another tidal barrage is located in the Bay of Fundy, Canada. The Annapolis tidal barrage was constructed in 1984 as an experimental prototype of its kind in the Bay of Fundy and has a generating capacity of 20 MW (Percy, 1996). The other barrages are located in Russia (Kislaya Guba power facility) and on the East China Sea (Jangxia Creek) respectively (O'Rourke *et al.*, 2010). Both Kislaya Guba and Jangxia Creek power facilities have relatively smaller power generating capacities ($\leq$ 500 kW).

Although the technology for constructing and operating tidal barrages is available and reliable, investment on tidal barrages has been very restricted, due to the high capital cost associated with construction and environmental concerns. Tidal barrages are designed to hold

large volumes of water for a period of time until there is a significant hydrostatic head difference across the barrage. Restricting the natural water movement in this manner will alter the flow and the tidal dynamics of the system. The enhanced sediment transport due to retaining water behind the barrage affects water quality, and hence the ecology and marine life in the vicinity of the tidal barrage.

Considering the UK coasts, the largest tidal range resource is available in the Severn Estuary. According to DECC (2010), 5% of the UK's current electricity generation could be provided by a tidal barrage constructed across the Severn Estuary. The Severn Estuary is situated at the upper reaches of the Bristol Channel, which has one of the largest tidal ranges worldwide. At spring tides, the Severn Estuary has a peak tidal range of approximately 14 m (Xia *et al.*, 2010a; Ahmadian and Falconer, 2012).

There are several sites suggested for construction of a tidal barrage across the Bristol Channel. Among these, the Cardiff-Weston site is found to be the most feasible with the lowest energy cost (DECC, 2010). The total installed capacity of a Cardiff-Weston tidal barrage (also referred as the Severn Barrage) is 8640 MW and the annual energy generation is estimated to be 15.6 TWh/yr.

Operation of a tidal barrage, however, changes the tidal dynamics of the system, primarily by reducing the tidal range within the basin (Yates *et al.*, 2013). A previous study conducted by Xia *et al.* (2010a) estimates the change in the water levels in the vicinity of the Cardiff-Weston Barrage to be between 0.5 m - 1.5 m. The same study states a considerable change in the current velocities in the main Channel. Several other studies have been conducted to understand the change in the environment (i.e. water quality and sediment transportation) and the tidal hydrodynamics of the system (Radford, 1982; Harris *et al.*, 2004; Xia *et al.*, 2010b; Kadiri *et al.*, 2012). In addition to the environmental concerns, constructing a tidal barrage across the Severn Estuary would incur very high capital costs compared to other kinds of renewable energy technologies. Overall, the DECC report (2010) concludes that it is not feasible to invest in any tidal barrages in the Channel to accomplish the UK renewable energy production goals by 2020.

1.2.2. Tidal Lagoons

Tidal lagoons operate in a similar manner to the tidal barrages, which make use of the water level difference occurring between flood/ebb tides. Rather than enclosing an entire bay or estuary as is done in tidal barrage construction, tidal lagoons impound a sub-region of water. (DECC, 2010).

The report published by DECC (2010) explains that the several lagoon proposals are considered in the Bristol Channel, and among these the Bridgwater Bay lagoon (between Hinkley Point and Weston-super-Mare) is found to be potentially feasible due to lower capital coasts and environmental impact when compared to the barrage proposals. The installed capacity of the Bridgwater Bay lagoon is 3600 MW and the annual energy generation is estimated to be 6.2 TWh/yr. Other advantages of constructing the Bridgwater Bay lagoon are its estimated long-term value in terms of the energy supply costs, the benefits in carbon emission and increased employment opportunities in the local community (DECC, 2010). However, the shipping in the region will be disturbed due to the operation of the tidal lagoon. The DECC (2010) report reveals that the UK Government is hesitant to invest in a lagoon as it may interfere with the cost-effectiveness of any future tidal barrage across the Severn Estuary.

1.2.3. Tidal Stream Turbines

There has been a considerable interest in exploiting the tidal currents as a potential renewable energy resource due to the lower capital costs as well as lower environmental impact when compared to barrage and lagoon schemes (Xia *et al.*, 2010c).

Extracting the energy from the tidal stream requires converting the kinetic energy of the flow into useful extractable power (Bryden and Couch, 2006). Much of the proposed technology to exploit tidal currents has effectively been translated from wind energy technology (O'Rourke *et al*., 2009; Bryden and Couch, 2006). However, tidal power devices are at a much less mature stage of development than wind power, with only a few prototype-scale devices installed around the world (Gross, 2004; Denny, 2009). The tidal power devices have to be designed to operate in the free surface flow water of density approximately 1000 times that of air, whereas wind turbines are situated in unconstrained flow fields (Kadiri *et al*., 2012; Garrett and Cummins, 2008; Bryden *et al.*, 2004). Regarding the device design, the

proposed tidal power turbines can be broadly divided into three main categories (McAdam, 2011):

- Axial-flow devices,
- Cross-flow devices (e.g., Darrieus-type) and,
- Other devices (e.g., oscillating turbines).

Of these designs, the axial-flow devices (see Figure 1.2-Left) resemble conventional wind turbines, and so have gained substantial attention by investors due to the previous research conducted by the wind industry over decades (McAdam, 2011). In January 2010, the axial-flow SeaGen device (Figure 1.2-Right) designed by Marine Current Turbines (MCT) was deployed in Strangford Lough, Ireland with a capacity of 1.2 MW and has been operating since then (Fraenkel, 2007). However, in order to extract a useful amount of power from the tidal stream, the turbines need to be installed in an array format to cover a large cross-sectional portion of the tidal stream (Divett *et al.*, 2013; Vogel, 2012; Draper 2011; McAdam, 2011). In this respect, MCT has recently been granted permission to install a 10 MW prototype-scale tidal turbine array off Anglesey (Wales) in 2015. This project is likely to be the first array-scale application of tidal turbines in a real tidal site.

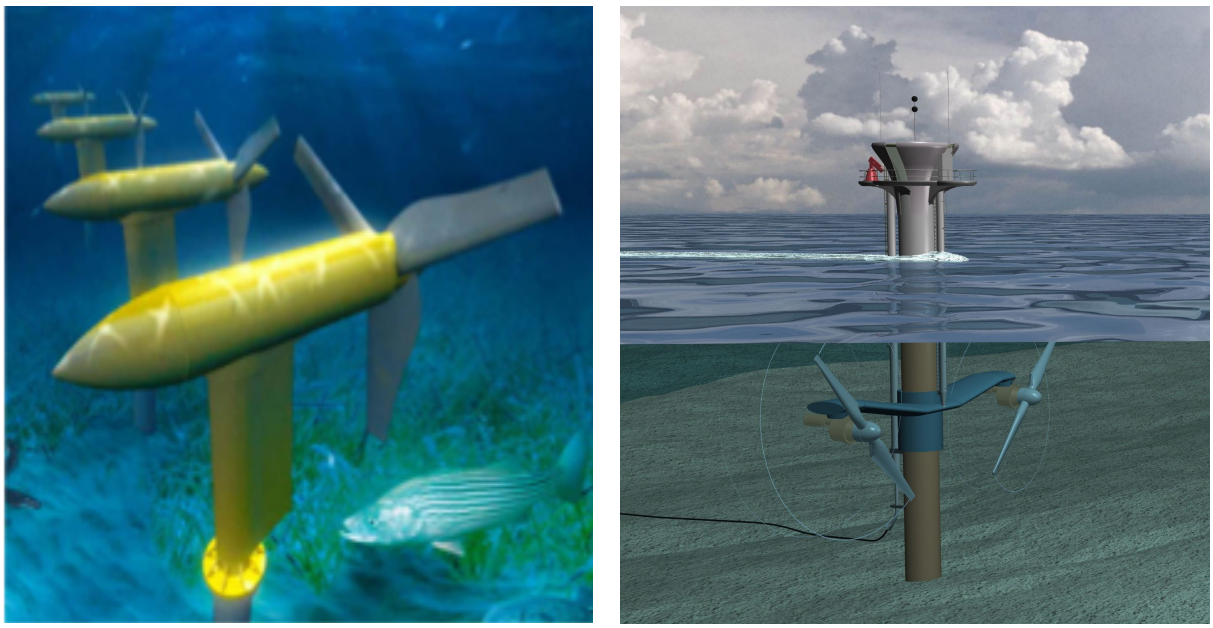

Figure 1.2 – Left: Verdant Power Ltd. Axial-flow tidal turbine; Right: MCT SeaGen axial-flow tidal turbine. Images are taken from O'Rourke *et al.* (2010).

The selection of a tidal turbine for an array-scale project depends on several factors, such as the device construction and maintenance cost, electricity transmission and load conditions

(Draper, 2011; McAdam, 2011; O'Rourke *et al*., 2010). For axial flow turbines, the power that can be generated with one single turbine is mainly restricted by the size of the turbine, due to the limited bathymetric depths (McAdam *et al*., 2013; McAdam, 2011). Some devices, such as the Transverse Horizontal Axis Water Turbine (THAWT) device could be installed so that the device occupies a greater proportion of the channel cross-section (see Figure 1.3). This would allow a device to utilise blockage effects that are not available to be a more conventional axial flow turbine (McAdam *et al*., 2013). As with other innovative tidal turbine designs, the THAWT device has been tested under experimental conditions, but a full-scale application of the device at a tidal site has not yet occurred (McAdam *et al.*, 2012). There are various other designs proposed to utilise the fast tidal currents, two of which are given in Figure 1.4.

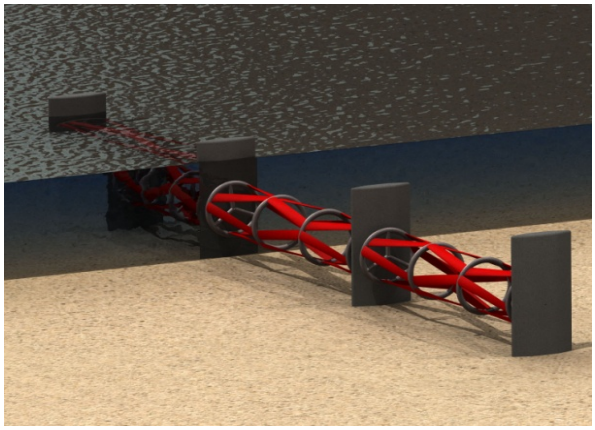

Figure 1.3 – THAWT device installed in an idealised channel (McAdam, 2011).

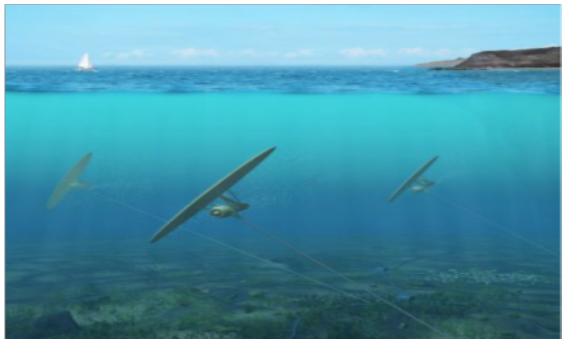

Figure 1.4 – Left: Minesto Deep Green Tidal Kite (http://www.minesto.com/deepgreentechnology/index.html); Right: Pulse Tidal Hydrofoil (http://pulsetidal.com/our-technology.html).

Most of these alternative devices are at a design (or prototype) stage, and thus will not be reviewed in this thesis. However, it is possible that when compared to the conventional tidal

turbine devices, some of these designs may be more feasible to develop at specific tidal sites (McAdam, 2011).

From an environmental point of view, the hydrodynamics of the system will inevitably change in the vicinity of the tidal array. Extracting energy from the tidal flow results in a head drop across the turbines, which translates into an increase in the downstream flow velocity (Draper, 2011; Bryden and Couch, 2007). The presence of the tidal turbine arrays (regardless of the turbine design) alters the flow conditions as they introduce an additional resistance to the flow, reducing the mass flux passing through the turbines, and thus reducing the extractable power (Garrett and Cummins, 2008). Research regarding the understanding of the physics of extracting energy from the tidal currents is therefore well established. However, characterising the available tidal resource is still an on-going research field. The following section aims to provide a literature review on the methodologies adopted to quantify the tidal resources.

1.3. Tidal Stream Resource Assessment Methodologies

Different approaches have been taken towards estimating the available power that can be extracted from tidal flows, noting that a certain percentage of the energy will be dissipated owing to frictional effects (Garrett and Maas, 1993). In some previous studies, the available power was quoted as a percentage of the kinetic energy flux in the tidal stream (DTI, 2008; Black and Veatch, 2005; Fraenkel, 2002), but this neglects the potentially significant impact of tidal arrays on the hydrodynamics. As Sutherland *et al.* (2007) note, the deployment of large arrays in coastal basins will eventually block the flow, causing the by-pass flow to increase, along with a decrease in power generation. Consequently, several analytical (Garrett and Cummins, 2005; Blanchfield, *et al.*, 2008) and numerical (see e.g. Draper, *et al.*, 2010; Karsten *et al*., 2008) studies have been conducted to assess the available energy to be extracted from tidal streams and to improve the understanding as to how this power extraction will affect the far-field hydrodynamics. The present study examines these approaches and adopts the numerical method developed by Draper *et al*. (2010), discussed in detail in Chapter 3, in order to assess the maximum available power at a coastal site and investigate the far-field effects of extracting energy. The following sections summarize the methodologies proposed to date to assess the energy potential of a tidal site.

1.3.1. Theoretical Approaches

Methods based on actuator disk theory are useful for evaluating the flow regime around a tidal device (Vogel, 2012). Actuator disk theory was first developed by Rankine (1865) and then extended by Froude (1889) to provide a one-dimensional analysis of the steady incompressible flow field around a propeller, approximated as an infinitely thin (porous) disk that exerts a thrust force to the fluid passing through it (Horlock, 1978). In the analysis, the thrust on a real propeller is replaced by the uniform normal pressure distribution on the actuator disk (Van Kuik, 2007). Lanchester (1915) and Betz (1920) independently applied actuator disk theory to assess the performance of an inverse propeller in an infinite flow, such as a wind turbine, and defined an upper limit to the kinetic energy that can be converted to usable power (Bergey, 1979). In the literature, this is known as the Lanchester-Betz limit, which gives the maximum theoretical energy conversion ratio as 16/27 of the upstream kinetic energy flux of the wind stream. Although the Lanchester-Betz limit cannot be attained by real turbines due to various energy losses (e.g. mechanical, electrical) and non-uniformities in the incident flow conditions, the theory has proven to be a useful tool by which to design and compare wind turbines over the years (Kalenauskas, 2010). Owing to the constrained nature of the tidal flow field however, Lanchester-Betz theory is not directly applicable to tidal streams (Houlsby *et al.*, 2008; Bryden and Couch, 2006). With this limitation in mind, several techniques are considered to evaluate the power potential of sites where strong tidal currents are observed. An early attempt to characterise the tidal sites as well as estimating the maximum available power from a site was suggested by Black and Veatch (2005), who used a relation based on the undisturbed kinetic energy flux of the tidal flow,

$$P_{MAX} = \frac{1}{2}\rho u^3 A(SIF). \qquad 1.5$$

where ρ is the water density, u is the flow velocity and A is the total swept area of the turbines and *SIF* is the 'Significant Impact Factor', which accounts for any constrictions that may limit the available power from tidal currents. Equation 1.5 provided values for the power density range around the coasts of the UK, which was then used to estimate an upper limit for available power within a site. However, this approach has been criticised by MacKay (2007) and Garrett and Cummins (2005) who suggest that there is no direct relation between the

undisturbed kinetic energy flux of the tidal stream and the average maximum power to be extracted from it.

Methods based on a simple undisturbed kinetic energy flux calculation do not consider the change in the flow field due to the presence of the tidal turbine arrays, and hence give overestimates of the available power in selected tidal areas (Vogel *et al*., 2013; Draper, 2011). Bearing in mind that the turbines will act as an additional resistance to the flow, increasing the thrust applied to the flow by the array results in a flow diversion at the edges of the array (Draper, 2011). As the flow diverts, the mass flux entering through the array is decreased resulting in a reduction on the available power to the turbines (Vogel *et a*l., 2013; Draper *et al*., 2013). Garrett and Cummins (2005) further explain that the maximum average available power is dependent on the number of the turbines and the array locations in the designated coastal area. Referring back to the Lanchester-Betz theory, the installation of a small number of axial flow turbines in a basin will result in hardly any energy being extracted, whereas choking the flow by installing too many turbines will cause a significant reduction of the amount of energy to be extracted due to the flow bypassing the turbine array (Draper, 2011; Sutherland *et al.*, 2007).

To accurately evaluate the available power where strong currents occur, Garrett and Cummins (2005) considered an idealised channel that connects two large basins, where the flow is driven by the head difference, and the tidal fences span the entire width of the channel. The analysis assumes that the free-surface of the flow in the channel has a fixed lid (i.e. is volume constrained) and that the Froude number may be neglected. In their analysis, Garrett and Cummins (2005) related the maximum average power to the peak pressure head and the undisturbed mass flux through the channel. In reality, the turbine fences cannot occupy the entire channel cross-section, thus it is of importance to understand the effect of turbine arrays to the flow field that blocks the channel only partially. To address this issue, Garrett and Cummins (2007) extend their previous analysis (Garrett and Cummins, 2005) to consider a partially blocked channel, in which the turbines are uniformly spaced from each other across the channel cross-section. Their results indicate that the power available to the turbines is dependent on the mass flux passing through the turbine(s), which is associated with the force applied to the flow by the turbine(s). In their analysis, Garrett and Cummins (2007) also

included the downstream mixing that extends beyond the turbine wake, leading to a description for tidal turbine efficiency, which is defined as the ratio of power that is available to the turbines to the total power that is removed from the stream (including frictional and mixing losses). Their analysis show that, depending on the blockage ratio, operating the turbines with a high wake induction factor ($\alpha_4 = 1/3$) increases the available power at an expense of decreased turbine efficiency due to the increased level of energy loss through mixing.

The effect of array scale hydrodynamic interactions on the turbine efficiencies is studied by Vennell (2010). In their analysis, Vennell (2010) also employed an analytical model that uses low Froude numbers (volume constraint). The analysis considers evaluating the optimum turbine operating velocity that maximises the available power for known blockage ratios and array configurations. When multiple arrays are deployed in a tidal channel, Vennell (2011) and Vennell (2012) show that extending the length of the array is more effective in terms of extracting power than adding further rows of turbines in the system. In their analysis, Vennell (2012) and Vennell (2013) discuss that, increasing the array thrust by adding additional rows of turbines, significantly decrease the flow passing through the entire turbine arrays, and hence decrease the power that is available to the individual turbines in the arrays. This conclusion is then numerically verified by studies of Adcock *et al.* (2013) and Draper *et al.* (2013). As explained by Vogel (2012), the Garrett and Cummins type models provide a significant understanding of the physics involved in tidal energy extraction, however an extension is required to approximate the real open channel flows that considers variable Froude numbers. In this respect, Whelan *et al.* (2009) employ the Garrett and Cummins type model whereby the free surface was allowed to deform and the Froude number could be finite in the analysis. The power coefficient obtained by Whelan *et al* is dependent on the operating conditions of the turbines (turbine size and porosity) as well as the upstream flow conditions. However, the model proposed by Whelan *et al.* (2009) does not include downstream mixing in the analysis, which leads to restrictions on the upstream flow conditions. This issue was addressed by Houlsby *et al.* (2008) by considering an open-channel flow past a row of turbines that are uniformly spaced across the width of a channel in which the flow had a deformable free-surface and downstream mixing. Draper (2011) concludes that the approach

proposed by Houlsby *et al* is a combination of the separate ideas by Garrett and Cummins (2007) and Whelan *et al* (2009). Houlsby *et al.* (2008) derives a relation between the turbine specifications (turbine size and porosity) and the associated flow change in terms of upstream and downstream flow velocities and depths. The relation presented by Houlsby *et al.* (2008), which describes the change in the free-surface head, is of importance as it provides the basis by which to include a momentum sink in a depth-averaged model (Draper *et al.*, 2010; Draper, 2011). Chapter 3 describes the inclusion of a momentum sink in a selected depth-averaged shallow water solver using the linear momentum actuator disk model developed by Houlsby *et al* (2008) as a sub-grid model.

Draper *et al* (2010) and Draper (2011) apply the linear momentum actuator disk theory developed by Houlsby *et al* (2008) to investigate the flow conditions where the turbines are only partially blocking the channel. This work showed that as the blockage of the turbines increases (for optimum wake velocity coefficient), the bypass flow is increased, which inevitably reduces the amount of power extracted by the turbines. A further investigation on the relation between the upstream flow bypassing the array and the power extraction within the array is undertaken by Nishino and Willden (2012b). In their analysis, Nishino and Willden distinguish the two scales involved, turbine scale and the array scale, which ultimately have an effect on the power extraction. However, the analysis conducted by Nishino and Willden (2012b) is based on a zero-Froude number model, as proposed by Garrett and Cummins (2007), and is restricted to small blockage ratios. Vogel (2012) extended the model proposed by Nishino and Willden to include finite Froude numbers in their analysis. The results provided by Vogel (2012) agree well with the previous studies regarding the effect of high blockage on the available power. This analysis also shows that extracting the maximum power from the flow has a significant effect on the flow field at the vicinity of the tidal turbines. Considering an infinitely wide channel, Vogel (2012) concludes that the available power is only dependent on the Froude number of the flow and the turbine blockage ratios.

Although the foregoing theoretical approaches have provided useful insight into the power extraction by tidal turbines, further analysis is still required by using numerical models to

understand the effects of installing tidal arrays in tidal basins. The following section provides a summary of the numerical methodologies used for tidal resource assessment.

1.3.2. Numerical Approaches

Theoretical models are capable of predicting the change in the flow regime in a channel or basin due to the presence of the tidal devices, as well as predicting the velocities in the immediate vicinity of the turbines (Vogel *et al.*, 2013). A variety of numerical methods at different scales are employed to: a) design tidal devices, b) investigate the interaction between turbines in an array, c) investigate the hydrodynamic interactions between arrays, and d) evaluate how much power can be generated by the turbine(s).

Models employed to evaluate the immediate flow characteristics around an array considers using three-dimensional CFD models, where the devices are represented by using actuator disks or by other techniques (see e.g. Nishino and Willden 2012a; Schluntz and Willden, 2013, Fleming *et al*., 2013). Vogel (2012) discusses that the main advantage of such models is that their capability to properly resolve the wake mixing, thus predict the power available to the turbines more accurately. However, modelling of a large number of devices deployed at a coastal site by using three-dimensional models is computationally challenging. At basin-scale, it is most practicable to use numerical solvers based on the two-dimensional shallow water equations to simulate the change in the flow field due to the operation of proposed tidal arrays (Adcock *et al.*, 2013; Walkington and Borrows, 2009) and to evaluate the environmental impact of these arrays (Ahmadian and Falconer, 2012; Xia *et al.*, 2010c).

Commonly, two methods are used to represent the tidal devices in shallow water models. Either the turbines can be represented as a discontinuity in the flow (e.g. Draper *et al.*, 2010) or the drag applied by the turbines can be smeared over an area by enhancing the bed friction of given mesh nodes (e.g. Sutherland *et al.*, 2007; Bryden *et al.*, 2007). The latter approach is often used in numerical models as it requires few (or even no) changes to the source code, and produces results that are reasonably close to those provided the alternative momentum sink approach. However, a major drawback of using an increased bed friction coefficient is that the power extracted from the site includes both the available power (extracted by the turbines), and power lost due to frictional forces and downstream mixing (Draper, 2011). Also, there is no direct relation between the tidal array configurations (parallel or series connections) to the

total available power extracted from the tidal farm site (Vogel, 2012; Draper, 2011). In the literature, the enhanced bed friction method has been used to assess the tidal current resources at real sites. Examples of such research studies are given by Blunden and Bahaj (2007) who investigated the tidal potential of Portland Bill, UK, Sutherland *et al*. (2007) and, Karsten *et al*. (2008) who conducted similar analyses respectively for the Johnstone Strait and the Minas Passage in Canada. Karsten *et al*. (2008) demonstrate that a maximum of 7 GW is extractable from Minas Passage, which corresponds to a 40 per cent reduction in the flow through the passage. However, the results obtained by using an increased bed friction applied on a small passage imitate the effect of constructing a barrage across the Minas Passage. For this reason, it is important to develop a more elaborate method to represent the tidal devices in an array using a two-dimensional numerical model, first to quantify the power potential of the site, and secondly to evaluate the altered flow field more accurately. In this respect, Draper *et al.* (2010) implemented a numerical method using linear momentum actuator disk theory as a sub-grid model to represent the tidal turbine operating condition, which is incorporated as a line sink of momentum in a two-dimensional shallow water solver. This method has been used by Draper *et al.* (2010) and Draper (2011) to assess tidal energy potential of idealised geometries, such as headlands, straits, enclosed bays or estuaries and islands, near to the mainland, where the fast tidal currents occur.

The shallow water model used in the present thesis is based on a discontinuous Galerkin finite element method, which enables discontinuities to be included properly in the solution. The line sink of momentum is then imposed at specified edges of the elements that represent the tidal array. On an edge where the line discontinuity occurs, the upstream and downstream flow conditions (i.e. axial flow velocities and total water depths) are modified according to linear momentum actuator disk theory (Houlsby *et al*., 2008). In order to solve the system of equations related to LMADT, the blockage ratio and porosity of the turbines (i.e. wake velocity coefficient) are prescribed as an input to the numerical solver.

The momentum sink method developed by Draper *et al*. (2010) and Draper (2011) has been applied in various recent studies. One such study considers evaluating the tidal energy potential of an idealised headland (Draper *et al.*, 2013). Draper *et al*. (2013) found that the power extracted by the turbines is very sensitive to the turbine operating conditions for a

partially blocked flow. When high thrust is applied to the flow, it tends to bypass the tidal array. This in turn causes a reduced mass flux passing through the array, which inevitably reduces the power extracted by the turbines. The same method was applied to the Pentland Firth by Adcock *et al*. (2013) to estimate an upper limit on the available power that can be extracted from the Firth. In their analysis, Adcock *et al*. use M_2 and S_2 tidal constituents to force the model at the open ocean boundaries. The analysis indicated that for a high blockage ratio (B = 0.4), and using two rows of tidal turbine arrays that extend across the entire width of the channel, an average power of 1.9 GW can be generated from the Pentland Firth. Similarly, Serhadlıoğlu *et al.* (2013) used a line sink of momentum method to quantify the tidal resource of the Anglesey Skerries off the Welsh coast. A parameter study was used to evaluate the importance of the turbine operating conditions, array connectivity and array locations on the available power. In their analysis, Serhadlıoğlu *et al*. also considered the disturbance caused by turbine arrays to the local hydrodynamics. Quantification of the disturbance was undertaken by computing the changes to the M_2 tides caused by the presence of the turbines. The study showed that neither the amplitude nor the phase of the M_2 constituent changed significantly even at maximum power extraction. Chapter 5 of this thesis describes an extended version of the analysis conducted by Serhadlıoğlu *et al*. (2013).

1.4. Tidal Sites Around the UK

According to the DTI Atlas of Marine Renewables (2008), locations with high current velocities around the UK have been mapped as promising sites for future tidal turbine array deployments. Draper (2011), categorised locations with fast currents as:

- Straits between large bodies of water, which have a large tidal phase difference in tidal amplitude,
- Headlands,
- Estuaries with a large tidal range and,
- Occluded basins where flow is forced through a narrow channel.

All four categories can be identified along the coast of the UK. The Pentland Firth is essentially an example of a strait between two oscillating water bodies; the north-west and south-west coasts of Wales contain headland sites, the Bristol Channel is an estuary with a large tidal range, and Strangford Lough can be idealised as an occluded basin. In addition

there are other locations, which are more complicated and less easy to categorise (e.g. around Alderney) or represent combinations of the above categories (e.g. between the Mull of Galloway and the Isle of Man).

At any site, the deployment of a tidal array will alter the local hydrodynamics. In order to minimise this effect and extract sufficient power from the tidal stream, an informed selection of the tidal site is as important as the turbine design and the configuration of the arrays. There are several factors that influence the positioning of tidal arrays (or farms in general), including accessibility of the site, local geotechnical conditions, and shipping lanes. The overall goal of the array configuration is to maximise the power that can be generated cost-effectively while keeping the environmental impact within acceptable levels. In general, the optimisation procedure should be based on changes observed at basin scale.

The present thesis considers the Bristol Channel and Anglesey sites, which are examples of an estuary with high tidal range and a headland, respectively. The following sections outline the reasons for selecting these sites.

1.4.1. Anglesey (Headland)

In the UK, a number of sites may be characterised as headland sites. Examples include Anglesey, Portland Bill, Mull of Kintyre, and Cromer. Herein, the Anglesey Skerries has been selected as a typical headland site, and a parametric study conducted on evaluating its extractable tidal power potential. The Anglesey Skerries is located on the north west coast of the Wales, with fast currents exceeding 2 m/s. The Anglesey site is selected and being developed by MCT through SeaGen Wales. The proposed installation would have a maximum capacity of 10 MW using a tidal array of seven twin-rotor turbines (http://www.marineturbines.com accessed on 17 February 2014). In this respect, the Anglesey Skerries is likely to be the first array to be deployed in the UK. Figure 1.5 presents an artist's image of the tidal array under consideration for the Anglesey site.

In terms of developing a numerical model of the site, a factor influencing the choice was the availability of adequate data for model validation purposes. Moreover, the Anglesey Skerries is located relatively close to the Bristol Channel, and so it was feasible to include both regions in a single numerical model and hence investigate the possibility of

hydrodynamic interactions between the two sites when extracting energy from the tidal currents.

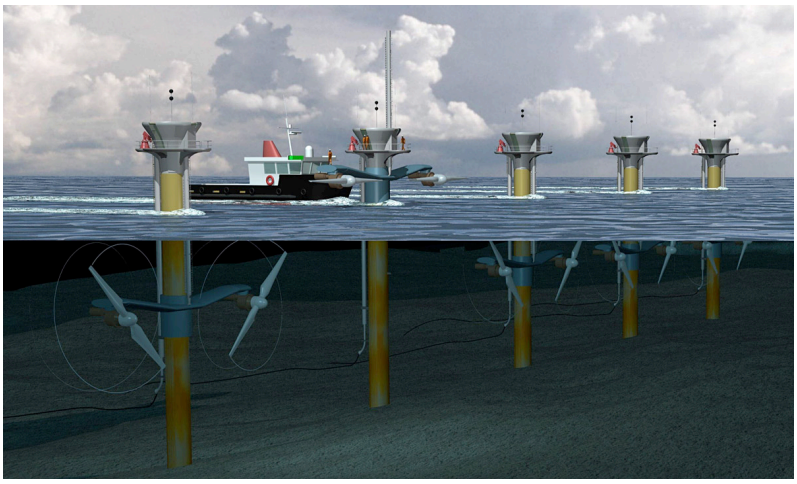

Figure 1.5 – Artist's impression of the tidal turbine array located at the Anglesey site. The image is taken from MCT SeaGen website (http://www.marineturbines.com/3/news/article/44/marine_current_turbines_kicks_off_first_tidal_array_for_wales *accessed* 17 February 2014).

1.4.2. Bristol Channel

The Bristol Channel is famous for having one of the largest tidal ranges in the world (~14 m peak at spring tides). For this reason, great attention over many years has been paid to the developing the case for constructing a tidal barrage to utilise the rise and fall of the tides (Xia *et al.*, 2010b; Rainey, 2009; Bondi, 1981). However, due to political, economic and environmental issues, the deployment of tidal stream turbines has become a viable alternative to a tidal barrage for extracting power from the fast currents observed in the Bristol Channel.

The Bristol Channel is a dynamically complex system, which is well documented in the literature mainly due to the proposed Severn Barrage scheme (Kadiri *et al.*, 2012; Crickmore, 1982; Clarke, 1982). The high tidal range is mainly due to a combination of tidal resonance between the continental shelf and the estuary with the amplitude enhanced by the funnelling effect owing to the shape of the estuary (Fong and Heaps, 1978; Prandle, 1980). Noting these factors, especially the resonance of the system, it is of importance to include the continental shelf in the computational domain to model accurately the tidal movement in the Bristol Channel (Zhou *et al.*, 2014; Adcock *et al.*, 2011).

The Bristol Channel is selected here to evaluate the tidal energy potential of the site due to its historical importance as well as the likelihood of being one of the first sites to be developed around the UK.

1.5. Aims of this Thesis

The research reported in this thesis was undertaken within the PerAWAT project funded by the Energy Technologies Institute (ETI). The aim of this work is to assess the tidal power resource and the far-field hydrodynamic effect of tidal stream turbine arrays located at selected coastal sites off the UK. The research has the following objectives:

- To verify the selected shallow water code (DG-ADCIRC) using standard benchmark tests, including uniform flow in a sloping channel, still water over non-uniform bathymetry, laminar flow in an open channel, recirculation in the lee of a sidewall expansion in a channel, and Coriolis-induced wave motion.
- To develop a validated two-dimensional model of the south-west coast of the UK that simulates the naturally occurring major tidal constituents in the region,
- To modify the DG-ADCIRC code in order to represent the tidal turbines using linear momentum actuator disk theory and to compute the associated momentum sinks due to the presence of the arrays in the model and,
- To carry out a parametric study on the effect of turbine operating conditions, array configurations and locations, on available power and the hydrodynamics of selected coastal basins.
- To investigate the far-field hydrodynamic effects of energy extraction.

1.6. Thesis Outline

This thesis considers tidal power resource assessment for several selected sites in UK territorial waters. An open-source hydrodynamic model (DG-ADCIRC) is modified using a momentum sink to represent the effect on the flow field of deploying a conceptual tidal turbine array. This Chapter has outlined the motivation behind this thesis, providing a brief review of the physical behaviour of tides and presenting state of knowledge regarding tidal stream power as a renewable energy resource. Although this Chapter has included a literature review, the remaining chapters also include brief literature reviews where appropriate. Chapter 2 presents the two-dimensional Shallow Water Equations (SWEs), which are used to

model the ocean tides, and provides a summary of the discontinuous Galerkin finite element method used to solve these equations. The Chapter also describes the benchmark test cases used to validate the selected hydrodynamic numerical solver DG-ADCIRC, which uses the discontinuous Galerkin method to solve the SWEs. Chapter 3 describes the near-field momentum sink representation of the tidal turbines in a free surface flow field. This enables a distinction to be made between the power available to the turbines and the total power that is extracted from the tidal stream. Chapter 4 presents validation of the numerical model constructed to model the tides occurring in the vicinity of the western coastline of the UK. The model is then extended to include the intertidal zones. For numerical stability, a wetting and drying treatment is included in the computations to correctly model the mass transfer during ebb and flood tides. Chapters 5 and 6 provide a tidal resource assessment conducted for the Anglesey Skerries (headland) and the Bristol Channel (an oscillating bay) respectively. The assessment includes a parametric study to evaluate the importance of turbine operating conditions, array locations and array configurations on the maximum available power. Chapter 7 focuses on tidal farm interactions. The analysis considers the principal lunar tidal constituent M_2 to quantify the change in the local hydrodynamics. Chapter 8 presents the main conclusions of this thesis and proposes areas for future work. Appendix 1 presents a summary of Linear Momentum Actuator Disk Theory (LMADT) applied in open-channel flow, which is the near-field approximation used in this thesis.

Chapter 2 Depth-Averaged Flow Fields and Their Numerical Modelling

Two of the primary objectives of this thesis are to investigate the far-field effects of tidal energy devices and to investigate ways of maximising the amount of energy that can be extracted from tidal streams. To achieve these objectives, it is intended to model the ocean tides using the long wave equations, commonly known as the shallow water equations.

2.1. Introduction

Many meteorological and oceanic flows are described as shallow water flows. The main characteristic of these flows is that the vertical dimension of the flow is considerably smaller than the horizontal scale,

$$\delta = \frac{H}{L} \ll 1.0. \qquad 2.1$$

In equation 2.1, δ is the aspect ratio of different length scales, H is the vertical scale of the flow, which is usually taken to be the total water depth, and L is the characteristic horizontal scale (e.g. wavelength). Le Méhauté (1976) reports that long waves in shallow water flow satisfy $\delta < 0.05$.

Regarding the shallowness of the flow, it is sensible to describe such flows as nearly-horizontal, which is justified by assuming that the pressure distribution is hydrostatic (see e.g. Falconer, 1993). Although shallow water flows are three-dimensional by nature, this assumption allows a simplification to be made in the mathematical formulation by integrating the horizontal velocity over the vertical direction (depth-averaging) to obtain a representative velocity flow field (Vreugdenhil, 1994; Weiyan, 1992). This integration reduces the three-dimensional free-surface boundary problem to a two-dimensional fixed boundary problem (Aizinger and Dawson, 2002). The resulting equation system is referred to as the shallow water equations (SWEs), where the primary variables are the free surface elevation and the depth-averaged horizontal velocity components (see Section 2.2).

The shallow water equations are widely used to model many coastal phenomena such as tidal flows, storm surges, tsunami waves, dam break waves, and large river flows. Herein, the shallow water equations are employed in order to model naturally occurring tidal flows off the coasts of the UK, and to investigate the change in the flow field due to the presence of tidal turbines. The following section briefly introduces the two-dimensional shallow water equations.

2.2. Two-Dimensional Shallow Water Equations

The shallow water equations can be obtained through three different methods. One approach employs a control volume in an open channel flow under the hydrostatic pressure assumption, and adopts mass and momentum conservation laws within the control volume (see e.g. Abbott and Minns, 1979). A second approach is through solving the three-dimensional Laplace equation using kinematic boundary conditions and an additional dynamic boundary condition at the free surface (see e.g. Eskilsson and Sherwin, 2005). The third approach, which is adopted in this thesis, involves depth-integration of the continuity and Navier-Stokes equations (see e.g. Falconer, 1993).

In deriving the shallow water equations, it is assumed that the flow is nearly horizontal, thus the acceleration of the particles in the vertical direction is negligible (Falconer, 1993). By defining the system as nearly horizontal, the pressure distribution in the vertical direction is assumed hydrostatic. The established governing equations can be expressed as the following time-dependent two-dimensional system of non-linear partial differential equations of hyperbolic type (Toro, 2001):

$$\frac{\partial \zeta}{\partial \mathrm{t}} + \frac{\partial}{\partial \mathrm{x}}\left(Hu\right) + \frac{\partial}{\partial \mathrm{y}}\left(Hv\right) = 0 \tag{2.2}$$

$$\begin{aligned}\frac{\partial}{\partial \mathrm{t}}\left(uH\right) + \frac{\partial}{\partial \mathrm{x}}\left(Hu^2 + \frac{1}{2}\mathrm{g}\left(H^2 - h^2\right)\right) + \frac{\partial}{\partial \mathrm{y}}\left(Huv\right) \\ = \mathrm{g}\zeta\frac{\partial h}{\partial \mathrm{x}} - \mathrm{c_f}\, u\sqrt{u^2 + v^2} + fv + \mathrm{F_x}\end{aligned} \tag{2.3}$$

$$\begin{aligned}\frac{\partial}{\partial \mathrm{t}}\left(vH\right) + \frac{\partial}{\partial \mathrm{x}}\left(Huv\right) + \frac{\partial}{\partial \mathrm{y}}\left(Hv^2 + \frac{1}{2}\mathrm{g}\left(H^2 - h^2\right)\right) \\ = \mathrm{g}\zeta\frac{\partial h}{\partial \mathrm{y}} - c_f v\sqrt{u^2 + v^2} - fu + \mathrm{F_y}\end{aligned} \tag{2.4}$$

Equation 2.2 is the mass conservation equation, where ζ represents the water elevation above a certain datum, h is the bathymetric depth of the water column below the geoid, H is the total depth of the water column ($H = h + \zeta$), which is equivalent to the sum of the free surface elevation (ζ) and the bathymetric depth, h. The variables u and v represent the depth-averaged velocity components in x- and y- directions.

Equations 2.3 and 2.4 are the horizontal momentum conservation equations in x- and y-directions respectively, where g is the gravitational acceleration, c_f is an empirical friction coefficient that depends on the bottom resistance, f is the Coriolis force, and F_x and F_y represent additional forces in the system such as tidal potential forces, wind or wave radiation stresses. An empirical formula or constant is usually employed to estimate c_f. Typical examples include the Chézy friction law or Manning's formula. When the Chézy friction law is employed, the frictional coefficient can be given as,

$$c_f = \frac{g}{C^2}, \tag{2.5}$$

whereas Manning's formula gives (Chow, 1959),

$$c_f = \frac{g n_M}{h^{1/3}}. \tag{2.6}$$

In equation 2.5, C is the Chézy coefficient and n_M is the Manning friction coefficient.

The Coriolis force is represented by the parameter,

$$f = 2\Omega \sin\theta_0, \tag{2.7}$$

where $\Omega = 2\pi$ rad/day is the angular velocity of the Earth's rotation and θ_0 is the latitude of the location of interest. At a new latitude $\left(\theta_0 + \delta\theta\right)$, application of Taylor series to equation 2.7 provides an approximation to the Coriolis effect, which is given by (Verkley, 1990),

$$f = f_0 + \beta y. \tag{2.8}$$

where $f_0 = 2\Omega \sin\theta_0$, $\beta = \left(2\Omega/R\right)\cos\theta_0$, R is the radius of the Earth and y is the coordinate positive northwards between latitudes θ_0 and $\left(\theta_0 + \delta\theta\right)$ (Stommel, 1948).

The two-dimensional shallow water equations can be written in divergence form as,

$$\frac{\partial \mathbf{u}}{\partial t} + \nabla \cdot \mathbf{F}(\mathbf{u}) = \mathbf{s}(\mathbf{u}), \tag{2.9}$$

where **u** is the vector for conserved variables,

$$\mathbf{u} = \left[\zeta, uH, vH\right]^T, \tag{2.10}$$

F is the flux vector,

$$\mathbf{F} = \left[\mathbf{f}_x, \mathbf{f}_y\right] = \begin{bmatrix} uH & vH \\ Hu^2 + \frac{1}{2}g(H^2 - h^2) & Huv \\ Huv & Hv^2 + \frac{1}{2}g(H^2 - h^2) \end{bmatrix} \tag{2.11}$$

and **s** is the source (sink) term vector,

$$\mathbf{s} = \left[0, g\zeta\frac{\partial h}{\partial x} - c_f u\sqrt{u^2 + v^2} + fv + F_x, g\zeta\frac{\partial h}{\partial y} - c_f v\sqrt{u^2 + v^2} - fu + F_y\right]^T. \tag{2.12}$$

In this divergence form, it is seen that the two-dimensional flux vector defines the transport of $\mathbf{u}(\mathbf{x}, t)$.

In order to solve the equation system, appropriate initial and boundary conditions must be provided.

2.3. Mathematical Boundary Conditions

The governing equations described in Section 2.2 are a hyperbolic system of partial differential equations that describe the propagation of long waves. To solve the system of equations, appropriate initial and boundary conditions must be supplied. Considering the boundary conditions, the method of characteristics (see i.e. Abbott and Minns, 1979) is a useful tool to specify different boundary types in shallow water models.

The set of partial differential equations and the boundary conditions are well-posed provided that the solution is unique and stable (Stephenson, 1970). The solution obtained by the boundary conditions must be unique due to the fact that, in nature, for prescribed conditions, there is one and only one outcome. Considering the large scale of the problem at hand (i.e. basin tides) slight adjustment in the boundary conditions would result in a similarly small change in the results.

Mathematically, there are three categories of boundary conditions that are applicable in numerical models. The first of these is the Dirichlet (essential or prescribed) boundary

condition. In this type of boundary condition, the value of the conservative variable is specified at the boundary,

$$u = L_D \text{ on } \Gamma_D . \quad 2.13$$

The second is the von Neumann (natural or transmissive) boundary condition, in which the gradient normal to the boundary of a variable is supplied at the boundary,

$$\partial_n u = L_N \text{ on } \Gamma_N . \quad 2.14$$

The third is a combination of Dirichlet and von Neumann conditions and is called the Robin (radiation) boundary condition. Using infinite domains to solve hyperbolic equations (such as the shallow water equations) numerically is not practicable. Thus, artificial boundaries are used to divide the domain of interest from the rest of the physical system. Such boundaries are called open boundaries, where the conditions outside of the model domain are imposed. In order to obtain a stable solution, it is desired that waves propagate from the interior of the model domain, and pass through the open boundaries without any reflections (Bayliss and Turkel, 1980). Radiation boundary conditions are often used on the open boundaries for this purpose. For a hyperbolic solution system, the method of characteristics (see e.g. Abbott and Minns, 1979) is used to specify different boundary conditions at open and internal boundaries.

2.4. Limitations of the Two-Dimensional Shallow Water Equations

For many years, the two-dimensional shallow water equations (SWEs) have been employed to model various hydrodynamic phenomena including the tidal movements. Solving the shallow water equations numerically is challenging due to a number of factors including the nature of the shallow water equations, which are a system of non-linear partial differential equations, as well as the selected numerical method to discretise them (Aizinger and Dawson, 2002).

A fundamental limitation arises as the depth-averaged models assume that the flow is nearly horizontal; thus the vertical velocity component is negligible in comparison to the horizontal velocity components (Falconer, 1993). In shallow water models, the vertical velocity profile is represented by a fixed log profile, which is related back to the bed friction

coefficient applied in the model (Draper, 2011; Stansby, 2006). However, in practice, the real vertical velocity profile differs significantly from the profile described by a log law. Stansby and Lloyd (2001) emphasise that the fixed vertical velocity profile assumption is valid given that, in the water column, the boundary layer is fully developed. However, in the same study Stansby and Lloyd (2001) argue that it is not possible to specify the bed friction coefficient accurately without further modelling the boundary layer. This argument is of importance when including shallow wakes in depth-averaged models. One common example to demonstrate such flow conditions would be the modelling of large-scale horizontal eddies that occurs when a coastal flow passes a headland or an island (Stansby, 2006).

Stansby (2006) presents a comparative study, which considers modelling a flow passing a conical island using both a two-dimensional shallow water model and a three-dimensional boundary layer model that is validated against experimental data. In this study, Stansby shows that the wake behind the island is poorly represented in the depth-integrated model when compared to the boundary layer model. The numerical results presented by Stansby (2006) show that the vortex shedding wakes in the depth-integrated models are of similar nature with the three-dimensional boundary-layer models. However, the stable wakes were poorly modelled in the two-dimensional shallow water models due to the misrepresentative value of the bed friction coefficient applied in the model. Draper (2011) suggests that in depth-averaged models the bed friction vector, which leads the bottom current vector, is defined according to the depth-averaged velocity. This implies that the velocity at the seabed is assumed to be a constant fraction of, and is always in-phase with the depth-averaged velocity. However, in reality the velocity near the seabed will be different from the depth-averaged velocity, and may on occasions even differ in magnitude and sign (Draper, 2011; Owen, 1980). Thus, the frictional dissipation on the seabed will be delayed (i.e. overestimation of phase) in depth-averaged models, which results in a similar but different wake profile.

Use of a three-dimensional model obviously would improve the accuracy of computed velocity profiles, as the model is not bound to a fixed velocity profile at all times. However, it is important to choose an appropriate turbulence model, so that the vertical and horizontal mixing are computed accurately, which eventually affects the frictional dissipation (Draper, 2011). Nadaoka and Yagi (1998) emphasise that direct application of turbulence models in the

shallow water models is not realistic, primarily due to the size of the computational domain (e.g. realistic tidal basins) with different source terms involved in the models (e.g. bottom friction, wind shear stress), as well as the nature of the turbulence models. In the past, two-equation depth-integrated k-ε turbulence models have been used where free shear layer turbulence and turbulent advection are important (Rodi, 1993; Falconer, 1993). However, the validity of inclusion of turbulence in depth-integrated models is still under investigation (Rodi *et al.*, 2013).

Two-dimensional shallow water models also perform poorly in modelling areas where abrupt variations in density occur. This is generally observed in regions where fresh water resources connect to estuaries.

Recently, shallow water models have been used to estimate the total power that can be extracted from tidal stream in areas of interest. Vogel *et al.* (2013) emphasise that estimation of the maximum available power to the turbine arrays is dependent on accurately modelling the mass flux and velocity variations in the flow that passes through the turbines. In the literature, an enhanced resistance to the flow is commonly introduced in the governing equations to represent the tidal devices. However, this approach is found to be inadequate in evaluating the power potential of a site, as it overestimates the power extracted from the flow field due to the incorrect velocity variations across the turbines (Vogel *et al.*, 2013; Draper 2011).

Analytical models provide a good approximation to the velocity at the turbines as well as the velocity across the turbines (Nishino and Willden, 2012b; Vogel *et al.*, 2014). Regarding the purpose of this project, an analytical model based on Linear Momentum Actuator Disk Theory (LMADT) applied on an open-channel (Houlsby *et al.*, 2008) has been used as a sub-grid model in order to approximate the horizontal velocities more accurately.

2.5. Numerical Methods to Solve the Shallow Water Equations

Numerical solutions of hyperbolic shallow water equations have been obtained using different numerical schemes (see e.g. Abbott and Minns, 1979; Vreugdenhil, 1994; Weiyan, 1992). Selection of the numerical scheme is of importance with respect to discretization, which in turn affects the accuracy obtained (García-Navarro *et al.*, 2008).

The shallow water equations describe flows which may be in principle steep-fronted or discontinuous in gradient, and thus have to be solved using integral techniques such as finite volume or finite element methods, with a Riemann approximation which prove to be successful in dealing with fronts and discontinuities. The following sections provide a brief summary of the commonly used differential (finite difference) and integral (finite volume and finite element) techniques to solve the shallow water equations.

2.5.1. Finite Difference Method

One of the numerical methods used to solve the system of nonlinear hyperbolic conservation laws is the finite difference method. This method uses the differential form of the governing equations. The spatial domain of the partial differential equations (PDEs) is discretised into a set of grid points. The method approximates the derivatives at each point by using a Taylor series expansion. However, solving such systems is numerically challenging as the derivatives of the flux function may involve discontinuities (e.g. contact discontinuity or shock type discontinuities). The finite difference method is based on the assumption that the solution is smooth, and for this reason most of the finite difference schemes induce oscillations behind the shock (Sod, 1978) or they simply break down near the discontinuities as the differential equations do not hold (LeVeque, 2002). The method is easy to implement for simple geometries. However, the application of the method to two- and three-dimensional computational domains is complicated due to the imposition of the boundary conditions (Ferrer, 2012).

2.5.2. Finite Volume Method

The finite volume method applied to a conservation law approximates the solution using the integral form of the governing equations, rather than the derivatives. In this case, the computational domain is discretised into small cells that are represented by either, triangles, rectangles, or a combination of both. The numerical scheme is designed to approximate the cell averages of the exact solution. The spatial discretisation requires use of Green's Theorem to rewrite the diffusive and convective terms (Ferrer, 2012). The line integrals appearing in the formulation is generally discretised using Gaussian quadrature points (Shu, 2003). Approximate or exact Riemann solvers are used to replace the flux term in the formulation,

which eases the implementation of the boundary conditions using the finite volume method. The method imposes the boundary conditions using this flux term. However, the main advantage of using this method comes from spatial discretisation of the conservation equations using the integral form, as this ensures the mass and momentum conservation locally (Hirsch, 1988). However, using higher order solutions within finite volume scheme would require a larger stencil of cells, which in turn complicates the implementation of the boundary conditions (Ferrer, 2012).

2.5.3. Finite Element Method

The method was originally implemented by structural engineers in 1960s, and first used to solve linear plane elasticity problems (Karniadakis and Sherwin, 2005). The finite element method is preferred over the finite difference method primarily due to its efficiency and accuracy in solving problems with complex geometries. The spatial discretisation of the computational domain is established by using either structured or unstructured elements (e.g. triangular), which are connected to each other at nodal points.

The method employs a weak formulation of the governing equations by multiplying the equations with a test function and integrating over the domain (Zienkiewicz and Taylor, 2005). The exact solution in the weak formulation is approximated using base functions that are often piecewise linear functions. Test and base functions are both continuous across elements and the selection of these functions is dependent on the chosen methods (e.g. Galerkin, Petrov-Galerkin). The standard (continuous) Galerkin method conserves mass and momentum globally. However, it does not ensure conservation of these quantities locally. In order to represent a line sink of momentum in the solution, conservation of mass locally at each element is of importance, thus the discontinuous Galerkin method is used to solve the shallow water equations in this project.

2.6. Discontinuous Galerkin Finite Element Method

The discontinuous Galerkin (DG) finite element method is selected here to solve the shallow water equations. The main difference between the DG method and the continuous finite element methods is that, in the DG method, the solution is approximated individually in each element, which enables discontinuities to be modelled properly within the solution

system (Eskilsson and Sherwin, 2005). In continuous methods, elements in the computation domain share a common node where information is transferred, whereas in the DG method the computation is handled within individual elements and the propagation of information between neighbouring elements is maintained by a numerical flux of choice on nodal or modal points on the shared edge of those elements (Hesthaven and Warburton, 2008).

The spatial discretisation described herein is similar to that of Cockburn and Shu (1998), which uses the modal expansion. The first stage of space discretisation in the DG method is to divide the flow domain Ω into N_e number of non-overlapping, but not necessarily conforming, elements e, each with an elemental domain of Ω_e and elemental boundary of $\partial\Omega_e$,

$$\Omega = \bigcup_{e=1}^{N_e} \Omega_e \,. \tag{2.15}$$

Following the standard Galerkin method and recalling from equation 2.9, the divergence form of the shallow water equations in matrix-vector form is given as,

$$\frac{\partial \mathbf{u}}{\partial t} + \nabla \cdot \mathbf{F}(\mathbf{u}) = \mathbf{s}(\mathbf{u}) \,.$$

To construct a weak formulation of the governing equations, the above equation is multiplied with a test function $\phi_h \in V_h$, and integrated over each element,

$$\left(\frac{\partial \mathbf{u}}{\partial t}, \phi_h\right)_{\Omega_e} + \left(\nabla \cdot \mathbf{F}(\mathbf{u}), \phi_h\right)_{\Omega_e} = \left(\mathbf{s}(\mathbf{u}), \phi_h\right)_{\Omega_e} . \tag{2.16}$$

In equation 2.16, $\left(f, g\right)$ denotes the inner product of f and g taken over the element domain Ω_e. The test function ϕ_h belongs to V_h, which is a discrete space of piecewise polynomial functions that are differentiable over an element, while allowing discontinuities between elements,

$$V_h = \left\{ \phi_h \in L^2\left(\Omega\right) : \phi_h \middle| \Omega_e \in P^k\left(\Omega_e\right), \forall \Omega_e \right\} . \tag{2.17}$$

In equation 2.17, $P^k\left(\Omega_e\right)$ shows the space of polynomials of order k for elements with linear elemental mappings. The next stage in writing the weak DG formulation consists of substituting the exact solution $\mathbf{u}$ by an approximate solution $\mathbf{u}_h$ and then integrating the advection term in equation 2.16 by parts to obtain,

$$\left(\frac{\partial \mathbf{u}_h}{\partial t}, \phi_h\right)_{\Omega_e} - \left(\nabla \phi_h, \mathbf{F}\left(\mathbf{u}_h\right)\right)_{\Omega_e} + \langle \mathbf{F}\left(\mathbf{u}_h\right) \cdot \mathbf{n}, \phi_h \rangle_{\partial\Omega_e} - \left(\mathbf{s}\left(\mathbf{u}_h\right), \phi_h\right)_{\Omega_e} = 0 \,. \qquad 2.18$$

In equation 2.18, $\langle f, g \rangle$ denotes the inner product of f and g taken over element boundary $\partial\Omega_e$, $\mathbf{n} = \left[n_x, n_y\right]^T$ is the outward normal vector to $\partial\Omega_e$. Along the element boundaries ($\partial\Omega_e$) discontinuities are allowed. For this reason, the discrete solution $\mathbf{u}_h$ and the flux $\mathbf{F}\left(\mathbf{u}_h\right)$ in equation 2.18 may be dual-valued along $\partial\Omega_e$, whereas the functions defined within V_h are continuous on the interior of each element (Karniadakis and Sherwin, 2005; Houston *et al.*, 2002).

Equation 2.18 can be solved by replacing the flux term in the boundary integral by a single-valued numerical flux of choice $\widehat{\mathbf{F}}\left(\mathbf{u}_h^{int}, \mathbf{u}_h^{ext}\right)$, which depends on the trace values of the discrete solution $\mathbf{u}_h$ on the interior $\mathbf{u}_h^{int}$ and exterior $\mathbf{u}_h^{ext}$ of the element (see Figure 2.1).

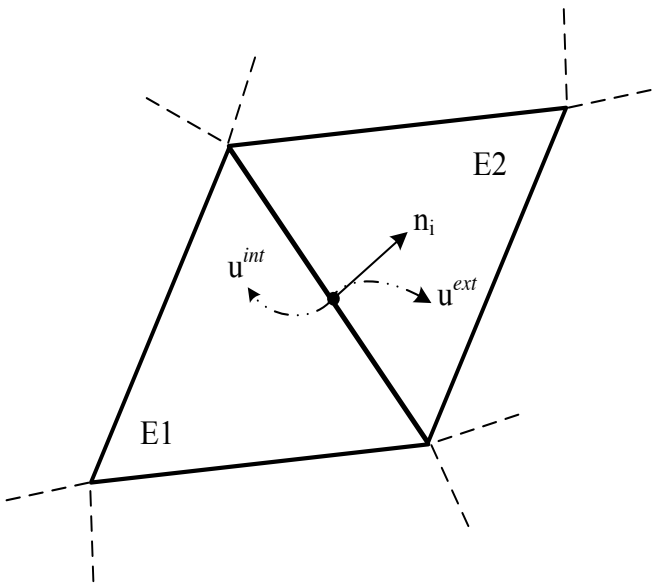

Figure 2.1 – Representation of a pair of neighbouring elements (E1 and E2). The element E1 has a common edge *i,* where n_i is the normal to the edge, u^{int} is the solution on the egde *i* when approaching from inside of element E1 and u^{ext} is the solution on the edge *i* when approaching outside the element (reproduced from Kubatko *et al.*, 2006b).

Substituting the numerical flux in equation 2.18 provides the semi-discrete formulation,

$$\left(\frac{\partial \mathbf{u}_h}{\partial t}, \phi_h\right)_{\Omega_e} - \left(\nabla \phi_h, \mathbf{F}\left(\mathbf{u}_h\right)\right)_{\Omega_e} + \langle \widehat{\mathbf{F}}\left(\mathbf{u}_h^{int}, \mathbf{u}_h^{ext}\right) \cdot \mathbf{n}, \phi_h^- \rangle_{\partial\Omega_e} - \left(\mathbf{s}\left(\mathbf{u}_h\right), \phi_h\right)_{\Omega_e} = 0 \,. \qquad 2.19$$

Equation 2.19 shows that the boundary flux is normal to the element edges, which means that a local Riemann problem can be solved for given interior $\mathbf{F}\left(\mathbf{u}_h^{int}\right)$ and exterior $\mathbf{F}\left(\mathbf{u}_h^{ext}\right)$ fluxes. Any upwinding numerical flux method can be used in equation 2.19. In DG literature, the most commonly used numerical fluxes are: Roe's average flux (Kubatko *et al.*, 2006a; Aizinger and Dawson, 2002; Roe, 1981), Lax-Friedrich flux (Li and Liu, 2001) and, HLL/HLLC flux (Toro, 2001). Eskilsson and Sherwin (2000) explain that the Lax-Friedrich flux is often used in numerical models, despite the fact that it can be more dissipative when slope limiters are applied in cases of shocks. However, the HLLC numerical flux proves to be capable of capturing shocks without producing spurious oscillations (Toro, 2001). In this project, the HLLC numerical flux is used in the computations.

2.6.1. HLLC Numerical Flux

Rewriting the numerical flux term given in equation 2.19 using the elemental inner product expansion,

$$\langle a, \boldsymbol{b} \rangle_{\partial\Omega_e} \equiv \int_{\partial\Omega_e} a\boldsymbol{b} \cdot \mathbf{n} d\Gamma \,, \tag{2.20}$$

we obtain,

$$\sum_{\ell}^{\Gamma} \left\{ \int_{\ell} \left(\phi_h^{int} - \phi_h^{ext} \right) \widehat{\mathbf{F}} \left(\mathbf{u}_h^{int}, \mathbf{u}_h^{ext} \right) \cdot \mathbf{n} d\Gamma \right\}, \tag{2.21}$$

in which a single edge on an element is denoted as ℓ and the set of all edges in the flow domain (including the domain boundary) is $\Gamma \equiv \Omega \cup \partial\Omega$. The set of interior edges is denoted as Γ^{int} and the set of exterior edges where the boundary conditions are applied is given as $\Gamma^{ext} \equiv \Gamma^{BC}$. Since the numerical flux $\widehat{\mathbf{F}}\left(\mathbf{u}_h^{int}, \mathbf{u}_h^{ext}\right)$ is normal to the element boundary edge, a one-dimensional local Riemann problem can be solved for the fluxes when the trace values $\mathbf{u}_h^{int}$ and $\mathbf{u}_h^{ext}$ are imposed. The trace value of $\mathbf{u}_h^{ext}$ is dependent on the boundary condition $\mathbf{u}_h^{ext} = \mathbf{u}^{BC}$, which is applied at edges that belong to the flow domain $\ell \in \Gamma^{BC}$. Considering that the flux is conservative, an approximation to $\mathbf{u}_h^{int}$ is applicable.

In the conventional HLL method, the relations provided above are used to estimate wave speeds on the interior (s^{int}) and exterior (s^{ext}) of the edge, which are used to construct an

approximate Riemann solution (Mignone and Bodo, 2005; Toro, 2001). The approximate Riemann solution proposed by HLL method assumes that a single constant solution (or a state) exists, where the two solutions are bounded by s^{int} and s^{ext} wave speeds (Toro, 2001). However, this approximation ignores the contact (or tangential) waves (Mignone and Bodo, 2005; Toro, 1997). This drawback is addressed in HLLC method by replacing the proposed single state value $\mathbf{u}_*$ by two approximate state values $\mathbf{u}_*^{int}$ and $\mathbf{u}_*^{ext}$ to construct the full wave structure of the Riemann fan (see Figure 2.2).

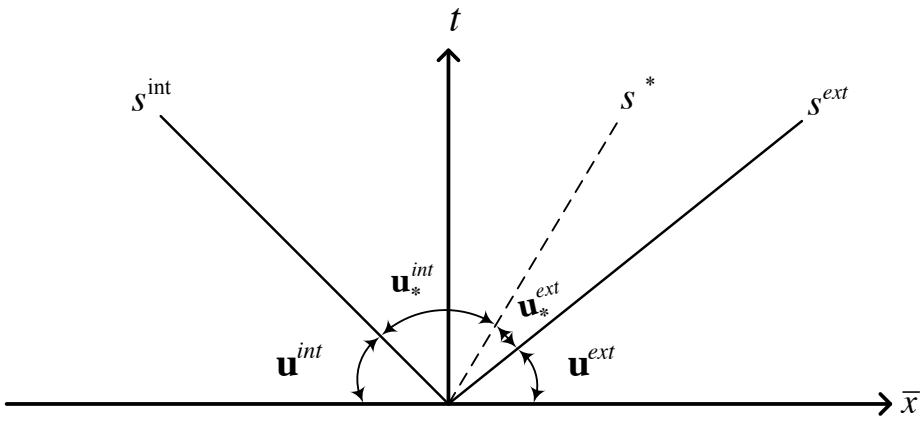

Figure 2.2 – Riemann fan structure on a coordinate normal to an edge of an element. The solid lines represent the non-linear waves (rarefaction or shock) and the dashed line represents the contact wave, which occurs with respect to the tangential velocity (Figure reproduced from Mignone and Bodo, 2005).

In Figure 2.2, the two non-linear (either shock or rarefaction) waves are separated by a contact wave, which is assumed to have a constant wave speed of s^* (Mignone and Bodo, 2005). The contact wave speed is computed using the estimate wave speeds,

$$s^{int} = \overline{u}^{int} - \sqrt{g H^{int}}\, q^{int}, \tag{2.22}$$

$$s^{ext} = \overline{u}^{ext} + \sqrt{g H^{ext} q^{ext}}\ , \tag{2.23}$$

to provide,

$$s^* = \frac{s^{int} H^{ext}\left(\overline{u}^{ext} - s^{ext}\right) - s^{ext} H^{int}\left(\overline{u}^{int} - s^{int}\right)}{H^{ext}\left(\overline{u}^{ext} - s^{ext}\right) - H^{int}\left(\overline{u}^{int} - s^{int}\right)}. \tag{2.24}$$

In equations 2.22 and 2.23, $\overline{u}$ is the velocity component normal to the edge, $\sqrt{gH}$ is the celerity of a gravity wave, H is the total water depth and, q is a correction factor (see equation 2.25). The estimated contact wave speed $s*$ (Equation 2.24) is equivalent to $\overline{u}^*$ in exact Riemann solvers (Toro, 2001). Especially in the presence of shock waves a correction factor q is required to calculate the wave speeds,

$$q^{\left(int,ext\right)} = \begin{cases} \sqrt{\left(H_*^2 + H_* H^{\left(int,ext\right)}\right) \Big/ \left(2\left(H^{\left(int,ext\right)}\right)^2\right)} & ,if\ H_* > H^{\left(int,ext\right)} \\ 1 & ,if\ H_* \le H^{\left(int,ext\right)} \end{cases} \quad 2.25$$

In the equation above, H_* is the water depth at the contact wave, which is calculated by (Toro, 2001),

$$H_* = \frac{1}{g}\left(\frac{1}{2}\left(\sqrt{gH^{int}} + \sqrt{gH^{ext}}\right) + \frac{1}{4}\left(\overline{u}^{int} - \overline{u}^{ext}\right)\right)^2 . \quad 2.26$$

After the wave speeds are estimated, the HLLC flux can be expressed as,

$$\mathbf{F}^{HLLC} = \begin{cases} \mathbf{F}^{int} & s^{int} < 0 \\ \mathbf{F}_*^{int} & s^{int} \le 0 < s^* \\ \mathbf{F}_*^{ext} & s^* \le 0 \le s^{ext} \\ \mathbf{F}^{ext} & s^{ext} < 0 \end{cases}. \quad 2.27$$

where,

$$\begin{aligned} \mathbf{F}_*^{int} &= \mathbf{F}^{int} + s^{int}\left(u_*^{int} - u^{int}\right), \\ \mathbf{F}_*^{ext} &= \mathbf{F}^{ext} + s^{ext}\left(u_*^{ext} - u^{ext}\right). \end{aligned} \quad 2.28$$

Equation 2.28 is used to calculate the fluxes related to the contact wave. The fluxes on the interior and exterior of the edge are given as $\mathbf{F}^{int} = \mathbf{F}\left(\mathbf{u}^{int}\right)$ and $\mathbf{F}^{ext} = \mathbf{F}\left(\mathbf{u}^{ext}\right)$, and the states $\mathbf{u}_*^{int}$ and $\mathbf{u}_*^{ext}$ are obtained by,

$$\mathbf{u}_*^{(int,ext)} = H^{(int,ext)}\left(\frac{s^{(int,ext)} - \overline{u}^{(int,ext)}}{s^{(int,ext)} - s^*}\right)\begin{bmatrix} 1 \\ s^* \\ \overline{v}^{(int,ext)} \end{bmatrix}. \quad 2.29$$

2.6.2. Basis Function

Cockburn and Shu (1998) explain that a suitable basis function with sufficient degrees of freedom may simplify the implementation of the DG method while providing the improvement in computational efficiency.

By using the hierarchical and orthogonal basis function proposed by Dubiner (1998), high-order elements are constructed by means of adding terms to the lower-order elements. The basis function is obtained as a tensor product of polynomials, which can be given as (Karniadakis and Sherwin, 2005),

$$\psi_{ij}\left(\varepsilon_1,\varepsilon_2\right) = P_p^{0,0}\left(\eta_1\right)\left(\frac{1-\eta_2}{2}\right)^p P_q^{2p+1,0}\left(\eta_2\right). \qquad 2.30$$

In equation 2.30, $P_K^{\alpha,\beta}$ defines the K^{th} order Jacobi polynomial of weights α and β. ε_1 and ε_2 correspond to the coordinates of the master triangle shown in Figure 2.3, whereas η_1 and η_2 are the coordinates of the quadrilateral element. This mapping can be formulated as,

$$\eta_1 = 2\frac{\left(1+\varepsilon_1\right)}{\left(1-\varepsilon_2\right)} - 1, \qquad \eta_2 = \varepsilon_2. \qquad 2.31$$

Using equation 2.31, the approximate solution is rewritten as,

$$\mathbf{u}_h = \sum_{p=0}^{P}\sum_{q=0}^{P} \tilde{\mathbf{u}}_{pq}\psi_{pq}. \qquad 2.32$$

where $\tilde{\mathbf{u}}_{pq}$ contains the model degrees of freedom and $\psi_{pq}(\varepsilon_1,\varepsilon_2)$ is the trial (or test) function described in equation 2.30.

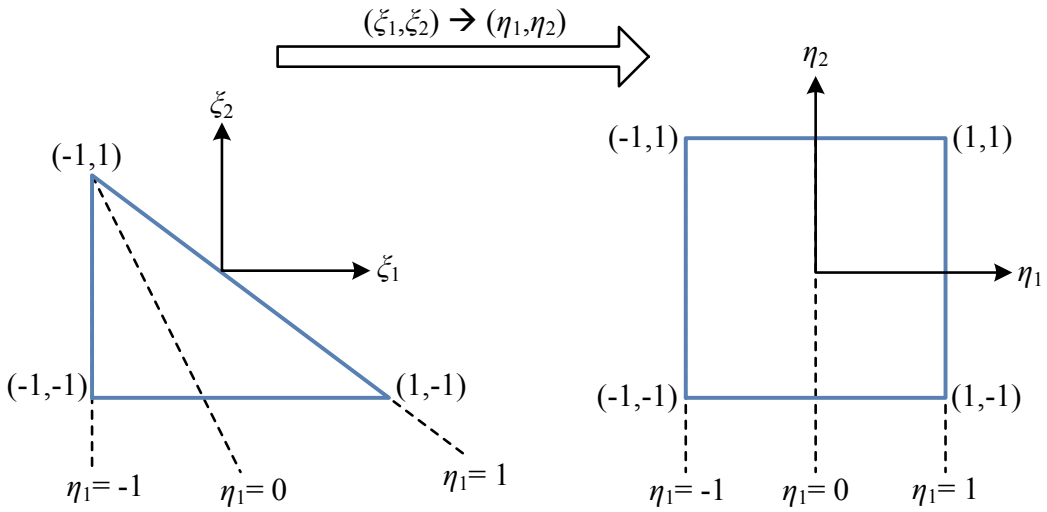

Figure 2.3 – Mapping of the master triangle in collapsed coordinates (reproduced from Kubatko *et al.*, 2006a).

2.6.3. The Runge-Kutta Time Discretisation

The application of spatial discretisation of shallow water equations using DG method reduces the system of hyperbolic partial differential equations to ordinary differential equations. After inverting the mass matrix, the semi-discrete form of the ODEs is given as,

$$\frac{\mathrm{d}\mathbf{u}_h}{\mathrm{dt}} = \mathrm{L}_h\left(\mathbf{u}_h\right). \tag{2.33}$$

where L_h is some corresponding operator, which is dependent on the spatial discretisation.

An explicit total variation diminishing (TVD) Runge-Kutta scheme (Shu, 1987; Cockburn and Shu, 1998) is selected to discretise equation 2.33 in time. Using a third-order scheme, assuming that time is advancing from n to $n + 1$, equation 2.33 becomes,

$$\mathbf{u}_h^1 = \mathbf{u}_h^t + \Delta t \mathrm{L}_h\left(\mathbf{u}_h\right), \tag{2.34}$$

$$\mathbf{u}_h^2 = \frac{3}{4}\mathbf{u}_h^t + \frac{1}{4}\left(\mathbf{u}_h^1 + \Delta t \mathrm{L}_h\left(\mathbf{u}_h^1\right)\right), \tag{2.35}$$

$$\mathbf{u}_h^{t+1} = \frac{3}{4}\mathbf{u}_h^t + \frac{2}{3}\left(\mathbf{u}_h^2 + \Delta t \mathrm{L}_h\left(\mathbf{u}_h^2\right)\right). \tag{2.36}$$

Because of the explicit nature of the scheme, a limitation on the time step is essential, which is defined by the Courant-Friedrichs-Lewy (CFL) condition,

$$|c|\frac{\Delta \mathrm{t}}{\Delta \mathrm{x}} \leq \frac{1}{2p+1}. \tag{2.37}$$

In equation 2.37, c is the characteristic wave speed,

$$c = u \mp \sqrt{gH}, \tag{2.38}$$

p is the polynomial degree, Δx is the smallest grid space and Δt is the time step.

2.6.4. Slope Limiter

In Runge-Kutta Discontinuous Galerkin (RKDG) methods, using high order polynomial approximations may cause local oscillations (Bunya *et al.*, 2009; Hesthaven and Warburton, 2008). To ensure the stability of the solution, a slope limiter is applied at each Runge-Kutta sub-step to avoid unphysical oscillations.

To determine if a slope limiter is necessary, the jump between the elements is computed for the linear part of the approximation. If the computed jump is higher than a prescribed limit, the associated order of the time stepping scheme is lowered by one degree (i.e. a third-order Runge-Kutta scheme would be lowered to a second-order scheme) and then the limiter is applied (Eskilsson and Sherwin, 2000).

A commonly used slope limiter is the general $\Lambda\Pi_h$ slope limiter introduced by Cockburn and Shu (2000). The operant $\Lambda\Pi_h$ is applied accordingly on the assumption that the oscillation takes place in the $\mathbf{u}_h^1$ of the time marching. If this is the case then the higher order part is omitted and the below equality is considered,

$$\Lambda\Pi_h \mathbf{u}_h = \Lambda\Pi_h \mathbf{u}_h^1 . \qquad 2.39$$

The operant $\Lambda\Pi_h$ is computed considering elements, and their mid-points (i.e. geometry of the mesh). The geometric information is used to approximate a mean value of $\mathbf{u}_h$ for first modal expansion. Further details for computing the slope limiter operant and its application on the governing equations are given in detail in Cockburn and Shu (2000).

However, for the problems considered in this thesis, it was not found necessary to apply any slope limiter.

2.7. Verification Tests

The verification tests explained in this section aim to examine each source term, one at a time, in the shallow water equations.

2.7.1. Steady Uniform Flow in a Sloping Channel

This verification test examines the ability of the numerical solver to handle the bed slope and bed shear stress terms in the shallow water equations. The test consists of a rectangular channel, with dimensions $(x, y) \in [0,1000]\times[0,400]$ m with a constant slope of 0.001. The water depth throughout the channel is 5m. The numerical mesh consists of 320 structured elements and has a resolution of 50 m. The time step is set to 0.5 s, a value that satisfies the CFL condition. On the lateral walls, slip boundary conditions are applied, whereas the free surface elevation is prescribed by constant values at the upstream and downstream boundaries. In this test, the kinematic eddy viscosity, Coriolis force, and wind stress are all

ignored. Using a quadratic bed friction coefficient of $c_f = 0.005$, an analytical value of depth-averaged velocity can be calculated from (Rogers, 2001),

$$u = \sqrt{\frac{gRS_o}{c_f}} \qquad 2.40$$

which is obtained by balancing the water weight component along the inclined channel to the bed resistance. In equation 2.40, g is the acceleration due to gravity, R is the hydraulic radius that can be taken as the water depth (for a wide channel), and S_o is the bed slope. The theoretical velocity is calculated as 3.132091952673 m/s. The numerical model reached equilibrium at a flow simulation time t = 2880 s, and predicted a steady state velocity value of 3.13209195267285 m/s to 12-digit accuracy. The excellent agreement between the numerical and analytical predictions indicates that the discontinuous Galerkin ADCIRC model is capable of modelling flows in an inclined channel with bed shear stress. This verifies the bed friction term and the (constant) bed slope term.

2.7.2. Laminar Flow Past a Sideways Expansion

Two-dimensional laminar flow through an idealized rectangular channel with a sudden side-wall expansion provides a test as to how well the model reproduces viscous flow separation. Free surface flow in an open channel with a sudden width expansion, is analogous to flow over a backward facing step, which has been a well-studied test case in the hydraulics literature. At steady state, the flow separates at the expansion and forms a recirculation zone downstream of the expansion. Experimental data from Denham and Patrick (1974) and O'Leary and Mueller (1969) show that, for laminar flow, the length of the recirculation zone is dependent on the upstream Reynolds number (*Re*). However, for upstream Reynolds numbers greater than 2000, O'Leary and Mueller (1969) show that the recirculation length is independent of the Reynolds number. The Reynolds number is defined as,

$$Re = \frac{U_c L_c}{\upsilon} \qquad 2.41$$

in which U_c is a characteristic velocity, L_c is a characteristic length, and υ is the kinematic viscosity coefficient. In the literature, the Reynolds number (*Re*) has been defined in at least

two ways in terms of the domain dimensions. According to Denham and Patrick (1974) the *Re* is defined as,

$$Re = \frac{U_{inlet} h}{\upsilon} \qquad 2.42$$

where U_{inlet} is the average upstream velocity across the inlet section, h is the step-size (half the distance across the upstream channel). However, Armaly *et al.* (1983) take the characteristic length scale to be *2h,* is the distance across of the upstream channel (which represents the hydraulic diameter of the upstream channel). In the present work, the approach used by Denham and Patrick (1974) is adopted.

The computational domain geometry used in this verification test is the same as adopted by Denham and Patrick (1974), which can be seen in Figure 2.4.

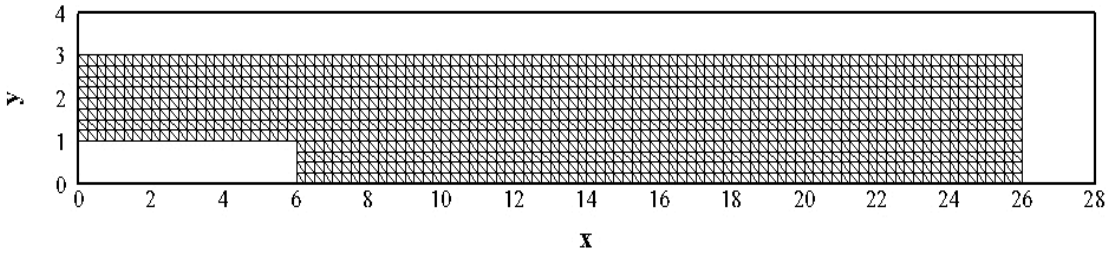

Figure 2.4 –Triangular structured mesh used in laminar flow passing a sideways expansion test.

Two approaches have been taken to force the model. The first involved prescribing uniform flow at the inlet boundary, while keeping the inlet length long enough to create an almost fully developed parabolic velocity profile by the time the flow reaches the expansion.

The second involved specifying the fully developed parabolic velocity profile at the inlet boundary (essentially the analytical solution for *Poiseuille* flow - Schlichting, 1968). In this case, the inlet flow velocity profile is,

$$U(y) = \frac{3}{2} U_{inlet} \left(\frac{y\left(2h - y\right)}{h^2} \right). \qquad 2.43$$

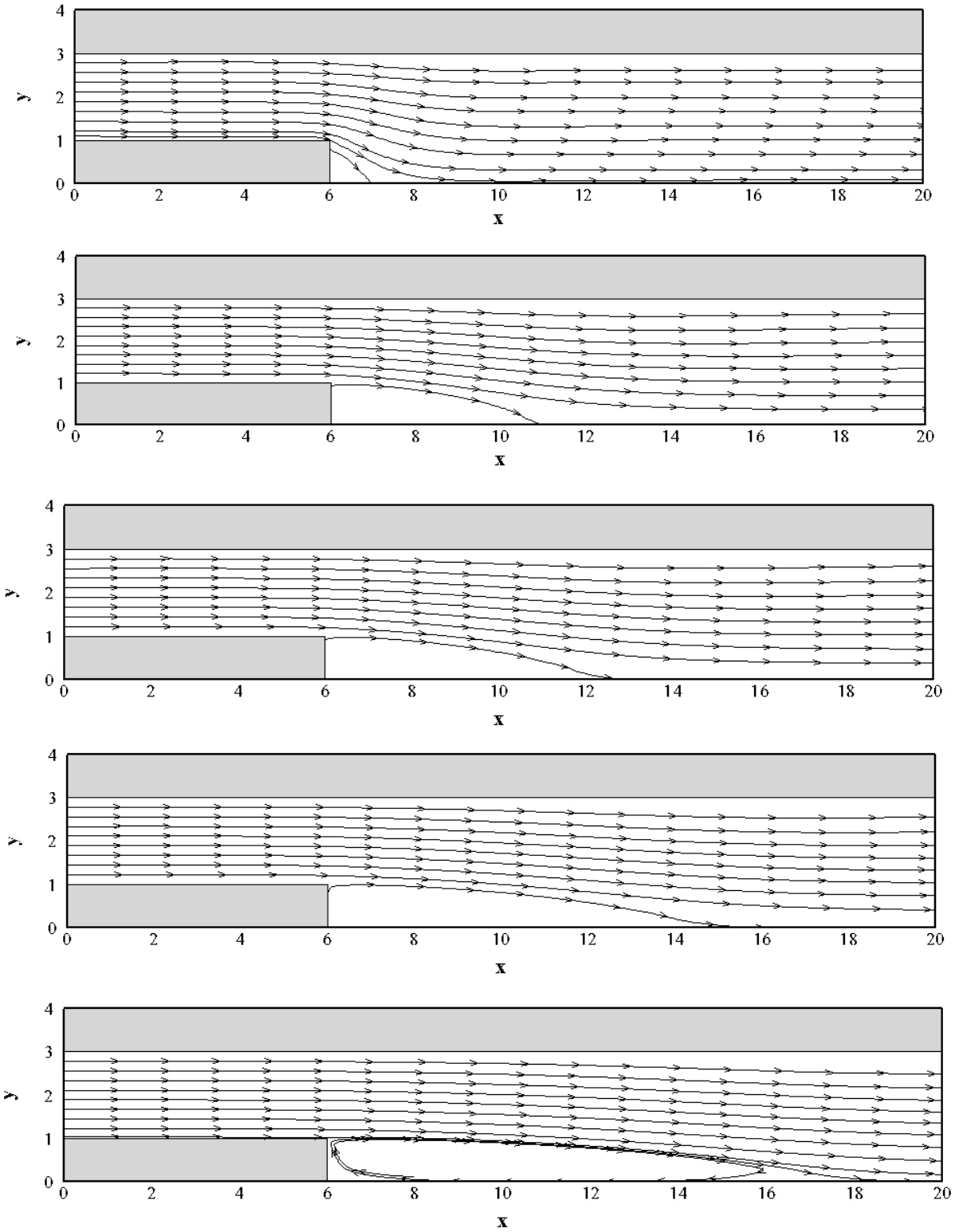

Figure 2.5 – Streamlines obtained for (a) Re = 7.9, (b) Re = 73, (c) Re =98, (d) Re = 150, and (e) Re= 229.

In the numerical model, h = 1.0 m. A ramping function is used to prevent shocks in the computation. The test is run for a polynomial order of $n = 3$. The computational mesh has a resolution of 0.25 m with 2304 structured elements. The streamlines shown in Figure 2.5 are created using Tecplot post-processor. It can be seen that the reattachment length varies with the inlet Reynolds number.

2.7.3. Equatorial Kelvin Wave

This test is aimed at validating the Coriolis source term in the shallow water equations. Here, the linearised shallow water equations without bed friction are,

$$\begin{aligned} &\frac{\partial h}{\partial t} + \frac{\partial u}{\partial x} + \frac{\partial v}{\partial y} = 0, \\ &\frac{\partial u}{\partial t} + g\frac{\partial h}{\partial x} = fv, \\ &\frac{\partial v}{\partial t} + g\frac{\partial h}{\partial y} = -fu. \end{aligned} \qquad 2.44$$

Following Eskilsson and Sherwin (2000) and Giraldo and Warburton (2008), the system of equations given in equation 2.44 is solved in non-dimensional form. Using primes to denote non-dimensional variables, the dimensional variables can be expressed as,

$$\mathbf{x} = \frac{R}{E^{1/4}}\mathbf{x}', t = \frac{E^{1/4}}{2\Omega}t', h = h_O h', \mathbf{u} = \sqrt{gh_O}\mathbf{u}', f = \frac{2\Omega}{E^{1/4}}y' \qquad 2.45$$

where E denotes the Lamb parameter,

$$E = \frac{4\Omega^2 R^2}{gh_o}, \qquad 2.46$$

R is the radius of the Earth, Ω is the angular velocity of the Earth's rotation (i.e. 2π/day), and h_o is the mean depth, which is taken as 0.4 m. The initial conditions (Eskilsson and Sherwin, 2000) define a mound of water that should propagate westward under the influence of the Coriolis force, and are expressed as,

$$h'\left(\mathbf{x},t\right) = exp\left(-\frac{y'^2}{2}\right)exp\left(-\frac{\left(x'+5-t'\right)^2}{2}\right),$$
$$\mathbf{u}'\left(\mathbf{x},t\right) = exp\left(-\frac{y'^2}{2}\right)exp\left(-\frac{\left(x'+5-t'\right)^2}{2}\right), \qquad 2.47$$
$$\mathbf{v}'\left(\mathbf{x},t\right) = 0.$$

A non-dimensional computational domain of $(x', y') \in [-10,10]\times[-5,5]$ is used, with 4096 structural triangular elements and third order polynomials. Using the beta-plane approximation, the Coriolis parameter is written $f = f_o + \beta y$.

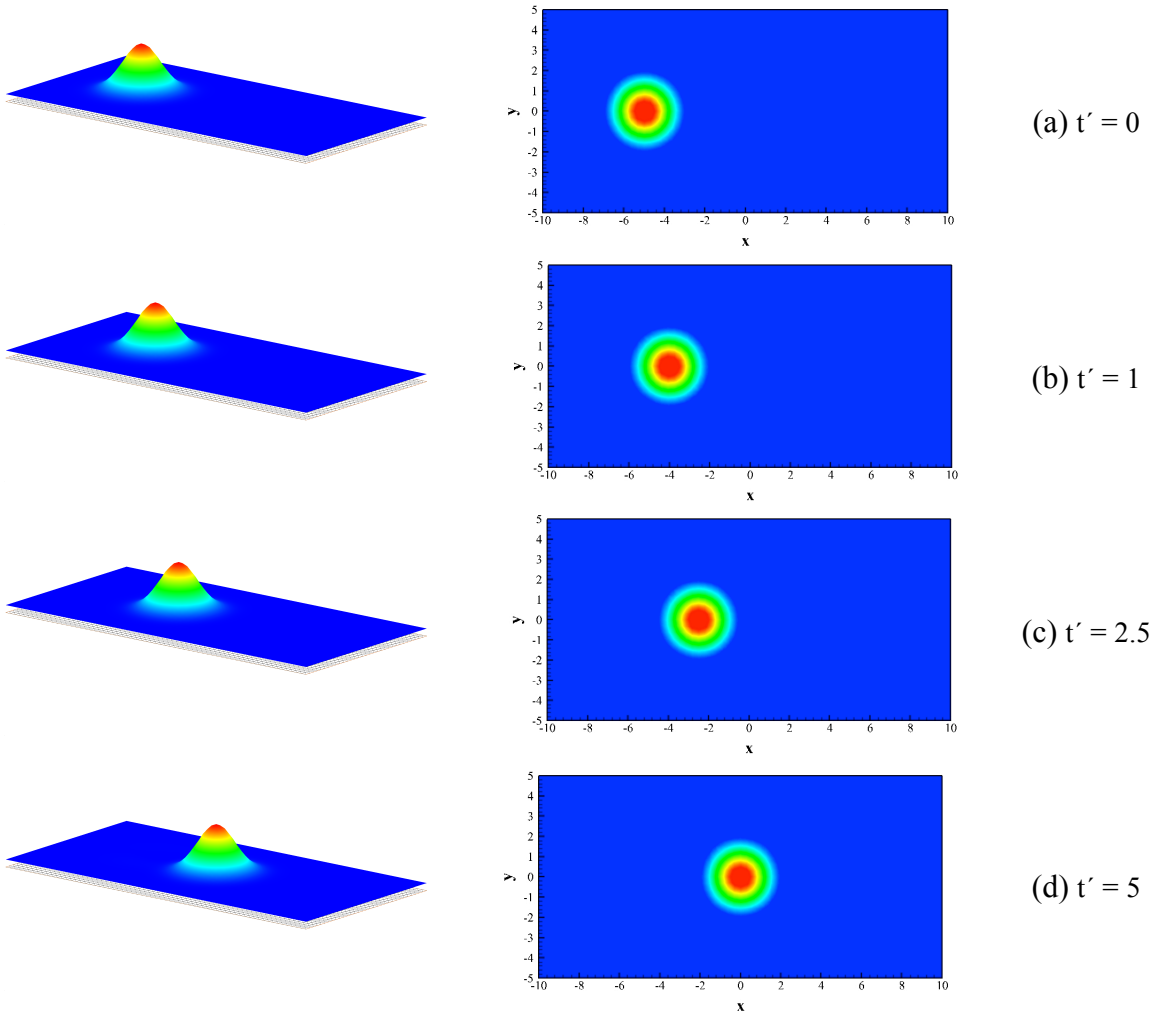

Figure 2.6 – Propagation of Kelvin wave using third order polynomials at selected times.

By setting f_o to 0, the β parameter is obtained as $\left(2\Omega/\mathrm{R}\right)$, while y is the coordinate positive northwards between latitudes. Boundary conditions at the inflow and outflow boundaries are defined by specifying the normal flux using equation 2.47. On the walls, a slip boundary condition is applied. The mesh resolution is $r = 0.3125$. Figure 2.6 shows the propagation of the linear Kelvin wave.

2.7.4. Preservation of Still Water

In this test case, it is aimed to check that the discretization of the bed source terms properly balances the flux gradient terms in the numerical model. In certain applications, problems may arise due to the irregular geometry of the numerical domain, which may include extreme slopes with high bed roughness (Brufau *et al.*, 2002). When those terms are not handled correctly, spurious flows may appear in the solution (Bermudez and Vazques, 1994; Bunya *et al.*, 2009). To carry out the check, the benchmark case proposed by Ern *et al.* (2008) is used to verify the discontinuous Galerkin ADCIRC model for still water over non-uniform bathymetry. Ern *et al*. (2008) considered a one-dimensional domain. Initially the water level is set to 1 m above a fixed horizontal datum and the flow flux set to zero throughout the domain. The grid resolution is 0.5 m and a second order polynomial is used. The bed profile is obtained by equation 2.48.

$$b(x) = \frac{10e^{-x^2} + 15e^{-(x-2.5)^2} + 10e^{-\frac{(x-5)^2}{2}} + 6e^{-2(x-7.5)^2} + 16e^{-(x-10)^2}}{20} \qquad 2.48$$

The two-dimensional grid is illustrated in Figure 2.7. The model is run for 1 day of simulation time. Still water level is maintained as shown in Figure 2.8. The still water level remains exactly consistent throughout the simulation.

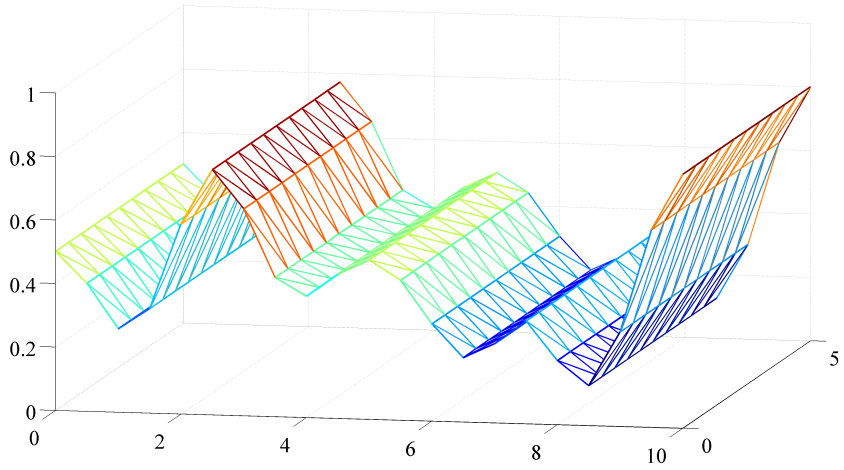

Figure 2.7 – Bed profile and model mesh used in still water test.

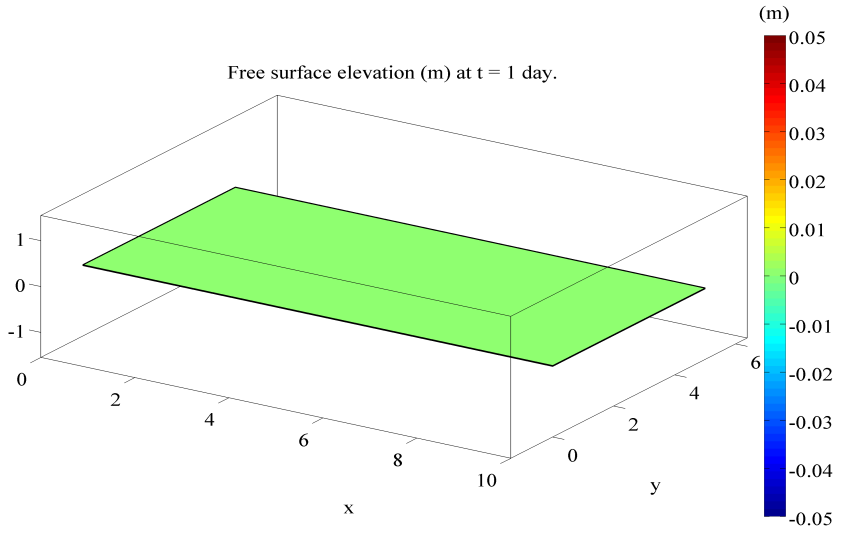

Figure 2.8 – Simulation results for free surface water elevation (ζ) for t = 1 day.

2.8. Conclusions

This chapter firstly presented the two-dimensional shallow water equations (SWEs), which are employed to model naturally occurring tidal flows at coastal basins. A brief summary of the mathematical boundary conditions was also provided. The chapter also provides a discussion of the limitations of the shallow water equations.

The chapter then introduced the discontinuous Galerkin finite element method to solve the SWEs. The DG method was preferred mainly due to its ability to include discontinuities within the solution while conserving mass individually at each element. This feature of the DG methods is of importance as one of the aims of this project is to represent the effects of tidal turbines as a line discontinuity in the simulations. An open-source numerical solver (DG-

ADCIRC), which uses the discontinuous Galerkin finite element method to solve the shallow water equations was chosen and verified against several benchmark tests. It was demonstrated that DG-ADCIRC accurately solves the shallow water equations.

Chapter 3

Representation of Tidal Turbine Arrays in a Discontinuous Galerkin Solver

This Chapter aims to present the methodology adapted to describe the tidal turbine devices in an array format in the selected numerical solver. Section 3.1 provides an introduction to the techniques employed to represent the effect of tidal turbines in the flow field in the literature. Section 3.2 presents inclusion of linear momentum actuator disk theory, which is adapted as a sub-grid model to represent the tidal arrays in the computations studied in this thesis, to the selected two-dimensional shallow water solver. Section 3.3 presents the verification of the algorithm for a number of problems considering an idealised channel for different flow conditions. Conclusions and discussions are presented in Section 3.4.

3.1. Introduction

Various approaches have been taken to assess the amount of useful extractable power from tidal stream resources. One of the commonly used methods is based on the undisturbed kinetic energy flux (Black and Veatch, 2005). This approach provides an incorrect estimate of the resource, as there is no direct proportionality between the kinetic energy flux and available power (Garret and Cummins, 2005; Draper *et al.*, 2013). A second, numerical modelling, approach has been applied, in which the far-field effects of the tidal array deployment are represented by means of an additional bed roughness coefficient in the governing equations (Blunden and Bahaj, 2007; Karsten *et al.*, 2008). Including enhanced bed friction in the model is straightforward, however, it is unclear how much of the power extracted from the flow is usefully available to the tidal devices. Thus, a third approach has been suggested by Draper (2011) in which the turbine arrays are described using a near-field approach that is embedded in a two-dimensional shallow water solver. The near-field approach enables a distinction to be made between the available power and total power extracted from the site. Assuming that the

tidal devices are evenly spaced and the length of the downstream mixing zone is sufficiently small compared to the mesh discretisation, Draper (2011) demonstrated that the effects of tidal arrays can be represented using line sinks of momentum. Following Draper's approach, this chapter summarises the implementation of a line sink of momentum within the selected numerical solver, DG-ADCIRC (Kubatko *et al.*, 2006a). The verification of the algorithm is undertaken for a number of different configurations and problem settings.

3.2. Implementation of Sub-Grid Model to Represent the Effect of Tidal Turbines

The inclusion of the tidal turbine devices in a depth-averaged model requires a simplification of real physics due to limitations within the governing equations. In the literature, two methods have commonly been adopted to account for the influence of tidal devices in the flow field, and to represent the relative momentum loss in two-dimensional shallow water models (see Chapter 1). In the first methodology, an additional bed shear stress term is considered (Sutherland *et al.*, 2007; Blunden and Bahaj, 2007), whereas the second methodology uses Linear Momentum Actuator Disk Theory (LMADT), following its application in the wind energy industry (Burton *et al.*, 2001; van Kuik, 2007).

The additional bed shear stress approach has the advantage that it is straightforward to apply and gives realistic answers provided the calibration is accurate. However, the approach has the disadvantages that it is semi-empirical and does not incorporate the physics of the momentum losses across tidal turbines. It is also difficult to relate the additional drag coefficient to varying combinations (geometries and characteristics) of tidal turbines in arrays within parameter studies.

Linear Momentum Actuator Disk Theory (LMADT) has a long history, having been first applied by Froude (1889) to the design of ship propellers. The approach involves fitting a control volume around the object of interest (i.e. the turbine, represented as a porous disk) and deriving relationships based on mass and momentum conservation supplemented by Bernoulli's energy equation along streamlines. Conventional one-dimensional LMADT as applied to wind turbines assumes unbounded flow conditions, and so is not applicable to tidal turbine design without modification. Bryden *et al.* (2007) emphasise that conventional LMADT theory is derived assuming that the flow is incompressible and unconstrained,

whereas for applications to tidal basins, the flow is constrained by the seabed and free surface. This problem has been overcome by Houlsby *et al.* (2008) who extended conventional one-dimensional LMADT to include a finite medium for a dense fluid that characterises open-channel flow (see Appendix 1). Houlsby *et al.*'s derivation of LMADT also accounts for the wake mixing downstream of the turbines, which enables a distinction to be made between the power extracted by the turbine and the total power removed from the tidal stream.

In this thesis, LMADT has been adopted to represent tidal fences in a two-dimensional discontinuous Galerkin hydrodynamic solver (DG-ADCIRC) by means of a line sink of momentum. In this regard, the difference in water level across a tidal turbine needs to be determined as a function of relevant parameters characterising the turbine devices and the flow conditions. Draper (2011) developed a numerical model (OxTIDE) that uses a momentum sink to represent turbines in idealised flow domains. This thesis aims to extend this work in order to evaluate the power potential of selected geophysical sites.

The use of a momentum sink in a two-dimensional model involves several assumptions, which are (Draper, 2011),

- tidal devices are installed in parallel to each other with uniform centre-to-centre spacing,
- the thrust applied by the tidal turbines is sufficient to dominate other source terms, such as the bed friction and inertia forces,
- the fence and basin characteristics (e.g., blockage ratio, water depth) change slowly with time, and
- the wake mixing length is significantly smaller than the element size.

Considering the space discretisation of the flow domain using the discontinuous Galerkin method in addition to the assumptions presented above, it is possible to represent the turbines as an edge of an element in the computational domain. The relative momentum sink is computed by modifying the numerical flux across the edges between adjacent elements, where the discontinuity due to the presence of the turbines would occur. Figure 3.1 depicts two elements that share a common edge representing an array of turbines where a line discontinuity occurs.

When approaching the turbine edge from the interior of the element A, the primitive variables on a Gaussian point along the edge are given as, $\mathrm{H}^{int}, \bar{u}^{int}, \bar{v}^{int}$ and when approaching from the exterior, the corresponding variables are $\mathrm{H}^{ext}, \bar{u}^{ext}, \bar{v}^{ext}$. The nomenclature for these primitive variables follows: H is the total depth of the water column; $\bar{u}$ is the depth-averaged normal velocity component in the x- direction; and $\bar{v}$ is the tangential velocity component in the y- direction. Considering that the elements are coupled by the numerical flux computed at each edge of an element, the associated momentum sink at the 'turbine' edge could be introduced by manipulating the flux term.

The common edge (blue line shown in Figure 3.1) where the line discontinuity is imposed yields a one-dimensional Riemann problem in order to alter the flux term. Assuming that the flow remains sub-critical at the location of the turbines, the wave structure at this common edge is that of a fan of rarefaction waves (Draper, 2011). Figure 3.2 shows the linearised characteristic lines projected along a coordinate normal to the turbine edge. The associated momentum sink is implemented by altering the fluxes within the contact region, which consists of the flux out of element A, $F_A\left(H_*^{int}, \bar{u}_*^{int}, \bar{v}_*^{int}\right)$ and into the element B, $F_B(H_*^{ext}, \bar{u}_*^{ext}, \bar{v}_*^{ext})$.

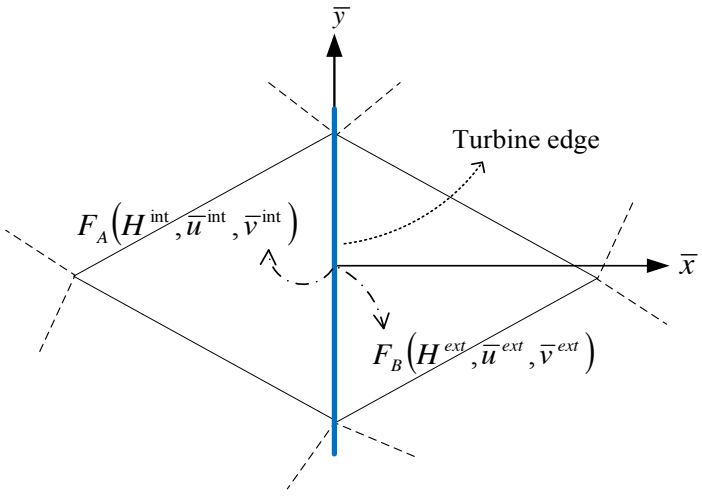

Figure 3.1 – Neighbouring elements whose common edge is described as a turbine edge, where the line discontinuity occurs (indicated by blue line). Figure is reproduced from Draper (2011).

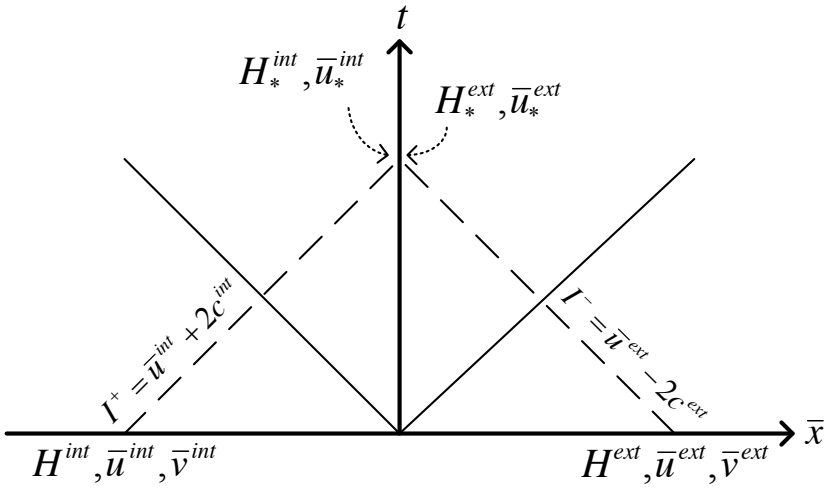

Figure 3.2 – Linearised characteristic lines along a coordinate normal to the line discontinuity (turbine edge). The Riemann invariants are projected along the characteristic lines (dashed lines). The solid lines represent the rarefaction waves.

LMADT derivation used herein to represent the effect of tidal turbines assumes that the devices will not exert a force in the tangential direction, thus no change on the tangential momentum will occur (Draper, 2011; Houlsby *et al.*, 2008). However, it should be acknowledged that the real turbine arrays would inevitably alter the tangential momentum. The magnitude of that momentum change will be dependent on the design of the selected tidal turbine.

The tangential velocity changes play an important role on the efficiency of the turbines that are especially placed at the ends of an array, where the flow diverts and thus reaches these outer turbines at an angle (i.e. skew flow). Regarding this problem, Belloni *et al* (2013) conducted a detailed turbine-scale analysis considering the effect of skew flow on the performance of selected tidal turbine designs. However, considering the analyses conducted in this thesis do not consider a specific tidal turbine design, change in the tangential momentum is not accounted for in the sub-grid model.

In Figure 3.2, the interface values $H_*^{int}, \bar{u}_*^{int}, H_*^{ext}, \bar{u}_*^{ext}$ represent the solution of a one-dimensional local Riemann problem that would satisfy the conditions,

$$H_*^{int}\,\bar{u}_*^{int} = H_*^{ext}\bar{u}_*^{ext}\,, \tag{3.1}$$

$$\bar{u}^{int} + 2c^{int} = \bar{u}_*^{int} + 2c_*^{int}, \tag{3.2}$$

$$\bar{u}^{ext} - 2c^{ext} = \bar{u}_*^{ext} - 2c_*^{ext}\,. \tag{3.3}$$

Equation 3.1 ensures mass conservation at the edge of the element. Equations 3.2 and 3.3 conserve the Riemann invariants along the characteristic lines normal to the boundary. In order to account for the momentum sink across the turbine edges, one more condition must be assigned. The fourth condition is obtained from the pressure-volume-constrained (for open-channel flows) derivation of LMADT that gives a relation between the upstream and downstream water depths. The relative head difference across the turbines is given as (Houlsby *et al.*, 2008),

$$\frac{1}{2}\left(\frac{\Delta H}{H}\right)^3 - \frac{3}{2}\left(\frac{\Delta H}{H}\right)^2 + \left(1 - Fr^2 + \frac{C_T B Fr^2}{2}\right)\frac{\Delta H}{H} - \frac{C_T B Fr^2}{2} = 0. \qquad 3.4$$

In equation 3.4, ΔH is the depth change across the turbine

$$\Delta H = \left|H_*^{int} - H_*^{ext}\right|, \qquad 3.5$$

and Fr is the upstream Froude number

$$Fr = \frac{\overline{u}^{int}}{\sqrt{gH^{int}}}. \qquad 3.6$$

The above derivations use the upstream and downstream values that are assigned according to the direction of the flow. For instance, consider a flood tide in which the internal characteristic line represents the upstream location of the turbine arrays. As the tide reverses, the upstream variables must of course be re-assigned as downstream variables, and *vice versa*. In this respect, the numerical solver is configured to compute the direction of the flow first.

The routine included in the DG-ADCIRC code is configured to compute the relative head difference ($\Delta H/H$) across the turbines (equation 3.4). In order to solve equation 3.4, several parameters must be provided. The LMADT derivation used in this project (see Appendix 1) requires the blockage ratio (B), wake velocity coefficient (α_4) and the upstream Fr number to be prescribed in order to compute the relative head drop and the associated momentum sink.

To ensure that the analysis conducted in this thesis is not dependent on specific turbine geometries, the blockage ratio B corresponds to the total cross-sectional area that the tidal devices in an array occupy within the water column. To define a certain number of turbines in an array requires an assumption to be made about the turbine geometry. For axial flow

turbines with a specified turbine diameter, it is possible to calculate the blockage ratio as (Adcock *et al*., 2013),

$$B = \frac{\pi D^2}{4(DH)} = \frac{\pi D}{4H}, \tag{3.7}$$

In equation 3.7, D is the axial flow turbine diameter, and H is the total water depth. In equation 3.4, the thrust coefficient (C_T) must also be supplied to evaluate the head drop across the turbines. The thrust applied to the flow by the turbines is given as (Houlsby *et al.*, 2008),

$$C_T = \beta_4^2 - \alpha_4^2 . \tag{3.8}$$

In equation 3.8, β_4 is the bypass flow velocity coefficient, and α_4 is the turbine wake velocity coefficient. As the wake velocity and bypass flow coefficients are inter-related, one of them must be predefined in order to calculate the other. Following Houlsby *et al.* (2008), the wake velocity coefficient α_4 is chosen as the prescribed parameter, while the bypass flow coefficient β_4 is calculated by a subroutine written in DG-ADCIRC.

The derivation of the bypass flow coefficient β_4 is related back to the upstream Fr number using the Bernoulli equation applied to the bypass flow in accordance with mass and momentum conservation laws applied between the upstream and downstream of the turbine (see Appendix 1). The resulting relation is a three-parameter set that defines the flow conditions,

$$\begin{aligned} \frac{Fr^2}{2}\beta_4^4 + 2\alpha_4 Fr^2\,\beta_4^3 - \left(2 - 2B + Fr^2\right)\beta_4^2 - \left(4\alpha_4 + 2\alpha_4 Fr^2 - 4\right)\beta_4 \\ + \left(\frac{Fr^2}{2} + 4\alpha_4 - 2B\alpha_4^2 - 2\right) = 0. \end{aligned} \tag{3.9}$$

Equation 3.9 is quartic in β_4 and is computed within DG-ADCIRC for prescribed wake velocity coefficient α_4 and blockage ratio B, using the Newton-Raphson method for small Froude number flows. The computed β_4 can then be substituted in equation 3.8 to calculate the thrust coefficient C_T. Once C_T is computed, equation 3.4, which is a cubic in relative depth change ($\Delta H/H$), can be solved for known upstream Fr number and blockage ratio B. Rewriting the relative depth change as,

$$\frac{\Delta H}{H} = \frac{H_*^{int} - H_*^{ext}}{H_*^{int}} = 1 - \frac{H_*^{ext}}{H_*^{int}} \qquad 3.10$$

enables the cubic expression in equation 3.4 to be simplified to a "depressed cubic" equation. Equation 3.11 shows the depressed cubic relation where Θ is the ratio between the downstream and upstream total water column heights ($\Theta = H^{ext}/H^{int}$),

$$\Theta^3 + \left(C_T B Fr^2 - 2Fr^2 - 1\right)\Theta + 2Fr^2 = 0\,. \qquad 3.11$$

Equation 3.11 is solved within each computational iteration using the trigonometric method to evaluate the roots of the depressed cubic. Choosing the real root, which provides a physically admissible solution, Θ is used to evaluate the upstream and downstream flow characteristics.

Using the conservation of mass equation in equation 3.1, the relations between the horizontal velocity component $\bar{u}$, and celerity c across the turbines become,

$$\bar{u}_*^{ext} = \frac{\bar{u}_*^{int}}{\Theta}, \qquad 3.12$$

$$c_*^{ext} = \sqrt{\Theta} c_*^{int}\,. \qquad 3.13$$

Equations 3.12 and 3.13 are then substituted into the Riemann invariant conservation relations (equations 3.2 and 3.3) in order to calculate the altered normal velocity ($\bar{u}_*^{int}, \bar{u}_*^{ext}$) and celerity ($c_*^{int}$, c_*^{ext}) values at the contact region, where the line discontinuity is imposed. Using the computed values for celerity it is possible to evaluate the upstream and downstream total heads,

$$H_*^{(int,ext)} = c_*^{(int,ext)2} g. \qquad 3.14$$

Assuming that the tangential velocities are not affected by the energy extraction from the stream, the routine ends by computing the momentum fluxes internal and external to the turbine edge. Finally, the routine evaluates the numerical flux at the edge boundary and returns to the main routine to continue the computation.

3.2.1. Power Analysis

One of the advantages of using LMADT is that it provides a distinction between the power that is available to the turbines and the total power that is extracted from the tidal stream (Houlsby *et al.*, 2008; Draper, 2011). The power available to the turbines is defined by the

multiplication of the velocity of the fluid at the turbines with the thrust applied to the flow by the devices,

$$P_{available} = \alpha_2 u\, T. \tag{3.15}$$

In equation 3.15, α_2 is the turbine velocity coefficient, u is the upstream flow velocity and T is the thrust applied to the flow by the turbines. Houlsby *et al.* (2008) define the thrust by the relation below,

$$T = \frac{1}{2}\rho u^2 BbH(\beta_4^2 - \alpha_4^2) = \frac{1}{2}\rho u^2 BbH C_T. \tag{3.16}$$

In the above equation, ρ is the density of the fluid, u is the upstream flow velocity, B is the blockage ratio, b is the width of the open channel, H is the upstream water level, β_4 is the bypass flow velocity coefficient, α_4 is the turbine wake velocity coefficient and C_T is the thrust coefficient as given in equation 3.8.

Using equation 3.16, the available power can be written as,

$$P_{available} = \alpha_2 u\, T = \frac{1}{2}\rho u^3 BbH\alpha_2(\beta_4^2 - \alpha_4^2) = \frac{1}{2}\rho u^3 BbH C_P. \tag{3.17}$$

Draper (2011) presents several conclusions using the relations between the power coefficient, C_P and wake velocity coefficient, α_4 for prescribed flow conditions. For a set of known upstream Fr numbers and blockage ratios B, the power coefficient, C_P is increased with increasing blockage ratio, B. For a very wide range of realistic parameters, the analysis shows that the power is maximised when the wake velocity coefficient, α_4 is close to $1/3$. Another interesting finding from the analysis is that the turbines extract the potential energy from the stream (head drop across the turbines) and results in an increment in the kinetic energy at the downstream of the tidal devices.

The derivation of LMADT by Houlsby *et al.* (2008) considers the downstream mixing once the flow passes through the turbines. The power loss due to the wake mixing is given as,

$$P_{wake} = \frac{1}{2}\rho u^3 BbH\alpha_2\alpha_4^2 + \frac{1}{2}\rho u^3 bH(1 - B\alpha_2)\beta_4^2 - \frac{1}{2}\rho u^3 bH\left(\frac{H}{H - \Delta H}\right)^2 + Hbu(H_4 - H_5)\rho g. \tag{3.18}$$

The total power (P_{total}) extracted from the stream is simply the sum of the power available ($P_{available}$) to the turbines with the power lost (P_{wake}) in the downstream mixing,

$$P_{total} = P_{available} + P_{wake} = \rho g u b H \Delta H \left(1 - Fr^2 \frac{1 - \Delta H/2H}{(1 - \Delta H/H)^2}\right). \qquad 3.19$$

Equation 3.19 considers the potential energy lost in the tidal stream due to the presence of the turbines with a correction (given in the brackets) for the increment in the kinetic energy of the flow at the downstream of the turbines (Houlsby *et al*., 2008).

3.2.2. Turbine Efficiency

The ratio of power that is extracted solely by the turbine to the total amount of power removed from the tidal stream defines the turbine efficiency. Using equations 3.17 and 3.19, the turbine efficiency η is given as,

$$\eta = \frac{P_{available}}{P_{total}} = \frac{P_{available}}{\rho g u b H \Delta H}\left(1 - Fr^2 \frac{1 - \Delta H/2H}{(1 - \Delta H/H)^2}\right)^{-1} \qquad 3.20$$

For partially blocked flows, the flow tends to divert around the ends of the array. Thus, the mass flux passing through the turbine array decreases, which limits the maximum amount of power that the turbines can extract. In this case, the efficiency parameter becomes important as it provides an indication on how the turbines operate in an array (Draper, 2011).

3.2.3. Manipulation of the DG-ADCIRC Source Code

The DG-ADCIRC is an open-source numerical solver that consists of a series of FORTRAN77/90 programs, which are compiled consecutively using a "makefile". The DG-ADCIRC is capable of accessing any user-specified routine through altering the makefile. The makefile consists of the description of the computational resources (e.g. computational platform) that are available to the user as well as the compilation rules and the subroutines that are essential to compile the executable code.

The inclusion of sub-grid model using LMADT requires writing several FORTRAN 90 subroutines to compute a line sink of momentum in the computation for specified turbine array locations. The array locations are indicated in the mesh information input file by specifying the node numbers associated with the turbine array edges. When the code is executed, this information is automatically read in by an in-built DG-ADCIRC subroutine,

which creates the list of the edges in the computational domain and assigns the relevant boundary conditions to each of these edges.

The original DG-ADCIRC code does not include a description for a “turbine” edge. To include the LMADT sub-grid model, a new boundary segment type is created to flag any user-specified internal edge as a turbine array edge. During the course of the simulation, at each time step, when the code encounters these turbine edges, the momentum sink subroutines are called to compute the upstream and downstream flow characteristics, which enforce a head drop due to the energy extraction. The available and extracted power values are also computed for the predefined turbine operating conditions and upstream flow conditions for each turbine edge. The momentum sink calculation is then followed by computing the numerical flux term in order to maintain the information flow in the computational domain. The computed power values are also written in an output file, which has been coded in by the author, for each recording time step.

3.3. Verification Tests

The verification test cases consist of two general configurations of an idealised fence of tidal devices inserted in an open channel. The first of these considers a narrow channel where a fence is deployed completely across the width of the channel. In this scenario, it is expected that the flow will separate around the area of a turbine and then mix with the flow passing through it, creating a mixing zone downstream on the fence (Draper, 2011). In the second configuration, similar ideal fences are deployed in a partially blocked flow. The partially blocked flow case is then extended to different problems, which consider different configurations within the computational domain, in order to test the accuracy and stability of the modified DG-ADCIRC code.

3.3.1. Turbine Fence Across the Width of the Channel

The test case used for the verification of the algorithm is based on an idealised channel, which is forced by an inflow of constant discharge at the upstream boundary and has a specified water depth at the downstream boundary. The channel width and length are set to 400 m and 1000 m respectively. The model uses the Cartesian coordinate system. The depth of the channel is constant and is set to 1 m. In the simulation the bed friction is ignored. The

turbine fence is located in the middle of the channel, and extends across the entire width of the channel. In order to test the algorithm, various flow rates are selected in order to alter the upstream Froude number.

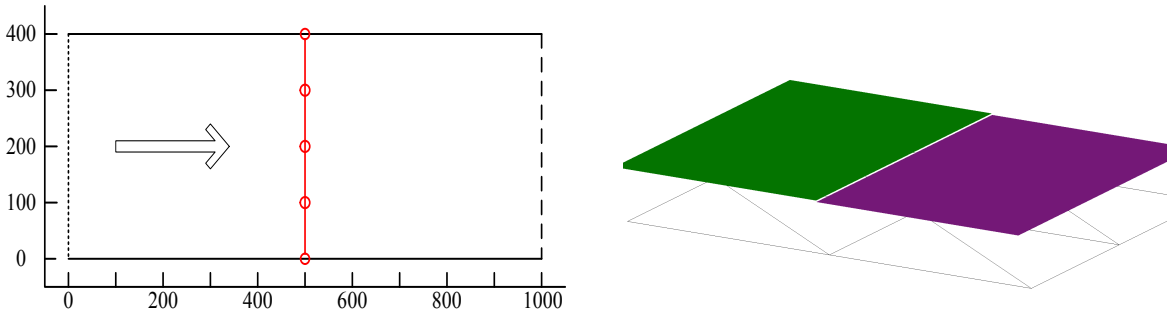

Figure 3.3 – The problem geometry (left- image reproduced from Draper, 2011). The turbines are located in the middle of the channel across the width of the channel. The channel is forced with a specified flux on the upstream, and on the downstream the elevation is defined. The arrow shows the direction of the inflow. Relative head drop seen in the flow field (right).

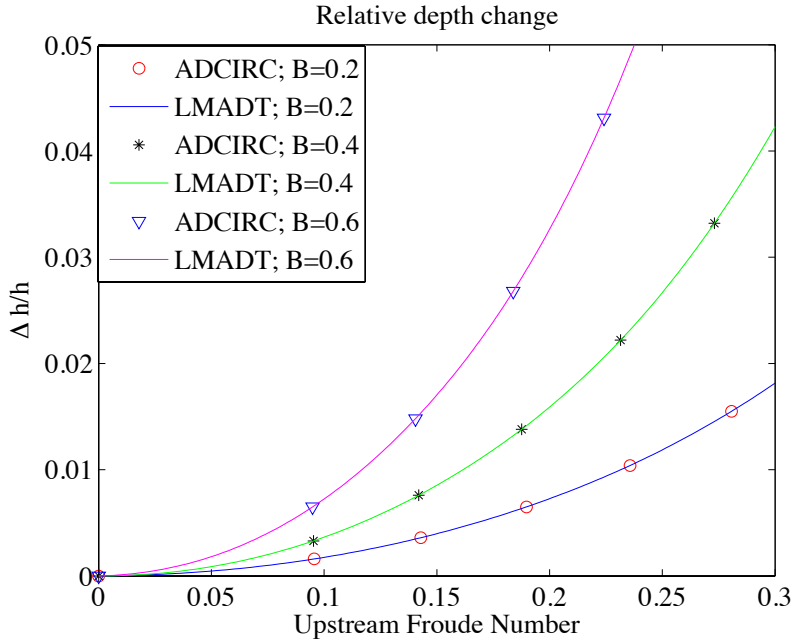

Figure 3.4 – Comparisons against the analytical (LMADT) solution and numerical (DG-ADCIRC) solution for different upstream conditions. The results are plotted against different blockage ratios for $B = 0.2$, $B = 0.3$, and $B = 0.4$.

The comparisons are then undertaken against different upstream blockage ratios and wake induction factors to differing upstream Froude numbers, obtained from the analytical solution (LMADT), and the numerical results. These comparisons are plotted in Figure 3.4. The DG-

ADCIRC model results are in a very good agreement with the analytical solution. Figure 3.3 shows the problem geometry (left) and the relative head difference observed on the flow domain (right), which is plotted on top of the computational mesh.

3.3.2. A Partially Blocked Idealised Channel

In this example, a tidal fence that does not extend entirely across the channel is given. Figure 3.5 shows the unstructured triangular mesh, in which the domain size is 4000 m in width and 10000 m in length. The model uses the Cartesian coordinate system. The tidal fence is placed 2500 m away from the upstream forcing boundary (shown as a red line in Figure 3.5). The length of the tidal fence is 1000 m. The water depth is set to 1.0 m, and the bed friction coefficient is $c_f = 5\times10^{-4}$ throughout the domain. In this example, bed friction has been added to the problem in order to achieve a steady solution and to avoid wake instabilities (following Draper, 2011). The upstream boundary is forced using a constant flow rate to achieve an upstream Froude number of approximately 0.1. A ramping duration of 0.5 days is implemented in order to prevent a shock wave in the solution. The downstream boundary is an elevation specified boundary, which is set to $H = 1.0$ m. Slip boundary conditions are applied at the sidewall boundaries. The turbine fence is characterized by a wake induction factor of $\alpha_4 = 1/3$ and a blockage ratio of $B = 0.6$. The effects of the momentum sink on free surface elevation (ζ) and depth-averaged velocity field are shown in Figure 3.6 and Figure 3.7. It should be acknowledged that the mesh resolution used in this test is too coarse to capture the local flow features of the by-pass flow and array wake in detail. However, the main objective of including LMADT sub-grid model in the calculations is to approximate the amount of momentum sink due to energy extraction from the overall flow as accurately as possible and not to attempt to model the details of the wake as this is beyond the capabilities of the two-dimensional shallow water solvers.

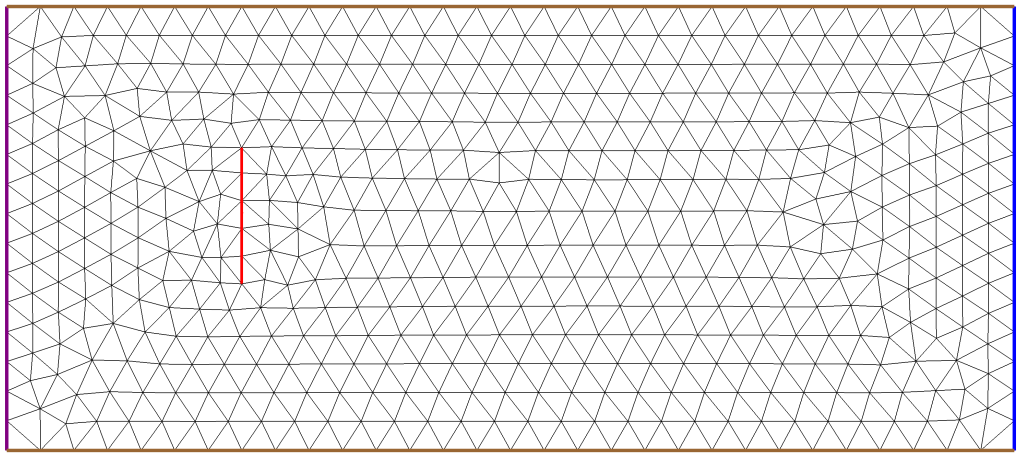

Figure 3.5 – The unstructured triangular mesh used in the unbounded turbine configuration test case; the purple line shows the upstream boundary which is flux specified; blue line shows the downstream boundary which is held at a fix elevation of 1.0 m; red line demonstrates the location of turbine fence in the domain; and the brown lines show the sidewall boundaries.

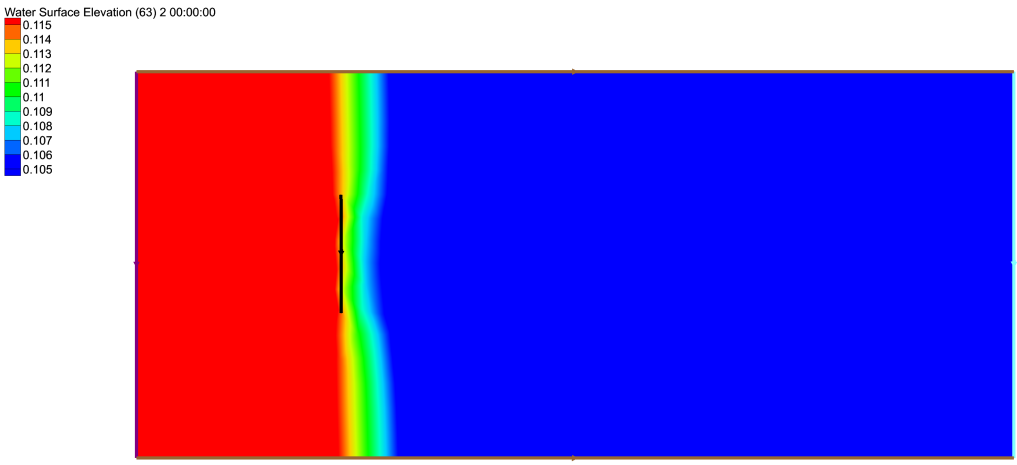

Figure 3.6 – The effect of momentum sink on the free surface elevation profile. The brown line indicates the tidal fence configuration. The water surface elevations are in metres.

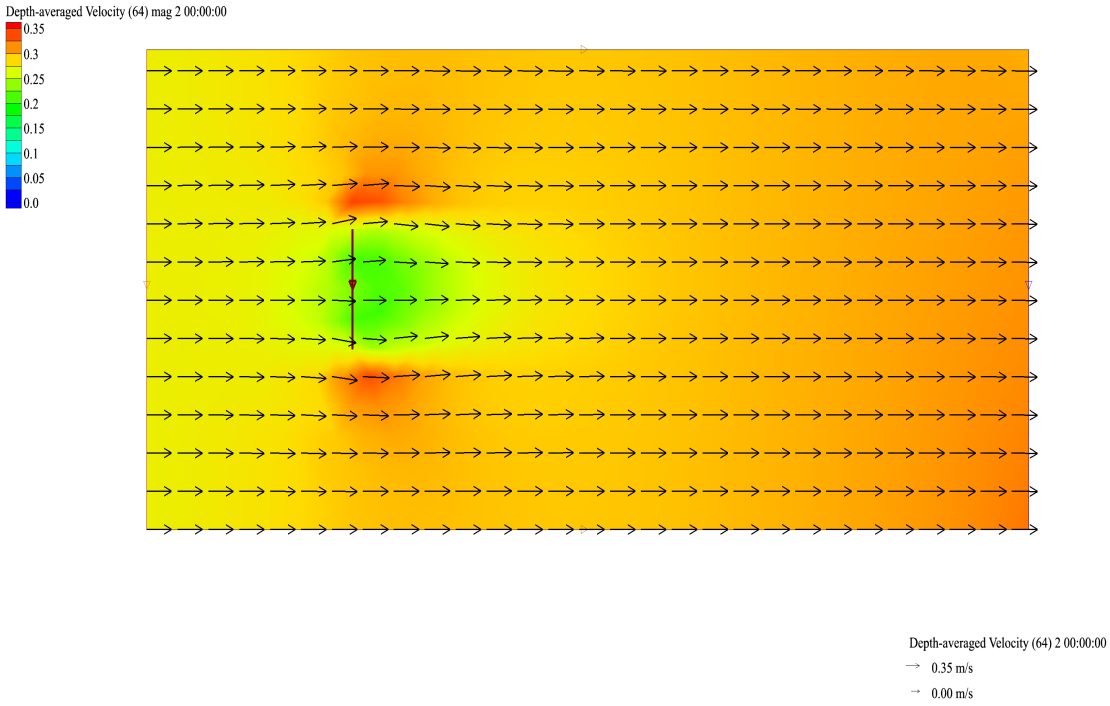

Figure 3.7 – The effect of a momentum sink on the local velocity profile. The vectors indicate the magnitude and direction of the flow and are superimposed onto a regular grid. The depth-averaged velocity contours are in m/s.

In Figure 3.6, the water surface elevation contour colours are set between 0.105 m to 0.115 m to present the head difference across the turbine array clearly. Due to the bounds for the contour levels the regions where the free surface water elevation is less than 0.105 m are also represented by the blue colour. A comparison of the computed and intended depth change along the fence is given in Table 3.1.

Position along the fence (m)	Analytical solution (LMADT) for $\Delta H/H$	Numerical solution (DG-ADCIRC) for $\Delta H/H$
0.0	0	0
100	0.0075	0.0074
200	0.0076	0.0076
300	0.0079	0.0079
400	0.0079	0.0079
500	0.0081	0.0082
600	0.0079	0.0079
700	0.0079	0.0079
800	0.0076	0.0076
900	0.0075	0.0074
1000	0	0

Table 3.1 Comparison of computed and intended relevant depth change along the tidal fence.

DG-ADCIRC results are in good agreement with the intended relative depth change computed using LMADT. In the next subsection, the modified DG-ADCIRC code is tested against more complex problems.

3.3.3. Partially Blocked Channels with Complex Flow Conditions

In this subsection, the modified DG-ADCIRC code has been tested for more complex problem settings. The first test considers an idealised channel, which is rotated by 30 degrees in the counter-clockwise direction. The purpose of this problem set up is to test the code's ability to cope with directionality in the flow domain. The total water depth is set to 1.0 m and the partial turbine fence is located in the first quarter of the channel, normal to the flow direction. The blockage ratio is set to 0.6 and the wake induction factor is 1/3. The boundary conditions are the same as the previous unbounded tidal fence test case. The coordinate system used is geographic (latitude and longitude). The resulting velocity field illustrated in Figure 3.8 is in very good agreement qualitatively with that in Figure 3.7 after rotation.

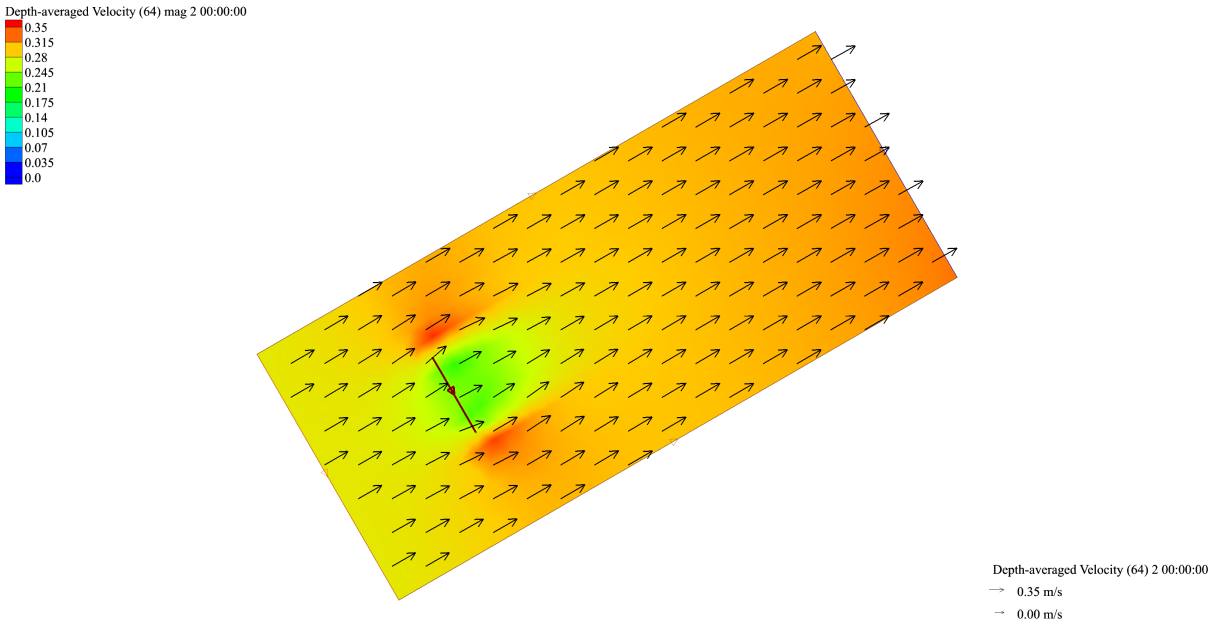

Figure 3.8 – Rotated domain test case with unbounded tidal fence placed normal to the flow direction.

The numerical models created in this project, are formed using the real bathymetric data, which indicates that the seabed changes arbitrarily within the computational domain. This test case therefore examines the capability of the modified DG-ADCIRC code to cope with non-uniform bathymetric conditions in the presence of tidal fences. Thus, the next test case

considers the rotated idealised channel introduced previously, with variable bed topography. The change in the bathymetry is calculated with respect to the longitude of the nodes. The bathymetric depth is calculated as follows,

$$H_{domain} = 1 + \frac{Longitude_{node}}{100}. \qquad 3.21$$

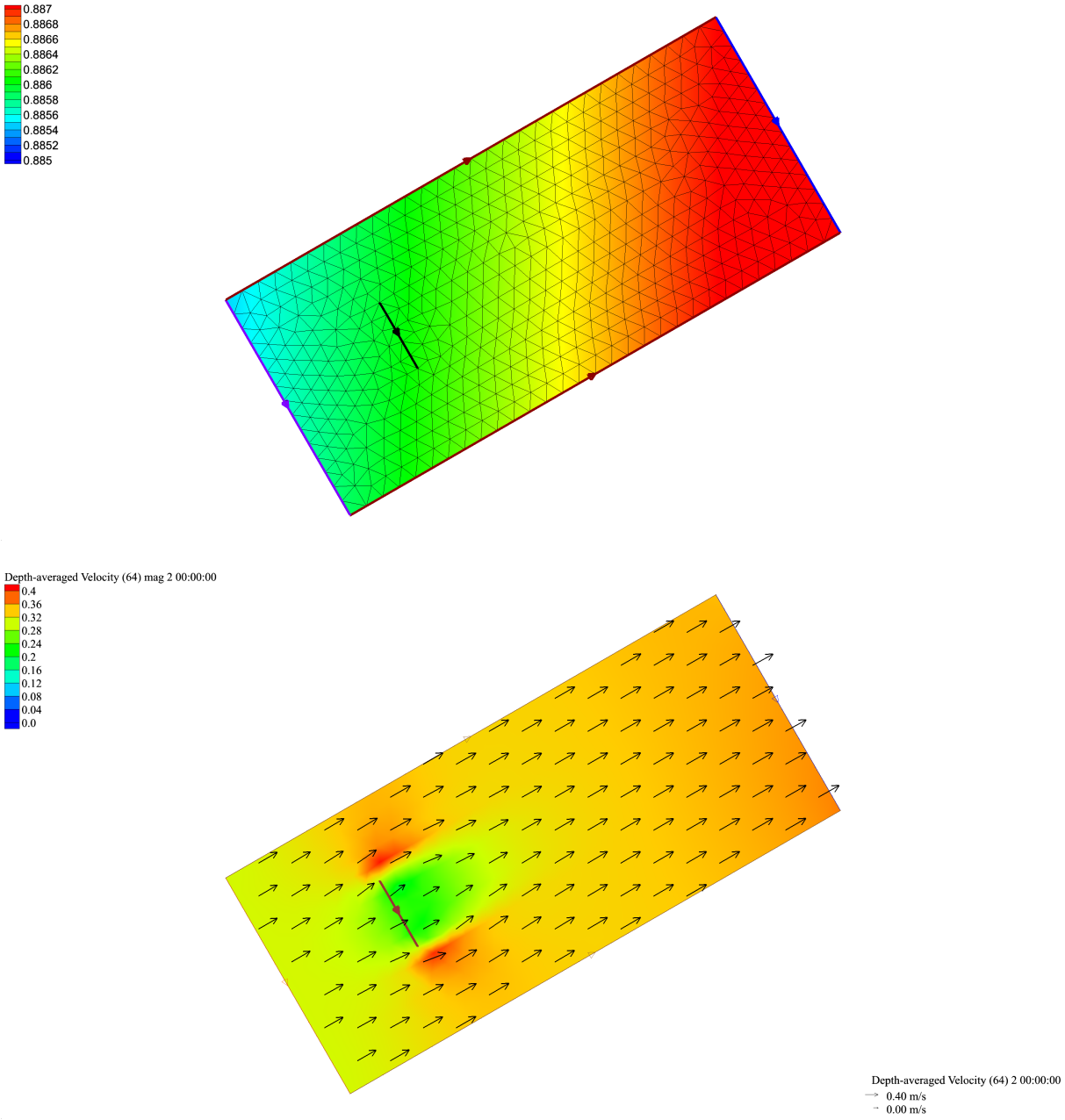

Figure 3.9 – The computational mesh used in the problem showing the bathymetric depths across the channel (top), and the computed velocity field for a rotated rectangular channel with variable bathymetry (bottom). The velocity vectors are interpolated to the domain. The contours are in metres.

Figure 3.9 shows the mesh used (top figure) and the predicted velocity field (bottom figure). The results show higher velocities within the domain due to the decrease in the total water depth within the computational domain. From the figure, it is also observed that the variation in the water depths across the channel causes a slight asymmetry in the velocity flow field. The next test case examines the behaviour of the turbine model to non-normal flows.

Figure 3.10 indicates the velocity field computed for an idealised horizontal channel, where the turbines are positioned at an angle of 60 degrees to the incoming flow. The figure shows that the by pass flow is accelerated due to the flow diversion, which agrees well with the theory. In this test case, as the flow reaches the tidal array at an angle (i.e. skew flow conditions), it is possible to approximate the local flow field by adapting a lift and drag relation approach.

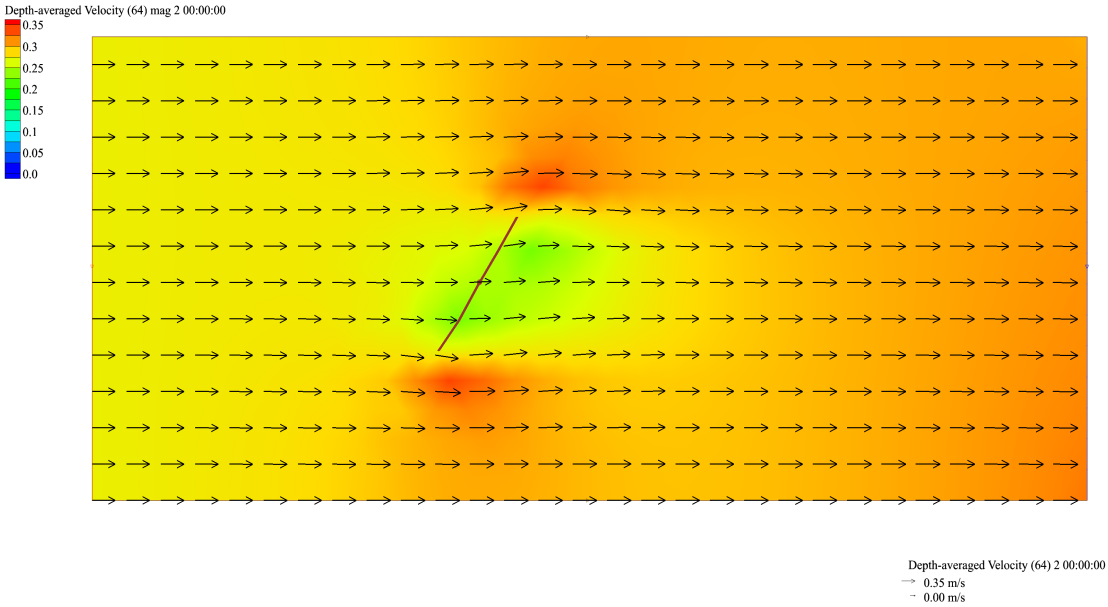

Figure 3.10 – Idealised horizontal channel with unbounded turbines installed with an angle to the flow. The velocity vectors are interpolated to the domain.

Lastly, a test case is created for an idealised horizontal channel with constant bed topography (1 m), where a rectangular island is located near to the upstream boundary. The unbounded tidal fence is inserted downstream of the island in order to test the capability of the modified code to cope with large-scale horizontal eddies, which are parameterised with a constant eddy viscosity coefficient. The computed velocities are shown in Figure 3.11. With this last test case, the modified DG-ADCIRC code, which uses the LMADT routine to represent the tidal turbines, proves to be stable when forced with realistic conditions.

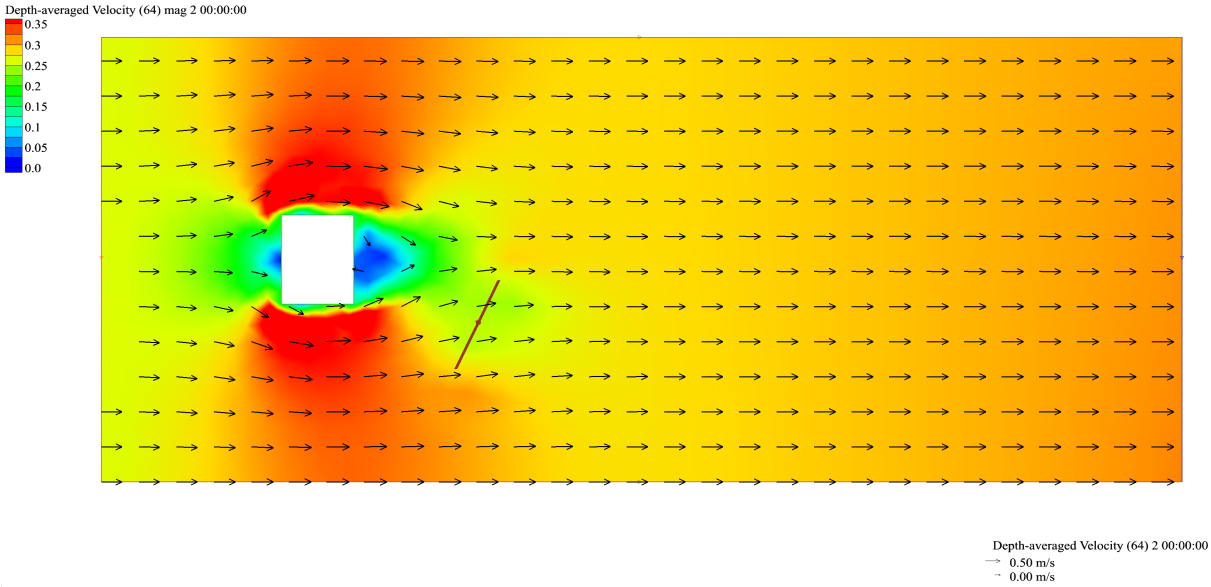

Figure 3.11 – Idealised horizontal channel containing rectangular island. The turbine fence is indicated with the brown line downstream of the island.

3.4. Conclusions

This chapter summarises the implementation of a sub-grid model that is based on Linear Momentum Actuator Disk Theory (LMADT) to approximate the local flow-field in the presence of tidal turbines.

The LMADT derivation considers a sufficiently long channel in which the presence of the turbines (actuator disks) does not affect the upstream flow conditions and allows the downstream wake to be fully mixed through the water column. LMADT assumes that the devices do not exert any force on the tangential direction, thus only horizontal (axial) velocity component is affected by energy extraction. The analysis provides the water level height and the horizontal velocity component of the downstream flow after wake mixing, where the pressure is equilibrated across the channel.

In the computations, the downstream flow conditions after wake mixing are calculated for prescribed turbine operating conditions (defined by α_4 and B) using LMADT at the edge of the element that is defined as a turbine array (line discontinuity). This is accomplished by altering the numerical flux that is used to couple the elements. Verification tests show that the implementation of the momentum sink using LMADT sub-grid model is in agreement with the theoretical model.

Another advantage of using LMADT is that it provides a distinction between the power extracted by the turbines (power available to the turbines) and the total amount of power that is removed from the tidal stream including the wake mixing losses. However, the available power is still overestimated by LMADT, as the analysis does not consider further mechanical and electrical losses as well as the energy loss due to mixing around the support structures.

Due to the one-dimensional nature of LMADT, there are several limitations to its application to model two-dimensional flows such as tides (Draper, 2011). LMADT assumes that the flow is steady, and does not account for the effects of bed friction, changes in bathymetry, or drag applied to the flow by the support structure of the devices. However, the length-scale of such factors to have significant implications on the theoretical results is assumed to be larger than the centre-to-centre spacing of the devices within an array.

Chapter 4

Validated Tidal Model of Anglesey and the Bristol Channel, U.K.

This chapter presents the implementation of two unstructured shallow water models. The models are developed using the discontinuous Galerkin method version of the ADCIRC (DG-ADCIRC) shallow flow model. The tidal basin off the south west coast of the UK including the Anglesey Skerries (a headland) and the Bristol Channel (an oscillating bay) has been modelled using unstructured triangular grids. Input data include bathymetric data provided by SeaZONE Ltd and tidal forcing data taken from the LeProvost tidal database (LeProvost *et al.*, 1995). The difference between the two models is solely due to the presence of inter-tidal zones that require a wetting and drying treatment within the computation. The wetting and drying scheme implemented in the DG-ADCIRC numerical solver accounts for both wet and dry elements at each Runge-Kutta time step, thus increasing the total computation time (Bunya *et al.*, 2009). In this respect, the objective was to develop the best possible model without using a wetting and drying treatment, and then explore whether the costly addition of wetting and drying was worth implementing in terms of improved modelling. As discussed in Section 4.5, inclusion of wetting and drying treatment improved the model results, especially for the current predictions.

Section 4.1 provides information about the model area. Section 4.2 introduces the model details of the DG-ADCIRC model (without wetting and drying treatment). In this section, a grid convergence study is introduced, which provided the optimal mesh resolution. The optimal model is calibrated against various bed friction coefficients. The calibrated model is then validated against available measurements of tidal elevation amplitudes and current magnitudes and directions, which is explained in Section 4.3. Section 4.4 discusses the model accuracy of the DG-ADCIRC model, which does not apply a wetting and drying treatment in the computation. Section 4.5 introduces the modified model, DG-ADCIRC-WD, which

includes the inter-tidal zones and uses a wetting and drying algorithm in order to represent correctly the mass flux in the tidal flats. Sections 4.6 and 4.7 discuss the improvements obtained by DG-ADCIRC-WD model and the conclusions respectively.

4.1. Introduction

This section describes a two-dimensional shallow water model of the tidal basin off the west coast of the UK that includes the Anglesey Skerries and the Bristol Channel. Chapter 1 has provided the rationale behind selecting the Anglesey Skerries and the Bristol Channel as potential tidal power sites. Provided that the selected sites are located in the same coastal basin containing the Irish Sea, it is possible that hydrodynamic interaction might occur between both sites if tidal turbines are installed. To account for this, both sites are modelled in the same numerical model domain.

Figure 4.1 depicts the area covered by the numerical model, which stretches from the continental shelf to the strait between Belfast (Northern Ireland) and Stranraer (Scotland) and includes the Irish Sea and the two regions of interest. The model has three open boundaries at which tidal elevations are specified. The first boundary is located in the Atlantic Ocean to the southwest, just beyond the continental shelf, in order to facilitate the tidal forcing without model reflections (Adcock *et al.*, 2011). The location of this boundary has been selected in order to capture properly the quarter wavelength resonance that occurs in the Bristol Channel (Fong and Heaps, 1978).

The second boundary is set at the western end of the English Channel, and is located between the Lizard in Cornwall to the tip of Brittany. A highly simplified section of the French coast in the vicinity of Cape Finisterre is included in order to allow the flux to and from the English Channel to be distinguished from other fluxes. Finally, there is a relatively small length of open boundary across the North Channel between Ulster and Galloway to reduce the mesh complexity that would have arisen if the Scottish islands had been included.

Figure 4.1 – Open boundaries of the computational domain depicted by red lines (Google Earth image, 2012).

4.2. Model Details

To create the computational mesh, the coastline of the overall region of interest is determined from bathymetric contour data provided by SeaZone Ltd in shapefile format, which is input to the meshing software SMS (Militello and Zundel, 1999). The shapefiles consist of mean sea level (MSL) and intertidal level contour data. An unstructured computational mesh is then constructed by SMS from the MSL contour data. To simplify meshing and ensure the CFL condition is met, small estuaries and islands have been removed from the numerical domain. Several manual corrections are made to enhance mesh quality. Section 4.2.2 presents results from the mesh convergence tests that confirm the optimum mesh resolution (noting accuracy and computational efficiency constraints).

For the Anglesey and Bristol Channel regions, bathymetric survey data were provided by SeaZONE Ltd at a spatial resolution of 2.78×10^{-4} degrees (approximately 30 m). Coarser resolution interpolated bathymetric data at a resolution of 1.7×10^{-3} degrees (approximately

180 m) were used elsewhere in the computational domain. The DG-ADCIRC model does not include intertidal zones, which are inundated during a flood tide and dried out during an ebb tide, where the flow boundary is moving (see e.g. Bunya *et al.*, 2009). The coastline for the model mesh is interpolated so that it acts effectively as a wall with a mean sea level of 6.0 m (the approximate largest half-amplitude of the tide) in order to prevent any instability that might occur due to the presence of mesh elements that would otherwise dry out (see Figure 4.2). The influence of wetting and drying on model results is explored later (see Section 4.5) using a modified model that includes the intertidal zones around the Bristol Channel. The following sections provide information about the tidal forcing model and grid convergence and calibration studies.

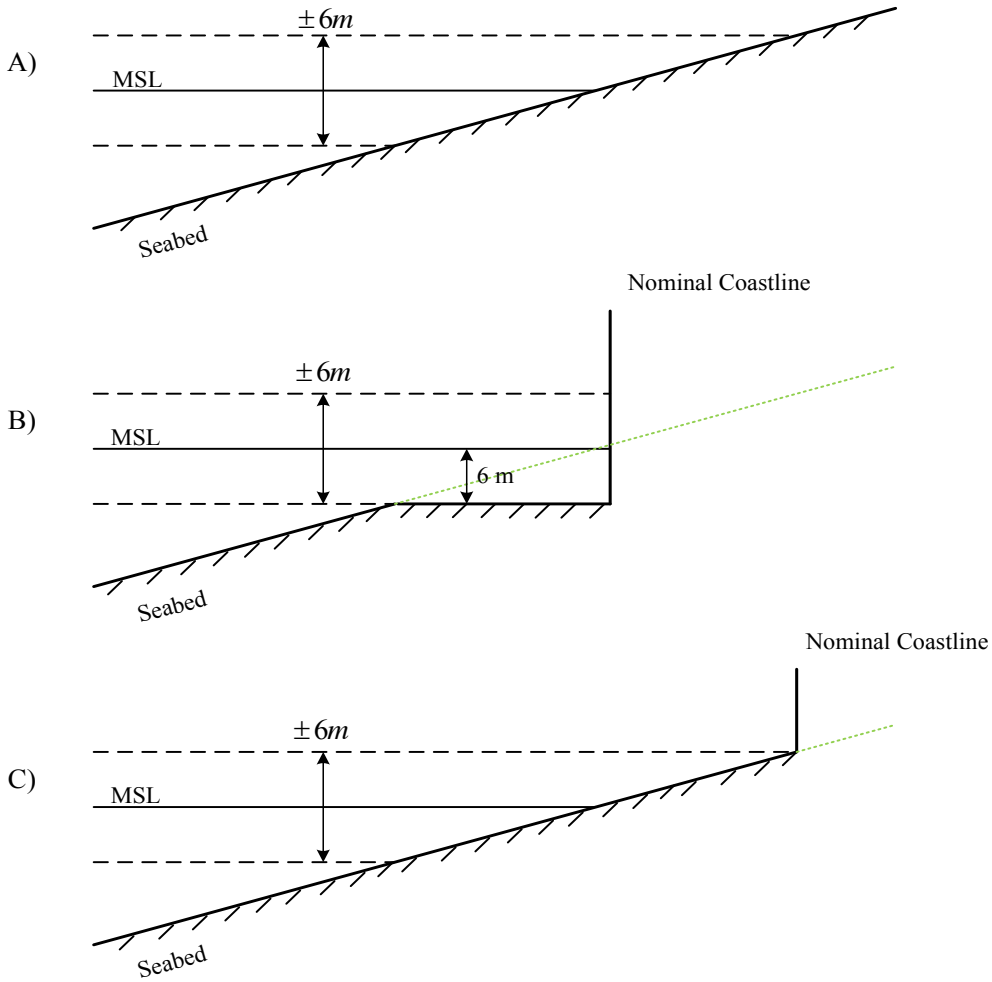

Figure 4.2 – The representation of coastlines in: A) natural case, B) DG-ADCIRC model without wetting and drying treatment, and C) DG-ADCIRC-WD model with wetting and drying treatment.

4.2.1. Tidal Forcing

In basin-scale modelling, the coastal domain is truncated through the use of artificial (open) boundaries that separate the area of interest from a connecting body of water. These open boundaries might be forced by tidal flows of specified free surface and/or flux time histories. The open boundaries of the numerical model are forced by specifying the amplitude and phases of prescribed tidal constituents.

In practice, these forcing parameters can be obtained from various tidal databases, which use low-resolution models to compute the tidal amplitudes and phases around the world. These values are then interpolated onto the open boundaries of the computational domain. Herein, the Le Provost tidal database (Le Provost *et al.*, 1995) is used to force the constructed numerical model.

The Le Provost database includes data concerning 13 principal tidal constituents ($2N_2$, K_1, K_2, L_2, M_2, MU_2, N_2, NU_2, O_1, P_1, Q_1, S_2, T_2). Considering the UK coasts, the tide is dominated by the M_2 and S_2 components (approximately 95% of the total tidal amplitude). Thus the model developed herein is forced by these two main semi-diurnal tidal components, M_2 and S_2.

As power is approximately related to the tidal current magnitude cubed, it is reasonable to neglect the remaining smaller components in energy resource assessment. Although higher-harmonic M_4 and M_6 components related to local bed friction and bed topography are not explicitly introduced at the open boundaries, their effects are nevertheless captured within the model and can be investigated through tidal harmonic analysis of the model outputs.

4.2.2. Mesh Convergence Analysis

Modelling of naturally occurring tides within a large domain is computationally demanding and requires a pragmatic approach with regard to mesh resolution. The finer the mesh, the smaller is the time step required in order to satisfy stability criteria, such as the Courant-Friedrichs-Lewy (CFL) condition, which is applicable given that an explicit time discretisation is used. There is a balance to be struck between resolution and computational performance. This section describes the development of a model at a resolution that captures the dominant hydrodynamic responses of the basins to the tides. In this respect, a grid convergence study is conducted to evaluate the necessary level of resolution required in the

numerical model to obtain a converged M_2 response (Westerink *et al*., 1994). The grid convergence tests involve five unstructured triangular finite element meshes. Table 4.1 presents the grid properties of each mesh created.

The model refinement is undertaken by changing the resolution of the coastal boundaries. The open boundary resolutions were kept unchanged as further resolving these boundaries was computationally inefficient (Westerink *et al*., 1994) and caused numerical instabilities due to the tidal database used in the model. The Le Provost tidal database has a coarse resolution with insufficient data points to interpolate accurately the forcing tidal elevation amplitudes and phases onto relatively narrow passages such as the North Channel.

Grid	Number of Nodes	Number of Elements	Minimum Δx(m) – Irish Sea	Minimum Δx(m) – Celtic Sea
U1	6669	12548	1700	1000
U2	13583	25879	800	600
U3	18967	36386	600	500
U4	30994	59799	400	300
U5	51597	100175	300	200

Table 4.1 Properties of grids constructed for the grid convergence study.

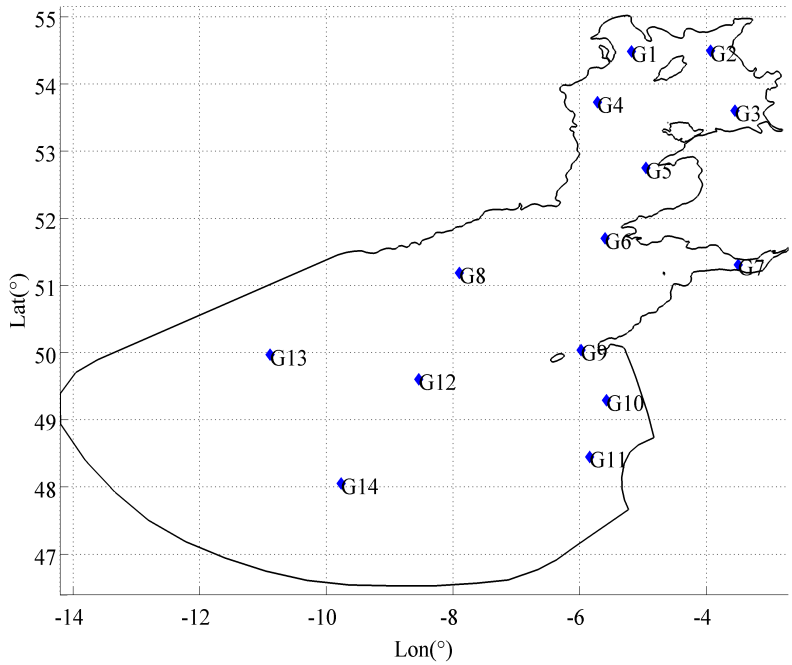

Figure 4.3 – Locations for the tidal elevation stations for grid convergence study.

The models have been run for 29 days in total, including a 1-day ramping period. Harmonic analysis has been conducted on the model results. Each numerical grid includes 14

observation stations throughout the model domain (see Figure 4.3). The M_2 tidal elevation amplitudes computed at each station are used to evaluate the convergence rate. In order to compute the error an exact solution would normally be required as a reference value. However, this study concerns modelling a hydrodynamically complex system and such an exact solution is not available. Regarding this, the results obtained from the finest grid (U5) were used as the reference values to compute the solution convergence (Roache, 1997). The errors were computed using a proportional standard deviation method for each model as suggested by Westerink *et al*. (1994),

$$E_{M2-amp}^{grid-finest} \equiv \left[\frac{\sum_{n=1}^{N} \left[\zeta_{M2}^{grid}(x_n, y_n) - \zeta_{M2}^{finest}(x_n, y_n) \right]^2}{\sum_{n=1}^{N} \left[\zeta_{M2}^{finest}(x_n, y_n) \right]^2} \right]^{1/2} . \qquad 4.1$$

In Equation 4.1, N is the total number of stations, n is the number of the specific observation station, (x_n, y_n) is the coordinates for each station, and ζ_{M2}^{grid} is the M_2 elevation amplitude for a given grid at specified stations. Table 4.2 presents the error measures for M_2 elevation amplitudes. From the table, it is seen that even the coarsest grid (U1) provides almost the same response as the finest grid. The computed errors concerning the entire domain do not exceed 3% and regional errors are within a similar error range. The U2 grid is chosen as the optimal model and a calibration test is conducted to evaluate the optimal bed friction coefficient to be applied in the model. This calibration of the model is presented in Section 4.2.4.

Grid	Entire Domain (G1-G14)	Irish Sea (G1-G5)	Celtic Sea (G6-G8)	Western UK (G9-G11)	Ocean (G12-G14)
U1	0.028	0.032	0.022	0.029	0.021
U2	0.020	0.022	0.020	0.018	0.019
U3	0.016	0.016	0.012	0.011	0.017
U4	0.013	0.011	0.010	0.009	0.016

Table 4.2 M_2 tidal elevation amplitude errors for the grids used in the convergence study. The reference values are obtained from the finest grid (U5) solutions.

4.2.3. Parallel Performance

Considering the size of the numerical domain as well as the long simulation periods, it is intended to run the simulations on a parallel platform. All simulations were performed on the University of Oxford Advanced Research Computing (ARC) HAL system, which is a SGI ICE 8200 MPI cluster consisting of 64 nodes and 8 processors assigned to each node, with a total of 512 Xeon/Harpertown 2.8 GHZ cores (accessed on 6th July 2014, http://www.arc.ox.ac.uk/content/services). The DG-ADCIRC source code has been ported onto the HAL system by the author, and compiled using Intel Fortran compilers for Linux platform installed on ARC-HAL system.

Parallel performance tests have been conducted using a fixed size mesh, which was selected according to the grid refinement study discussed in the previous section. The model chosen to conduct the parallel performance test was U2 consisting of 13583 nodes and 25879 elements. Following the methodology explained by Kubatko *et al* (2009), this section discusses the parallel speedup and efficiency of the DG-ADCIRC code on the ARC-HAL system. Running the DG-ADCIRC code in series and in parallel using the same model (here, U2), Kubatko *et al* (2009) explain the parallel speedup (S) parameter to be the ratio of the time of a single processor run (T_{single}) over the time of a parallel run ($T_{parallel}$). The efficiency is then calculated by dividing the parallel speedup parameter by the number of CPUs used in the parallel runs.

CPU	Run-time (hr:min:sec)	Memory (kb)	Virtual Memory (kb)	Efficiency
1	25:47:57	57752	99124	1 (by definition)
4	07:00:02	8724	32804	0.92
16	01:31:32	6232	51928	1.06
32	00:53:50	11772	65456	0.90

Table 4.3 Comparison between the run-times, memory and virtual memory required to run the DG-ADCIRC code on single processor and parallel platform on ARC-HAL supercomputer system.

The model is set to run for a period of 4 days, in which a ramping period of 1 day is included. The U2 model is forced with only M_2 tidal elevations, which are interpolated on the open boundaries. The Coriolis force is varied along the latitudes of the numerical domain and an eddy viscosity parameter is specified in the runs. Table 4.3 summarises the simulation run-

times and memory requirements for both serial and parallel runs. The efficiency is computed with respect to the run times and the number CPUs used in the parallel runs. From the table, it is seen that running the DG-ADCIRC model using 16 processors provides the highest efficiency in terms of the computational run times while ensuring minimal memory requirements per core.

4.2.4. Model Calibration

Calibration of the model has been conducted using five different bed friction coefficients for the chosen model U2. The open boundaries were forced using tidal elevations for M_2 constituent interpolated from Le Provost tidal database (Le Provost *et al.*, 1995). The simulations were spun up from initial conditions using a 1-day hyperbolic tangent ramp function and were run for 29 days in total. The elevation recordings were taken every half hour for each grid node. The calibration is undertaken using Admiralty Chart (2006) data for M_2 tidal elevation amplitudes at selected stations. Table 4.4 presents the predicted M_2 tidal elevation amplitudes for high bed friction coefficients ($c_f = 0.0050, c_f = 0.0100, c_f = 0.0150$) and the observation values. The simulations using lower bed friction coefficients ($c_f = 0.0025$ and $c_f = 0.0035$) did not achieve converged solutions due to instabilities occurring around the English Channel and North Channel boundaries. From the table, it is seen that there is not an exact value of bed friction coefficient that provides an unequivocal best agreement with the observations. The best fit overall between the observations and the model results is achieved by setting $c_f = 0.0050$.

Location	Observation (m)	Predictions ($c_f = 0.0050$)	Predictions ($c_f = 0.0100$)	Predictions ($c_f = 0.0150$)
Holyhead	1.81	1.66	1.16	0.96
Cemaes Bay	2.13	1.90	1.34	1.11
Amlwch	2.30	1.98	1.43	1.17
Ilfracombe	3.04	3.25	2.69	2.42
Barry	3.82	3.96	3.08	2.62
Flat Holm	3.90	4.02	3.14	2.67

Table 4.4 M_2 tidal elevation amplitudes at different stations for U2 grid using different bed friction coefficients.

Section 4.3 provides details for the model validation using the optimal bed friction coefficient ($c_f = 0.0050$) for both water levels and currents. The option of attempting to select different bed friction coefficients for different parts of the model was not pursued.

4.3. Model Validation

Model validation is undertaken against alternative predictions by the Admiralty's TotalTide software and the British Oceanographic Data Centre (BODC) observed current data, at locations in the Anglesey and Bristol Channel regions. The validation study includes a tidal harmonic analysis comparison against predictions by other numerical models (Davies and Jones, 1992; Robinson, 1979). Section 4.3.1 describes the harmonic analysis undertaken for M_2 and S_2 tidal constituents for the whole computational domain. Section 4.3.2 focuses on surface elevations and current velocities in the Anglesey region. Section 4.3.3 considers the Bristol Channel.

4.3.1. Tidal Harmonic Analysis

Tidal analyses are used to predict future tides from observed sea level and current data and to understand the hydrodynamic response of the sea to tidal forcing (Pugh, 1987). In the latter case, tidal analysis can be used to represent the tidal characteristics of a designated region. Harmonic analysis involves a Fourier decomposition of observed tidal data obtained over a time period into a finite number of harmonic constituents whose amplitude and phases relate to different astronomical parameters (Doodson, 1921). Each harmonic constituent is represented by (see e.g. Pugh, 1987),

$$H_n \cos\left(\sigma_n t - \varphi_n\right), \qquad 4.2$$

where H_n is the amplitude, σ_n is the angular speed (frequency), φ_n is the phase lag of the tidal constituent, and t is time. The numerical model is forced by specifying interpolated semi-diurnal M_2 and S_2 constituents on the open boundaries. The results are then compared against co-tidal maps provided by Davies and Jones (1992).

Figure 4.4 shows the predicted co-tidal contours of M_2 amplitude obtained using DG-ADCIRC; Figure 4.5 presents the predicted phase of M_2 in degrees. Figure 4.6 presents the corresponding results for the M_2 constituent obtained by Davies and Jones (1992) using an alternative numerical model.

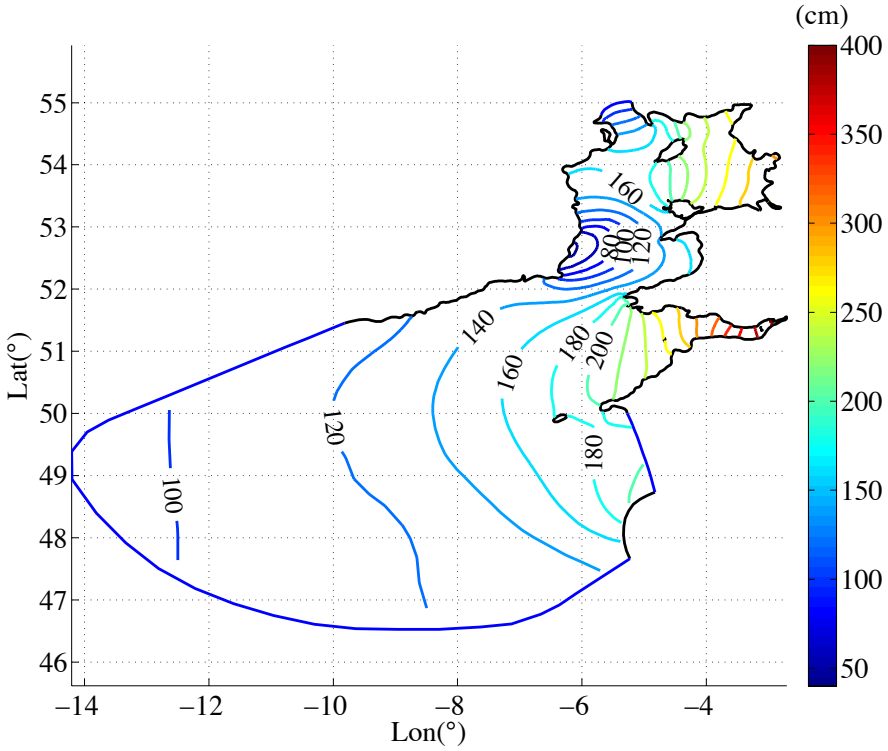

Figure 4.4 – M_2 co-tidal amplitude contours (cm) predicted using DG-ADCIRC.

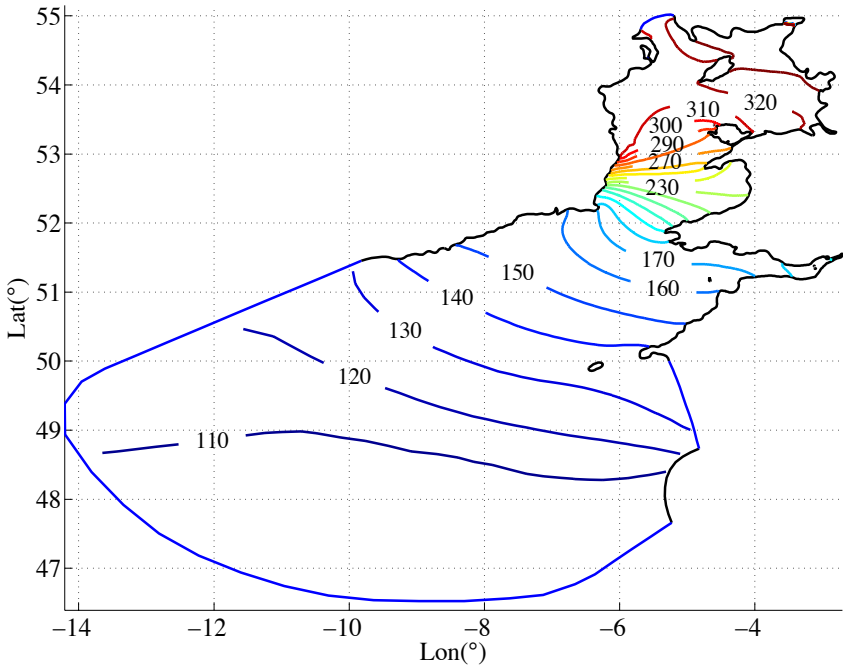

Figure 4.5 –M_2 co-tidal phase contours (degrees) predicted using DG-ADCIRC.

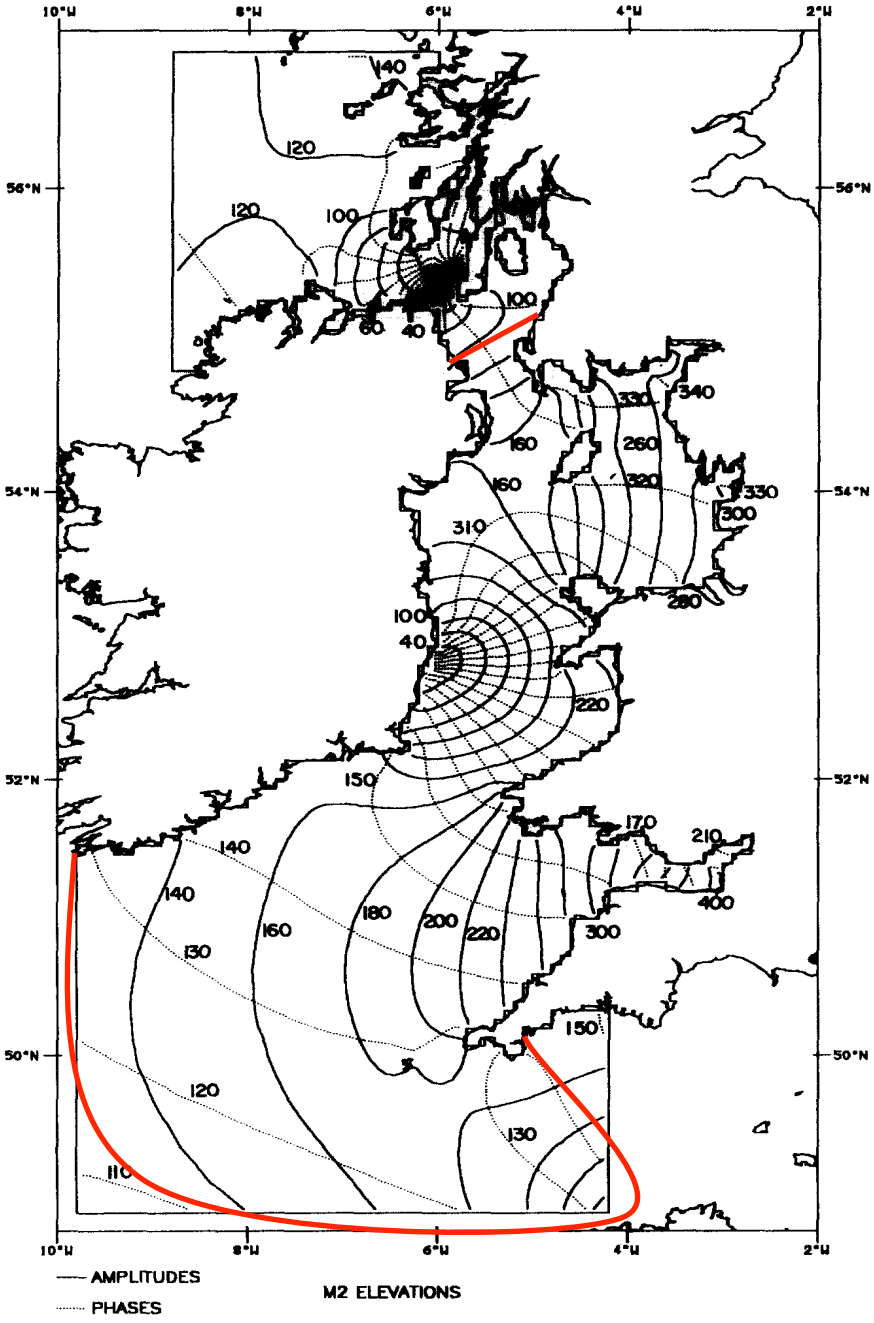

Figure 4.6 –M_2 co-tidal chart computed by Davies and Jones (1992). Solid lines = amplitudes in cm, dashed lines = phases in degrees. The boundaries of the DG-ADCIRC and the Davies and Jones' models are indicated with red lines.

The model predictions (Figure 4.4 and Figure 4.5) of the M_2 co-tidal charts are in very good visual agreement with charts presented by Davies and Jones (Figure 4.6) and Robinson (1979) (not shown). The present model reproduces the degenerate amphidromic point off the east coast of Ireland (see Chapter 5 for further explanation). The model simulations show that both the M_2 and S_2 tidal amplitudes increase substantially from Milford Haven to Avonmouth

within the Bristol Channel. The M_2 tidal amplitude is also amplified in the Irish Sea basin near the northwest Lancashire and Cumbrian coastline of the UK.

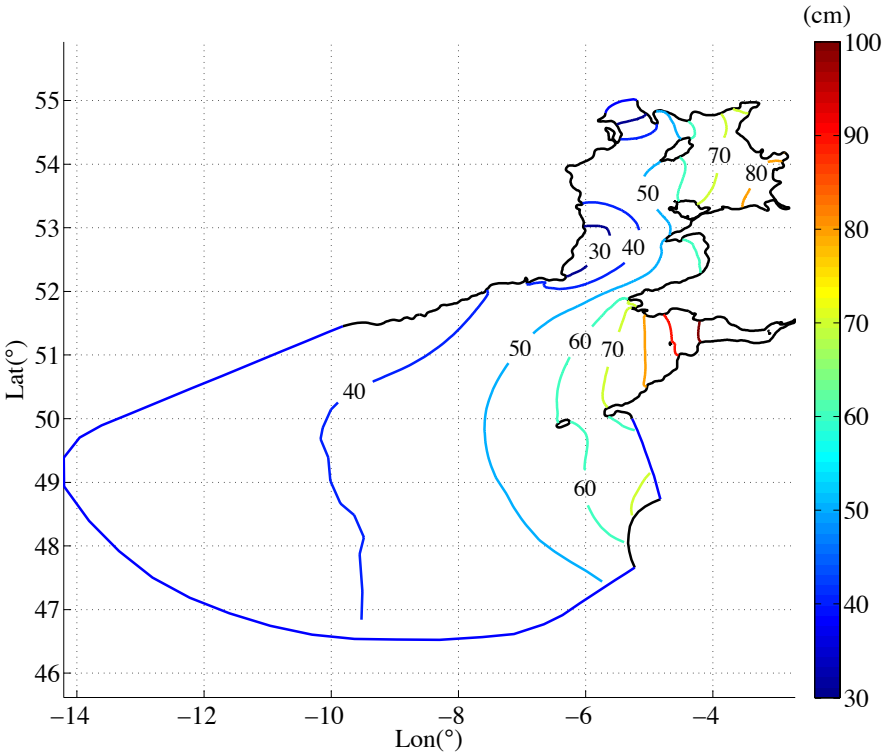

Figure 4.7 – S_2 co-tidal amplitude (cm) contours predicted using DG-ADCIRC.

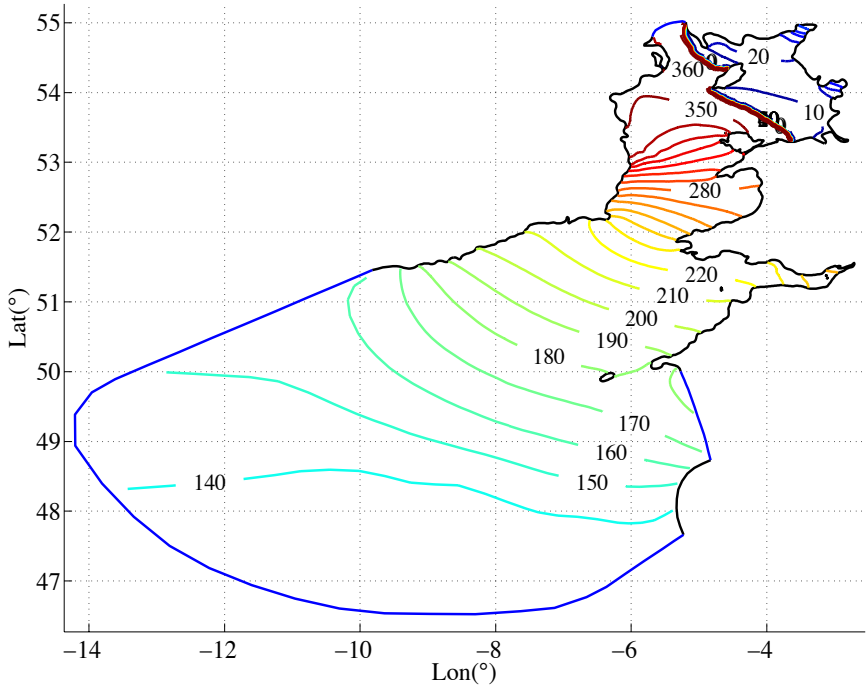

Figure 4.8 – S_2 co-tidal phase contours (degrees) predicted by DG-ADCIRC.

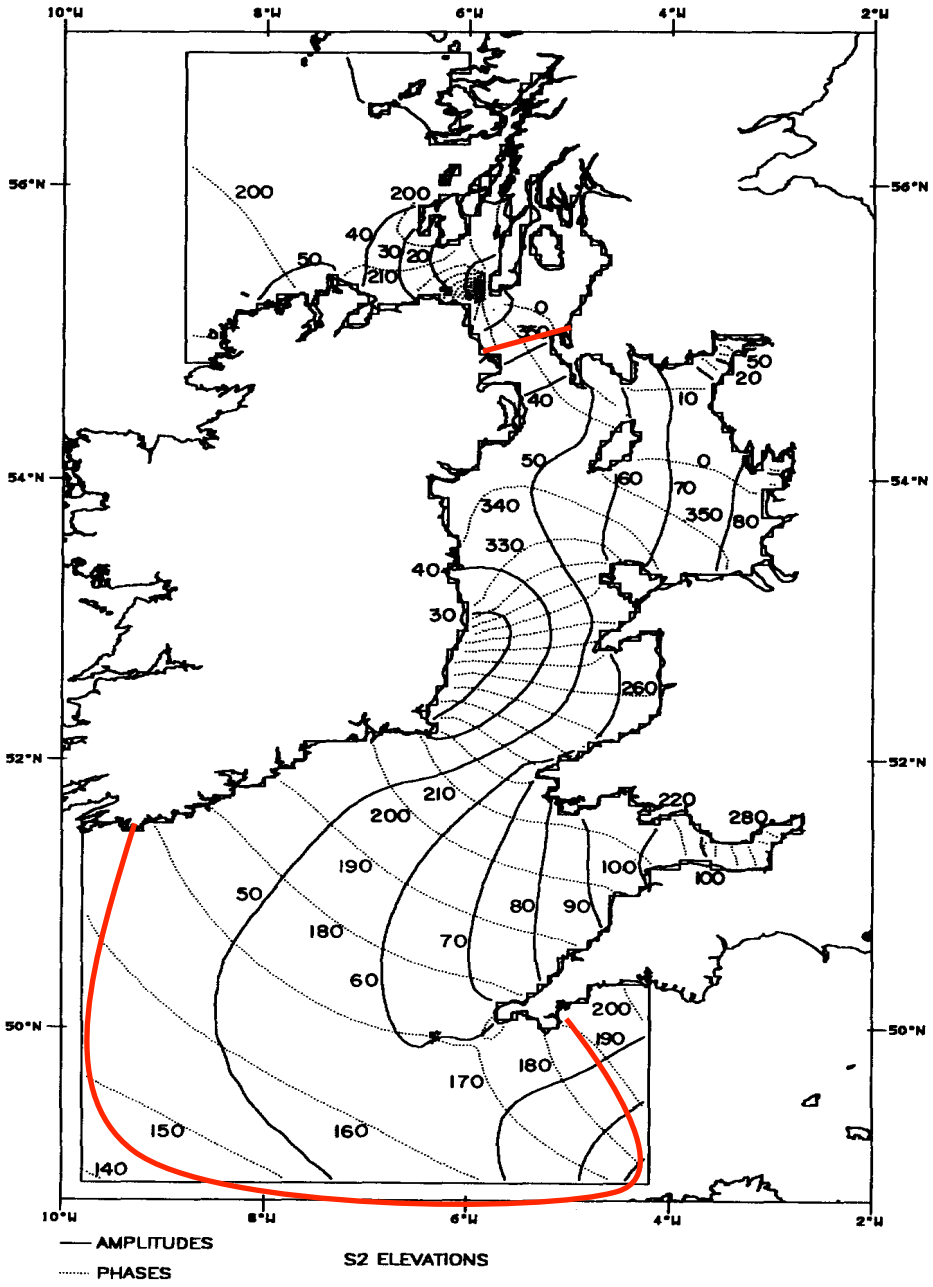

Figure 4.9 –S_2 co-tidal chart computed by Davies and Jones (1992). Solid lines = amplitudes in cm, dashed lines = phases in degrees. The boundaries of the DG-ADCIRC and the Davies and Jones' models are indicated with red lines.

Figure 4.7 and Figure 4.8 show the computed S_2 co-tidal charts for amplitude and phase respectively. The DG-ADCIRC model predictions again show a close visual agreement with the results presented by Davies and Jones (see Figure 4.9). Both sets of semi-diurnal constituents are similar, and include the degenerate S_2 amphidrome off the eastern Irish coasts.

In a previous study of tidal dynamics observed in the Irish Sea, Howarth (1984) reports that the semi-diurnal tides propagate into the Irish Sea both from the south (through the Celtic Sea) and from the north (the North Channel). Those two long waves interfere with each other in the vicinity of the Isle of Man and are then reflected by the Lancashire and Cumbrian coasts. This interaction forms a standing wave in the eastern Irish Sea, which translates into high tidal amplitudes that rapidly develop throughout the eastern Irish Sea. Figure 4.10 and Figure 4.11 present the predicted M_2 and S_2 tidal current magnitudes for the entire domain, using ADCIRC's tidal harmonic analysis function.

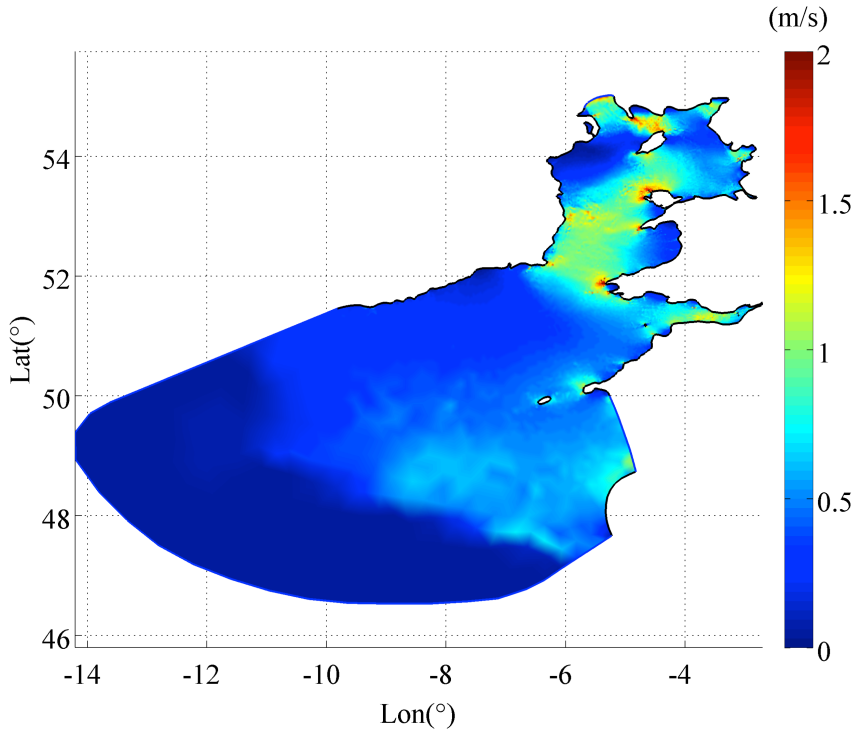

Figure 4.10 – M_2 tidal current amplitude magnitude (m/s) predicted by DG-ADCIRC.

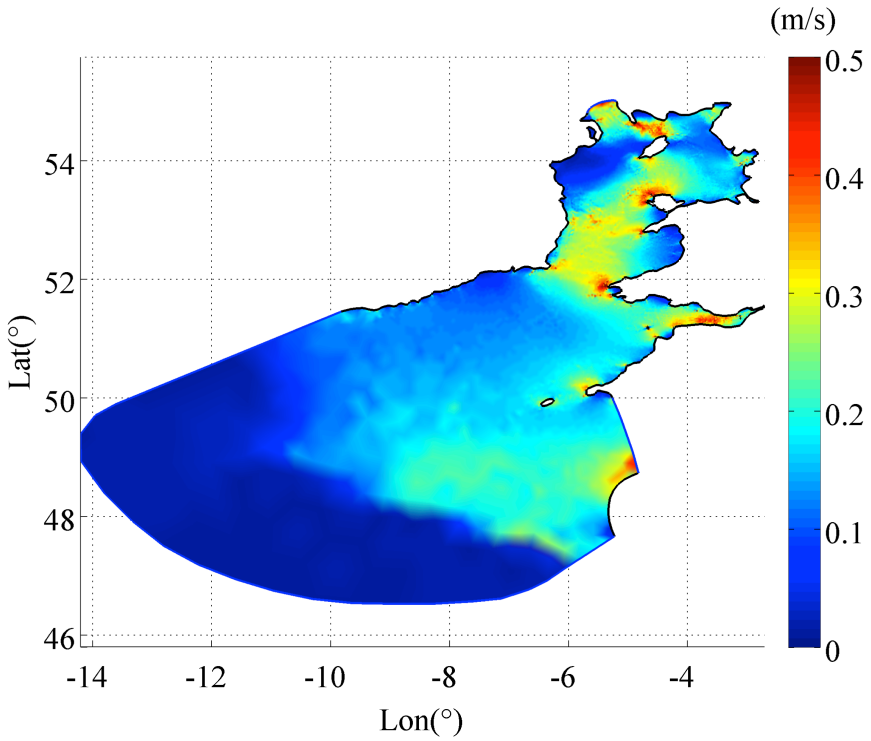

Figure 4.11 – S_2 tidal current amplitude magnitude (m/s) predicted by DG-ADCIRC.

Noting that the velocity legends of M_2 (Figure 4.10) and S_2 (Figure 4.11) tidal currents are different in scale, both figures show that fast semi-diurnal tides are predominant at several locations around the UK coasts. The regions with fast currents include the Anglesey headland, Bristol Channel, the strait between Mull of Galloway and the Isle of Man, and St. David's Head. This project aims to understand the far-field effects of extracting energy from the tidal currents at selected coastal sites around the UK. In order to evaluate the change in the tidal hydrodynamics in the presence of tidal turbines, it is necessary to model the naturally occurring tides as accurately as possible. In this respect, the following sections present results of the model validation tests concerning the areas of interest: Anglesey and the Bristol Channel.

4.3.2. Anglesey

The first set of model validation tests consider the predicted surface elevations and current velocities at selected locations in the Irish Sea in the vicinity of Anglesey headland. Predicted water elevations are compared against harmonically-analysed TotalTide data (Admiralty Charts, 2006). Predicted current velocities are compared against TotalTide and BODC data.

Harmonic analysis of surface elevation data predicted by TotalTide is used to extract the total contribution of the M_2 and S_2 tides in the regions of interest.

Water Levels

Figure 4.12 and Figure 4.13 show the water surface elevations (relative to mean sea level) for typical ebb and flood tides respectively. Energy of the incoming wave from the south is dissipated when propagating to the north due to the formation of the degenerate amphidromic system on the Irish coast (see Figure 4.4 and Figure 4.7). The Coriolis force from the Earth's rotation affects the propagation of the tide, leading to a difference in tidal range between the Irish coasts and the coasts of Wales and England (Howarth 1984). The tidal range difference can be seen in the figures below.

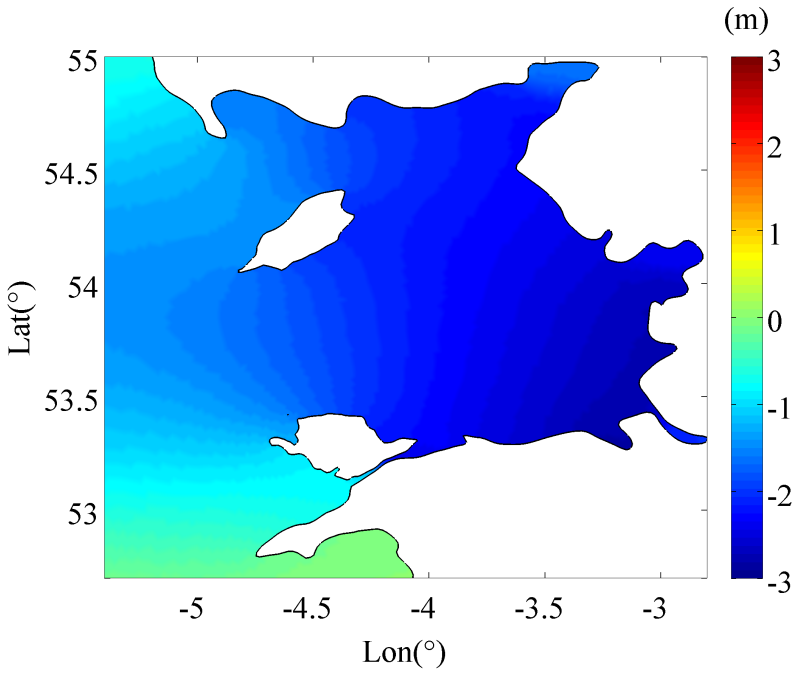

Figure 4.12 – Water surface elevation during an ebb tide in the vicinity of Anglesey, predicted by DG-ADCIRC. Contours: water elevations in metres.

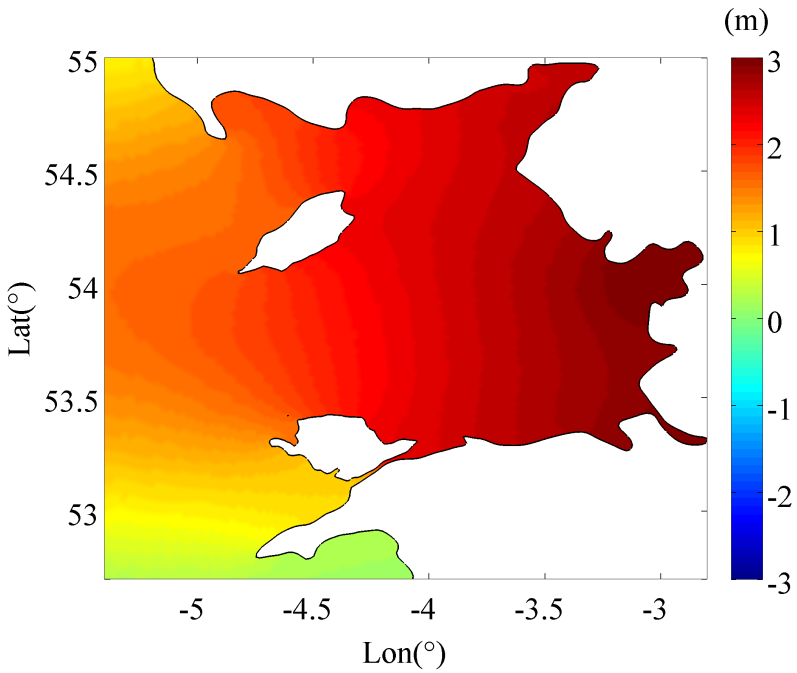

Figure 4.13 – Water surface elevation during a flood tide in the vicinity of Anglesey, predicted by DG-ADCIRC. Contours: water elevations in metres.

For Anglesey, the DG-ADCIRC model predictions of tidal amplitudes are compared against the Admiralty TotalTide predictions at Holyhead, Cemaes Bay and Amlwch (see Figure 4.14).

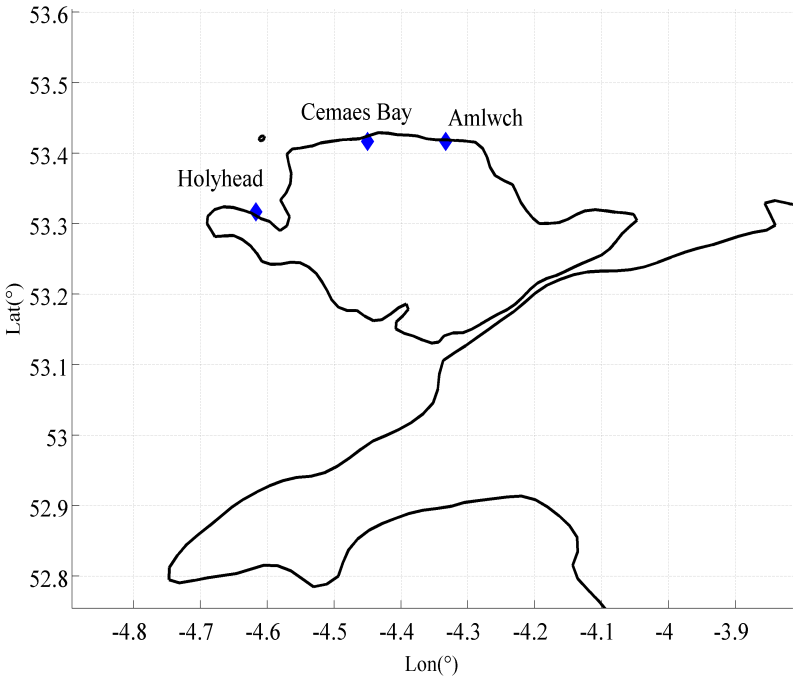

Figure 4.14 – Selected stations to compare numerical results against observation data.

The simulation period commences on 1st January 2012 and runs for a period of 29 days, with a spin-up period of one day. Tidal waves are ramped in gradually at the open boundary during the spin-up period in order to reduce the effects of initial transients. For this reason, the characteristics (amplitudes and phases) of the modelled long waves during this period are not representative when compared to the actual characteristics, and so predictions during the spin-up period are omitted from the data analysis. Consequently, the predictions used for comparison purposes start 24 hours after the initial start time. The comparison is presented for 7 days, which starts at 00:00 on 02 January 2012. Figure 4.15, Figure 4.16 and Figure 4.17 present comparisons between the model predictions and the processed measurements of sea surface elevation time histories at the selected stations.

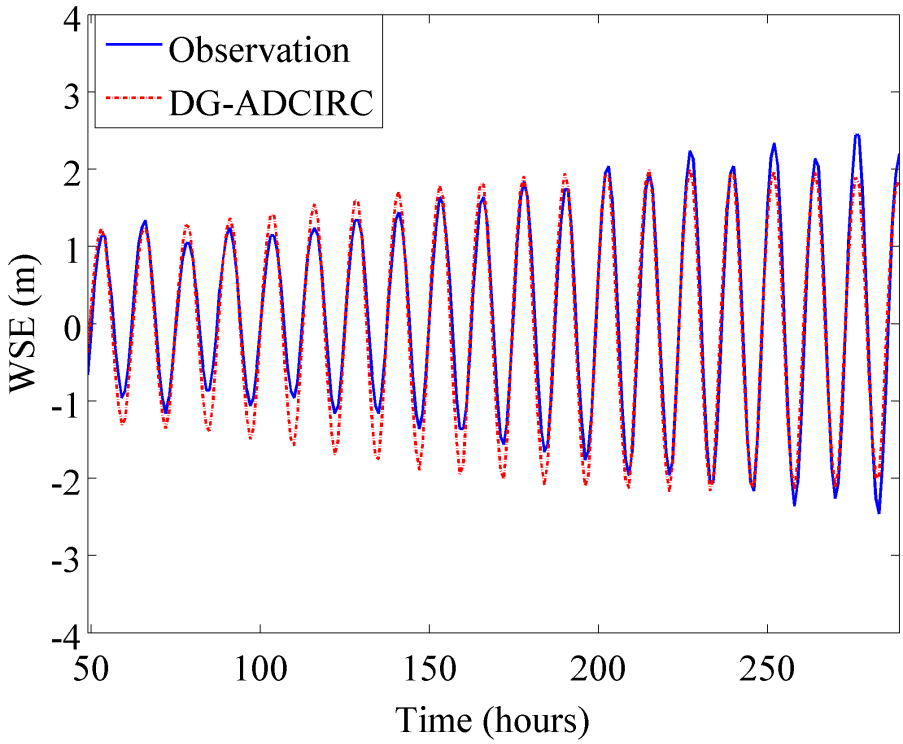

Figure 4.15 – Predicted (DG-ADCIRC) and harmonically-analysed (TotalTide) surface elevation levels at Holyhead, 53°19'N 4°37'W.

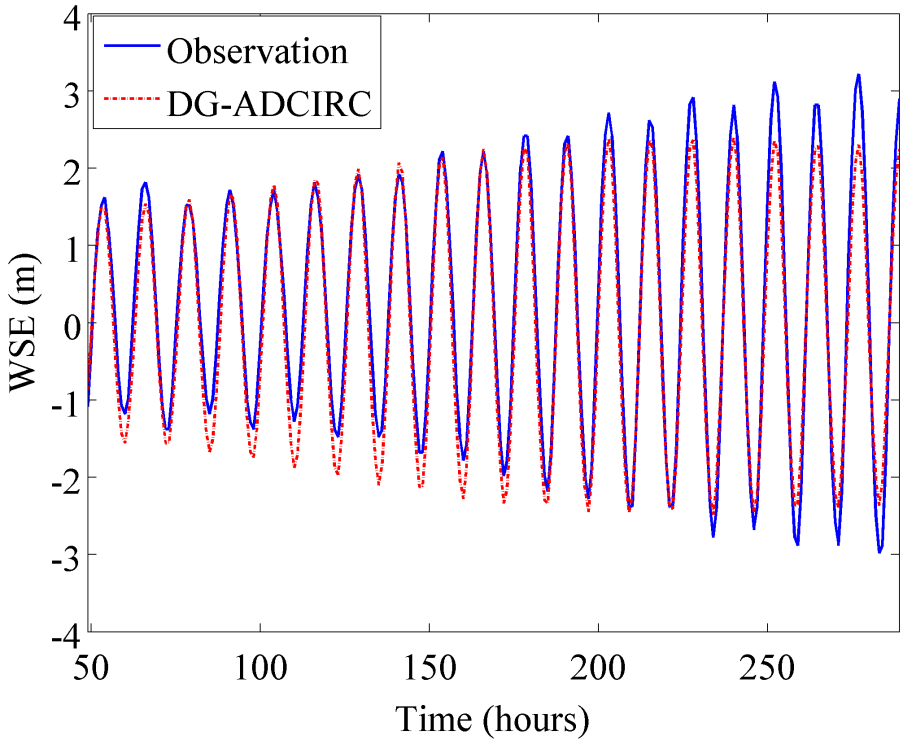

Figure 4.16 – Predicted (DG-ADCIRC) and harmonically-analysed (TotalTide) surface elevation levels at Amlwch, 53°25'N 4°20'W.

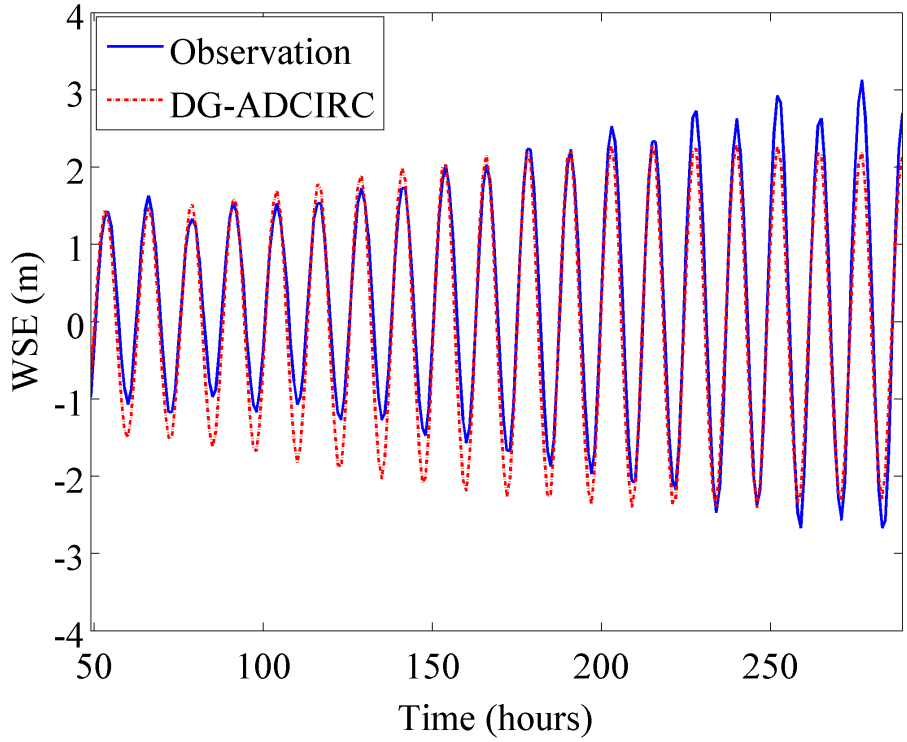

Figure 4.17 – Predicted (DG-ADCIRC) and harmonically-analysed (TotalTide) surface elevation levels at Cemaes Bay, 53°25'N 4°27'W.

The predictions and observations are in a reasonable agreement with respect to phase (Foundation for water, 1993). Tidal amplitude is under-predicted during neap tide and over-predicted at spring tide, which may be due to the use of a relatively high uniform bed friction coefficient throughout the computational domain. In practice, bed friction will vary across the domain. However, it is impractical to reproduce correctly the spatial change in bed friction in the numerical model. Moreover, the appropriate value for bed friction may be anisotropic (varying with direction) and also may not be constant with flow velocity. Soulsby (1998) provides a range of suggested values for different sea and bed conditions, which may be applied spatially in the numerical model. However, the accuracy of the model is not always improved by attempting more complex modelling of the bed friction (Richard Soulsby, personal communication).

Table 4.5 and Table 4.6 list the predicted and observed M_2 and S_2 tidal constituents. The observed data are extracted from Admiralty Charts. Table 4.5 indicates that there is a good agreement between predicted and observed M_2 phases, whereas the M_2 amplitudes, however, are underestimated by ~10%. Turning to the S_2 tidal constituent information in Table 4.6, it is evident that the S_2 phases are slightly overestimated whereas the S_2 amplitudes are under-predicted.

Station	Observation		Prediction	
	H_n (cm)	φ_n (°)	H_n (cm)	φ_n (°)
Holyhead	181	292	166	289
Amlwch	230	305	198	306
Cemaes Bay	213	307	190	303

Table 4.5 Predicted (DG-ADCIRC) and observed values of M_2 amplitude H_n (cm) and phase φ_n (°).

Station	Observation		Prediction	
	H_n (cm)	φ_n (°)	H_n (cm)	φ_n (°)
Holyhead	59	329	51	333
Amlwch	75	345	58	352
Cemaes Bay	71	345	56	349

Table 4.6 Predicted (DG-ADCIRC) and observed values of S_2 amplitude H_n (cm) and phase φ_n (°).

This discrepancy in amplitudes is due to the higher bed-friction coefficient used in the overall model. Although there are slight differences between the observed and predicted amplitudes and phases at specific stations, the overall model predictions appear to be in a satisfactory agreement with the global tidal dynamics of the region. The following section presents the comparisons undertaken to validate the model in terms of the predicted tidal currents.

Tidal Currents

The analysis of currents is different in certain key aspects to the analysis of water surface elevations. One main difference is that the water level observations are a scalar time series, where solely the height of the water is recorded, whereas the current observations are a vector time series of current speed and direction (Pugh, 1987). The reliability of the recorded current data is also affected by the elevation of the velocity gauge above the seabed (Godin, 1983). Data acquired near the seabed are highly sensitive to the exact nature of the local boundary layer, which in turn means that the extrapolation of such data to depth-averaged values is not robust. Current amplitude comparisons are possible using measurements recorded closer to the top of the water column. The results are plotted using the $1/7^{th}$ power law profile to approximate the mean velocities in a depth-averaged model. The current velocity comparisons are undertaken against the Admiralty's TotalTide predictions and BODC observed field data. Figure 4.18 shows the locations of the tidal current stations where the comparison data are available as observations from BODC and independent predictions from TotalTide.

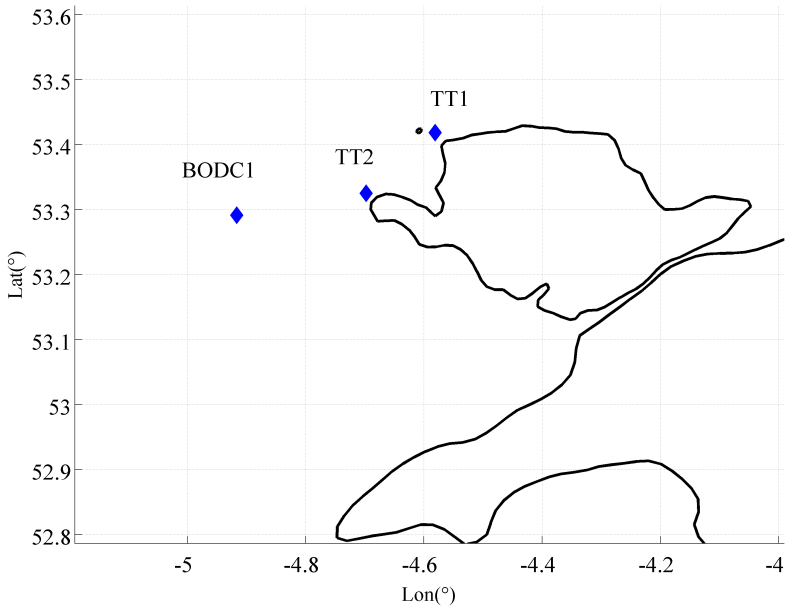

Figure 4.18 – Locations of stations near Anglesey used in the tidal current validation tests: TotalTide predictions (TT1: Anglesey Skerries and TT2: Holyhead stations) and observations from BODC (BODC1 station).

TotalTide provides predictions of surface velocities, as the software is designed for shipping purposes. Using the 1/7th power law, the depth-averaged velocity is calculated using,

$$\bar{u}_{mean} = u_{surface} \int_0^h \left(\frac{z}{h}\right)^{1/7} \frac{dz}{h} = \frac{7}{8} u_{surface}, \qquad 4.3$$

where $u_{surface}$ is the surface velocity, z is distance vertically above the seabed, and h is the local water depth. Figure 4.19 and Figure 4.20 present the predicted (hourly) time histories of tidal current magnitude obtained using DG-ADCIRC and TotalTide at the gauges off Anglesey Skerries and Holyhead, starting from 2nd January 2012 for a period of 11.5 days.

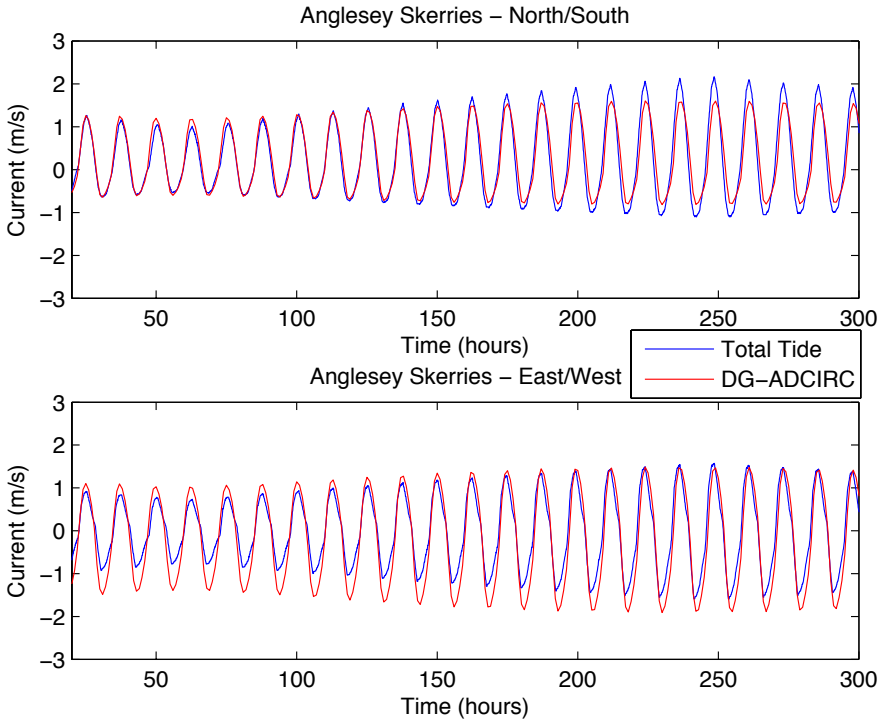

Figure 4.19 – Predicted tidal current magnitude time histories at Anglesey Skerries (TT1), 53°25.11'N 4°34.87'W, using DG-ADCIRC and TotalTide.

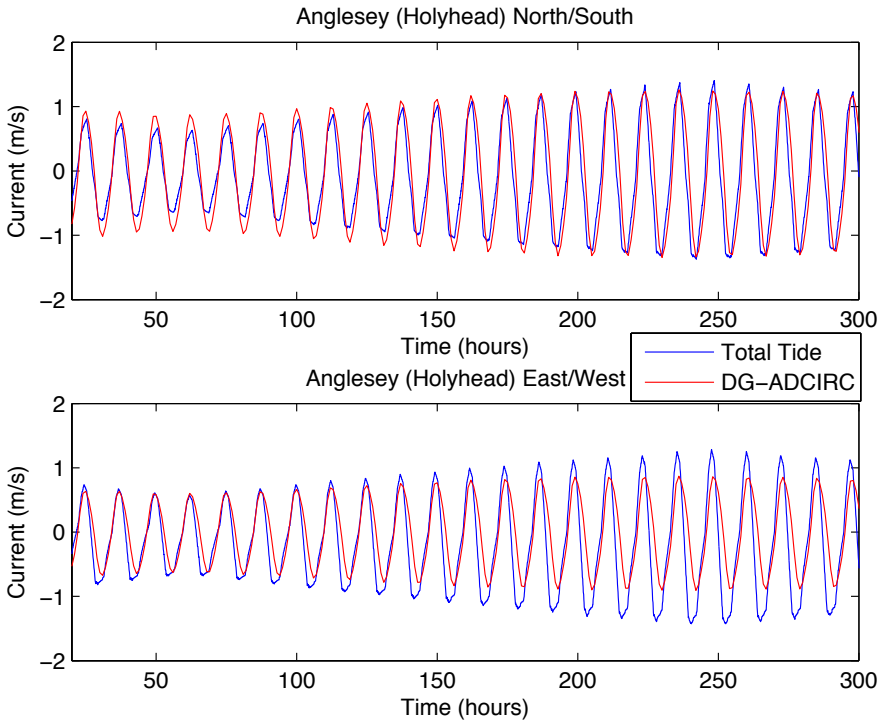

Figure 4.20 – Predicted tidal current magnitude time histories at Holyhead (TT2), 53°19.51'N 4°41.87'W, using DG-ADCIRC and TotalTide.

The predicted phases by DG-ADCIRC provide an encouraging level of agreement with the TotalTide predictions for both north-south and east-west current components at Anglesey Skerries (Foundation for water research, 1993). However, DG-ADCIRC predicts lower amplitude of north-south current and larger amplitude of east-west current amplitude, indicating a difference in predicted current direction. At Holyhead, there is close agreement between the two sets of predictions of the phase of the north-south current component, but a slight phase shift is evident in the east-west current component. The predicted amplitudes of the north-south current component are in acceptable agreement. However, the DG-ADCIRC model provides a lower estimate of the current amplitudes in the east-west direction than TotalTide. Table 4.7 lists the DG-ADCIRC and TotalTide predicted amplitudes of the major semi-diurnal tidal current components obtained using harmonic analysis. DG-ADCIRC predicts a current of lower amplitude than that by TotalTide at the Anglesey Skerries station. The discrepancy in magnitudes may be due to inaccuracy in the representation of eddies in the depth-averaged models. Closer agreement is obtained between the predictions at the Holyhead station.

Station	Observed harmonic current magnitude		Predicted harmonic current magnitude	
	M_2	S_2	M_2	S_2
Anglesey Skerries	1.92	0.62	1.60	0.40
Holyhead	1.60	0.51	1.67	0.43

Table 4.7 Comparison between TotalTide observed and DG-ADCIRC predicted magnitudes of the tidal current harmonic currents (m/s).

For further validation of the model, real-time observed data are obtained from BODC. Figure 4.18 shows the location of the selected observation station in the Anglesey region (BODC1 station). The water depth in the vicinity of the station is given to be 44.0 m and the current meter is located on 31.0 m above the seabed. The current recordings started on 1st November 1968 for a period of 16-days. Figure 4.21 and Figure 4.22 illustrate comparisons between the DG-ADCIRC predictions and BODC observations of north-south and east-west tidal current components over a period of 100 hours. Harmonic analysis (Pawlowicz *et al.*, 2002) of the simulated currents is used to predict the tides occurring during the time period of the BODC observations. There is a slight phase difference between the predicted and observed current components in the north-south direction. However, the predicted and

observed current components in the east-west direction are 180° out of phase. This disagreement may be due to the rather limited representation of turbulence in DG-ADCIRC and the assumption of full mixing in the vertical direction, which limits the modelling of eddying flows. Figure 4.23 compares the predicted and observed time histories of the total current magnitude. There is a slight overall phase difference between the model predictions and observations. The current magnitudes are over-predicted by the DG-ADCIRC model. Figure 4.24 presents the predicted and observed current direction time histories; the convention used is that zero degrees is eastward and the angle is positive anti-clockwise. The predicted current directions differ typically by about 50 degrees from the BODC observations for both of the flood tides, indicating that the present model has not entirely captured the direction of the tidal current at this location, which is another manifestation of the 180° out of phase of the east-west current component.

The omission of wetting and drying in the model inevitably results in an error with the results at regions with large tidal ranges, such as the Bristol Channel. As will be discussed in Section 4.3.3, the DG-ADCIRC model under-predicts both the tidal elevations and currents at individual stations located in the Bristol Channel. The observed discrepancies suggest that the model needs to be improved to use a smaller uniform bed friction coefficient in order to obtain a better agreement with the tidal current predictions. In this respect, Section 4.5 discusses the modifications DG-ADCIRC model was subjected to include a wetting and drying treatment in the computations.

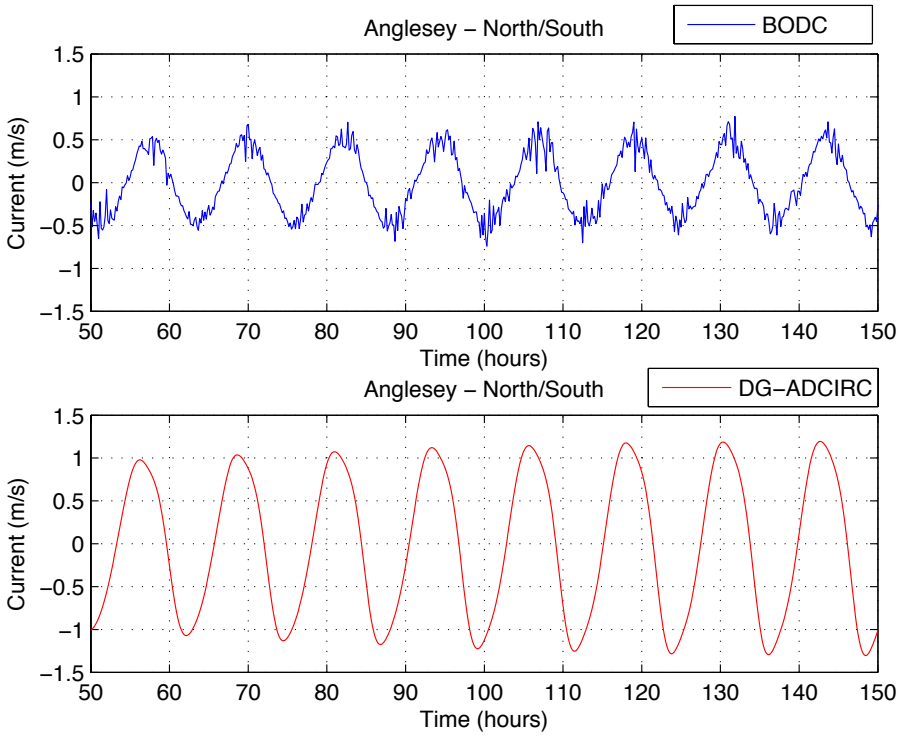

Figure 4.21 – Predicted (DG-ADCIRC) and observed (BODC) time histories of tidal current component in the north-south direction at 53°17.5'N 3°04.55'W.

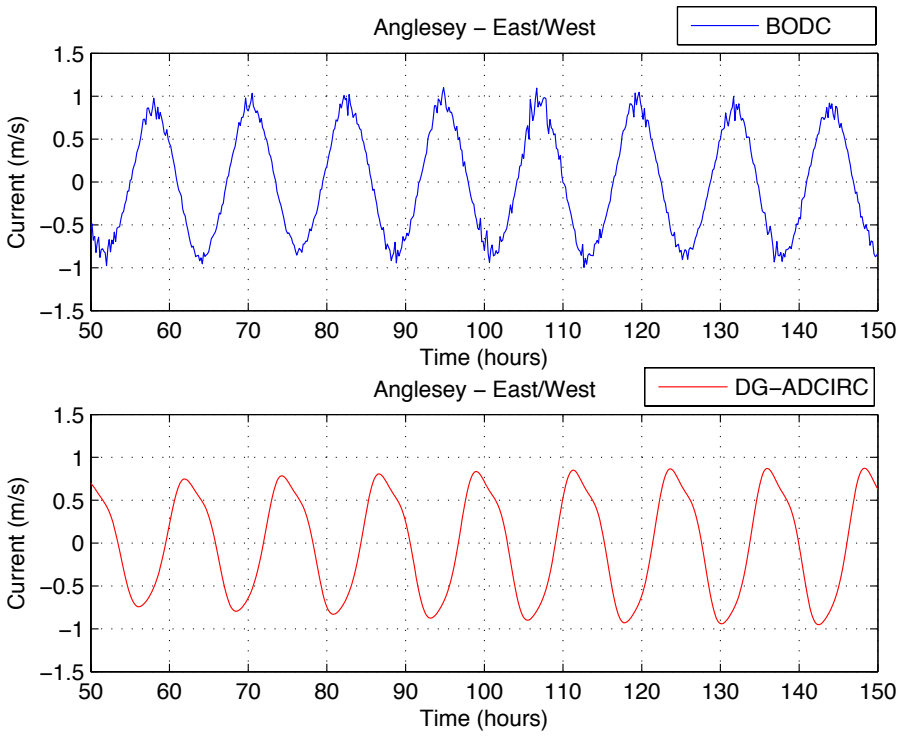

Figure 4.22 – Predicted (DG-ADCIRC) and observed (BODC) time histories of tidal current component in the east-west direction at 53°17.5'N 3°04.55'W.

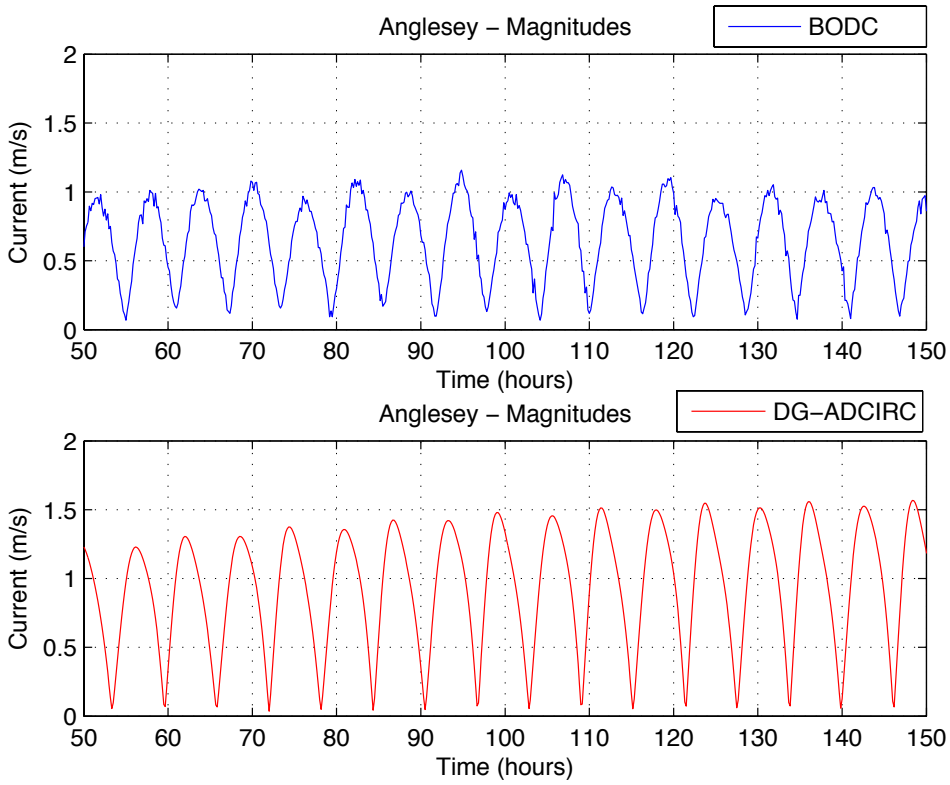

Figure 4.23 – Predicted (DG-ADCIRC) and observed (BODC) time histories of tidal current magnitude at 53°17.5'N 3°04.55'W.

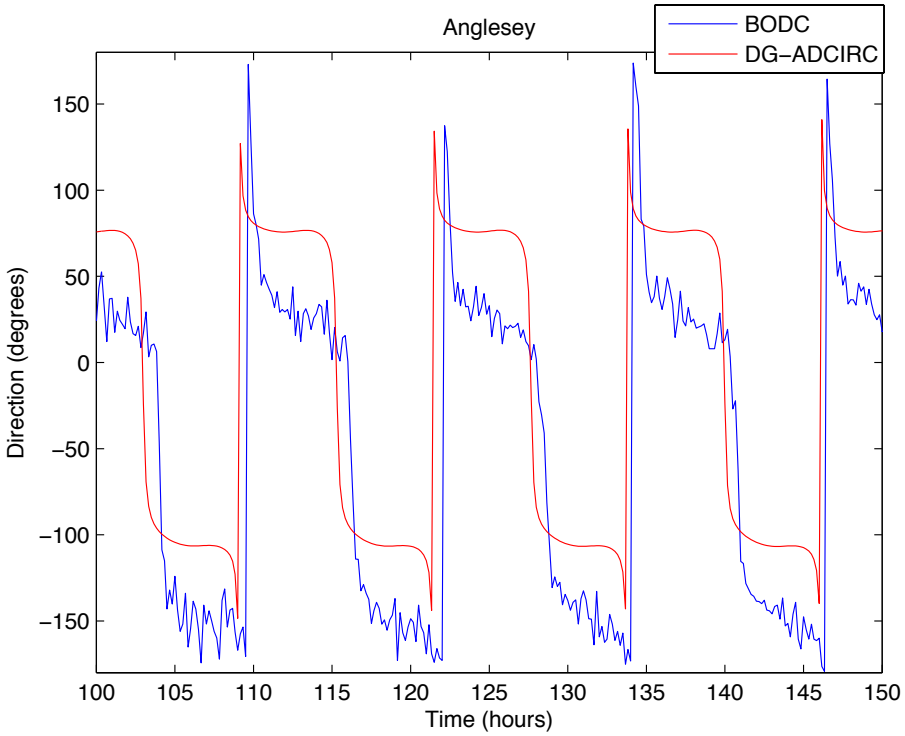

Figure 4.24 – Predicted (DG-ADCIRC) and observed (BODC) time histories of tidal current direction at 53°17.5'N 3°04.55'W.

4.3.3. Bristol Channel

This section considers the validation tests undertaken for surface elevations and current velocities in the Bristol Channel. The water elevation comparisons are undertaken against TotalTide data (Admiralty, 2006). Harmonic analysis of observed surface elevation data (obtained from Admiralty Tide tables) is used to extract the total contribution of the M_2 and S_2 tides in the regions of interest. The DG-ADCIRC current velocity comparisons are against TotalTide predictions and BODC measurements at different locations in the Bristol Channel.

Water Levels

A previous study focusing on the tides occurring in the Bristol Channel emphasises that flow circulation in the Channel, as well as in the Irish Sea, is mainly due to tidal movements (Uncles, 1983). The same study indicates that semi-diurnal tides are predominant in the region, and that M_2 tides are representative of an average tidal cycle. Figure 4.25 and Figure 4.26 illustrate the water surface elevations (relative to mean sea level) predicted by the DG-ADCIRC model for typical flood and ebb tides. The figures indicate that the predicted maximum tidal range within this basin is approximately 10 m, which is lower than the observed in practice but is within an acceptable bound of error.

Model predictions of the tidal amplitudes are now compared against corresponding predictions by TotalTide at several stations. Figure 4.27 indicates the locations of the comparison stations chosen for the water level validations. The simulation parameters are the same as described in Section 4.3.2. Figure 4.28, Figure 4.29, Figure 4.30 and Figure 4.31 present comparisons between the DG-ADCIRC and TotalTide model predictions of sea surface elevation time histories at the selected stations. At all locations considered, the present model predicts slightly larger amplitudes than TotalTide predictions, whereas a good level of agreement with respect to phase is obtained between the models. It should be noted though that it is not certain whether the present numerical model gives an over-prediction or the interpolations of the TotalTide predictions give an underestimate of the true conditions. A quantitative comparison can be found by harmonic analysis of the results. Table 4.8 lists observed data extracted from Admiralty Charts, DG-ADCIRC predictions, and alternative results obtained by Davies and Jones (1992) from two-dimensional analysis of the M_2 tidal component. Table 4.9 gives a similar comparison for the S_2 tidal component.

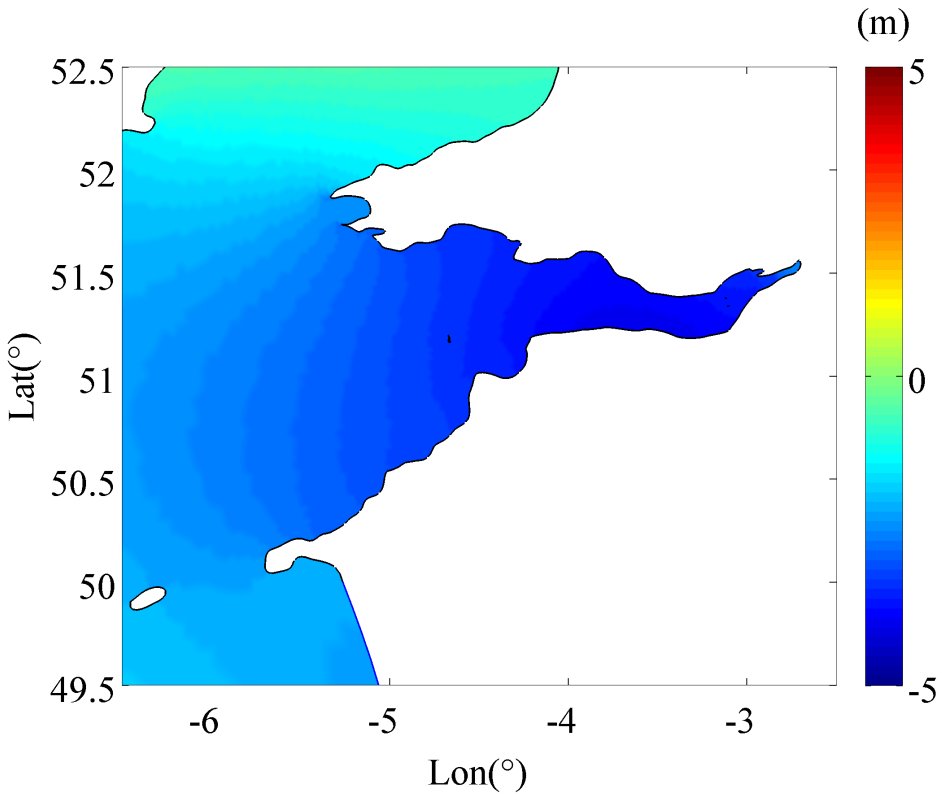

Figure 4.25 – Water surface elevation during an ebb tide in the vicinity of the Bristol Channel, predicted by DG-ADCIRC. Contours: water elevations (m).

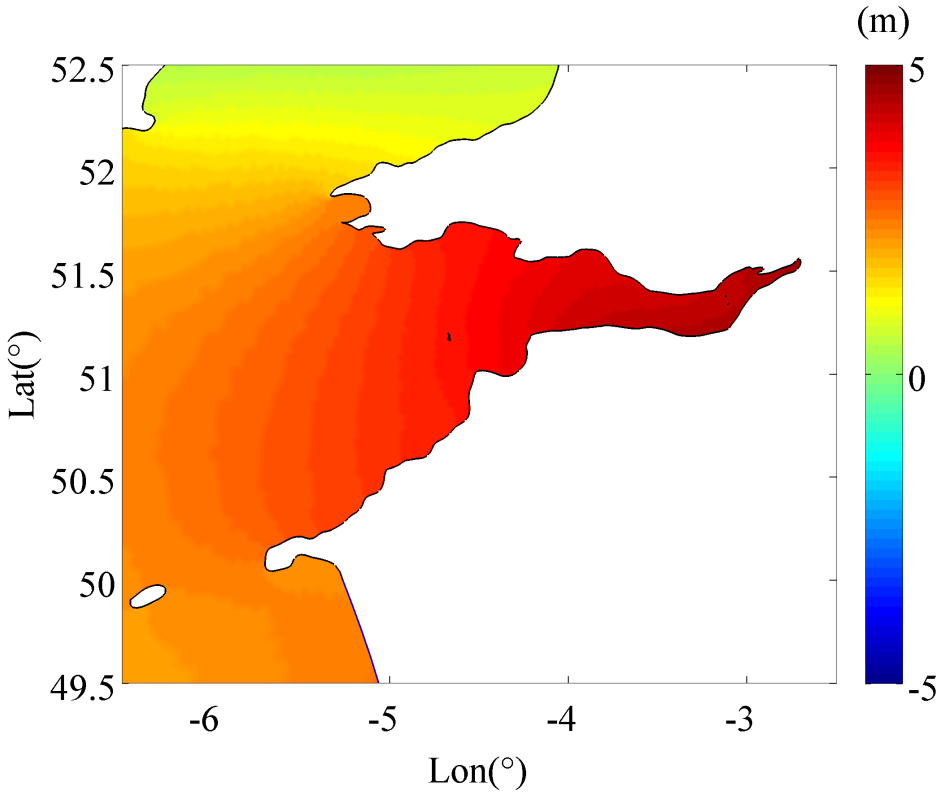

Figure 4.26 – Water surface elevation during a flood tide in the vicinity of the Bristol Channel, predicted by DG-ADCIRC. Contours: water elevations (m).

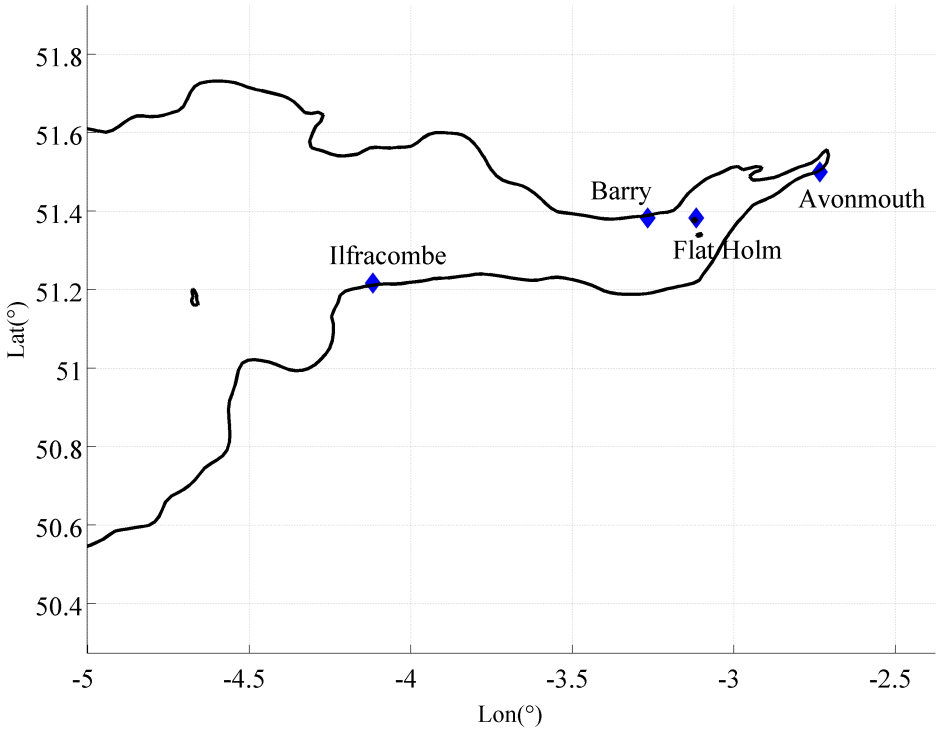

Figure 4.27 – Locations of water level stations in the Bristol Channel used in the tidal surface elevation amplitude validation tests.

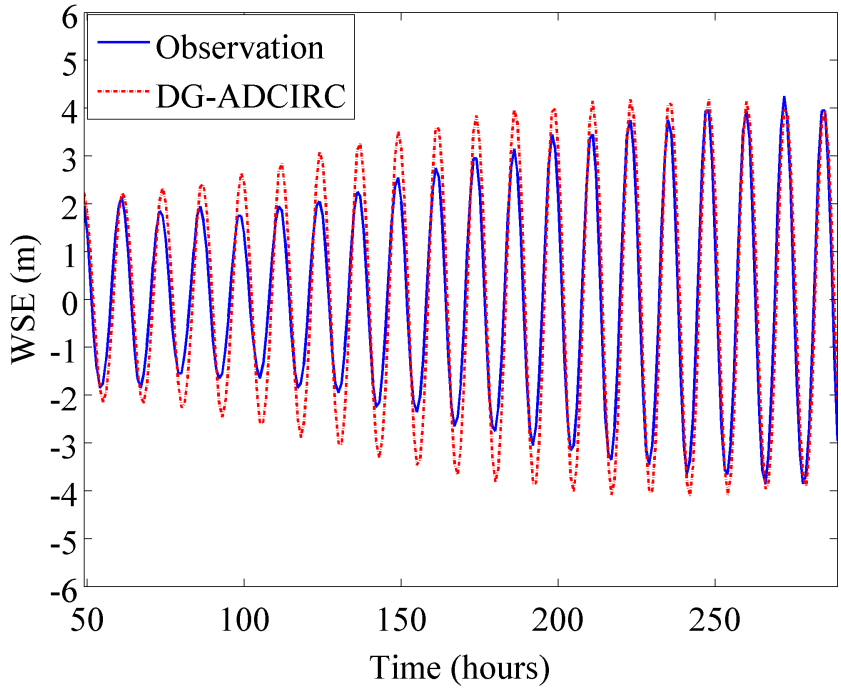

Figure 4.28 – Predicted (DG-ADCIRC) and harmonically-analysed (TotalTide) surface elevation levels at Ilfracombe, 51°13'N 4°07'W.

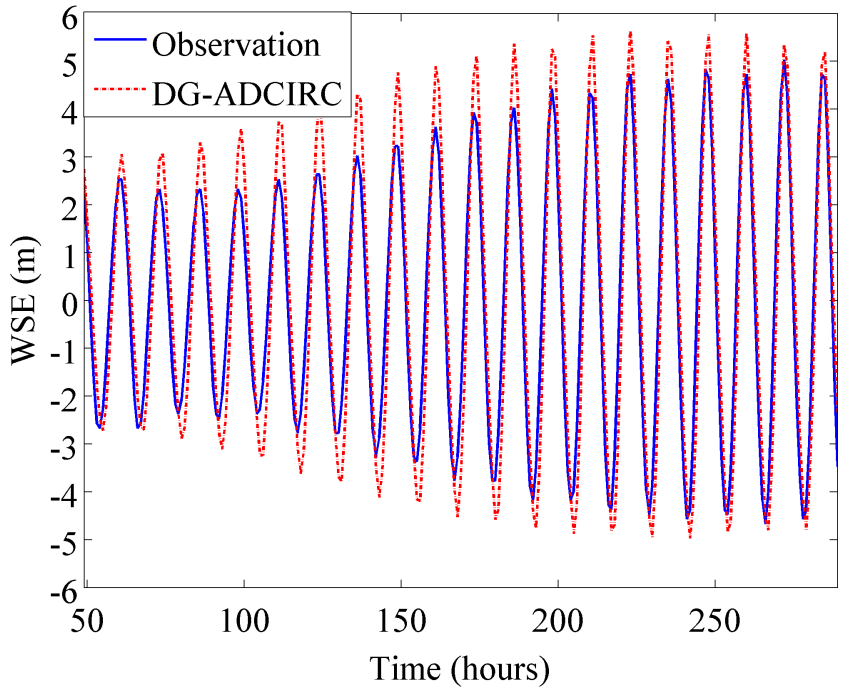

Figure 4.29 – Predicted (DG-ADCIRC) and harmonically-analysed (TotalTide) surface elevation levels at Barry, 51°23'N 3°16'W.

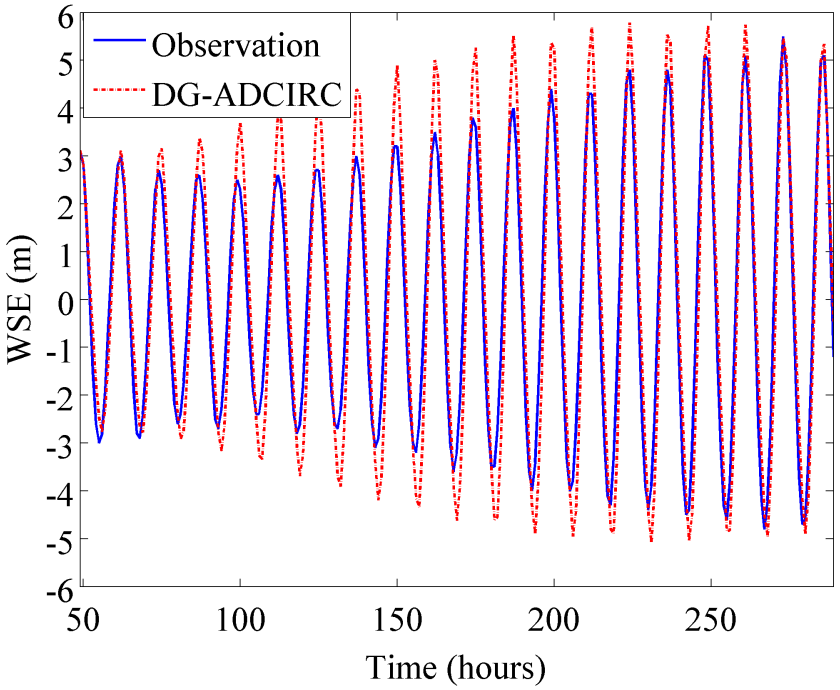

Figure 4.30 – Predicted (DG-ADCIRC) and harmonically-analysed (TotalTide) surface elevation levels at Flat Holm, 51°23'N 3°07'W.

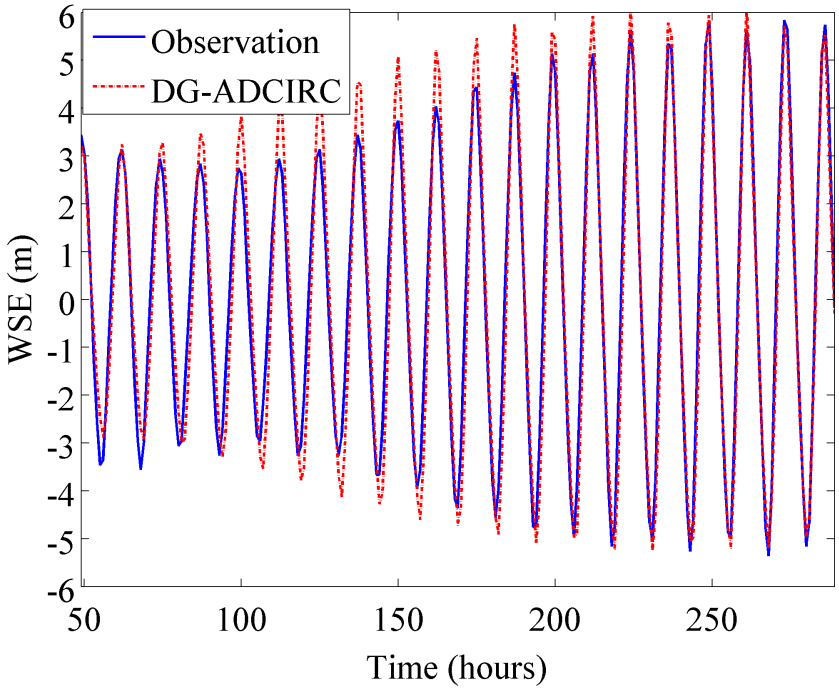

Figure 4.31 – Predicted (DG-ADCIRC) and harmonically-analysed (TotalTide) surface elevation levels at Avonmouth, 51°30'N 2°44'W.

The results show that the DG-ADCIRC model provides higher estimates of the M_2 tidal amplitudes at every station except Avonmouth. The reason for this discrepancy is possibly due to the omission of wetting and drying treatment in the computation. The M_2 phase results indicate that the time of high water is delayed by approximately 30 minutes. However, better agreement is observed for the S_2 tidal amplitudes and phases. When the two-dimensional models are compared, it is evident that the DG-ADCIRC model gives better results than that presented by Davies and Jones (1992). The observed difference in amplitudes is due to the fact that the DG-ADCIRC model uses an unstructured finite element mesh, which is more suitable to represent complex coastlines, with a higher resolution in the Bristol Channel region.

Stations	Observed (Admiralty Charts)		Model (DG-ADCIRC)		Predictions (Davies and Jones, 1992)	
	H_n (cm)	φ_n (°)	H_n (cm)	φ_n (°)	H_n (cm)	φ_n (°)
Ilfracombe	304	162	325	178	N/A	N/A
Barry	382	185	396	202	333	205
Flat Holm	390	190	402	204	N/A	N/A
Avonmouth	422	201	411	206	294	254

Table 4.8 Predicted and observed values of M_2 amplitude H_n (cm) and φ_n (°).

Stations	Observed (Admiralty Charts)		Model (DG-ADCIRC)		Predictions (Davies and Jones, 1992)	
	H_n (cm)	φ_n (°)	H_n (cm)	φ_n (°)	H_n (cm)	φ_n (°)
Ilfracombe	110	209	103	221	N/A	N/A
Barry	137	240	126	246	106	255
Flat Holm	135	246	131	248	N/A	N/A
Avonmouth	151	260	124	265	86	310

Table 4.9 Predicted and observed values of S_2 amplitude H_n (cm) and φ_n (°).

Tidal Currents

Model validation for the tidal current velocities in the Bristol Channel is undertaken by comparison against two sets of data: interpolated current predictions from TotalTide; and observed currents from BODC. Figure 4.32 illustrates the locations of the current stations, relating to TotalTide and BODC, used in the present validation study.

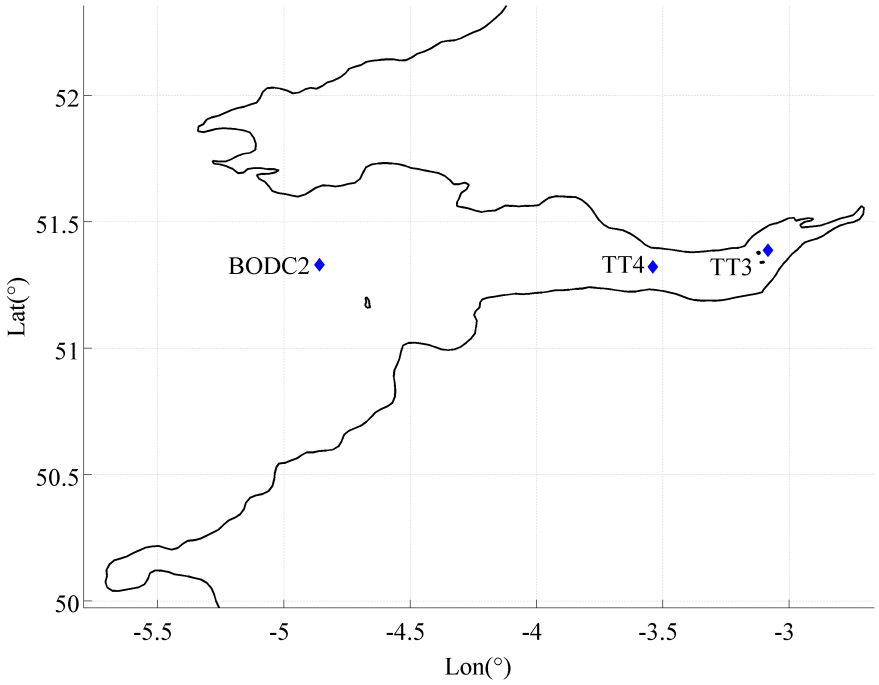

Figure 4.32 – Locations of stations in the Bristol Channel used in the tidal current validation tests: TotalTide predictions (TT3: Flat Holm and TT4: Bristol Channel stations) and observations from BODC (BODC2 station).

Figure 4.33 and Figure 4.34 provide plots of predicted and harmonically-analysed hourly current components in the north-south and east-west directions, starting from 2nd January 2012 for a period of 11.5 days. The results exhibit an encouraging level of agreement in terms of phase at both stations (Foundation for water, 1993). However, the current velocity

components predicted by DG-ADCIRC have lower magnitudes than those from TotalTide at the Flat Holm station (TT3) in both north-south and east-west directions. At the middle of the Bristol Channel (station TT4), the north-south current component predicted by DG-ADCIRC has a lower magnitude than that from TotalTide, whereas the east-west current component has a larger magnitude. In Figure 4.34, Total Tide analysis shows reoccurring sharp spikes at the north-south direction. These observed spikes may be related to a tidal bore occurring in the vicinity of the TT4 station. The discrepancies regarding the magnitude of the current components could be explained by the lack of wetting and drying treatment in the DG-ADCIRC model.

Section 4.5 discusses a modified version of the present model that includes wetting and drying treatment in the computation to represent the hydrodynamic response of the region more accurately.

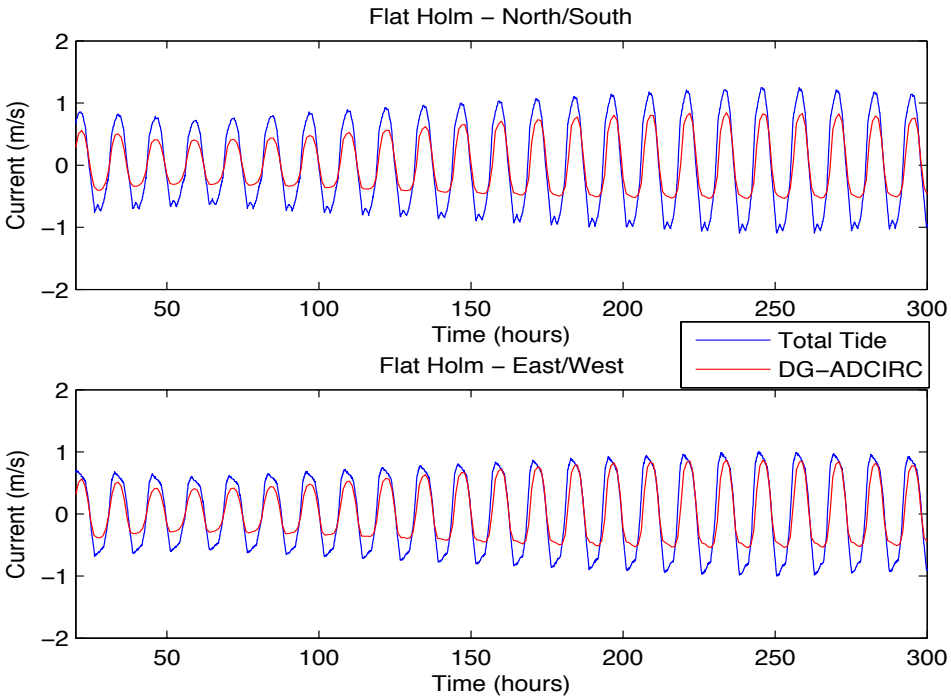

Figure 4.33 – Predicted (DG-ADCIRC) and harmonically-analysed (TotalTide) time histories of current components at Flat Holm Station (TT3), 51°23.23'N 3°04.98'W.

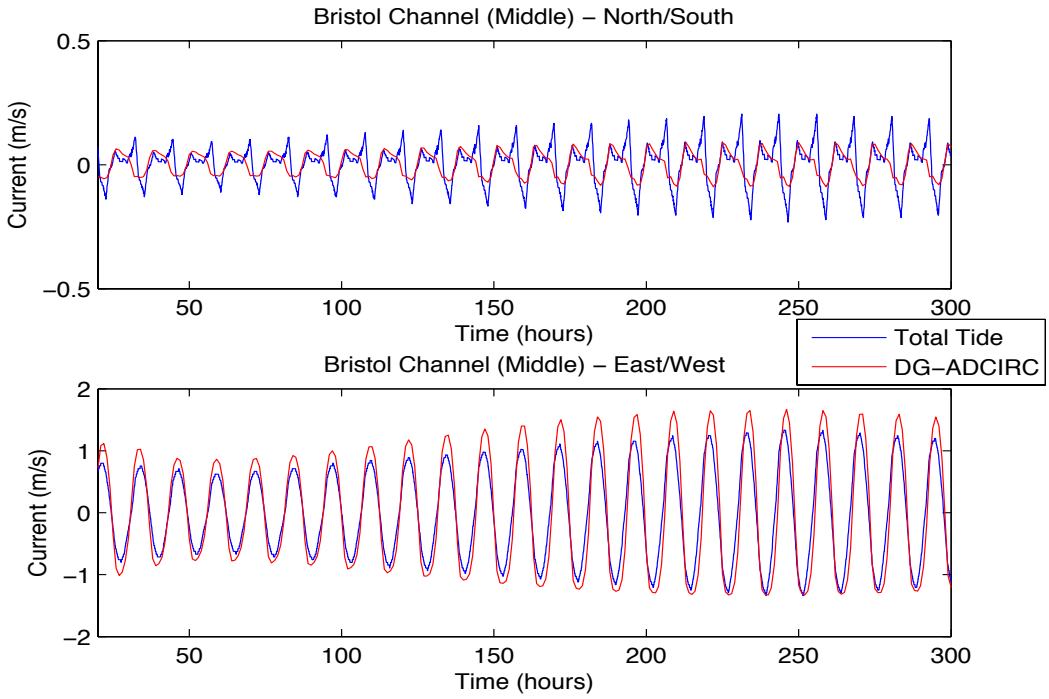

Figure 4.34 – Predicted (DG-ADCIRC) and harmonically-analysed (TotalTide) time histories of current components at the middle of the Bristol Channel (TT4), 51°19.33'N 3°32.38'W.

Table 4.10 lists the results of a harmonic analysis comparison between the major semi-diurnal tidal components predicted by DG-ADCIRC and TotalTide. The two-dimensional depth averaged hydrodynamic model (DG-ADCIRC) predicts lower current velocity amplitudes in the vicinity of Flat Holm station. It should be noted that depth-averaged models are not capable of capturing the large eddy formations around islands (Stansby, 2006). Relatively poor agreement is expected between the DG-ADCIRC and TotalTide predictions at locations in the vicinity of islands where eddy shedding occurs. The second station is situated in the middle of the Bristol Channel (51°19.33'N 3°32.38'W). At this observation station, the amplitudes of the tidal current harmonics predicted by TotalTide and DG-ADCIRC are in an encouraging level of agreement, as shown in Table 4.10.

Station	Predicted (TotalTide)		Predicted (DG-ADCIRC)	
	M_2	S_2	M_2	S_2
Flat Holm	1.50	0.46	0.85	0.30
Bristol Channel	1.16	0.38	1.00	0.34

Table 4.10 Comparison of magnitudes of tidal current harmonic components (m/s).

Considering that the Bristol Channel is a very dynamic system, in which sediment transport plays a major role in the bed topology and thus the currents, modelling the currents with a great accuracy is rather challenging. Further validation is undertaken against the field measurements obtained from the British Oceanographic Data Centre (BODC). At the majority of the available stations, the current data have been measured very close to the seabed making it impossible to extrapolate to obtain an accurate estimate of the depth-averaged velocity. There are a number of observation stations where the data recording has been undertaken closer to the water surface, but the duration of the recordings is not long enough for a reasonable comparison. Among these stations, the station located in the middle of the Bristol Channel is chosen for validation purposes (see Figure 4.32 station BODC2). The current measurements are recorded at 10 min intervals, starting on 6th June 1975 and lasting 13 days. The water depth in the vicinity of the station is 59 m and the current meter had been placed 36 m above the seabed.

Figure 4.35, Figure 4.36 and Figure 4.37 illustrate comparisons between observed data and model predictions over a period lasting 100 hours. Harmonic analysis (Pawlowicz *et al.*, 2002) has been undertaken on the predicted currents to estimate the tides occurring within the time period of the observations. It should be noted that the field data used in this cross-comparison exercise were measured more than 30 years ago at a site known to be a dynamically complex site, in which the flow characteristics change rather rapidly (Roger Falconer, personal communication). Additionally, the model resolution is relatively coarse (~200 m at finest), the model is not capable of capturing the physics as accurately as possible in the Bristol Channel site. It is thus expected that the model results would be in error with the observations.

The cross-comparison of the model predictions with the observed data shows a minor phase difference between the two datasets in both east-west and north-south directions. In terms of tidal current components, satisfactory agreement is obtained in the north-south direction, whereas the model over-predicts the east-west current component. As the measured data were sampled closer to the seabed, small discrepancies could occur in terms of the magnitude of the currents. Predicted and observed current directions are shown in Figure 4.38. The convention used in the plot is that zero degrees corresponds to the eastward direction, and the angle is

positive in the anti-clockwise direction. Figure 4.38 suggests that the general pattern of the current directions is well reproduced by the model, although there is a 3-hour phase difference between the predicted and observed directions. The reason for this discrepancy is presently unclear. One possible explanation relates to the altered coastline datum. There is no wetting and drying treatment in the analysis; instead, the coastline in the region is interpolated with a mean sea level of 6 m. Thus the phases of the incoming and reflected waves are expected to be in error. The model also excludes the River Severn, where the model boundaries are truncated at mean sea level in the Severn Estuary site. Bearing in mind that the hydrodynamics at the Bristol Channel site changes rapidly due to the sediment transport and riverine flows, the modelled current magnitudes are phases are expected to be in error with the observation data.

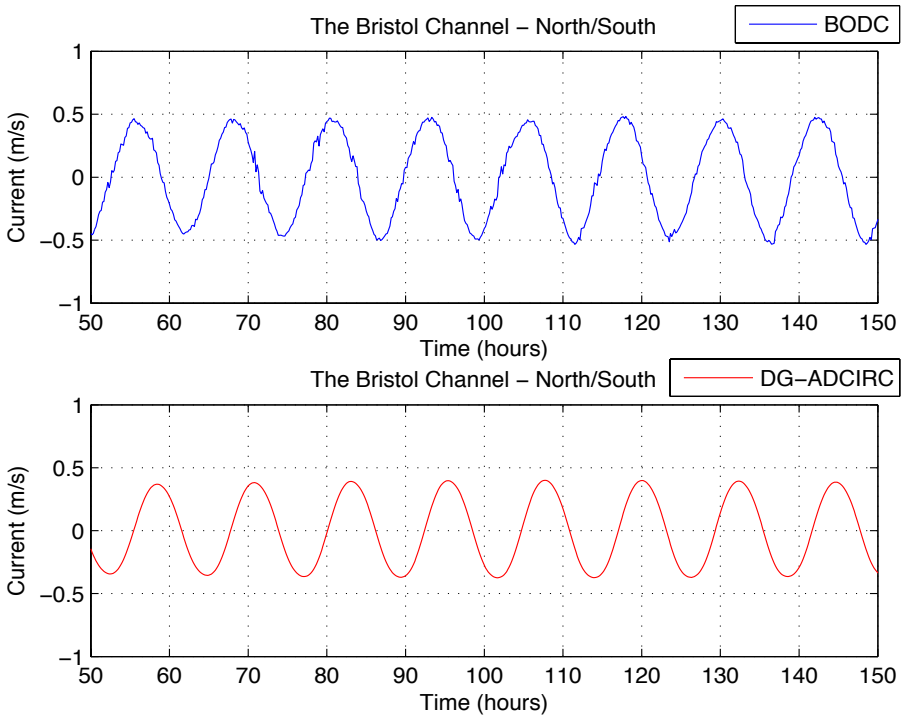

Figure 4.35 – Predicted (DG-ADCIRC) and observed (BODC) time histories of tidal current component in the north-south direction at 51°19.8'N 04°51.6'W.

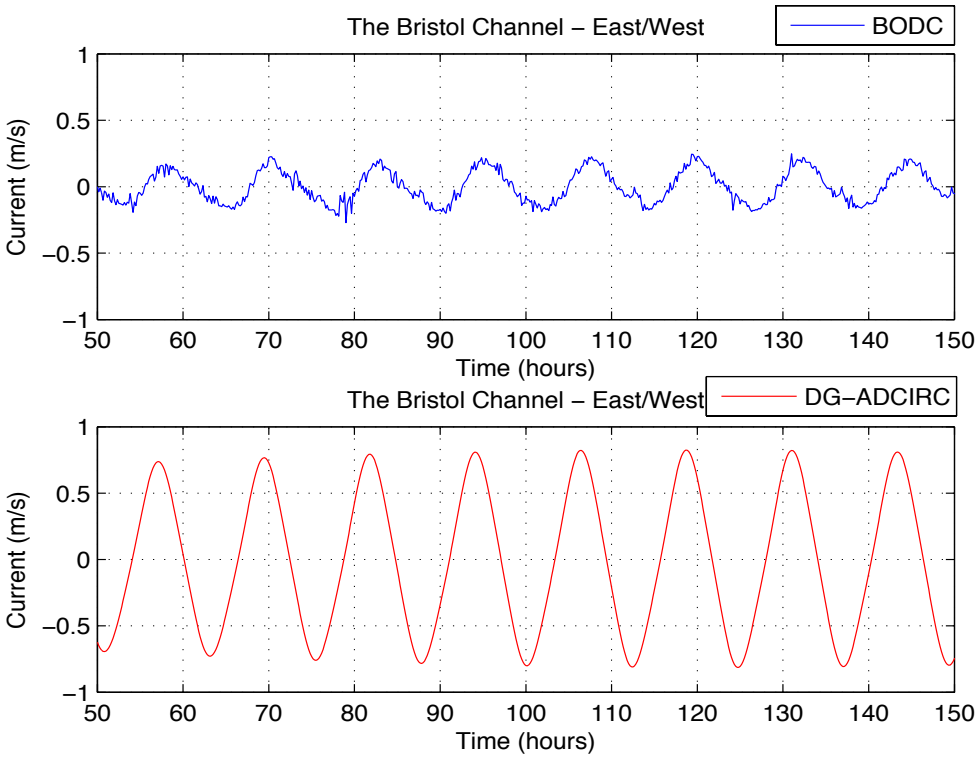

Figure 4.36 – Predicted (DG-ADCIRC) and observed (BODC) time histories of tidal current component in the east-west direction at 51°19.8'N 04°51.6W.

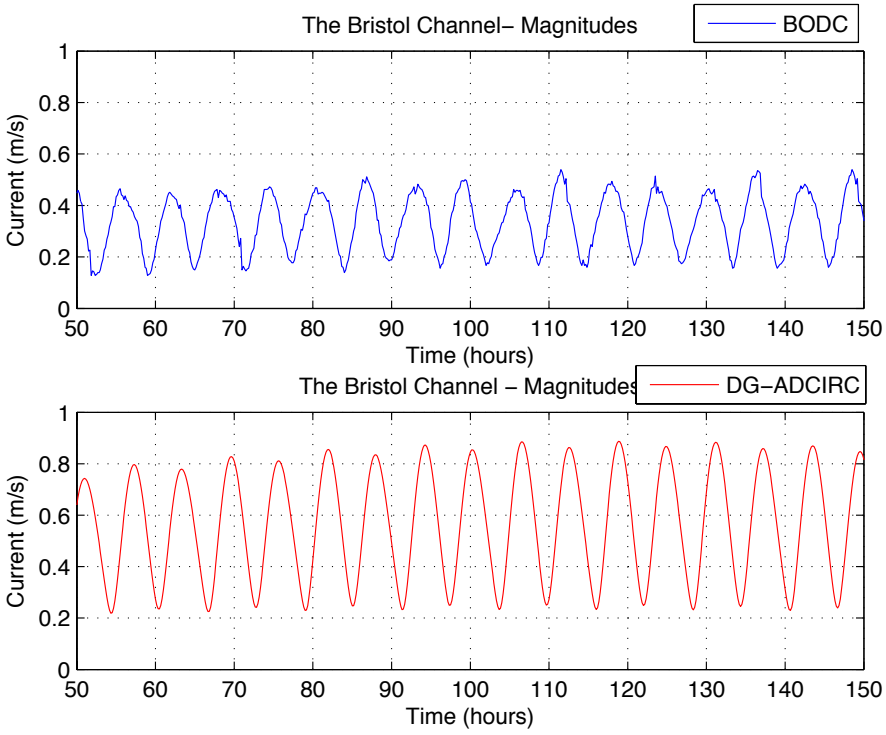

Figure 4.37 – Predicted (DG-ADCIRC) and observed (BODC) time histories of tidal current magnitude at 51°19.8'N 04°51.6W.

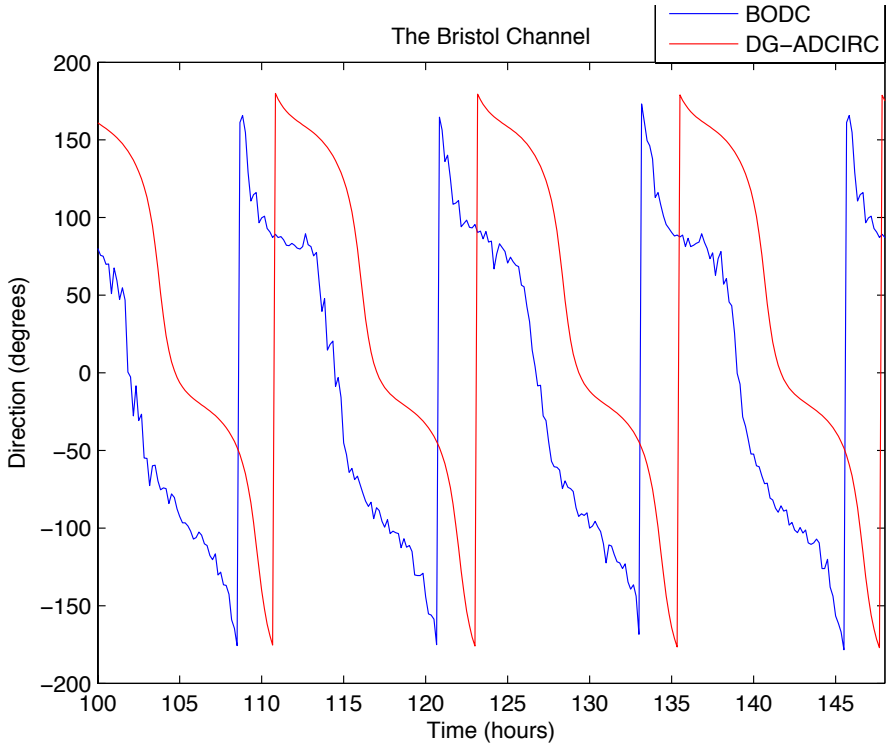

Figure 4.38 – Predicted (DG-ADCIRC) and observed (BODC) time histories of tidal current direction at 51°19.8'N 04°51.6W.

4.4. Discussion

A calibrated model of the M_2 and S_2 tidal flows in the south-west coasts of the UK has been presented, focusing particularly on the Bristol Channel and Anglesey regions. The model extends outward to the continental shelf, and is forced with appropriate tidal elevations. Comparisons with independent data sources demonstrate that the overall model achieves a satisfactory level of agreement with the pattern of tidal elevations throughout the region analysed. Detailed comparisons with individual stations demonstrate discrepancies at a reasonable bound of error.

Comparisons with current measurements are intrinsically more difficult because of uncertainties attaching to the observations. To validate the currents predicted by the model, two sets of data are used. The first dataset consists of the model predictions from TotalTide software. At both sites considered, the DG-ADCIRC model results show an encouraging level of agreement with the TotalTide predictions. However, less agreement is observed when the DG-ADCIRC results are compared against the BODC current measurements. It should be acknowledged that the BODC field measurements used to validate the model are more than

30 years old for both Anglesey and Bristol Channel sites. The model results are slightly better at the Anglesey Skerries site than the Bristol Channel site. It is believed that this difference is mainly due to the rocky bed topography at the Anglesey site, which is less sensitive to sediment transport. However, the Bristol Channel site has long sandy coastlines, which are very susceptible to the tidal movements, riverine flows, storms and thus the sediment transport. The Channel is hence a very dynamic system, where the currents are significantly affected by the aforementioned mechanisms. In terms of modelling accuracy, the model mesh has a relatively coarse resolution, which does not capture fine details in the Bristol Channel. The model boundaries do not include the River Severn at the upstream of the Bristol Channel area. This in turn affects the level of accuracy of the model results. It is possible to use a nested grid to resolve the coastlines much finer to increase the level of accuracy especially in the Bristol Channel site, however this is beyond the scope of this thesis. Differences are especially apparent in the detailed responses when considering the north-south and east-west current components separately. Bearing in mind the limitations of depth-averaged models, rather poor representation of currents is expected in regions where large-scale three-dimensional eddying flow structures occur.

The shortcomings of the present model are thought to relate primarily to two aspects:

- use of a single overall bed friction coefficient, and
- omission of wetting and drying from the analysis.

One of the main objectives of the research undertaken for this DPhil is to understand the far-field effects of extracting energy from tidal streams. Thus, it is important to construct a model that represents the physics of the model area as accurately as possible. For this reason, the model presented herein is modified to include the inter-tidal zones and calibrated in order to achieve closer agreement with the observed tides.

4.5. Improved Model Including Moving Boundary Fronts

The numerical model used in this section is a modified version of the DG-ADCIRC model presented in Section 4.2, which includes the inter-tidal zones around the Bristol Channel (see Figure 4.39), and uses a wetting and drying treatment in the computation (Bunya *et al.*, 2009).

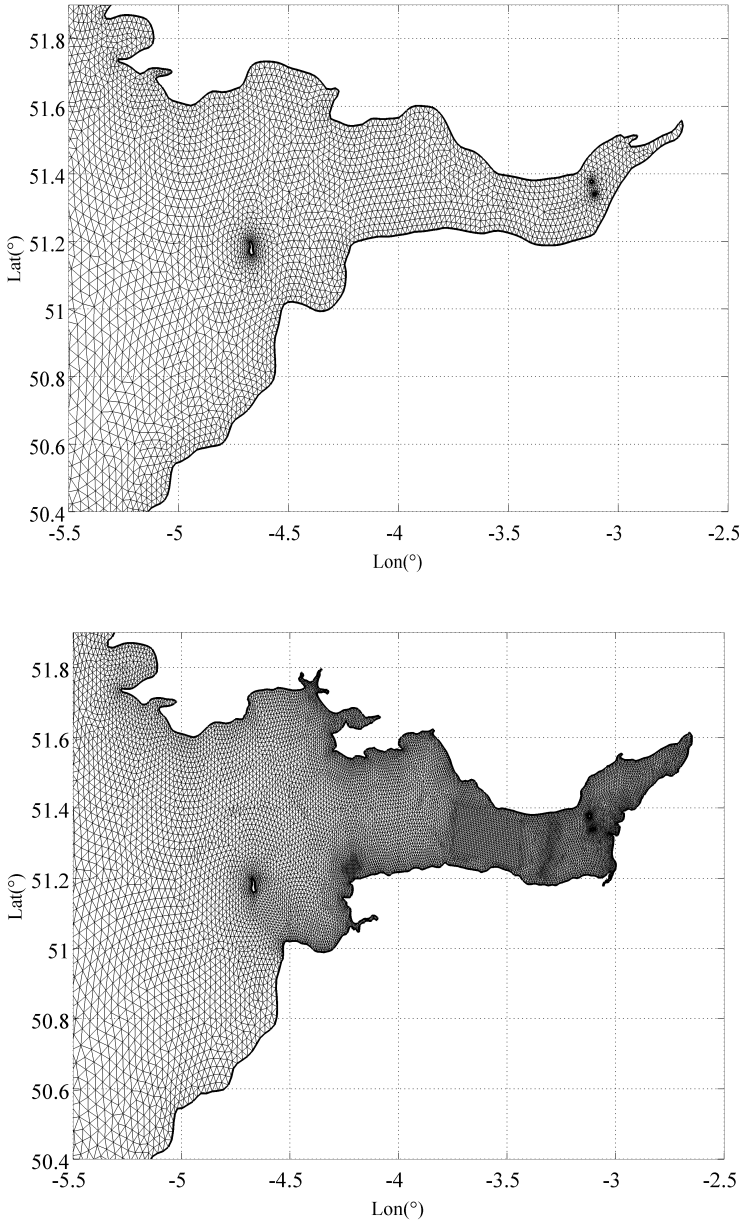

Figure 4.39 – Comparison between the parts of the computational mesh that focus on the Bristol Channel region, where the inter-tidal zones are included. The structural mesh embedded in the domain represents regions where tidal arrays will be inserted later.

Including the inter-tidal zones requires a finer mesh resolution in the vicinity of the wetting and drying fronts. The DG-ADCIRC-WD model consists a total of 28922 nodes and 55570 elements. The simulations are set up using the same model parameters used in the DG-ADCIRC model. This model also uses first-order piecewise linear elements. The numerical flux selected for the computations is the HLLC flux, introduced in Section 2.6.1. Second-order, two-stage Runge-Kutta time discretisation is used in accordance with the linear

elements used in the model. The DG-ADCIRC-WD model is also run on the ARC-HAL supercomputer (see Section 4.2.3). In order to compare the computational run-times, a parallel performance test is conducted as explained in Section 4.2.3. The parallel performance test for DG-ADCIRC-WD model considers a simulation period of 4 days. Table 4.11 presents a summary of the simulation run times and memory requirements for DG-ADCIRC-WD model on ARC-HAL system. The efficiency in computational run-times by increasing the number of CPUs is also included in the table.

CPU	Run-time (hr:min:sec)	Memory (kb)	Virtual Memory (kb)	Efficiency
1	56:28:18	117189	179828	1 (by definition)
4	16:06:14	11820	38368	0.88
16	03:59:09	14708	62300	0.89
32	01:46:53	14724	61428	0.99

Table 4.11 Comparison between the run-times, memory and virtual memory required to run the DG-ADCIRC-WD model (using a wetting and drying treatment) on single processor and parallel platform on ARC-HAL supercomputer system.

It is intended to evaluate if the run-times are significantly affected due to inclusion of the wetting and drying algorithm. Bearing in mind that the DG-ADCIRC-WD model consists almost double the amount of elements to that of the DG-ADCIRC model, a straightforward comparison between the run-times reported in Table 4.3 and Table 4.11 is not possible. In this respect an additional test is studied using the U4 model with the properties shown in Table 4.1. The U4 model consists of 30994 nodes and 59799 elements, in which the model domain does not include the inter-tidal zones and thus no wetting and drying treatment is applied in the computation. The U4 model is run on 16 processors for a simulation period of 4 days, which includes one-day of ramping period. Table 4.12 presents the model information (i.e. node and element numbers) as well as the reported run-times and memory requirements for DG-ADCIRC-WD and U4 models. From the table, it is seen that for 16 processors, the model without wetting and drying treatment (U4) is run slightly longer (~34 minutes) than the model using the wetting and drying in the computation. This observed difference is mainly due to the larger elemental numbers (approximately 4000 more elements) present in the U4 model. From the table, it is also possible to deduce that including the wetting and drying algorithm in the computation does not significantly affect the computational run-times.

Model	Node number	Element number	CPU	Run-time (hr:min:sec)	Memory (kb)	Virtual Memory (kb)
DG-ADCIRC-WD	28922	55570	16	03:59:09	14708	62300
U4	30994	59799	16	04:33:00	15836	65284

Table 4.12 Comparison of run-times and memory requirements between DG-ADCIRC-WD and U4 models to evaluate the influence of including wetting and drying treatment in the computations.

In calibrating the DG-ADCIRC-WD model (not shown explicitly here), the model is run for an entire spring-neap tide using 16 processors, in which the best fit to field observations after harmonic analysis is obtained by setting $c_f = 0.0025$. Including wetting and drying treatment in the model permits a smaller bed friction coefficient to be applied in the model, as energy is dissipated at the wet/dry fronts as well. The wetting and drying treatment used in DG-ADCIRC-WD is based on a thin-layer technique applied on a fixed mesh (Bunya *et al.*, 2009). The technique adopted in DG-ADCIRC-WD ensures local mass conservation at each element by checking the surface elevations at the end of each Runge-Kutta time stage. The model is run for a complete spring-neap cycle. The following subsections discuss the validation of the model focusing on Anglesey and the Bristol Channel. Model results are compared against field observations obtained from different resources.

4.5.1. Anglesey

The inter-tidal zones along the Cumbrian and Lancashire coasts are interpolated using survey data at a spatial resolution of approximately 30 m in order to correctly model the reflected waves directed towards the eastern Irish Sea. The local mesh size varies from 200 m close to the Anglesey Headland to over 1500 m within the Irish Sea. The modified model is used in the power analysis that is described in the following chapters. Thus, the mesh includes some areas of structured mesh that are embedded in the unstructured model domain. Figure 4.40 shows a portion of the mesh fitted to the eastern Irish Sea. A wetting and drying algorithm is used to model the moving shoreline in the inter-tidal zones (Bunya *et al.*, 2009; Ern *et al.*, 2008).

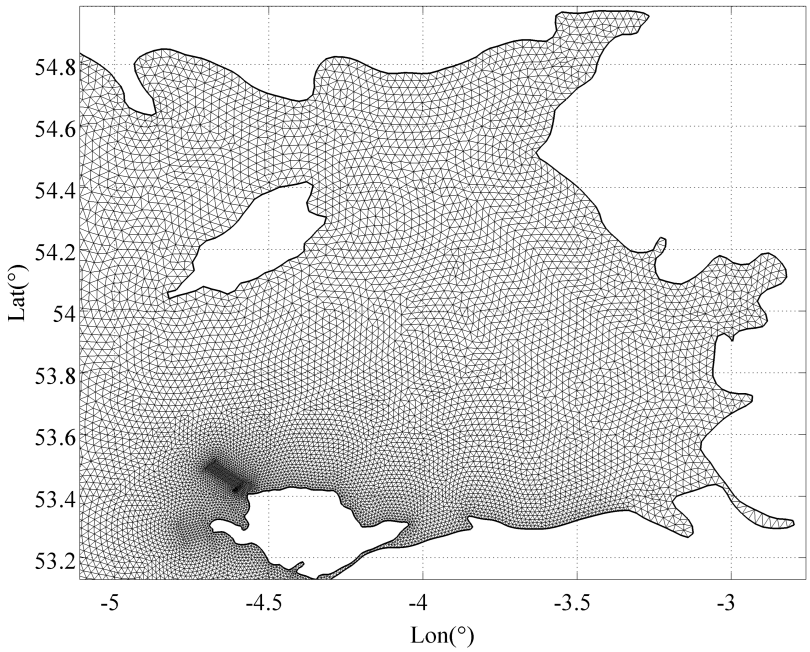

Figure 4.40 – A portion of the two-dimensional unstructured triangular mesh, focusing on the Irish Sea in the region of the Cumbrian and Lancashire coasts.

The model was run for a complete spring-neap cycle, and the results compared against tidal current velocity observations provided by the British Oceanography Data Centre and tidal water levels obtained from Admiralty Charts.

Water Levels

In terms of water surface elevation, model validation was undertaken against observed data obtained from the Admiralty Tide Tables for M_2 (Table 4.13) and S_2 (Table 4.14) constituents (Admiralty Charts, 2006). The model results are in very close agreement with the observations for both amplitudes and phases. The tidal harmonic amplitudes agree to within 5% and the small phase differences suggest that the model predicts the time of high water correct to within eight minutes for M_2 and 12 minutes for S_2 tides.

Location	Coordinates	Observations		Predictions (No WD)		Predictions (with WD)	
		H_n (m)	φ_n (°)	H_n (m)	φ_n (°)	H_n (m)	φ_n (°)
Holyhead	53° 19'N 04° 37'W	1.81	292	1.66	289	1.80	292
Cemaes Bay	53° 25'N 04° 27'W	2.13	307	1.90	303	2.12	304
Amlwch	53° 25'N 04° 20'W	2.30	305	1.98	306	2.26	307
Moelfre	53° 20'N 04° 14'W	2.47	308	-	-	2.42	311
Trywn Dinmor	53° 19'N 04° 03'W	2.47	310	-	-	2.49	312
Beaumaris	53° 16'N 04° 05'W	2.57	312	-	-	2.51	313
Port Trecastell	53° 12'N 04° 30'W	1.50	278	-	-	1.57	277
Trearddur Bay	53° 16'N 04° 37'W	1.56	280	-	-	1.61	280

Table 4.13 Tidal harmonic analysis comparisons for M_2 constituent: water surface elevation amplitudes H_n (m) and phase lags φ_n (°). The observations are compared against models: i) without wetting and drying, ii) with wetting and drying.

Location	Coordinates	Observations		Predictions (No WD)		Predictions (with WD)	
		H_n (m)	φ_n (°)	H_n (m)	φ_n (°)	H_n (m)	φ_n (°)
Holyhead	53° 19'N 04° 37'W	0.59	329	0.51	333	0.59	333
Cemaes Bay	53° 25'N 04° 27'W	0.71	345	0.56	349	0.67	345
Amlwch	53° 25'N 04° 20'W	0.75	345	0.58	352	0.71	350
Moelfre	53° 20'N 04° 14'W	0.81	348	-	-	0.76	354
Trywn Dinmor	53° 19'N 04° 03'W	0.80	351	-	-	0.78	356
Beaumaris	53° 16'N 04° 05'W	0.82	356	-	-	0.79	357
Port Trecastell	53° 12'N 04° 30'W	0.50	320	-	-	0.53	317
Trearddur Bay	53° 16'N 04° 37'W	0.54	315	-	-	0.54	320

Table 4.14 Tidal harmonic analysis comparisons for S_2 constituent; water surface elevation amplitudes H_n (m) and phase lags φ_n (°). The observations are compared against models: i) without wetting and drying, ii) with wetting and drying.

Tidal Currents

The observed data are obtained from the British Oceanographic Data Centre. The coordinates of the selected gauge are 53°17'N 4°55'W, located northwest of Holyhead (see BODC1 station illustrated in Figure 4.18). The bathymetric depth is 44 m, and the readings were conducted 31 m above the sea floor. Figure 4.41 displays the predicted and observed tidal velocity magnitude time histories; Figure 4.42 shows the corresponding tidal current directions with time. Figure 4.41 displays a comparison of the observed and modelled tidal currents at the selected gauge. The figure shows that the predicted current is slightly out of phase with the observations, however there is a good agreement with respect to the flow velocity magnitudes. A possible explanation for the discrepancy related to the phases might be the uniform bed friction coefficient applied in the model. As explained previously, using a constant bed friction coefficient in a two-dimensional depth-averaged model limits representation of the flow dynamics accurately, especially at a headland site (Stansby, 2006). Thus it is expected that the model results would be slightly in error with the observations. However, the level of agreement shown here indicates that the model is capturing the dominant tidal hydrodynamics.

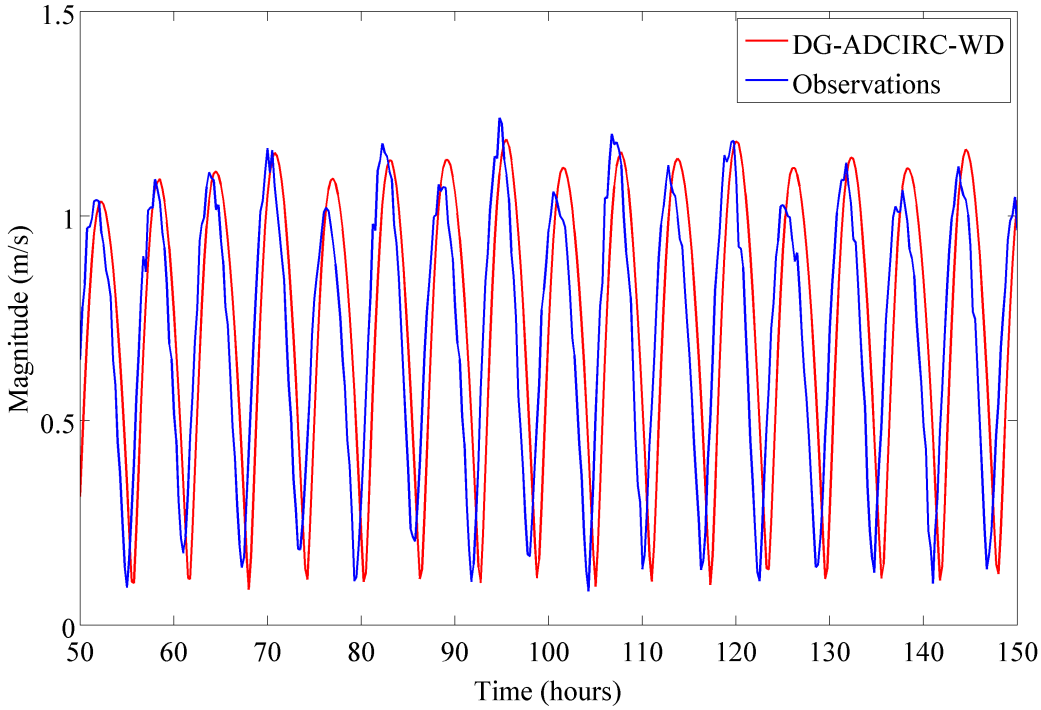

Figure 4.41 – Predicted and observed tidal current magnitude time histories at a gauge located at 53°17'N 4°55'W, north-west of Holyhead.

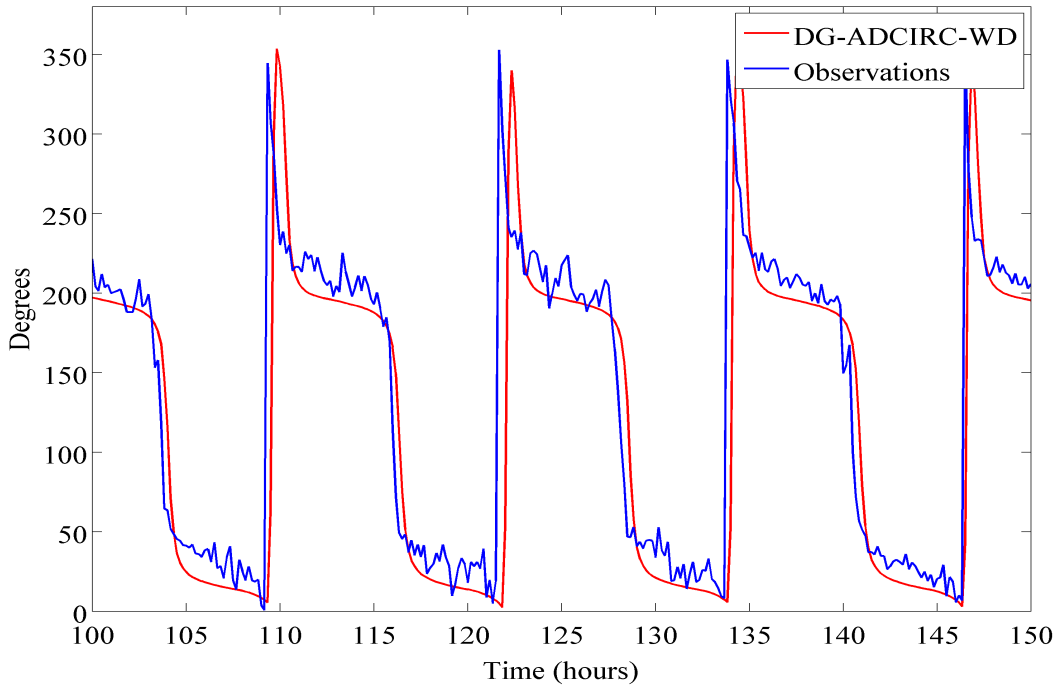

Figure 4.42 – Predicted and observed tidal current direction time histories at a gauge located at 53°17'N 4°55'W, north-west Holyhead.

Comparing Figure 4.42 with Figure 4.24 shows that the model including wetting and drying treatment provides a closer agreement in current directions with the observations. Figure 4.42 displays a similar phase difference between the predicted and modelled tidal currents at the observation gauge. Owen (1980) found a similar discrepancy between predicted and observed phases, and concluded that this was due to the limitations of using a depth-averaged shallow water model. Owen noted that the bottom current, which leads the frictional dissipation, cannot accurately be modelled in a depth-averaged model, resulting in delayed currents (indicated by the current phases).

4.5.2. Bristol Channel

The DG-ADCIRC-WD model includes the inter-tidal zones around the Bristol Channel (see Figure 4.39). The local mesh size varies from 200 m close to the Flat Holm and Steep Holm islands to over 700 m around the vicinity of the eastern Celtic Sea. The validation study of the Bristol Channel is similar to that of the Anglesey Skerries region, which was explained in the previous section. The subsequent sections provide the validation studies for surface water levels and tidal currents.

Water Levels

Table 4.15 shows the predicted and observed amplitudes and phases of M_2 tides at several stations in the Bristol Channel. The numerical model underestimates the M_2 phases in the inner channel region between Ilfracombe and Avonmouth. Inclusion of wetting and drying causes the high tides to occur approximately 10 min earlier than natural at the top of the Channel, where the wetting and drying is dominant; however the time of high tides around the Flat Holm and Steep Holm islands is predicted with great accuracy. The M_2 phases are over-predicted for other inter-tidal zones such as the Swansea Bay area. However, the results show that the high tides are only delayed approximately by 10 minutes.

Location	Coordinates	Observations		Predictions (no WD)		Predictions (with WD)	
		H_n (m)	φ_n (°)	H_n (m)	φ_n (°)	H_n (m)	φ_n (°)
Avonmouth	51° 30'N 02° 44'W	4.22	201	4.11	195	4.32	195
St. Thomas Head	51° 24'N 02° 56'W	4.25	194	-	-	4.06	188
Flat Holm	51° 23'N 03° 07'W	3.90	190	4.02	204	3.95	186
Steep Holm	51° 20'N 03° 06'W	3.87	186	-	-	3.92	184
Barry	51° 23'N 03° 16'W	3.82	185	3.96	202	3.79	184
Hinkley Point	51° 13'N 03° 08'W	3.80	185	-	-	3.87	182
Minehead	51° 13'N 03° 28'W	3.59	183	-	-	3.61	178
Ilfracombe	51° 13'N 04° 07'W	3.04	162	3.25	178	2.90	166
Swansea	51° 37'N 03° 55'W	3.19	173	-	-	3.09	176
Milford Haven	51° 42'N 05° 03'W	2.22	173	-	-	2.16	178
Lundy	51° 10'N 04° 39'W	2.67	160	-	-	2.50	165

Table 4.15 Tidal harmonic analysis comparisons for M_2 constituent; water surface elevation amplitudes H_n (m) and phase lags φ_n (°).

The predicted M_2 amplitudes are higher than the observed values at the inner Channel region; however they are under-estimated at the outer Channel region (considering Swansea

Bay as the mid-point). However, the error is within a reasonable limit (~ 5%), and thus is not of concern with respect to model accuracy. When moving from east to west of the Channel, the M_2 amplitudes increase rapidly from 2.2 m to 4.2 m. In the entrance of the Bristol Channel the M_2 phase is around 150°, and it increases to 200° towards the head of the Channel. This change indicates that high water occurs within a period of time less than 2 hours throughout the Channel.

Location	Coordinates	Observations		Predictions (no WD)		Predictions (with WD)	
		H_n (m)	φ_n (°)	H_n (m)	φ_n (°)	H_n (m)	φ_n (°)
Avonmouth	51° 30'N 02° 44'W	1.51	260	1.24	265	1.39	274
St. Thomas Head	51° 24'N 02° 56'W	1.44	250	-	-	1.33	248
Flat Holm	51° 23'N 03° 07'W	1.35	246	1.31	248	1.36	243
Steep Holm	51° 20'N 03° 06'W	1.37	240	-	-	1.35	241
Barry	51° 23'N 03° 16'W	1.37	240	1.26	246	1.31	240
Hinkley Point	51° 13'N 03° 08'W	1.42	237	-	-	1.33	238
Minehead	51° 13'N 03° 28'W	1.24	235	-	-	1.25	232
Ilfracombe	51° 13'N 04° 07'W	1.10	209	1.03	221	1.02	215
Swansea	51° 37'N 03° 55'W	1.14	221	-	-	1.07	226
Milford Haven	51° 42'N 05° 03'W	0.81	217	-	-	0.76	223
Lundy	51° 10'N 04° 39'W	0.94	207	-	-	0.87	212

Table 4.16 Tidal harmonic analysis comparisons for S_2 constituent; water surface elevation amplitudes H_n (m) and phase lags φ_n (°).

Table 4.16 presents the predicted and observed amplitudes and phases of S_2 tides at the selected stations across the Channel. The predicted S_2 tidal amplitudes are in good agreement with the observed data except at the Avonmouth and St. Thomas Head stations. These locations are susceptible to rapid changes in water level, and locally the mesh requires higher

resolution to capture the correct physics. However, in order to ensure that numerical solution of the model (the area between the North Channel and the European continental shelf) was computationally feasible, a compromise in the grid resolution has been made on the areas not part of the parametric study. Furthermore, adding more mesh resolution to every region subjected to the wetting and drying treatment, would mean an impracticably small time-step owing to the CFL limitation. Thus, the resolution of the region is not modified further. The model results indicate that the high water is delayed at the outer Channel region (from the Celtic Sea towards Ilfracombe) by approximately 10 minutes (~5°). However, the S_2 phases are under-estimated from Ilfracombe towards the head of the Channel.

Tidal Currents

DG-ADCIRC-WD model validation for the tidal current velocities in the Bristol Channel is undertaken by comparison against two sets of data: published observation data by Owen (1980); and observed currents from BODC, which was introduced in Section 4.3.3. Figure 4.43 illustrates the locations of the current stations, NL and SB relating to Owen (1980) and BODC2 relating to BODC.

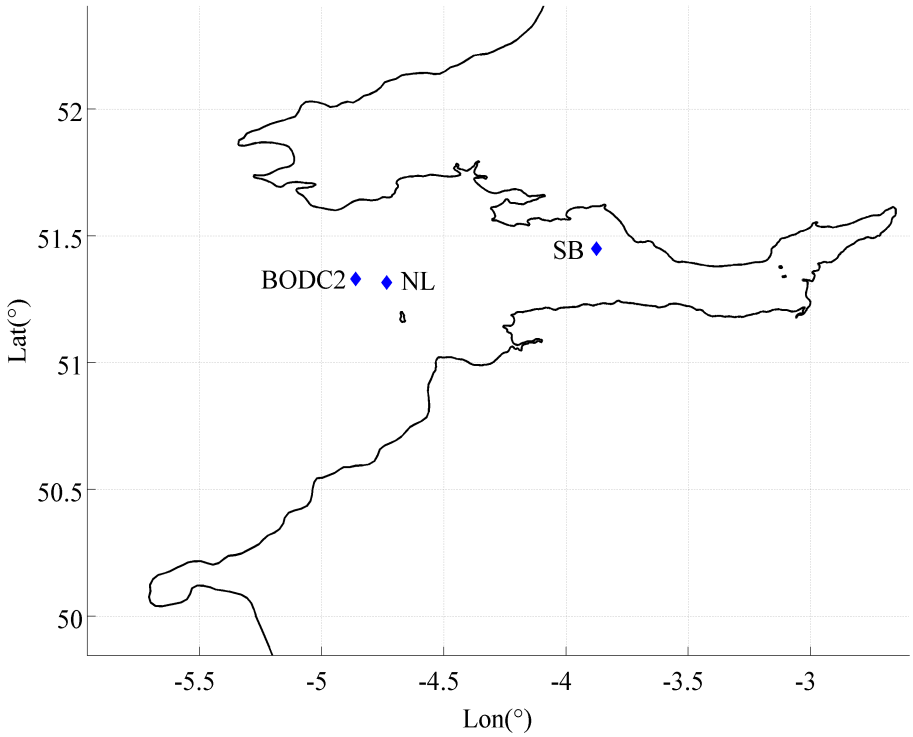

Figure 4.43 – Locations of the stations for tidal current readings. NL and SB stations are taken from Owen (1980). BODC2 station represents the current readings obtained from BODC.

Owen (1980) presents a comparison for eastward and northward components of M_2 tides observed at two locations. The first of these locations is towards the north of Lundy Island (Station NL: 51° 19'N; 4° 44'W) and the second one is at the south of the Swansea Bay (Station SB: 51° 27'N; 3° 52.5'W). Figure 4.43 illustrates the locations of the stations (NL and SB) and Table 4.17 compares the observed data taken from the mentioned study and the results obtained from the present depth-averaged model for M_2 tidal currents. A similar comparison is shown in Table 4.18 for S_2 tidal currents.

Table 4.17 and Table 4.18 show that the eastward velocity components at both stations are in good agreement with the observations for both tidal constituents. The northward velocity components, however, are ~50% overestimated by the model. As explained in Section 4.3.2, the measurements were taken by recording the direction and magnitude of the currents. Thus, even a small error in direction would cause a large error in the magnitude of the velocity components. In this respect, the observed discrepancy may be related to small errors in the tidal current recordings. Bearing in mind that the eastward component is approximately five times larger than the northward, it is seen that the model estimates the dominant direction accurately (see Table 4.19).

Station	$-z/h$	Direction	Observation		Prediction	
			Tidal current component amplitude (m/s)	Tidal current component phase (°)	Tidal current component amplitude (m/s)	Tidal current component phase (°)
NL	0.52	W-E	0.64	87	0.64	83
		S-N	0.13	126	0.20	129
SB	0.56	W-E	0.80	93	0.87	91
		S-N	0.13	283	0.19	276

Table 4.17 Observed (Owen, 1980) and predicted (DG-ADCIRC-WD) M_2 tidal current component magnitudes and directions in east and north directions.

Station	$-z/h$	Direction	Observation		Prediction	
			Tidal current component amplitude (m/s)	Tidal current component phase (°)	Tidal current component amplitude (m/s)	Tidal current component phase (°)
NL	0.52	W-E	0.23	134	0.21	137
		S-N	0.05	178	0.08	175
SB	0.56	W-E	0.30	146	0.28	149
		S-N	0.04	333	0.06	333

Table 4.18 Observed (Owen, 1980) and predicted (DG-ADCIRC-WD) S_2 tidal current component magnitudes and directions in east and north directions.

Station	M_2				S_2			
	Observation		Prediction		Observation		Prediction	
	Mag. (m/s)	Dir. (°)	Mag. (m/s)	Dir. (°)	Mag. (m/s)	Dir. (°)	Mag. (m/s)	Dir. (°)
NL	0.65	153	0.67	153	0.24	223	0.22	223
SB	0.81	298	0.89	291	0.30	364	0.29	365

Table 4.19 Observed (Owen, 1980) and predicted (DG-ADCIRC-WD) M_2 and S_2 tidal current amplitude magnitudes and directions.

Table 4.19 presents a comparison between the model predictions (DG-ADCIRC-WD) and the observations presented by Owen (1980) for the M_2 and S_2 tidal current magnitudes and directions. Considering the current magnitudes, the DG-ADCIRC-WD model results agree well with the observations, indicating that the model is capable of capturing the dominant tidal hydrodynamics. The computed directions are in excellent agreement for NL station for both tidal constituents. The predicted directions for SB station are within 2% error (~ 14 min delay) for M_2 tidal currents and are less than 1% error for S_2 currents.

Secondary comparisons are conducted using the time-series recordings obtained from BODC dataset (introduced in Section 4.3.3). Figure 4.44 and Figure 4.45 present the cross-comparisons of the model results in terms of current magnitudes and directions with the observations undertaken at BODC2 station illustrated in Figure 4.43. Figure 4.44 shows that the predicted and observed currents are in agreement in terms of phases, however the model slightly over-predicts the current magnitudes. When compared against the DG-ADCIRC

model results presented in Figure 4.37, the DG-ADCIRC-WD model shows a better agreement with the observations. Considering the current directions, Figure 4.45 shows that the model captures the dominant current direction accurately. Comparing Figure 4.45 with Figure 4.38 shows that using a smaller bed friction coefficient and applying the wetting and drying treatment has significantly improved the model accuracy.

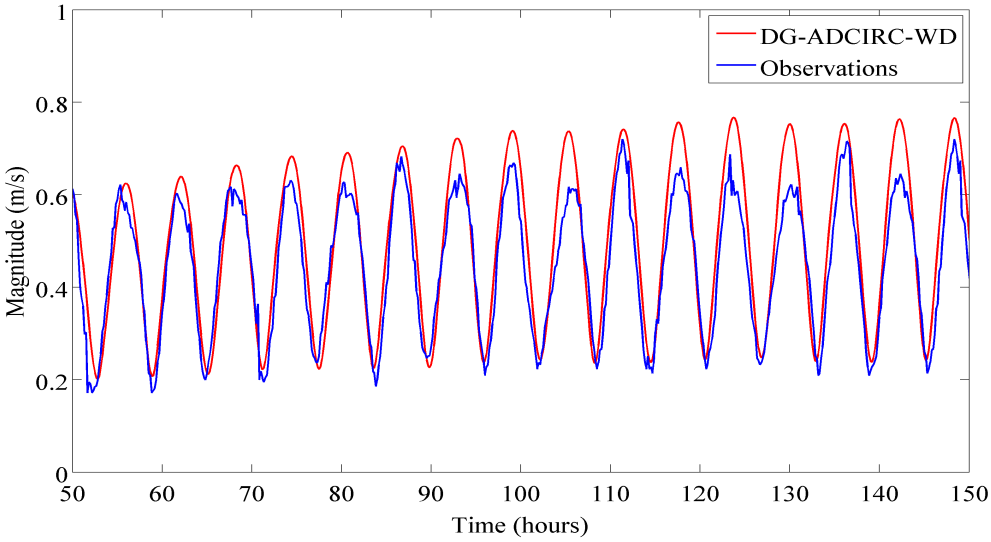

Figure 4.44 – Predicted and observed tidal current magnitude time histories at a gauge (BODC2) located at 51°19.8'N 4°51.6W, north of Lundy Island.

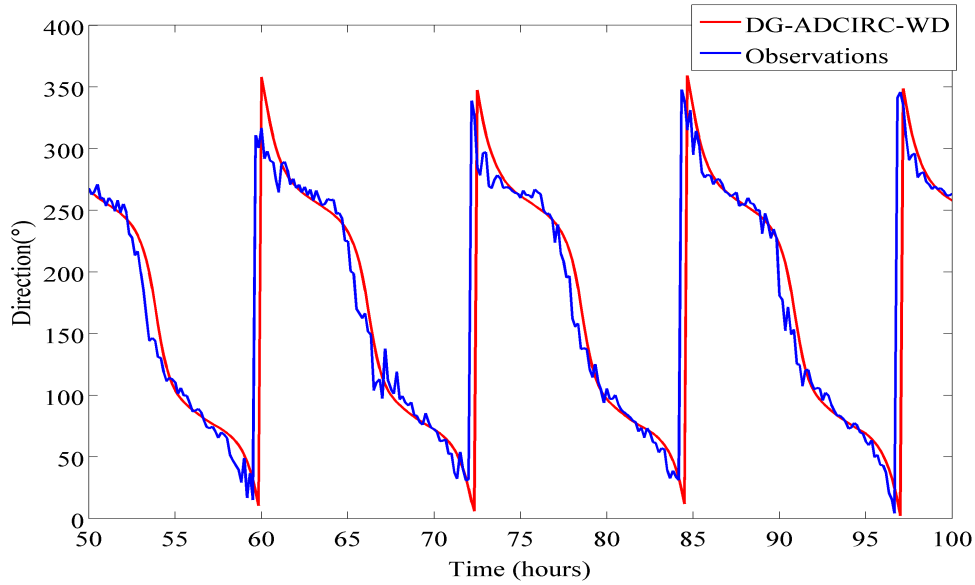

Figure 4.45 – Predicted and observed tidal current direction time histories at a gauge (BODC2) located at 51°19.8'N 4°51.6W, north of Lundy Island.

4.6. Discussion

A modified version of the calibrated model has been constructed, which includes the inter-tidal zones around the Bristol Channel and Anglesey regions. The model has been calibrated using different bed friction coefficients, and the model results are presented by using the best-fit data when compared to the observations. The DG-ADCIRC-WD model is capable of producing the physics observed in the Bristol Channel more accurately due to inclusion of wetting and drying in the computation. The model is next used to analyse the resource assessment in the south-west UK coasts. Some structured mesh is embedded within the numerical model in order to include a line sink of momentum to represent the effect of tidal array deployments in the regions. The following chapters describe the assessment of available tidal power at selected sites off the Anglesey Skerries and in the Bristol Channel.

4.7. Conclusions

The chapter presents the construction of a two-dimensional unstructured finite element model of the south-west coasts of the UK. Initially, the inter-tidal zones in the region were not included in the model. The objective was to develop the best possible model without using complex modelling techniques such as the wetting and drying treatment. A grid-convergence test has been conducted to evaluate the sensitivity of the results to the grid refinement. The grid convergence study showed that even the coarsest grid (U1) provides a good agreement with the reference values obtained from the finest grid (U5). The maximum error computed for the predicted M_2 elevation amplitudes within the domain does not exceed 4%. Considering the time required to run the models, U2 grid has been chosen as the optimal grid, which is used to conduct a calibration test to evaluate the optimal bed friction coefficient. A set of bed friction coefficients is used in the calibration tests and the best fit was achieved by setting $c_f = 0.0050$.The calibrated model (U2) is then validated against observation datasets obtained from various sources (e.g. Admiralty Charts, 2006 and BODC, 2011). The validation tests involve the water levels and currents at specific stations off the Anglesey headland and the Bristol Channel. Comparisons with independent data sources demonstrate that the overall model achieves a very good prediction of the pattern of tidal elevations throughout the region analysed. However, less agreement is observed for individual stations due to several shortcomings of the numerical model. These shortcomings are mainly related to the high bed

friction coefficient applied in the model, which affects the tidal current magnitudes and phases, and the lack of inter-tidal zones within the coastal domain. In order to evaluate the importance of wetting and drying in the computation, the DG-ADCIRC model has been modified to include the inter-tidal zones. The altered model, DG-ADCIRC-WD, is found capable of producing the tidal dynamics observed in the Bristol Channel more accurately. It is also observed that inclusion of the wetting and drying treatment in the computations ultimately enabled using a lower bed friction coefficient ($c_f = 0.0025$), which increased the level of agreement obtained in modelling the dominant semi-diurnal tidal currents.

Chapter 5

Tidal Stream Farm Deployment - I: Anglesey Skerries

This chapter aims to evaluate realistic estimates for the tidal stream power resource of the Anglesey Skerries. This is accomplished by considering the time-averaged available power extracted by the conceptual turbine arrays. The available power is defined as the usable energy, which is a fraction of the total power removed from the tidal stream (see Chapter 3). In the numerical model, the tidal turbines are represented by linear momentum actuator disk theory, which only accounts for the wake mixing losses and not for mechanical or electrical energy losses (Adcock *et al.*, 2013). Thus, the available power is overestimated in the model for similar flow conditions.

A validated depth-averaged model is used to estimate the extractable and available power from the site (see Chapter 4). The turbine properties are manually altered for different test cases studied in this chapter.

The methodology adopted in this chapter is applied in the following chapters to assess power potential of the Bristol Channel and a combination of several tidal farms operating simultaneously at Anglesey and Bristol Channel sites.

Section 5.1 summarises the tidal hydrodynamics observed in the Irish Sea. Section 5.2 presents the methodology adopted to calculate the maximum available power that is averaged over a tidal cycle. Section 5.3 and 5.4 present the results of the parametric study conducted to evaluate the maximum power available to the turbines and to assess the change in the local flow field in presence of the arrays, respectively. Section 5.5 presents the conclusions for this chapter.

5.1. Tidal Dynamics of the Irish Sea

The coastal features (i.e. dimensions) of a basin can have significant effects on regional tidal dynamics (Pugh, 1987). In a previous study, Howarth (1984) explains why a small enclosed sea such as the Irish Sea, does not respond directly to the astronomical forces. The

Irish Sea comprises the area from St. David's Head in the south to the North Channel in the north. In the Irish Sea, naturally occurring tidal motions are mainly driven by the interaction between two series of tidal waves entering from these regions. At the southern end, tidal waves originating from the Atlantic Ocean propagate into the Irish Sea through the Celtic Sea and St. George's Channel (Howarth, 1984). The other waves enter the system from the north through the Malin Shelf Sea and the North Channel. Standing waves form as a consequence of these two tidal waves meeting in the vicinity of the Isle of Man, which are reflected off of the Lancashire and Cumbrian coasts. Based on the observed tidal elevations, it appears that due to this standing wave formation the high water is occurring at the eastern Irish Sea almost simultaneously (Howarth, 1984; Pugh, 1981).

Two amphidromic systems form due to the reflection of the tidal waves. One is between Ireland and the Scottish island of Islay, and the other is towards the coast of Courtown, Ireland (Robinson, 1979; Pugh, 1981; Pugh, 1987). According to Pugh (1987), the latter is a degenerate amphidrome because of the energy dissipation across the eastern Irish Sea and St. George's Channel resulting in a much weaker reflected tidal wave than the ingoing wave. Consequently, as the reflected tidal wave is weaker than the incoming wave, the location amphidrome is shifted towards to the left of the incoming wave direction; in this case the eastern Ireland coast (Pugh, 1987). The other factor that affects the observed tidal ranges across the Irish Sea is the Coriolis force. Under the influence of the Coriolis force, tidal waves incoming from the south are directed towards the eastern Irish Sea, enhancing the water levels observed in the English/Welsh coasts (Howarth, 1984). In order to verify this conclusion by Howarth (1984), the DG-ADCIRC-WD model has been run without including the Coriolis force in the solution. The model results show that the M_2 degenerate amphidromic system that would normally occur off of the eastern Irish coasts cannot be formed without including the Coriolis force in the computation. It should also be noted that the model without the Coriolis force requires a larger bed friction coefficient ($c_f = 0.0050$) applied in the model to obtain a stable solution. The M_2 elevations across the eastern Irish Sea are underestimated by approximately 20 cm, whereas the elevations in the vicinity of the degenerate amphidrome are significantly overestimated.

Considering the currents, the standing wave system affects the structure of the naturally occurring tidal currents in the Irish Sea. Pugh (1987) reports that in such a system, the currents are predominantly rectilinear and the maximum currents occur near the nodes or the amphidromic points, as seen at the southern entrance to the Irish Sea. The amplitudes of the strong tidal currents in the Irish Sea reach up to 2 m/s (Howarth, 1984). More specifically, there are several regions where fast currents occur, such as western St. George's Channel, north of Anglesey, north of the Isle of Man and the North Channel (Howarth, 1984). Among these sites, the currents around the Anglesey are also strongly influenced by the Anglesey headland. In the vicinity of the Isle of Man, where the standing wave has an antinode, the minimum currents ($0.15 < u < 0.5$ m/s) occur.

The DG-ADCIRC-WD numerical model constructed to model the tides in the Irish Sea is explained in Chapter 4. The model mesh (see Figure 5.1) includes the inter-tidal zones along the Cumbrian and Lancashire coasts to model accurately the reflected waves directed towards the eastern Irish Sea. The mesh is unstructured except in the region where rows of tidal turbines are to be deployed. Within this area a structured mesh of elements is embedded. The local mesh size is 200 m close to the Anglesey Headland.

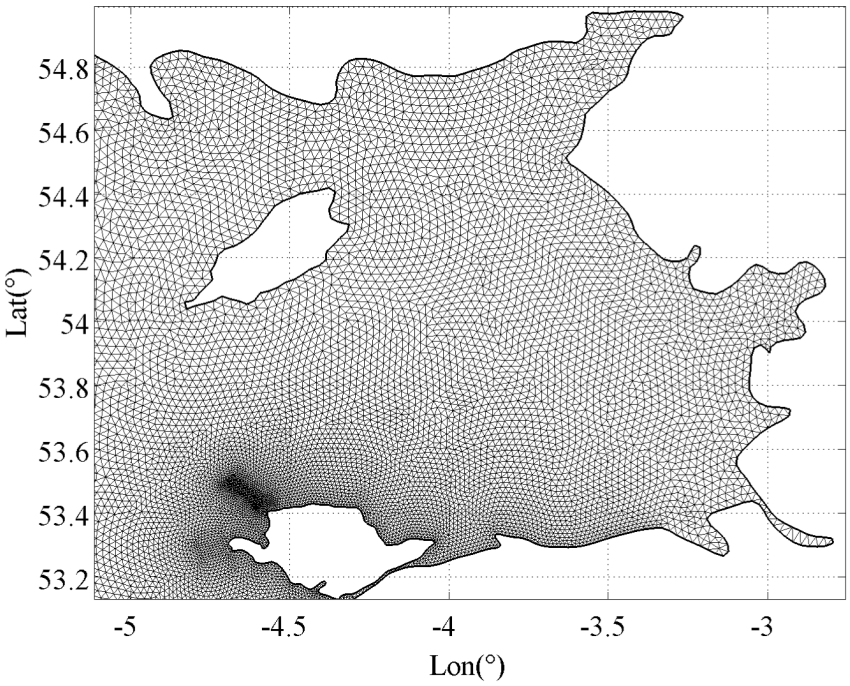

Figure 5.1 – Computational mesh of the Irish Sea – Welsh coastline.

A comparison of the required computational resources and simulation run-times of the models with and without the LMADT calculations is undertaken. In this respect, a parallel performance test, similar to the previous tests, using 16 CPUs located on the ARC-HAL supercomputer system is conducted. The test case using the modified DG-ADCIRC code, which incorporates a line sink of momentum approach to represent the effect of tidal turbine arrays, is set up for the ASA array configuration shown in Figure 5.6. Table 5.1 summarises the memory requirements per core and the computational run-times for a 4-day test run using only the M_2 tidal constituent. From the table, it is seen that the inclusion of the LMADT sub-grid model results in an insignificant change in the run-times.

Code	Run-time (hr:min:sec)	Memory (kb)	Virtual Memory (kb)
Original (no LMADT)	03:59:09	14708	62300
Modified (with LMADT)	04:03:14	6212	51936

Table 5.1 Comparison of run-times and memory requirements between original DG-ADCIRC code with the modified DG-ADCIRC code. The modified DG-ADCIRC code includes a sub-grid model based on LMADT analysis to represent the effect of tidal turbines in the flow domain. The comparison considers running the codes using 16 CPUs on the ARC-HAL system.

The following section introduces the methodology adopted to calculate the maximum available power that can be extracted for a specific array configuration.

5.2. Available Power Analysis

This section describes the methodology used to calculate the maximum average power output over a prescribed simulation period. As the M_2 tidal constituent represents the average tidal regime observed in the Irish Sea (Uncles, 1983), the DG-ADCIRC-WD model is forced by only the M_2 tidal forcing. Using only the M_2 tides allows running the simulations for shorter time periods, which in turn enables shorter computational run-times. The methodology explained herein is applied for power estimates throughout the remainder of the thesis.

The effect of turbine devices on the local flow field is represented by means of a line sink of momentum in a discontinuous Galerkin hydrodynamic model (following Draper, 2011, and explained in Chapter 3). The thrust applied to the flow is calculated using linear momentum

actuator disk theory (LMADT) in which the turbine characteristics (i.e. turbine operating conditions) are defined by local blockage ratio (B), and wake velocity coefficient (α_4) for prescribed flow conditions (upstream Fr number). For an actual tidal turbine, the thrust applied to the flow is often computed in terms of the local flow velocity. This parameter is defined as the local thrust coefficient C_{TL}, which is computed by equation 5.1 (Houlsby *et al*., 2008),

$$C_{TL} = \frac{C_T}{\alpha_2^2}, \qquad 5.1$$

where C_T is the thrust coefficient and α_2 is the turbine velocity coefficient. The optimal conditions for a wind turbine using the standard Betz derivation, gives C_{TL} to be 2. For tidal turbines, C_{TL} could potentially reach up to 6-8, however it is physically impractical to design a turbine which can exceed this limit (Houlsby, personal communication). It should be noted that the parametric study conducted herein considers very high local C_T values ($C_{TL} > 8$) as well as the physically admissible values as it is intended to assess the power potential of a chosen site. Figure 5.2 plots the local thrust coefficients (C_{TL}) against various wake velocity coefficients that are used in the parametric study for a typical spring tide ($u \cong 2$ m/s) at a site with an average bathymetric depth of 40 m (ASA2 array in Figure 5.6).

Figure 5.2 shows that for low blockage case ($B = 0.1$) the optimum wake velocity coefficient approaches to the Lanchester-Betz limit ($\alpha_4 = 1/3$) to obtain maximum C_{TL} and hence maximum available power. However, when using a high blockage ratio ($B = 0.5$), the feasible maximum C_{TL} is obtained for $0.5 < \alpha_4 < 0.6$.

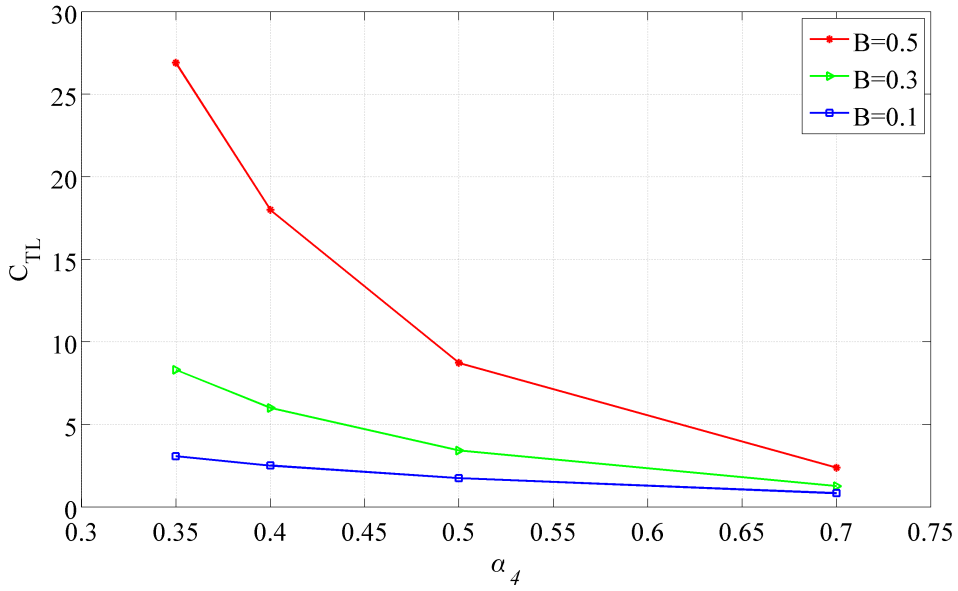

Figure 5.2 – Computed local thrust coefficients against wake velocity coefficients (α_4) for various blockage ratios. The upstream *Fr* number is 0.10.

Application of LMADT to the solution enables computation of the time series of power available to the turbines and the total power removed from the stream. As explained by Vennell (2011), there is an optimum wake velocity coefficient, α_4 that maximizes the available power. This value is dependent on the turbine arrangement as well as the coastal features near the area of interest. The optimum value may also vary through the spring-neap cycle owing to the fact that the dynamic balance may change in the area (Adcock *et al.*, 2013; Adcock and Draper, 2014). However, in the present analysis, the wake velocity coefficient is taken to be constant throughout the cycle, in which case the calculated available power values are slightly less than the maximum that would be determined if a variable wake velocity coefficient were utilised. A range of wake velocity coefficients is examined in order to evaluate the optimum α_4 value for which to compute the maximum available power. For instance, Figure 5.3 presents the raw power data obtained from a particular test case (ASA2 array in Figure 5.6) for a simulation period of 3 days. The figure shows the raw data that accounts for the power available to the turbine arrays (P_a) and the total power that is extracted from the stream (P_e). In this example, the time series of the power outputs is generated for an array (i.e. ASA2) that is defined by a blockage ratio (B) of 0.5 and a wake velocity coefficient (α_4) of 0.35. Averaging the obtained available power over the simulation time (i.e. 3 days) and repeating the same procedure for different predefined α_4 for a fixed B, it is possible to

evaluate the optimum wake velocity coefficient. The analysis conducted herein considers a set of four different wake velocity coefficients ($\alpha_4 = 0.35, 0.40, 0.50,$ and 0.70), which allows a cubic spline interpolation to determine the optimum α_4 value (see Figure 5.4).

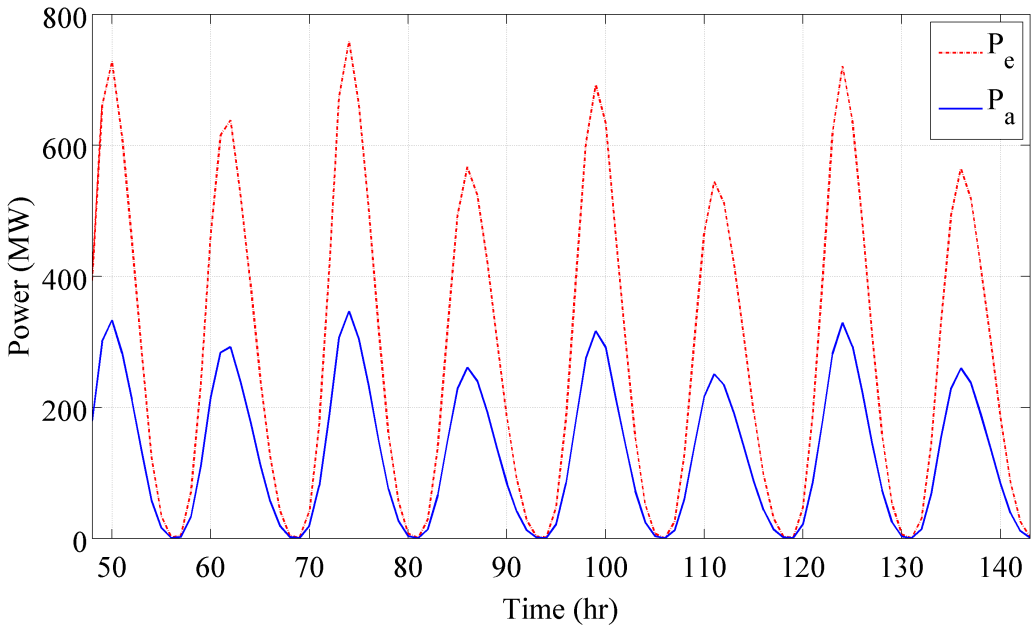

Figure 5.3 – Raw data time series indicating the power extracted (P_e) from the tidal stream and power available (P_a) to the turbines for $B = 0.5$ and $\alpha_4 = 0.35$ for a parallel array configuration (ASA2).

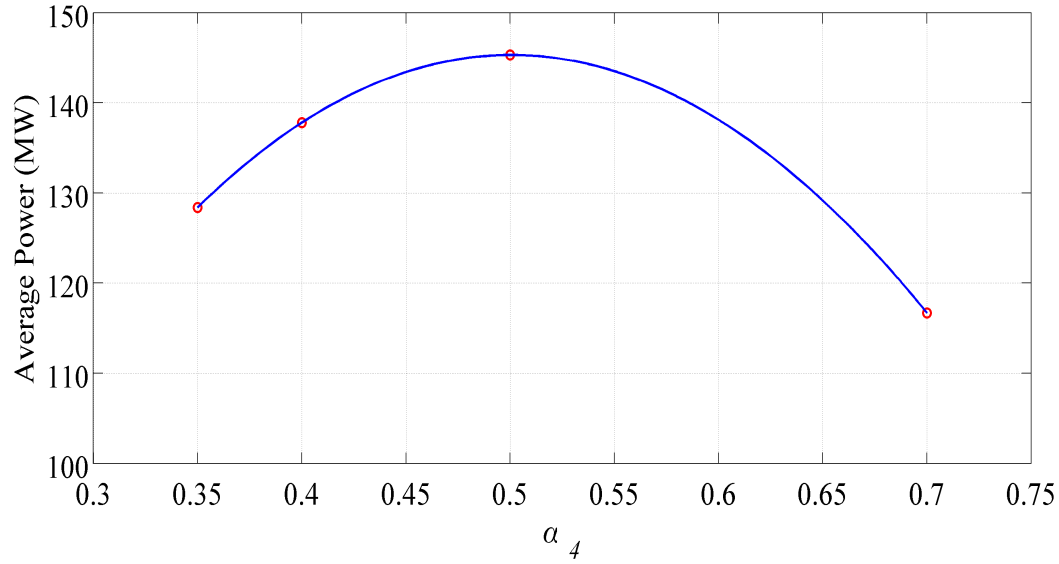

Figure 5.4 – Evaluation of the maximum available power (P_a) with respect to averaged power values obtained for various α_4 for $B = 0.5$ for an individual configuration (ASA2). Red dots provide the time-averaged available power output (P_a) for the studied α_4 values. Blue line corresponds to the fitted cubic spline.

The optimal α_4 is computed by differentiating the cubic that corresponds to the maximum available power output. Throughout the rest of this chapter (and the following chapters), the results are presented for optimum wake velocity coefficients, α_4 – i.e. when the available power is maximized.

The parametric study presented herein is undertaken to examine the effects of location and connectivity of the arrays for specified local blockage ratio and wake velocity coefficients on the available power. Chapter 6 presents a similar analysis, which has been conducted for the Bristol Channel.

5.3. Parametric Study: Deployment of Tidal Stream Devices in the Anglesey Skerries

5.3.1. Location

The naturally occurring flow around a headland with realistic bathymetry is highly complex, and so the optimum location to install an array of tidal devices is not obvious. Although undisturbed kinetic energy flux method is found insufficient of providing accurate estimates on available power at a chosen site, the method is a good indicator of determining the best position to deploy tidal turbine arrays (Draper *et al.*, 2013). In this respect, a snapshot of the naturally occurring flood tide in the vicinity of the Anglesey Skerries is plotted in Figure 5.5. The average flow velocity observed in the offshore of the Skerries is 2.1 m/s. Figure 5.6 indicates several trial locations for tidal turbine deployments offshore of the Skerries. The area selected for the analysis is based on two factors. First, the naturally occurring kinetic energy flux is relatively higher than at other regions around the Anglesey headland. Second, the bathymetry of the area is favourable for tidal farm deployment.

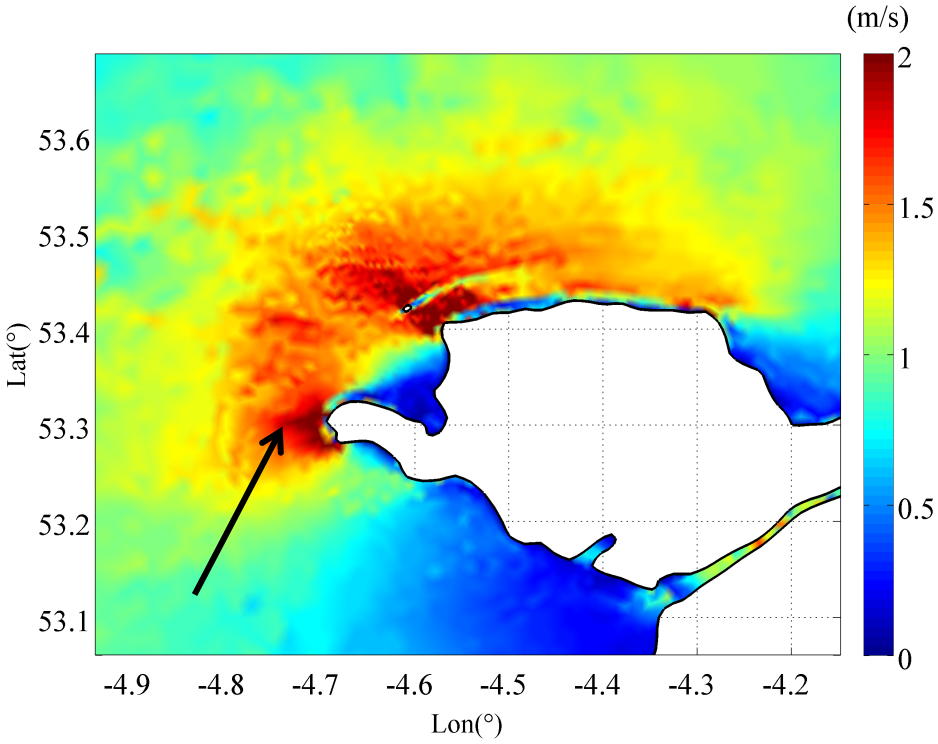

Figure 5.5 – Natural velocity flow field during a flood tide occurring around the Anglesey Skerries. The arrow indicates the flow direction.

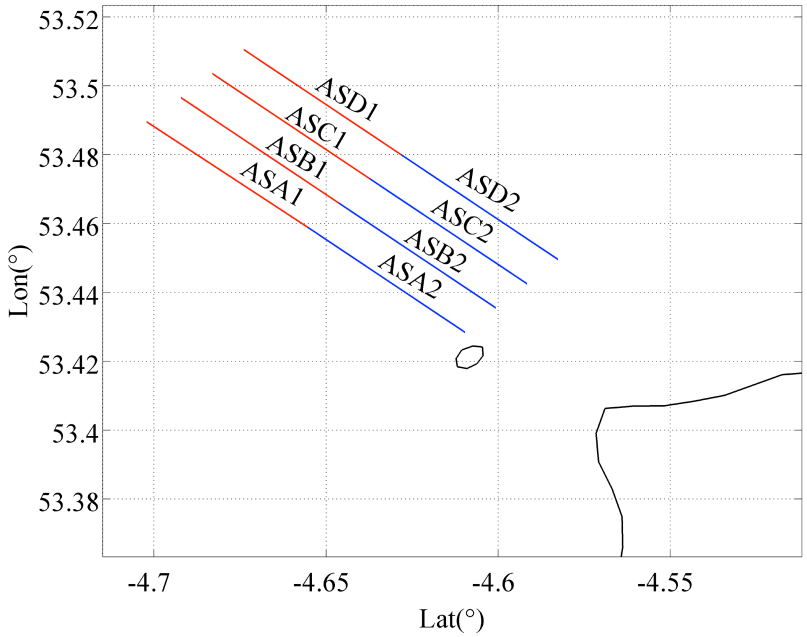

Figure 5.6 – Selected locations of tidal turbine arrays extending towards NE of the Anglesey Skerries.

The nomenclature for array configurations is based on the placement of the arrays in the SW-NE direction (ASA being the furthest SW and ASD the furthest NE) and how far the arrays are located away from the Anglesey coastline. Arrays that are further offshore are

labelled as Region 1, and those closer to the Skerries as Region 2. Each array has a total length of 4.5 km and is placed approximately 1 km apart from the next array. The arrays are located in regions with varying depths. The model mesh is discretisation is 200 m at finest in the area of the turbine arrays (the structural mesh), which is relatively coarse to capture by-pass flow mixing with the array wake. However, the power calculations are conducted within LMADT sub-grid solution that accounts for the local upstream flow velocity, the power calculations are not significantly affected by this scale of mixing. It should also be noted that resolving the array scale mixing is beyond the scope of this project.

Array	Blockage (B)	Optimum α_4	$P_{\text{available}}$ (MW)	$P_{\text{extracted}}$ (MW)	Power per swept area (kW/m^2)	$h_{average}$ (m)
ASA1	0.1	0.35	12.7	20.5	0.509	55.4
	0.3	0.37	54.7	97.7	0.731	
	0.5	0.46	124.3	211.3	0.997	
ASB1	0.1	0.35	11.3	18.1	0.436	57.5
	0.3	0.37	48.6	87.4	0.626	
	0.5	0.45	112	192.9	0.865	
ASC1	0.1	0.35	10.9	17.5	0.441	54.9
	0.3	0.37	46.5	83.1	0.627	
	0.5	0.46	106.3	181.5	0.860	
ASD1	0.1	0.35	10.6	17.1	0.442	53.3
	0.3	0.37	45	80.4	0.625	
	0.5	0.46	101.9	172.1	0.849	
ASA2	0.1	0.35	17.2	27.7	1.054	36.3
	0.3	0.39	70	122	1.430	
	0.5	0.50	145.3	230.1	1.781	
ASB2	0.1	0.35	16.6	26.8	0.976	37.8
	0.3	0.39	67.3	116.6	1.319	
	0.5	0.49	139.8	222.8	1.644	
ASC2	0.1	0.35	13.5	21.8	0.689	43.6
	0.3	0.39	57.1	99.9	0.971	
	0.5	0.48	124.5	202.5	1.270	
ASD2	0.1	0.35	12.1	19.6	0.570	47.2
	0.3	0.38	51.7	91	0.812	
	0.5	0.46	116	195.9	1.093	

Table 5.2 - Power values obtained for individual tidal arrays using different blockage ratios at optimum wake velocity coefficients.

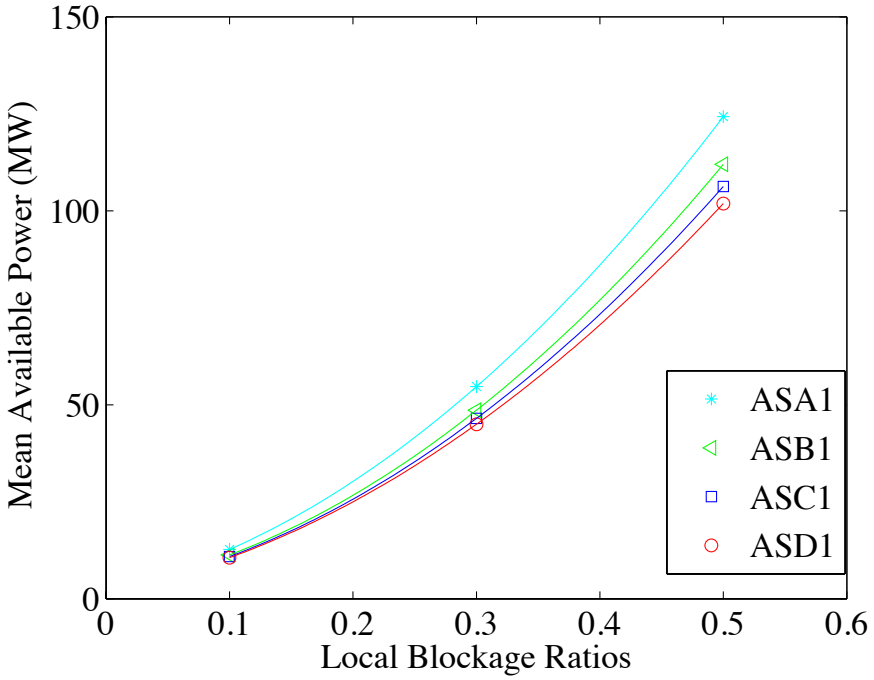

Figure 5.7 – Maximum available power as a function of blockage ratio for the arrays located in Region 1.

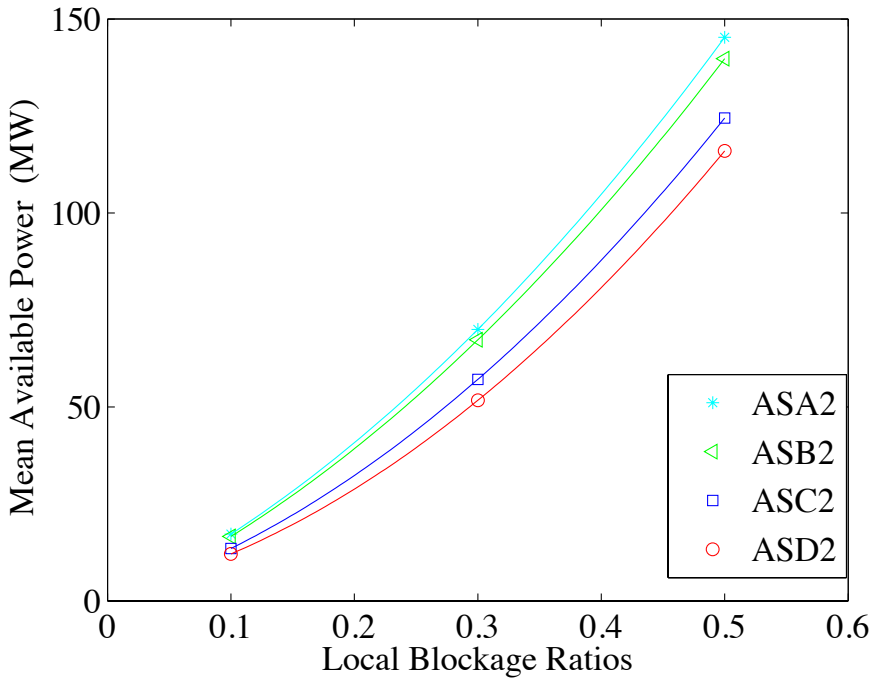

Figure 5.8 – Maximum available power as a function of blockage ratio for the arrays located in Region 2.

From Table 5.2, it can be seen that the mean depths in Region 1 are greater than in Region 2. Hence, the arrays in Region 1 have a larger swept area of turbines compared to the turbines located in Region 2, when working with a specified local blockage ratio. Table 5.2 summarises the maximum available power, the total power extracted and the power per swept

areas from the sites and for different blockage ratios, obtained for the optimum wake velocity coefficients. In the table, it is evident that arrays placed closer to the Skerries (Figure 5.8) extract more power when compared to arrays deployed further offshore (Figure 5.7).

Despite the fact that the turbines in Region 2 have smaller swept areas, they produce considerably more power than the turbines in Region 1. This difference can be shown by calculating the power produced per swept area, which is a metric introduced by Adcock *et al.* (2013). An example for this can be given by focusing on ASA1 and ASA2 turbine arrays. For a high blockage test case (B = 0.5), the power per swept area for ASA1 array is 0.997 kW/m^2, whereas this value is 1.781 kW/m^2 in ASA2. A similar relationship is observed for other arrays located in different regions when using fixed blockage ratios.

5.3.2. Array Connectivity

This section examines the effect of multiple array deployment on array performance. Studies such as that of Adcock *et al* (2013) have shown that there is significant interaction between multiple rows of arrays installed at a given site. Herein, the effect of array connectivity on the available power is investigated. This section considers two main configurations: series and parallel. The arrays that are connected in series refer to adding extra rows of array downstream of the initial tidal turbine array, whereas the parallel connection refers to extending the length of the array by adding more turbines within a turbine fence. The analogy adapted herein considers the flow and not the geographical locations of the array placements.

It should be noted that for the by-pass flow to fully mix with the wake flow before entering the secondary array (in terms of series configurations), the arrays should be deployed further apart from each other more than 1 km as studied in this section. The distance required for the by-pass flow to fully mix with the array wake is in the order of the array width (Nishino and Willden, 2012b). However, areas feasible for tidal turbine array deployments are rather small, thus the arrays need to be placed fairly close to each other. This, in turn, results in an increased amount of array thrust applied to the flow, which inevitably reduces the mass flux entering the arrays while enhances the flow diversion at the ends of the arrays. Following the same methodology for computing the maximum available and extracted power values as explained previously, Table 5.3 and Table 5.4 list the results obtained from parallel (e.g.

ASA1+ASA2) and series (e.g. ASA2+ASB2) array deployments respectively. Both tables consider the maximum available and extracted power values obtained for different blockage ratios using optimum α_4 values.

Array Configuration	Blockage	Optimum α_4	$P_{available}$ (MW)	$P_{extracted}$ (MW)	Economic Gain
ASA1 + ASA2	0.1	0.35	30.2	48.7	1.010
	0.3	0.38	130.8	232.5	1.049
	0.5	0.46	301.2	517	1.117
ASB1 + ASB2	0.1	0.35	28.1	45.1	1.007
	0.3	0.37	121.8	219.7	1.051
	0.5	0.45	284.5	494.8	1.130
ASC1 + ASC2	0.1	0.35	24.6	39.7	1.008
	0.3	0.37	108.4	196.7	1.046
	0.5	0.44	260.3	461.3	1.128
ASD1 + ASD2	0.1	0.35	22.9	37	1.009
	0.3	0.36	101.4	185.2	1.049
	0.5	0.44	245.2	434.3	1.125

Table 5.3 - Maximum available power estimates for parallel array configurations for various blockage ratios.

Array Configuration	Blockage	Optimum α_4	$P_{available}$ (MW)	$P_{extracted}$ (MW)	Economic Gain
ASA2 + ASB2	0.1	0.35	32.4	52.3	0.959
	0.3	0.44	114.6	183.1	0.835
	0.5	0.58	199.1	280.2	0.698
ASA2 + ASC2	0.1	0.35	29.8	48.1	0.971
	0.3	0.42	110.4	181.7	0.869
	0.5	0.56	199.9	289	0.741
ASA2 + ASD2	0.1	0.35	28.7	46.2	0.980
	0.3	0.41	109.6	182.4	0.901
	0.5	0.54	205.6	305.7	0.787
ASA2 +ASB2 +ASC2+ASD2	0.1	0.36	54.2	86.2	0.912
	0.3	0.48	167.9	253.1	0.682
	0.5	0.64	257	337.6	0.489

Table 5.4 - Maximum available power estimates for series array configurations for various blockage ratios.

Economic gain presented in Table 5.3 and Table 5.4 corresponds to the ratio of power extracted by a specific turbine array configuration (parallel or series) to the sum of the power

values obtained from individual arrays concerned in isolation. For instance, considering a series array configuration, ASA2+ASB2, using a high blockage case ($B = 0.5$), the economic gain is computed by dividing 199.1 MW (see Table 5.4) to the sum of 145.3 MW and 139.8 MW (see Table 5.2). In this case, the computed economic gain for the ASA2+ASB2 series array configuration is 0.698. The result indicates that there is approximately 30% loss in available power when ASA2 and ASB2 arrays are deployed in series.

Interpreting the results with respect to the array combinations, it is observed that connecting the arrays in parallel is more advantageous, especially when operating the arrays using high blockage ratios. The power available to the turbines in parallel connection is higher than the sum of the two arrays installed in isolation. An example can be given by focusing on the ASA arrays using a high blockage case ($B = 0.5$). When the individual available power values are summed, the total power is found to be 269.6 MW, whereas Table 5.3 shows that this is an underestimate of the actual value. For the ASA1+ASA2 configuration, the available power is 301.2 MW. There is approximately 12% power gain above the sum of the two individual array configurations. This percentage gain diminishes with decreasing blockage ratio because less thrust is applied to the flow. As an example, the ASB tidal array site is considered. Operating ASB1 and ASB2 arrays in parallel using a low blockage ratio ($B = 0.1$) while using the optimum α_4, the available power is computed as 28.1 MW (Table 5.3). However, operating only ASB2 array with a blockage ratio of 0.3 delivers 67.3 MW, which is more than twice the amount of power that can be generated by operating ASB1+ASB2 arrays in parallel with a lower blockage ratio ($B = 0.1$).

For arrays connected in series, the available power is reduced significantly with increasing blockage ratio mostly due to the high thrust applied to the flow by the turbine array that causes the flow to divert around the edges of the array. It should also be acknowledged that the total thrust applied to the flow by the series array configuration ultimately changes the flow regime within the area of interest, where a reduction in the flow is observed (Vennell, 2012). This implies a reduction in the total available power (Vennell, 2012; Vogel, 2012). Consider deploying the ASA2 and ASB2 arrays in series for $B = 0.5$. In this case, the sum of individual available power outputs is 285 MW whereas the maximum available power is computed to be 199 MW. The economic gain, explained earlier, shows that the ASA2+ASB2

array configuration in series deliver less power than the sum of the two arrays installed in isolation. This is another manifestation of the altered flow regime due to the high array drag applied to the flow. Noting that the arrays are deployed at a headland site, the flow is free to divert at the edges of the array, reducing the available energy to the turbines.

Although the flow regime is altered due to the deployment of arrays in series, it is observed that there is an increase in the available power when they are placed further apart from each other. In Table 5.4, the economic gain for ASA2+ASB2 array is 0.698 when using a high blockage ratio. This value is increased to 0.741 when the distance between the two arrays is doubled (i.e. ASA2+ASC2 array configuration). The economic gain is further increased by 5% when the distance between a two-array series configuration is at a maximum as in ASA2+ASD2 tidal farm. From these results, it is seen that even if there is an increment in the total available power when the arrays are placed away from each other, there is always a reduction in the available power extracted by the arrays deployed in series due to the increased array drag applied to the flow.

When operating the arrays in series using a low blockage ratio, the observed gain is less significant. Using the same array configurations, Table 5.4 presents that for a low blockage ratio of 0.1, the economic gain for ASA2+ASB2 array is 0.959, whereas this value is 0.971 for ASA2+ASC2 array configuration. The ASA2+ASD2 arrays provide a slightly higher economic gain, which is 0.980. It is evident that by increasing the distance between the arrays deployed in series, an increase in power extracted by the latter array increases due to greater mixing of the array flow with the bypass flow.

Similar to the findings from the parallel array configuration, it is observed that the percentage gain diminishes with decreasing blockage ratio. An example to such a scenario can be given by analysing the economic efficiencies of the ASA2+ASB2+ASC2+ASD2 series array configuration and the ASA2 individual array. The series array setting considers all the proposed array locations in Region 2, which constitutes a total array length of 18 km. Operating these arrays in series with a low blockage ratio ($B = 0.1$) delivers 54.2 MW in total (see Table 5.4), whereas a single array, ASA2 in this case, with an array length of 4.5 km would provide 70 MW when operating the array using a higher blockage ratio of 0.3 (see Table 5.2).

Overall, it is possible to deduce that for a highly blocked flow where a large thrust is applied, it is more advantageous to put the arrays in parallel than in series. However, for a low blockage case, as the disturbance to the flow field is reduced; the penalty from placing turbines in series is less severe. In general, arrays interact constructively when connected in parallel, and destructively when deployed in series.

5.4. Effects of Tidal Turbine Arrays in the Local Flow Field

One of the main objectives of this thesis is to evaluate the change in the flow field in the presence of tidal devices. A detailed analysis focusing on the hydrodynamic effects of installing tidal turbine arrays is presented in Chapter 7. However, this section provides some insight on how the local velocity flow field is affected due to the presence of the tidal arrays.

Local to the turbines, there will be a significant change to the flow field with increased flow between turbines that mixes with the slower moving flow, which has passed through the rotor plane downstream of the turbines (Vogel *et al.*, 2013). This complex mixing process cannot be modelled accurately with a depth-integrated model (Adcock *et al*., 2013). In the present model, this intra-turbine mixing is accounted for in the sub-grid scale model using linear momentum actuator disk theory (LMADT). Even though the model does not consider the change to the flow field around an individual turbine directly, large-scale changes due to the operation of an array of turbines can be estimated. The change in the local velocity flow field is investigated by considering a high blockage case (B = 0.5) using the optimum wake velocity coefficients computed for a parallel array configuration (ASA1 + ASA2) and a series configuration (ASA2 + ASB2 + ASC2 + ASD2). For both test cases, once the arrays are installed, the flow bypasses the arrays, mainly on the offshore side of the Skerries.

Figure 5.9 and Figure 5.10 show snapshots of the flow field in the presence of parallel and series array configurations respectively. From the figures, it is evident that the arrays provide additional resistance to the flow. Downstream of the arrays, the velocity magnitude decreases significantly due to the power extraction.

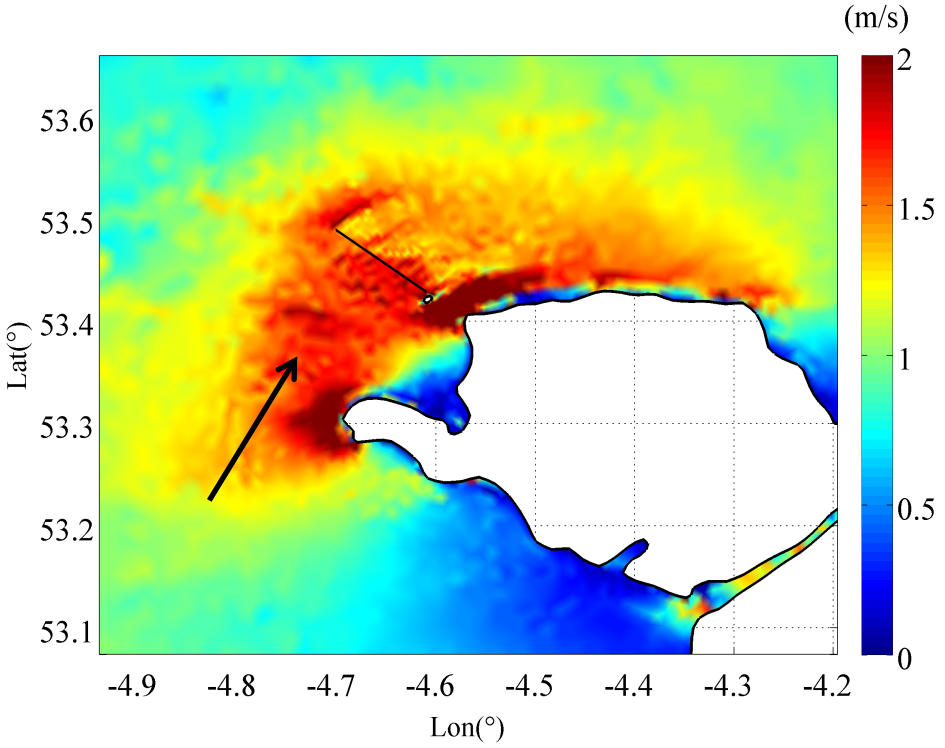

Figure 5.9 – Current velocity plot for a parallel tidal array (ASA1 + ASA2) deployment around the Anglesey Skerries using a blockage ratio of 0.5. The arrow indicates the flow direction.

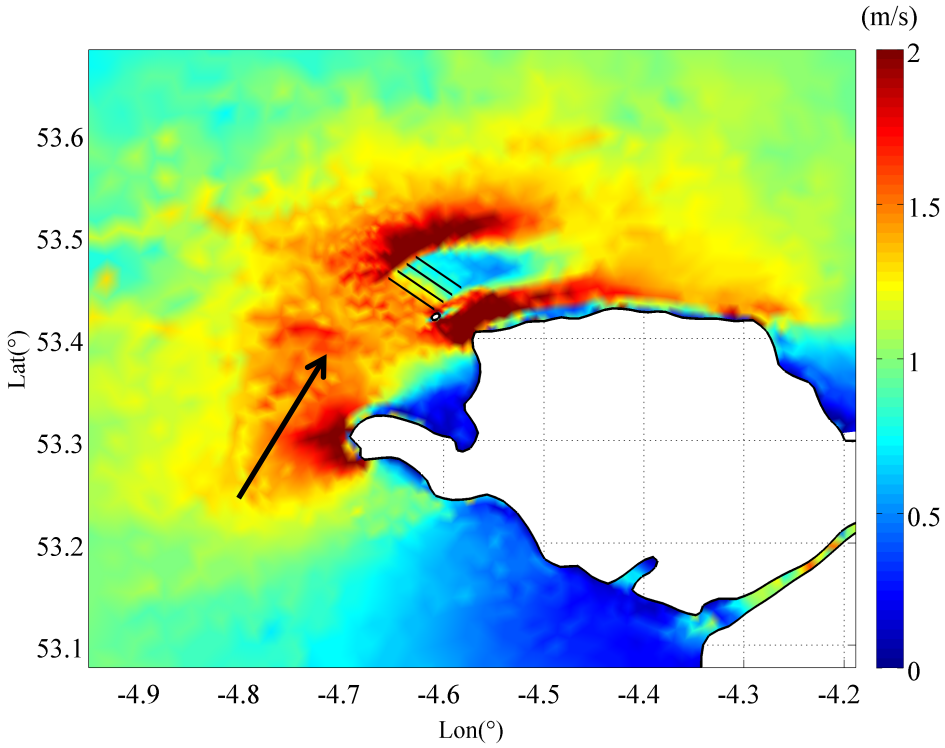

Figure 5.10 – Current velocity plot for a series tidal array (ASA2 + ASB2 + ASC2 + ASD2) deployment around the Anglesey Skerries using a blockage ratio of 0.5. The arrow indicates the flow direction.

Figure 5.11 and Figure 5.12 plot the difference between the natural flow field illustrated in Figure 5.5 with the velocity flow fields when ASA1+ASA2 parallel array (see Figure 5.9) and ASA2+ASB2+ASC2+ASD2 series array (see Figure 5.10) are operating respectively. From the figures, it can be seen that the flow diversion is not symmetric. The bypass flow is enhanced significantly towards further offshore of the Irish Sea when a parallel array configuration is deployed using a high blockage ratio (Figure 5.11). Figure 5.12 shows the change in the local flow field due to the deployment of four rows of arrays connected in series using a high blockage ratio. From the figure it is seen that the bypass flow towards the ocean side is similarly more enhanced than in the Skerries region. The flow diversion indicates that the available power is restricted with respect to the thrust applied to the flow in a partially blocked flow regime (Draper *et al.*, 2013).

As discussed in Section 5.3.1, the Anglesey Skerries is a headland site, in which the flow is unbounded towards the offshore of the Irish Sea. At a headland site such as the Anglesey Skerries, when an additional resistance to the flow is introduced, as in deploying an array of tidal turbines, the flow is free to bypass the array by diverting towards the ocean side (see Figure 5.9 and Figure 5.10). This behaviour inevitably results in a reduction in the mass flux through the arrays, which ultimately limits the power available to the turbines (Vogel *et al.*, 2013). The study conducted herein shows that this observed diversion is significant when higher blockage ratios are used to define the turbine operating conditions. When the effect of array connectivity is concerned, it is seen that increasing the thrust applied to the flow by additional tidal arrays (i.e. arrays deployed in series) results in significantly reduced flow velocities (see Figure 5.12). This in turn has an adverse effect on the performance of all the turbines within the array.

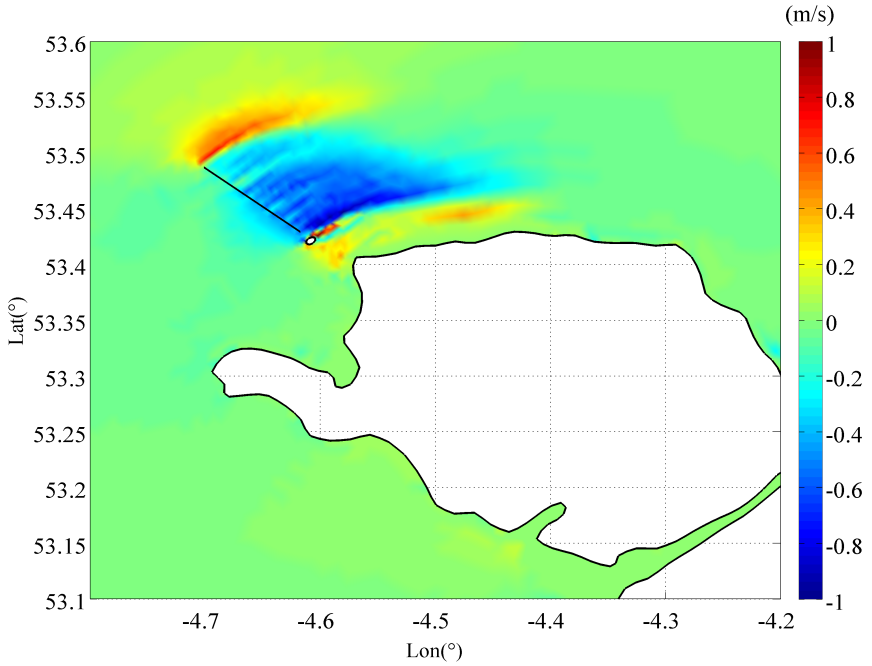

Figure 5.11 – Change in the velocity flow field with respect to the deployment of tidal arrays ASA1 + ASA2 in the vicinity of the Skerries using a blockage ratio of 0.5.

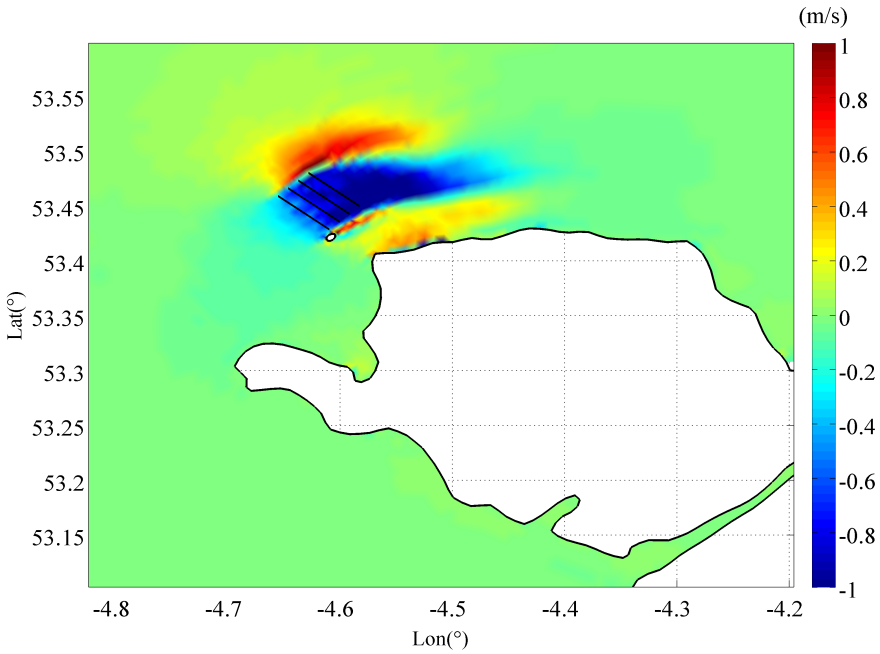

Figure 5.12 – Change in the velocity flow field with respect to the deployment of tidal arrays ASA2 + ASB2 + ASC2 + ASD2 in the vicinity of the Skerries using a blockage ratio of 0.5.

5.5. Conclusions

The presence of turbine arrays has been included in a validated discontinuous Galerkin tidal flow model by means of a line sink of momentum (following Draper, 2011). The associated

momentum sink is controlled by the upstream flow condition, blockage ratio and wake velocity coefficient. A parametric study has considered the effects of array operating conditions, array location, and array configuration in series or in parallel for sites off the Anglesey Skerries.

The model simulations indicate that relative to the arrays placed in Region 1, the arrays deployed in Region 2 delivers more power (see Figure 5.6). Taking the tidal array site ASA (see Figure 5.6) as an example, comparing the available power extracted by using only ASA1 and only ASA2 (see Table 5.2) shows that ASA2 array always delivers greater power for the studied blockage ratios. ASA2 array provides approximately 26% more power when using a low blockage ($B = 0.1$). However, this gain diminishes with increasing blockage ratio. Using a high blockage ($B = 0.5$), ASA2 array provides only 14% more power than ASA1 array. This is another manifestation of the flow diversion limiting the available power. Another result obtained from the analysis considering the array locations, is that the turbines closer to the Skerries is more effective in delivering power. This case can be explained by comparing the available power extracted by the ASA2 array (closest to the Skerries) and the ASD2 array (furthest from the Skerries). This comparison shows that ASA2 array delivers more power than ASD2 array for all blockage ratios studied. When a low blockage is defined ($B = 0.1$), the ASA2 array delivers approximately 30% more power than ASD2 array, however, this observed gain is decreased when the blockage is increased. Considering the case when the blockage is set to 0.5, the ASA2 array delivers 145.3 MW, which is only ~20% more than what ASD2 array would provide. This result again shows that increasing the thrust applied to the flow by increasing the blockage of the turbines, results in the flow to divert around the edges of the arrays, which inevitably limits the power extracted by the turbines.

Regarding the connectivity of the arrays, for high blockage ratios, it is seen that extending the length of an array further offshore (parallel connectivity) is more effective than placing arrays in series. For blockage ratio 0.5 comparing the economic gain computed for parallel arrays (Table 5.3) with the series arrays (Table 5.4) shows that there is an increase of ~13% available power when using parallel arrays. However, there is a considerable power loss when the arrays are connected in series. Using the economic gain parameter, it is seen that for two rows of arrays connected in series, the available power is decreased by approximately 30%.

However, when four rows of arrays are deployed in series using a high blockage ratio, the economic gain is further reduced to 0.49 indicating 51% loss in the available power. For low blockage ratios, however, as the local flow field is less disturbed the turbines perform better, which in turn increases the economic gain of the overall array configuration. It should also be acknowledged that increasing the distance between two arrays allows for a greater array-scale wake recovery, which enhances the performance of the secondary arrays.

The bypass flow is found to be greater on the offshore side than regions closer to the Skerries. This result agrees well with the findings of an idealised headland case studied by Draper *et al.* (2013). The turbine array configurations studied in this analysis block the flow partially, which in turn increases the by-pass flow around the edges of the arrays. As the blockage ratio increases, the amount of the by-pass flow increases due to the high thrust applied to the flow.

Chapter 6

Tidal Stream Farm Deployment - II: Bristol Channel

The Bristol Channel is located in the south-west coasts of the UK. The Severn Estuary is situated at the upper reaches of the Bristol Channel, which has one of the largest tidal ranges worldwide. At spring tides, the Severn Estuary has a peak tidal range of approximately 14 m. For this reason, the Bristol Channel, especially the Severn Estuary, has been considered as a possible tidal barrage site for over a century. However, constructing a barrage across the Severn Estuary requires high capital costs and would alter the environment adversely. An alternative way to exploit the tides in the Bristol Channel is to deploy tidal stream arrays. The parametric study conducted herein intends to evaluate an upper bound for the tidal stream power resource of the Bristol Channel. Due to the resonant nature of the Channel, modelling of the region requires special attention. Thus, a two-dimensional model is constructed that extends to the UK continental shelf including the Celtic Sea and the Irish Sea (see Chapter 4 for model details).

The present chapter includes a literature review (Section 6.1) on tidal hydrodynamics of the Bristol Channel and presents preliminary results (see Section 6.1.2) for investigating the response curve of the Bristol Channel for the undisturbed flow field. Section 6.2 summarises the proposed tidal turbine schemes to exploit the tidal currents in the Bristol Channel. Section 6.3 presents the parametric study to evaluate the maximum available power that can be extracted from the site using different turbine operating conditions, for various array locations and configurations. The methodology used in the calculations was described in Chapter 5. Section 6.4 explains the effect of installing turbine arrays to the local flow field. Section 6.5 presents the conclusions.

6.1. Tidal Hydrodynamics of the Bristol Channel

This section evaluates the general tidal hydrodynamics observed in the Bristol Channel and the Celtic Sea, which connects the Channel to the Atlantic Ocean.

A previous study focusing on the Bristol Channel emphasises that the circulation in the Channel, as well as the Irish Sea, is mainly due to tidal movements (Uncles, 1983). The same study indicates that semi-diurnal tides are predominant in the region, in which the principal lunar (M_2) tide is representative of an average tidal cycle. The secondary tidal constituent is the principal solar (S_2) tide, which is approximately 35% of the M_2 tides regarding both the elevations and currents. When the M_2 tidal elevations are concerned, it is observed that the M_2 tides increase rapidly from 2.67 m around the Lundy Island to 4.22 m at Avonmouth (see e.g. Table 4.12). The corresponding phases increase from 160° to 200°, indicating approximately 1.3 hours of difference in the times of the high water across the Bristol Channel. The daily variations of the overall tidal amplitudes are caused by the K_1 and O_1 tides (Uncles, 1983). However, these tidal constituents contribute to the overall tidal elevations by relatively small ratios. In this respect, the parametric study conducted in this chapter only considers the M_2 tides as it is the major tidal constituent in the Bristol Channel.

Considering the M_2 tidal movement, Bowden (1955) explains that the M_2 tides move progressively from the Celtic Sea to the Irish Sea. The phase difference ($\Delta\varphi$) between the water levels (φ_ζ) and the currents (φ_c) indicate whether a tidal wave is progressive ($\Delta\varphi = 0$), standing ($\Delta\varphi = 90$) or a combination of both (partially progressive and partially standing) (Pugh, 1987; Uncles, 1981). When the phase difference between the elevations and currents ($\Delta\varphi$) is considered, Uncles (1981) explains that in the Bristol Channel the interference of the incoming and reflected waves results in a partially progressive wave with $\Delta\varphi$ that is close to a standing wave. In such a partially progressive wave system, the flood tides are often faster than ebb tides and the slack water occurs within a short period of time after high water (Bowers and Al-Barakati, 1997).

The harmonic analysis of the M_2 currents is presented in Chapter 4 for model validation purposes. Figure 6.1 plots the predicted M_2 semi-major axes in the Bristol Channel. From the figure it is seen that, the M_2 semi-major axes line almost parallel from the Lundy Island to the centre of the Channel. These results agree well with results presented in Uncles (1983). The magnitude of the M_2 semi-major currents increases from 0.5 m/s observed at the entrance of the Channel to approximately 1.5 m/s observed at the mid-Channel region from Minehead to Barry. The current magnitudes are magnified near the headland sites.

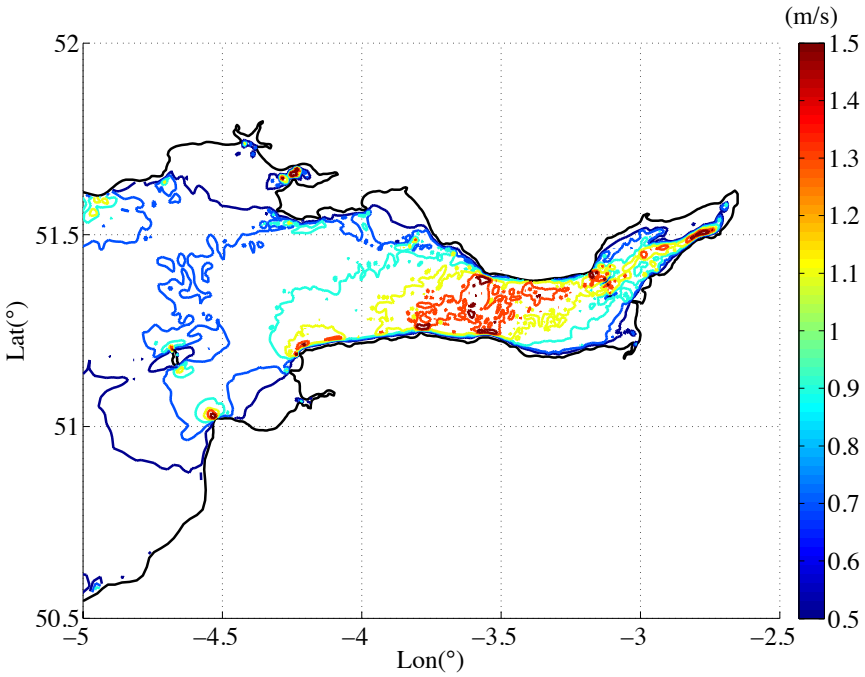

Figure 6.1 – Computed M_2 semi-major axes (magnitude in m/s).

An asymmetry is reported between the flood and ebb tides, which is due to the presence of higher harmonics in the system (Uncles, 1981; Uncles, 1983). Two of the most important quarter-diurnal tides in the Bristol Channel are reported to be the M_4 and MS_4 tides (Uncles, 1983). Among these, M_4 tides are naturally included in the shallow water models by including non-linear friction terms (Prandle, 1980).

Overall, the semi-diurnal tides observed in the Bristol Channel are one of the largest in the world, with a mean tidal range of 12.2 m at spring tides and 6.0 m at neap tides (Neill *et al.*, 2009; Robinson, 1980; Heath, 1981). In the literature, there are two main mechanisms mentioned that contribute to the large tidal ranges and fast currents observed in the Bristol Channel and the Severn Estuary (Xia *et al.*, 2012). These mechanisms are the resonance of the Channel with the incoming Atlantic tidal wave (Fong and Heaps, 1978) and the funnelling effect due to the wedge-shaped geometry of the Channel (Taylor, 1921; Robinson, 1980).

6.1.1. Funnelling Effect

In an earlier study, Robinson (1980) explains that the wedge-shaped topography of the Bristol Channel plays an important role in concentrating the tidal energy. In the same study, it is indicated that the resonance of the system results in large tidal ranges, which are further amplified by the funnelling effect at the mouth of the estuary. The funnelling effect observed

in the Bristol Channel was first analysed by Taylor (1921). Using a simple model based on the linear frictionless one-dimensional equations of motion, Taylor (1921) demonstrated the tidal variation along the Bristol Channel. The Channel was characterised as a wedge-shaped estuary with linearly varying width and depth. Robinson (1980) discusses that Taylor's model did not account for energy dissipation due to friction, and thus demonstrated a standing wave where there was no net energy transport. The results obtained by Taylor's simple wedge-shaped model were found to satisfactorily represent the funnelling effect observed in the Channel and to estimate the tidal elevations. However, due to the standing wave character of the model, the phase lag and energy transport along the Channel were not included (Robinson, 1980). These are fundamentally important parameters in order to understand real tidal dynamics observed in the region.

To estimate the available power from a particular barrage design, Robinson (1978) applied a similar approach based on a one-dimensional frictionless analytical model, forced with single frequency tidal oscillation in a wedge-shaped estuary. However, investigating the actual tidal dynamics of the system was also beyond the scope of this analysis. Therefore, an accurate representation of the naturally occurring tides in the Bristol Channel to estimate the potential power was not established with these earlier analytical models. In this thesis, a numerical model has been constructed, which represents the coastline and the bathymetry of the Bristol Channel with greater accuracy, thus naturally involves the funnelling effect in the calculations.

6.1.2. Resonance Effect

In the literature, it is acknowledged that the large tidal elevation amplitudes observed in the upper reaches of the Bristol Channel are due to the quarter wavelength resonance of the Channel with the North Atlantic tidal wave (Flather, 1976; Fong and Heaps, 1978; Robinson, 1980; Pugh, 1987). An indicator of this resonance is the energy that is transmitted by the Atlantic tidal wave through the Celtic Sea into the Bristol Channel (Flather, 1976; Fong and Heaps, 1978; Robinson, 1980). To investigate the possible resonance in the system, Fong and Heaps (1978) first consider the amplification of the main semi-diurnal tidal constituents (K_2, S_2, M_2, N_2, K_1) magnitudes from the Atlantic continental shelf to the Celtic Sea into the Bristol Channel. Their results show that the magnitudes of the semi-diurnal constituents are

increased approximately four times from the outer continental shelf to the Severn Estuary (Avonmouth). In their study, Fong and Heaps (1978) found that the possible resonance is not only dependent on the length of the Channel but also on the resonant period. Their results show that the resonant period of the Bristol Channel is close to that of the semi-diurnal tidal band (see Table 6.1). Fong and Heaps (1978) present a summary of the significant numerical studies conducted to estimate the resonant period of the Bristol Channel/Celtic Sea system. Table 6.1 is an extended version of the aforementioned summary. The analyses summarised in Table 6.1 include different domain areas to estimate the resonant period of the Celtic Sea. Fong and Heaps (1978) provides a summary of the previous studies listed in Table 6.1. In this thesis, the important conclusions from this summary are discussed.

Model	Areas Included			Fundamental Period (hours)	ω/ω_{M2}
	Ocean	Celtic Sea	Bristol Channel		
Rectangular shelf (Heaps, 1965)	No	Yes	No	10.21	1.22
Shelf with sloping bottom (Flather, 1972)	No	Yes	No	9.82	1.26
Shelf and ocean with rectangular step topography (Flather, 1972)	Yes	Yes	No	11.87	1.05
Continental shelf: two-dimensional, numerical (Flather, 1976)	No	Yes	Yes	11.05	1.12
One-dimensional, numerical (Fong and Heaps, 1978)	No	Yes	Yes	12.2 – 12.6	0.98 – 1.02
Fitted response model to the semi-diurnal tidal constituents (Heath, 1981)	Yes	Yes	No	10.8 – 11.1	1.12 – 1.15

Table 6.1 Estimates of the fundamental seiche period of the Celtic Sea derived from various theoretical models (extended table taken from Fong and Heaps, 1978).

Comparing the results presented by Heaps (1965) and Flather (1972), it is seen that the resonant period is affected by the model boundaries. Both studies are analytical models, which consider the resonant period of the Celtic Sea. Heaps (1965) accounts for only the

Celtic Sea and ignores the ocean and the Bristol Channel. However, Flather uses two approximations, one of which involves just the Celtic Sea and the other both the ocean and the Celtic Sea. The results show that the resonant period of the Celtic Sea increases and approaches closer to the M_2 period when the ocean boundary is included in the analysis.

The study presented by Flather (1976) is a two-dimensional model, which includes the Coriolis force and the bed-friction term in the governing equations. The continental shelf boundary is set as a radiation boundary condition, which may influence the free periods and modes of the system (Fong and Heaps, 1978). Flather (1976) estimates the resonant period of the Celtic Sea as 11.05 hours, which is slightly less than the M_2 period. The one-dimensional numerical model used by Fong and Heaps (1978) considers the Bristol Channel – Celtic Sea area, which extends towards the European continental shelf. The model excludes the Irish Sea and the English Channel. However, including these regions in the model is of importance as the long-wave oscillations may influence the tidal response in the area. The numerical model by Fong and Heaps (1978) does not include the bed friction and the Coriolis force. The one-dimensional model results show that the resonant period of the Celtic Sea is between 12.2 – 12.6 hours, which is slightly higher than the other results presented, but still in the proximity of the M_2 period.

Heath (1981) presents a fitted response model to the semi-diurnal tidal constituents to estimate the resonant period of the Celtic Sea. The model is then used to analyse the resonant period of the Bristol Channel relative to the tides in the Celtic Sea. The estimated Celtic Sea resonant period is between 10.8 – 11.1 hours, which agrees well with previous estimates by Heaps (1965), Flather (1972) and Flather (1976). Heath (1981) estimates the resonant period of the Bristol Channel to be 7.3 – 9.0 hours.

It is important to understand the resonant behaviour of the Bristol Channel/Celtic Sea system, as one of the main objectives of this thesis is to estimate the maximum available power of the Bristol Channel. Considering the location of the arrays, it may be possible to further tune in the system (i.e. bring it closer to the resonance), which might result in extracting more energy. Thus, the two-dimensional unstructured model is employed to investigate further the resonance of the system. The model domain includes the European continental shelf, as well as the Irish Sea, Celtic Sea, and Bristol Channel (see Figure 6.2). A

quadratic bed friction coefficient of 0.0025 is used in the computations. Variable Coriolis force is also included in the solutions. The model validation is explained in Chapter 4 (see Section 4.5).

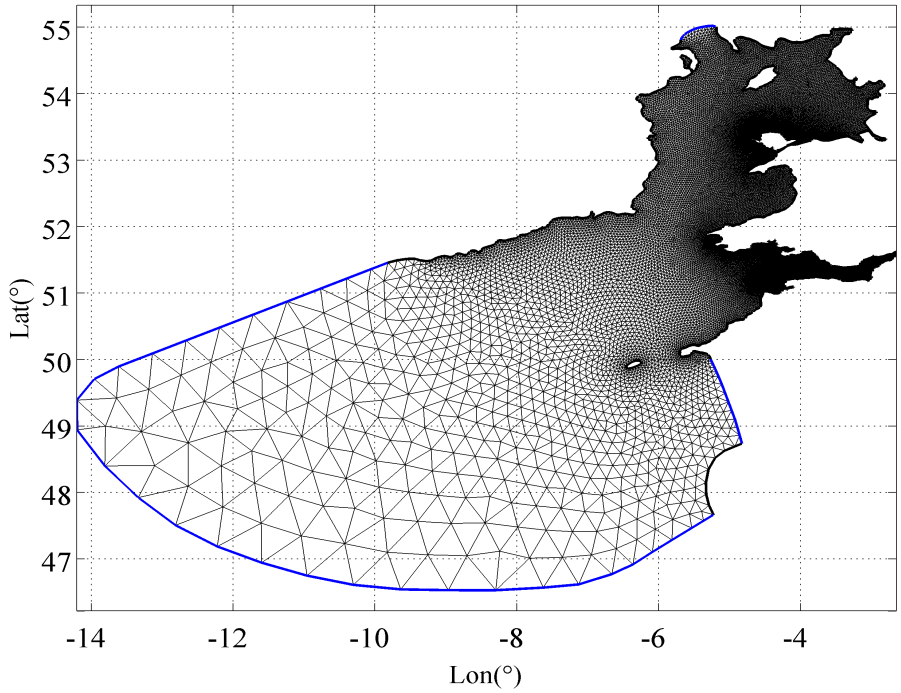

Figure 6.2 – Two-dimensional unstructured triangular model mesh. The model domain includes the Irish Sea, the Celtic Sea, and the Bristol Channel.

In this study, the response curve of the Bristol Channel has been investigated by exciting the model with a single tidal component (the M_2 tide), using various M_2 forcing frequencies that are artificially altered. In total, 24 M_2 frequencies are used to force the model. The ratios between the driving frequencies over the M_2 frequency (ω/ω_{M2}) vary between 0 and 5. However, the model is found to be unstable in case of decreasing the M_2 forcing frequency (increasing the wavelength of the tides). The instabilities occur in the vicinity of the English Channel entrance. When the forcing frequency is decreased, the model results show that the incoming and reflected waves build up on the shallower regions at the entrance of the English Channel, leading to extreme water levels. It is apparent that the waves with longer wavelength are not capable of propagating easily across the English Channel boundary. To overcome this problem, the model boundaries have been extended to include the English Channel to allow the long waves to propagate towards the North Sea. At the northern boundary, the model is

extended beyond the North Channel towards the Scottish Isles of Tiree and Coll including the north-west coasts of the Northern Ireland (see Figure 6.3).

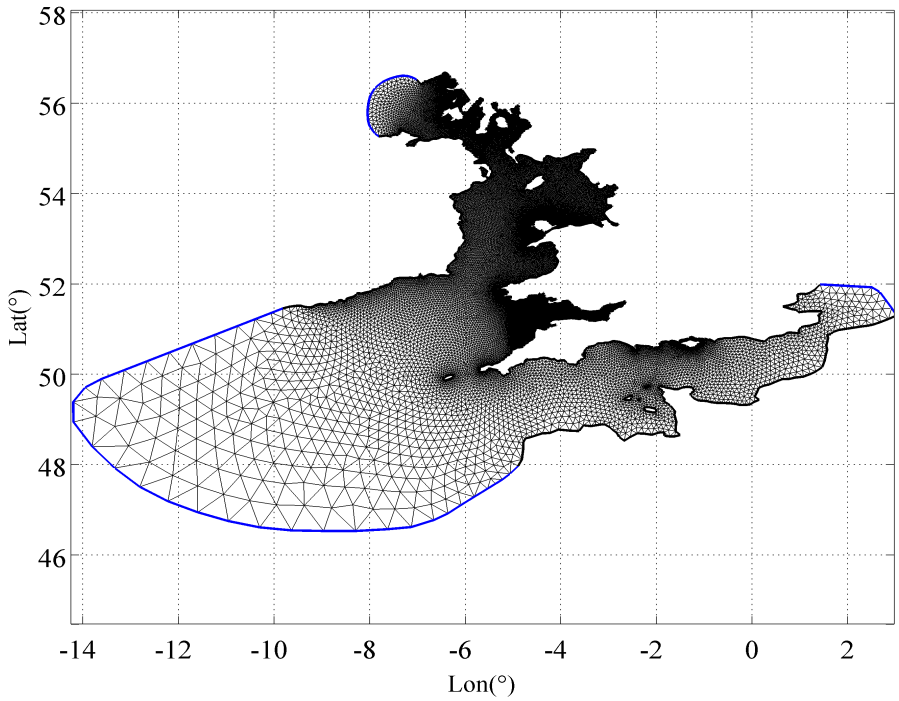

Figure 6.3 – Extended model mesh, which includes the English Channel on the eastern boundary. The northern boundary of the model is extended towards the Scottish Isles of Tiree and Coll and includes coasts of the Northern Ireland.

To calibrate the extended model, various bed friction coefficients (c_f) are used. Table 6.2 presents the comparison of the observed and computed M_2 tidal elevations at different stations obtained using different bed friction values. From the table, it is seen that the model using a bed friction coefficient, $c_f = 0.0025$ shows a good agreement with the observed data. At several stations a larger bed friction coefficient ($c_f = 0.00375$) shows better agreement with the observations, however, a compromise in selecting the optimum bed coefficient is needed as the whole system cannot be modelled by using a single bed friction coefficient value. Thus, the extended model presented in this section uses $c_f = 0.0025$.

A further validation is done against the M_2 currents. In Section 4.5.2 Tidal Currents, the previous model results are compared against the observations presented in Owen (1980). Similarly, the M_2 currents predicted by the extended model using a bed friction coefficient of 0.0025 are compared against the same dataset. The comparison of observed and calculated M_2 tidal current magnitudes and phases in east and north directions are presented in Table 6.3.

Table 6.4 provides a similar comparison between the observed and modelled M_2 tidal current magnitude amplitudes and overall directions.

Station	Amplitude (m)					Phase (°)				
	Obs.	$c_f(1)$	$c_f(2)$	$c_f(3)$	$c_f(4)$	Obs.	$c_f(1)$	$c_f(2)$	$c_f(3)$	$c_f(4)$
Milford Haven	2.22	2.36	2.23	2.14	2.07	173	166	174	179	183
Swansea	3.19	3.50	3.21	3.00	2.83	173	162	174	182	188
Port Talbot	3.13	3.52	3.23	3.02	2.84	173	162	174	182	187
Barry	3.82	4.37	3.97	3.65	3.37	185	167	183	195	203
Flat Holm	3.90	4.57	4.14	3.80	3.50	190	168	185	197	206
Steep Holm	3.87	4.52	4.10	3.77	3.48	186	166	183	195	205
Cardiff	4.01	4.64	4.20	3.85	3.55	191	169	187	199	208
Avonmouth	4.22	5.04	4.54	4.14	3.78	201	173	195	209	221
St. Thomas Head	4.25	4.74	4.28	3.92	3.61	194	168	186	199	209
Hinkley Point	3.80	4.45	4.05	3.72	3.44	185	164	180	192	201
Minehead	3.59	4.05	3.73	3.47	3.25	183	161	176	187	195
Ilfracombe	3.04	3.29	3.05	2.89	2.74	162	153	165	172	177
Appledore	2.57	2.84	2.61	2.45	2.33	165	158	170	177	183
Lundy	2.67	2.76	2.59	2.47	2.37	160	153	163	169	173
Newquay	2.24	2.45	2.29	2.19	2.11	142	138	146	150	154

Table 6.2 Comparison of the observed M_2 tidal elevations against model results using various bed friction coefficients; $c_f(1) = 0.00125$; $c_f(2) = 0.0025$; $c_f(3) = 0.00375$; and $c_f(4) = 0.005$. The simulation results that are closest to the observations are highlighted in grey.

For the North Lundy station, Table 6.3 shows that the estimated M_2 current magnitude in east-west direction is in excellent agreement. The north-south component is, however, overestimated by approximately 30%. The overall M_2 current magnitude at NL station is

approximately 3% in error with the observations (Table 6.4). Table 6.3 shows that the M_2 current phase results show a small discrepancy (~ 7%) in the east-west direction when compared to the observations. However, Table 6.4 shows that the current direction estimated by the model is only 2% in error with the observations. Overall, the model predictions are in good agreement with the observations at NL station.

Station	Observation				Model Results			
	East-West		North-South		East-West		North-South	
	Mag. (m/s)	Phase (°)	Mag. (m/s)	Phase (°)	Mag. (m/s)	Phase (°)	Mag. (m/s)	Phase (°)
North Lundy (NL)	0.64	87	0.13	126	0.64	81	0.19	126
Swansea Bay (SB)	0.80	93	0.13	283	0.88	90	0.18	276

Table 6.3 Comparison of observed and calculated M_2 tidal current magnitudes and phases in east and north directions.

Station	Observation		Model Results	
	Magnitude (m/s)	Direction (°)	Magnitude (m/s)	Direction (°)
North Lundy (NL)	0.65	153	0.67	150
Swansea Bay (SB)	0.81	298	0.90	290

Table 6.4 Comparison of observed and calculated M_2 tidal current magnitude amplitudes and overall directions.

Considering the Swansea Bay station, the extended model overestimates the M_2 current magnitudes in both directions. The computed error is 10% in the east-west direction (major direction) and approximately 40% in the north-south direction (Table 6.3). Table 6.4 shows that when the M_2 current amplitude is considered, the observed current is approximately 0.81 m/s and the model estimate is 0.90 m/s. Regarding the M_2 current phases, the model underestimates the phases by ~3% in both directions (see Table 6.3). Overall, the M_2 currents are underestimated by ~3% indicating a 16-minute delay (see Table 6.4). After calibrating and validating the extended model, the M_2 response curve is created by exciting the model with

various forcing frequencies. The M_2 elevations are recorded at 26 stations along the Bristol Channel (Figure 6.4) and at 21 stations across the entrance of the Channel (Figure 6.5).

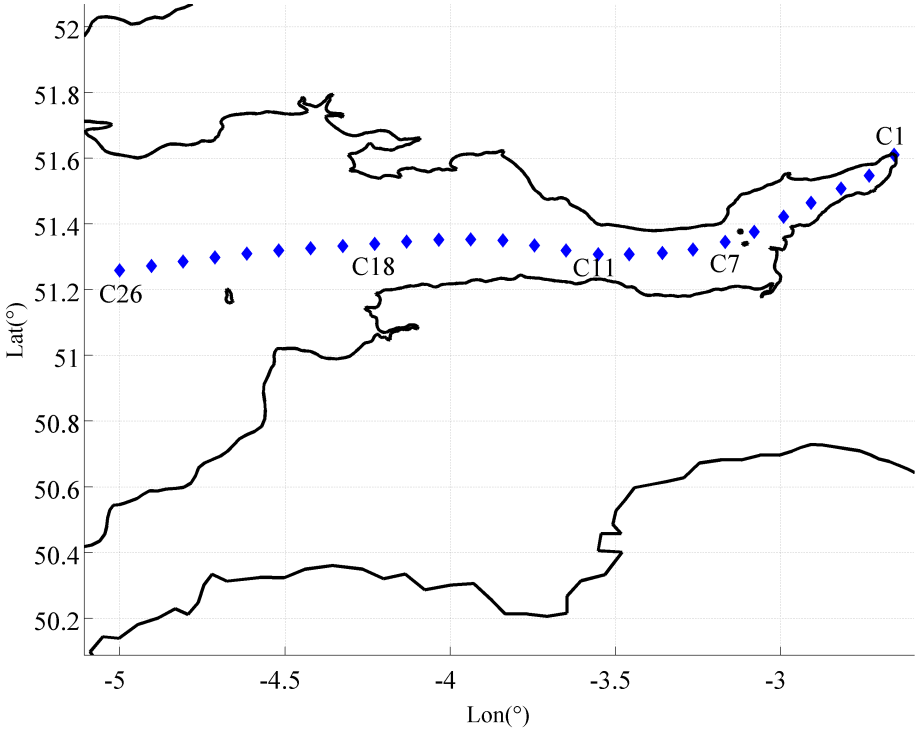

Figure 6.4 – The observation stations (illustrated as blue diamonds) along the Bristol Channel.

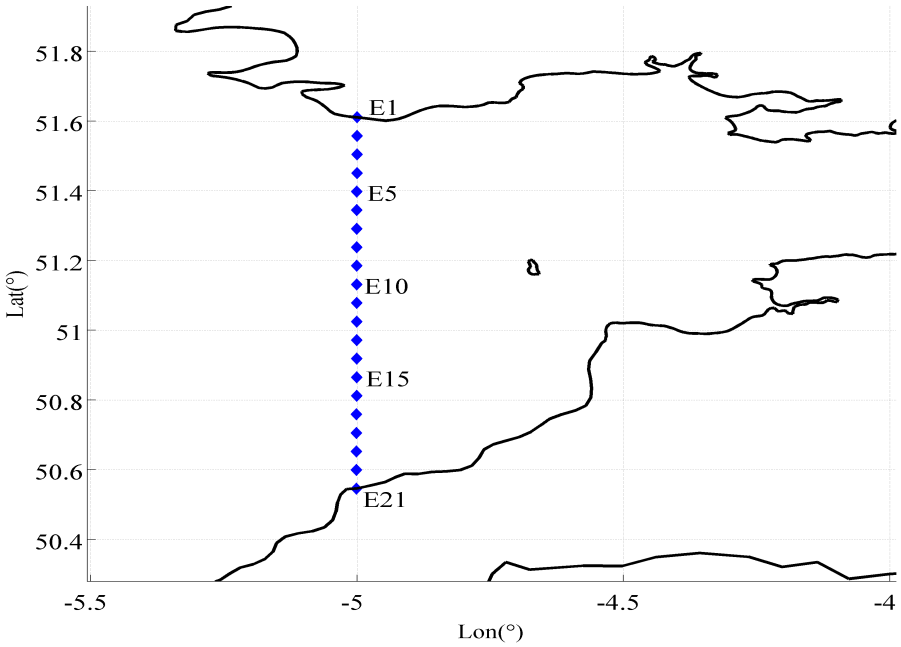

Figure 6.5 – The observation stations (illustrated as blue diamonds) at the entrance of the Bristol Channel.

The response curves of several stations taken along the Bristol Channel are plotted in Figure 6.6. Figure 6.7 shows a similar plot, which considers three stations across the entrance of the Channel. In Figure 6.6, it is seen that the response curves follow a similar pattern at all the stations considered, but differ in magnitude due to the location of the observation station. It is seen that when forcing the model with $\omega/\omega_{M2} = 2.5$, the response at the inner Channel (stations C4 and C7) decreases as the forcing frequency increases, whereas the response of the outer Channel (C11, C18 and C26) increases with increasing frequency. In Figure 6.7, the response at the entrance of the Bristol Channel is plotted. In this figure, it is seen that at the forcing frequencies of $\omega/\omega_{M2} = 2.5 - 3$ there is a slight increase in the response, which suggests a resonance occurring in the Celtic Sea at this frequency.

Both figures show a peak in response at approximately $\omega/\omega_{M2} = 1.1 - 1.2$ which indicates the quarter-wave length resonance of the system with a period of approximately 10.3 – 11.3 hours. This result is in good agreement with the previous research conducted on estimating the Celtic Sea resonant period. A second peak is observed in the system at $\omega/\omega_{M2} = 1.8$ - 2, which may be due to the half-wave resonance. However, when the model is excited with a lower frequency ($\omega/\omega_{M2} = 0.6$), a sudden drop occurs in the response curve. Bearing in mind the fact that, the tidal system is highly complex, there is no certain explanation why the response of the Bristol Channel drops at $\omega/\omega_{M2} = 0.6$. One possible explanation could be related to the quarter-wave length resonance has moved from the Bristol Channel towards the Irish Sea at this frequency.

Overall Figure 6.6 and Figure 6.7 suggest that the response of the Bristol Channel increases as the driving frequency increases. This result indicates that the Bristol Channel is shorter than the quarter-wavelength in the natural case thus reducing the tidal wavelength (increasing the forcing frequency), corresponds to greater response in the system. Considering the response of the system using the natural forcing frequency ($\omega/\omega_{M2} = 1.0$), it is seen that the Bristol Channel response stands on the left-hand side of the response curve plotted in Figure 6.6, which suggests that the basin length of the Bristol Channel is shorter than the quarter-wavelength required for resonance.

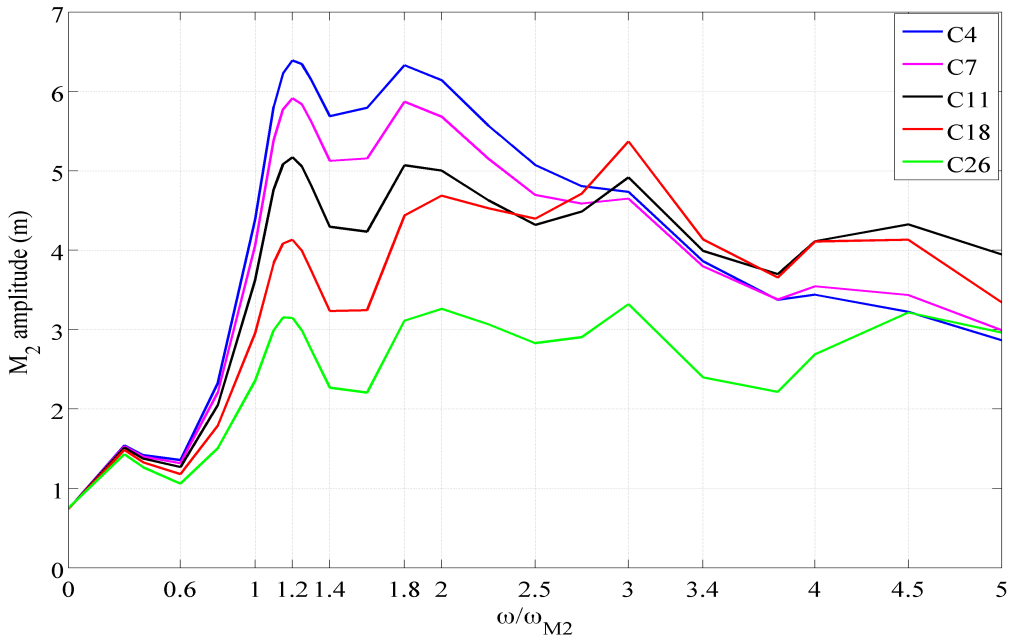

Figure 6.6 – The response curves of several stations along the Bristol Channel: C4 and C7 represent the inner Channel response, C11 and C18 represent the mid-Channel response and C26 represents the response at the entrance of the Channel.

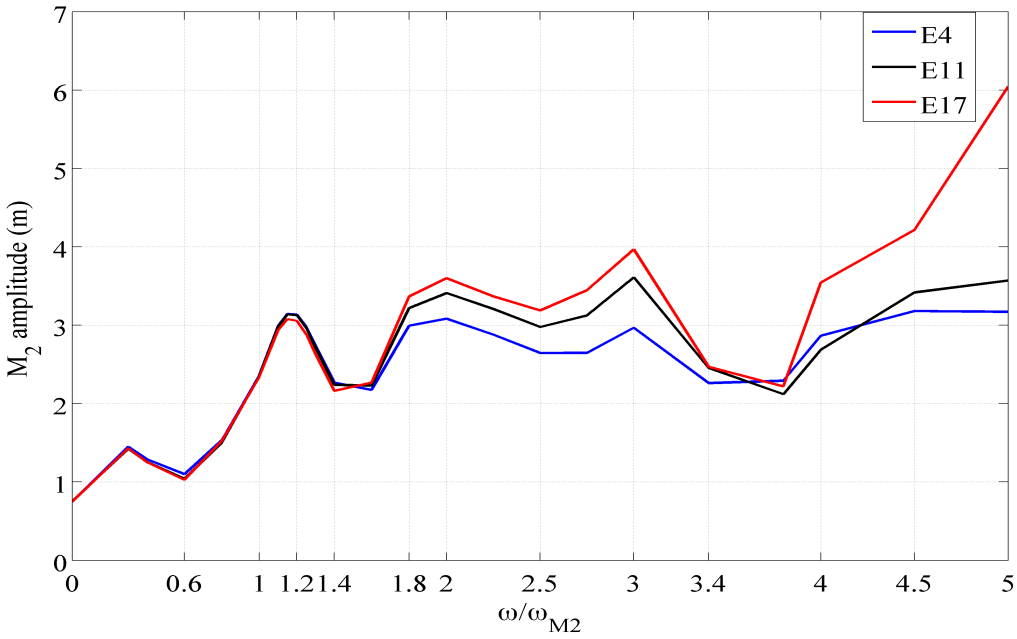

Figure 6.7 – The response curves of several stations at the entrance of the Bristol Chanel.

Figure 6.8 shows the amplification of the response along the Bristol Channel by normalising the response of the Channel by the elevation at the entrance of the Channel (indicated by the blue line). The figure also shows the amplification within the inner Channel (red line) and outer Channel (green line). Figure 6.8 suggests that the Bristol Channel cannot

simply be modelled as a single degree-of-freedom system. The observed response of the Bristol Channel to the tidal forcing seems to be the result of a series of coupled resonances; some of which are due to the response of the Bristol Channel to the forcing at its mouth, and some are related to the response of the Celtic Sea to the forcing at the edge of the continental shelf. The outer part of the Channel exhibits an apparent resonance at about $\omega/\omega_{M2} = 3.4$, whilst the inner section shows a sharper resonance at around $\omega/\omega_{M2} = 1.6$.

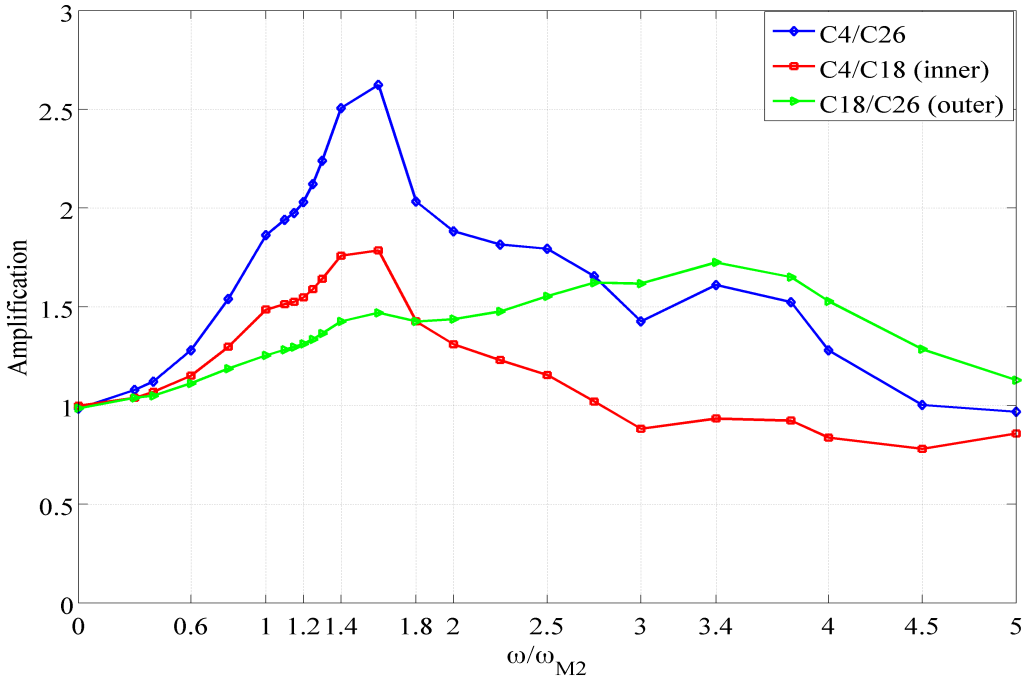

Figure 6.8 – Amplification of the response observed the Bristol Channel

To evaluate the importance of the location of the model boundaries on the model results, Figure 6.9 presents a comparison of the preliminary results obtained from the original model (DG-ADCIRC-WD) and the extended model at high forcing frequencies. The figure shows that the amplitude of the response is somewhat dependent on the location of the model boundaries (C11 and E11 response comparisons). The normalised response of the Bristol Channel (C11/E11 in Figure 6.9) is also found to be sensitive to the mesh. This is mainly related to the location of the forcing applied in the model, where the phases of the harmonic constituent cannot be properly defined. Both models have three open boundaries where the forcing tidal elevations are prescribed. The original model shares one common open boundary with the extended model, which is located beyond the European continental shelf. In the original model, the other forcing boundaries are located at the entrance of the English Channel

and across the North Channel respectively. Using the natural forcing frequency ($\omega/\omega_{M2} = 1$), the tidal waves entering the domain in the original model are propagating freely. However, when the wavelength is shortened the forcing conditions at the two subsidiary boundaries (English Channel and North Channel) become inconsistent with the overall system response. By moving these boundaries further away from the region of interest their influence on the model results can be diminished.

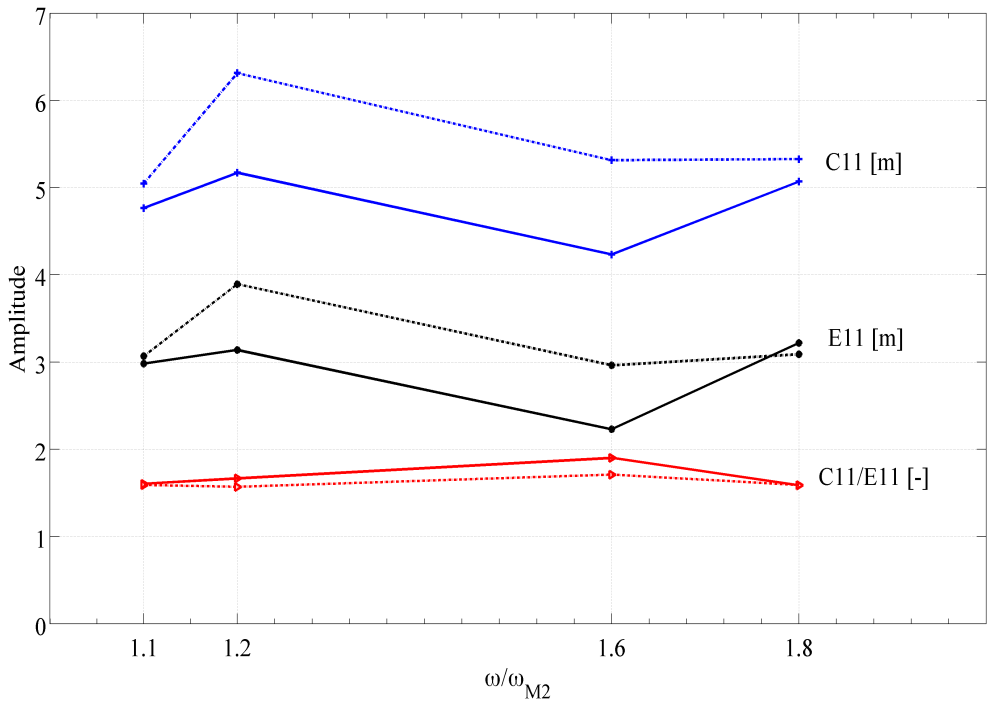

Figure 6.9 – Comparison of the amplitudes of the M_2 tides at stations C11 and E11 Solid lines represent the results taken from the extended model, dashed lines are the results from the original model.

Further analysis is required to investigate the importance of the location of continental shelf on the observed response of the system. As part of the future work, a larger model considering the entire UK coasts, which also includes the European continental shelf and the North Sea, is proposed to be constructed to analyse the importance of the model boundaries on the model results.

6.2. Literature Review on Deploying Tidal Stream Turbines at the Bristol Channel

As explained in Chapter 1, constructing a barrage across the Severn Estuary requires high capital costs and would alter the environment adversely. In this respect, tidal stream turbines

are suggested to utilise the tides in the area. Regarding the deployment of a large tidal turbine array across the Bristol Channel, Giles *et al.* (2010) present the preliminary results from the Severn Tidal Fence Consortium (STFC), which was part of the UK Government's Severn Embryonic Technologies Scheme (SETS). The STFC considers two locations to install tidal arrays. One is between Lavernock Point (Wales) and Brean Down (England), which is close to the proposed Severn Barrage location, and the other is between Aberthaw (Wales) and Minehead (England). The research is conducted for the latter location (Aberthaw-Minehead). The proposed array configuration consists of two rows of 19 km arrays that are connected in series. The distance between the two arrays is 1 km. There is also a navigation gap of 650 m in the middle of the tidal fences. The installed capacity of the arrays is 390 MW and the annual energy generation is estimated to be 0.9 TWh/yr. The analysis is based on a one-dimensional hydraulic model that is extended to the entire width of the Channel. This approach enables calculation of the cross channel flow profile. The study reports the advantages of installing a second row of turbines in the system, which increases the power capture and decreases the flow velocity, observed in the navigational gap. However, the result contradicts the results presented in this chapter regarding the performance of arrays connected in series (see Section 6.3.2). The parametric study results show that additional rows contribute in extracting available power by increasing the total drag applied to the flow by the tidal farm, however with a diminishing return on each additional rows due to the reduced flow passing through the arrays.

Research regarding the operation of tidal turbine arrays in the Bristol Channel primarily investigates the environmental impact of the array deployment within the Channel (Neil *et al.*, 2009; Ahmadian *et al.*, 2012; Kadiri *et al.*, 2012; Ahmadian and Falconer, 2012). The resource assessment, however, is often investigated as a secondary objective.

Neill *et al.* (2009) present a one-dimensional morphological model applied to the Bristol Channel to investigate the sediment transport and bed change within the system in the presence of tidal turbines extracting a small amount of energy. Their results show that extracting energy from sites where strong tidal asymmetry is observed, the bed topography changes significantly due to increased level of sediment transportation. Ahmadian *et al.* (2012) use a two-dimensional hydrodynamic model of the Bristol Channel to investigate the

far-field hydro-environmental impact of operating tidal turbine arrays. The turbines are represented as external forces applied to the momentum equations, which involves calculating the thrust and drag applied to turbines. The study considers a single array configuration that partially blocks the Channel. The maximum available power is estimated to be 245.5 MW, however the main focus of the paper lies in estimating the change in the environment. Kadiri *et al.* (2012) consider the change in the water quality in presence of different tidal energy schemes including a conceptual tidal array. Ahmadian and Falconer (2012) investigate the importance of array layout and configuration on the power output and estimate the environmental impact of operating tidal arrays in the Bristol Channel. The study considers a two-dimensional hydrodynamic model that is modified to represent the tidal turbines as momentum sinks in the solution. The model results indicate that the blockage of the turbines plays an important role in altering the flow field. In case of a highly blocked flow, the current velocities both upstream and downstream of the arrays are reduced and the bypass flow velocities are increased. In terms of the power availability, Ahmadian and Falconer (2012) show that there is a difference between the available power associated with the undisturbed kinetic energy flux within the turbine array location and the estimated available power by the model. For the array configurations considered in the study, the maximum available power range is between 100 to 140 MW. Considering the array configurations, their results show that blocking a larger area using a lower blockage ratio would produce more power than a highly blocked but relatively shorter array. It should be noted that this conclusion is in contradiction with the findings of Nishino and Willden (2012b). In their study, Nishino and Willden (2012b) considered an array that partially blocks a channel. The study shows decreasing the spacing of the turbines in an array increases the power extracted by the array due to the local blockage effect. However, if the spacing is reduced too much, due to array-scale choking effect, the power output decreases.

The following section provides a parametric study of the Bristol Channel region to investigate the importance of: a. turbine operating conditions, b. array locations, and c. array configurations. The turbine operating conditions are included implicitly in the analysis of available power for various array locations and array configurations.

6.3. Parametric Study: Deployment of Tidal Stream Devices in the Bristol Channel

This section considers a parametric study conducted to evaluate the maximum available power that can be generated in the Bristol Channel by deploying various tidal turbine array configurations. The applied methodology to compute the maximum available and extracted power values in this section is explained in Chapter 5. Sections 6.3.1 and 6.3.2 explain the significance of array location and array connectivity on the available power.

6.3.1. Location

High tidal ranges occurring in the Bristol Channel are mainly due to the funnelling effect as well as the resonance between the Atlantic Ocean boundary and the Bristol Channel.

Adopting the naturally occurring kinetic energy flux methodology in the Bristol Channel, there are three regions indicating favourable places for tidal array deployment. The first two are the area between Lundy Island and Hartland headland; and the Ilfracombe headland. Given that a detailed investigation of a headland site as a tidal energy resource has already been undertaken for the Anglesey Skerries, these regions are considered to be secondary tidal resource development sites and so will not be considered for further investigation in this chapter.

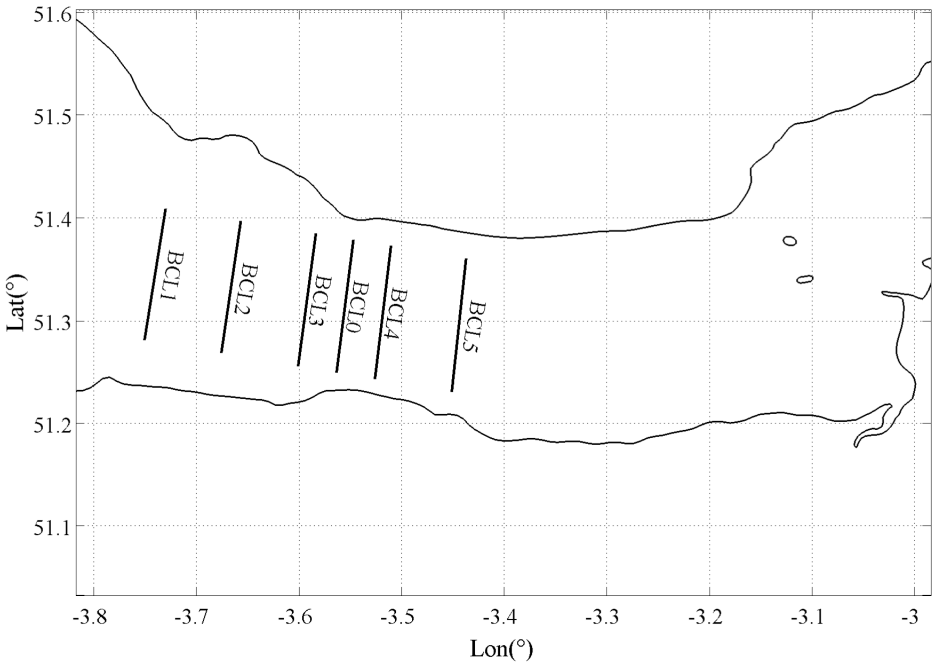

Figure 6.10 – Array locations considered in the Bristol Channel

The third favourable area is between Minehead and Aberthaw, which is the narrowest part of the Channel with fast currents (see e.g. Figure 6.1 for M_2 tidal currents). The computed velocities reach 1.5 m/s and the average depth is approximately 30 m. The locations for the tidal arrays considered are given in Figure 6.10. The array placed at the narrowest section of the Channel is BCL0, which is taken as the base test. The rest of the arrays are deployed sequentially from the far west of the Channel where fast flows occur towards to the east. Each array is approximately 14 km long and they are 5 km apart from each other except BCL3, BCL0 and BCL4 arrays. BCL0 array is located in between BCL3 and BCL4 arrays.

A parametric study has been conducted for the aforementioned tidal arrays for various wake velocity coefficients (α_4) with fixed blockage ratios. In this work four different α_4 values have been considered, which are 0.35, 0.40, 0.50 and 0.70. Table 6.5 summarises the maximum available power that can be generated for different blockage ratios at the computed optimum wake velocity coefficients.

Array	Blockage	Optimum α_4	$P_{available}$ (MW)	$P_{extracted}$ (MW)	Power per Swept Area (kW/m^2)
BCL1	0.1	0.35	13.3	21.4	0.314
	0.3	0.35	61.4	115.7	0.483
	0.5	0.40	163.7	315.7	0.773
BCL2	0.1	0.35	14	22.6	0.339
	0.3	0.35	64.8	122.3	0.523
	0.5	0.40	176.2	343.1	0.853
BCL3	0.1	0.35	18	29.1	0.477
	0.3	0.36	83.9	156.1	0.741
	0.5	0.40	233.9	456.9	1.240
BCL0	0.1	0.35	17.1	27.6	0.424
	0.3	0.35	80.9	152.8	0.669
	0.5	0.38	232.2	471.7	1.152
BCL4	0.1	0.35	16.4	26.4	0.417
	0.3	0.35	77.1	145.5	0.654
	0.5	0.38	220.1	443.5	1.120
BCL5	0.1	0.37	10.4	16.3	0.264
	0.3	0.35	49.8	94	0.421
	0.5	0.38	142.3	288.8	0.721

Table 6.5 - Power values for different blockage ratios at optimum wake velocity coefficients. The maximum power outputs for each blockage ratio studied are highlighted in grey.

Considering the maximum available power values, it is seen that BCL3 performs better for all cases. The optimum α_4 values are increased slightly as the blockage is increased, although they do not exceed 0.40. However, once the arrays are deployed further in the west towards Swansea Bay or in the east towards the Severn Estuary, the available power values decrease significantly. From this result, it is possible to deduce that BCL3, BCL0 and BCL4 arrays are located in the Channel where highest velocities occur.

Another interesting result from the parametric study is that the available power increases significantly with increasing blockage ratios. For instance, if we consider BCL0 array, the maximum available power is 17.1 MW for a blockage ratio of 0.1. Increasing the blockage by a factor of 3 on the other hand, results in an increase of 4.7 times that of 17.1 MW. A similar trend is observed for each test case considered here.

The power per turbine swept area parameter also shows that BCL3 is the best performing array. Considering that the average water depth within the area of the arrays is not changing significantly, the change in the power per swept area parameter is mainly due to the distance of the array towards the head of the Channel, where fast currents occur.

6.3.2. Array Connectivity

This section discusses the effects of connecting arrays in series or in parallel on the power availability. For brevity, this section considers three array locations, which were studied in the previous section. Considering BCL3, BCL0 and BCL4, in order to investigate the effects of parallel connectivity, each of these arrays are divided into two sub-array sections. The arrays closer to the English coasts are considered to be located in Region 1 (R1-), whereas the ones closer to the Welsh coasts are deployed in Region 2 (R2-). Figure 6.11 shows the altered array configurations. Each sub-array is approximately 7 km in length. The distance between arrays is 2.5 km in the east-west direction.

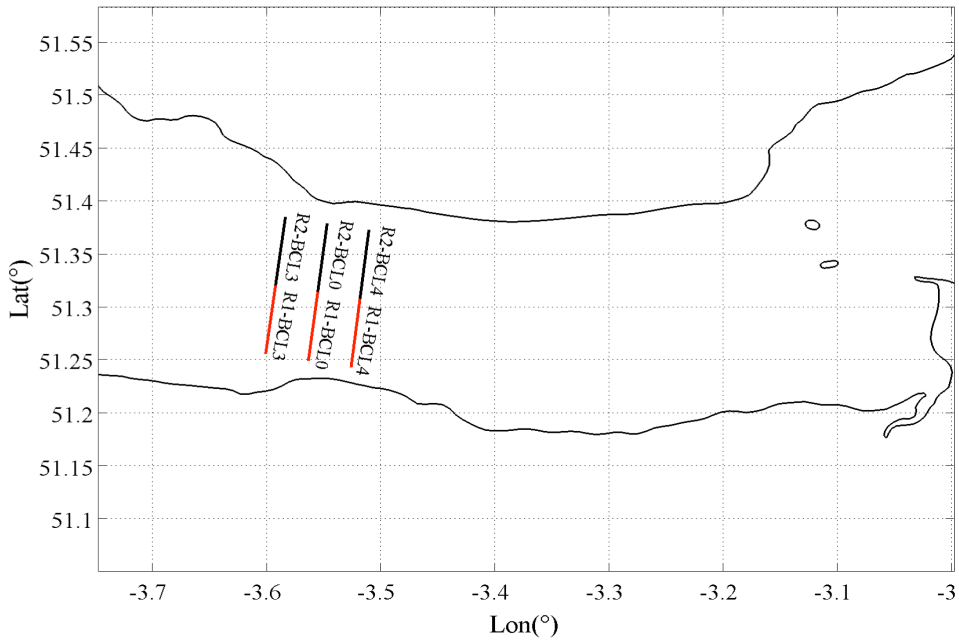

Figure 6.11 – Locations of individual arrays in the Bristol Channel selected for investigating the effects of array connectivity (series and parallel).

In order to compare the maximum available power extracted from the possible combinations, it is important to calculate the power values for the individual arrays. Table 6.6 summarises the maximum $P_{available}$ averaged over the simulation period (i.e. 3 days) for the separate arrays obtained for the optimum α_4 values.

Table 6.6 shows that the maximum available power values do not change significantly between the two regions, although arrays located in Region 1 (Figure 6.12) perform approximately 20% better than arrays in Region 2 (Figure 6.13). The table also shows the power per swept area (PpSA) parameter computed for each array using different blockage ratios. From the table, it is observed that the PpSA is very similar between regions 1 and 2, where region 2 is often delivering slightly more power. The only exception is seen in array site BCL4. At BCL4 tidal array site, the turbine areas for Region 1 and Region 2 are very close to each other. As the flow is faster towards Region 1, the turbines extract more power when compared to R2-BCL4.

Array	Blockage	Optimum α_4	$P_{available}$ (MW)	Power per Swept Area (kW/m^2)	Average Depth (m)
R1-BCL3	0.1	0.35	9.6	0.469	28.4
	0.3	0.37	41.9	0.683	
	0.5	0.44	101.8	0.996	
R2-BCL3	0.1	0.35	8.3	0.478	24.1
	0.3	0.37	35.9	0.690	
	0.5	0.45	84.4	0.973	
R1-BCL0	0.1	0.35	8.7	0.404	29.9
	0.3	0.37	38.9	0.602	
	0.5	0.42	95.7	0.889	
R2-BCL0	0.1	0.35	8.1	0.420	26.8
	0.3	0.37	35.7	0.617	
	0.5	0.43	86.8	0.900	
R1-BCL4	0.1	0.35	8.6	0.430	27.8
	0.3	0.37	38.2	0.636	
	0.5	0.43	94.4	0.943	
R2-BCL4	0.1	0.35	7.6	0.391	27.0
	0.3	0.37	32.9	0.564	
	0.5	0.44	79.5	0.818	

Table 6.6 - Maximum available power extracted from individual array configurations. Power per swept turbine area is also given for each blockage ratio. The maximum power outputs for each blockage ratio studied are highlighted in grey.

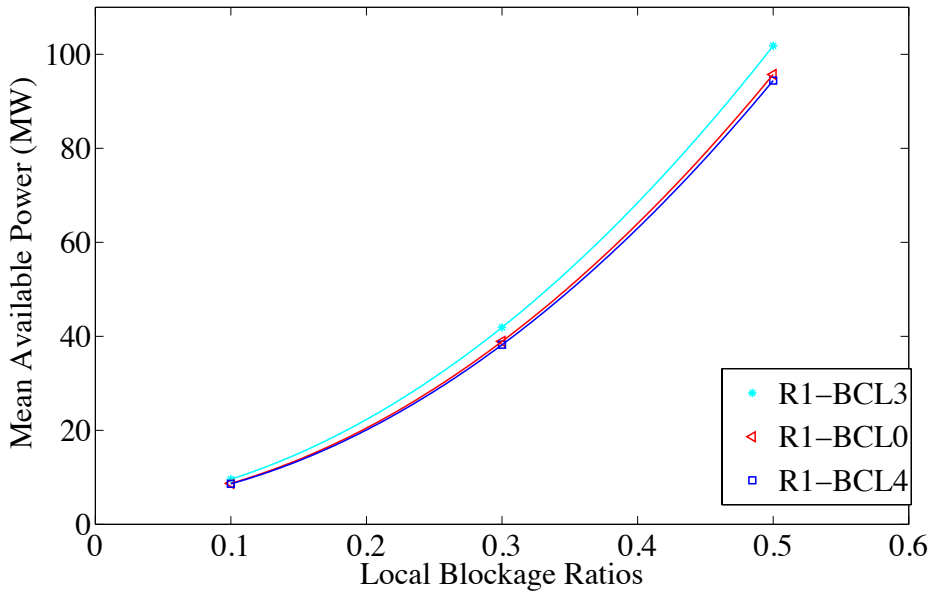

Figure 6.12 – Maximum available power as a function of blockage ratio for the arrays located in Region 1.

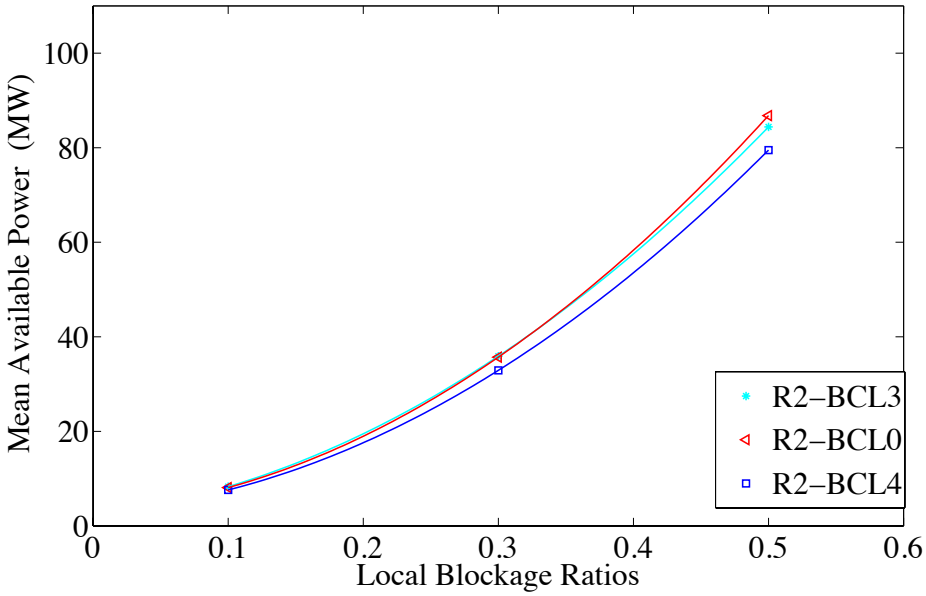

Figure 6.13 – Maximum available power as a function of blockage ratio for the arrays located in Region 2.

Parallel Configuration

This section discusses the performance of arrays when deployed in parallel. Table 6.7 shows a brief comparison for BCL3, BCL0 and BCL4 arrays, which correspond to the parallel configuration of arrays installed in isolation. From the table, it is evident that extending the length of an array (as in parallel configuration), the power gain is increased with increasing blockage ratio. For the high blockage case (B = 0.5), it is seen that the available power output is increased by 25% for Location 3, 27% for Location 0 (base test) and 34% for Location 4. The placement of the arrays is an important factor in exploiting the energy of fast currents. Overall, in terms of available power, the arrays located in Location 4 (L4) are performing worse compared to the other arrays, as the currents are slowed down due to the increase in the cross-section length of the Channel. For all blockage ratios considered, the turbine array located in Location (L3) is the best performing array (see $P_{available}$ in Table 6.7). The economic gain factor shows that occupying a larger cross-section (parallel connection) of the Channel increase the available power due to the increased array drag applied to the flow. The BCL4 parallel array shows the greatest gain in available energy.

Array Combination	Blockage	$\Sigma P_{available}$ (MW)	Corresponding Array	Blockage	$P_{available}$ (MW)	Economic Gain
R1-BCL3 + R2-BCL3	0.1	17.9	BCL3	0.1	18	1.006
	0.3	77.8		0.3	83.9	1.078
	0.5	186.2		0.5	233.9	1.256
R1-BCL0 + R2-BCL0	0.1	16.8	BCL0	0.1	17.1	1.018
	0.3	74.6		0.3	80.9	1.084
	0.5	182.5		0.5	232.2	1.272
R1-BCL4 + R2-BCL4	0.1	16.2	BCL4	0.1	16.4	1.012
	0.3	71.1		0.3	77.1	1.084
	0.5	163.9		0.5	220.1	1.343

Table 6.7 Comparison between arithmetic sums of arrays deployed in isolation and connecting them in parallel for different blockage ratios. The maximum power outputs for each blockage ratio studied are highlighted in grey.

As explained in Vennell (2012) increasing the total thrust applied by the array reduces the flow along the entire channel and hence reduces the available power to the turbines. The rate of this reduction in the flow influences the amount of power that can be extracted by the turbines. In this case, it is believed that the flow speed is reduced more rapidly when the arrays are placed in the narrower parts of the Bristol Channel (BCL3 and BCL0 arrays), and is reduced more gradually when placed closer to the mouth of the Channel (BCL4 array).

To analyse the effect of extending the array length on the power extracted by the turbines, a further problem is studied. Considering the BCL3 array, the array length is increased gradually from 700 m to 14000 m starting from the English coast towards the Welsh coasts.

For this analysis, the model is forced with both M_2 and S_2 tides to characterise the resource more realistically. The analysis is conducted for a high blockage case (B = 0.5) for optimum α_4 value of 0.4. The model is run for 9.6 days including 2 days of ramping period. The total available power obtained for each array length is then averaged over the spring cycle. Figure 6.14 depicts the increase in available power over the array length and Figure 6.15 shows the power per swept turbine area values for associated total swept area of the turbines. In Figure 6.14, the mean available power is increased almost more than linearly for the first quarter of the array ($700 < L_{array} < 3600$ m), which is a manifestation of the fast flow characteristics until the centre of the Channel is reached that contributes in the amount of available power output. From $L_{array} = 3600$ m, adding more turbines to the row increases the available power

almost linearly. In terms of power per swept area (Figure 6.15), this would indicate a reduction in the power extracted by the turbine. By extending the length of the array, the total drag applied to the flow is increased at the expense of reducing the flow passing through the array. This in turn affects the power available to the turbines, which results in a slight reduction in the amount of power delivered by each turbine (see Figure 6.15).

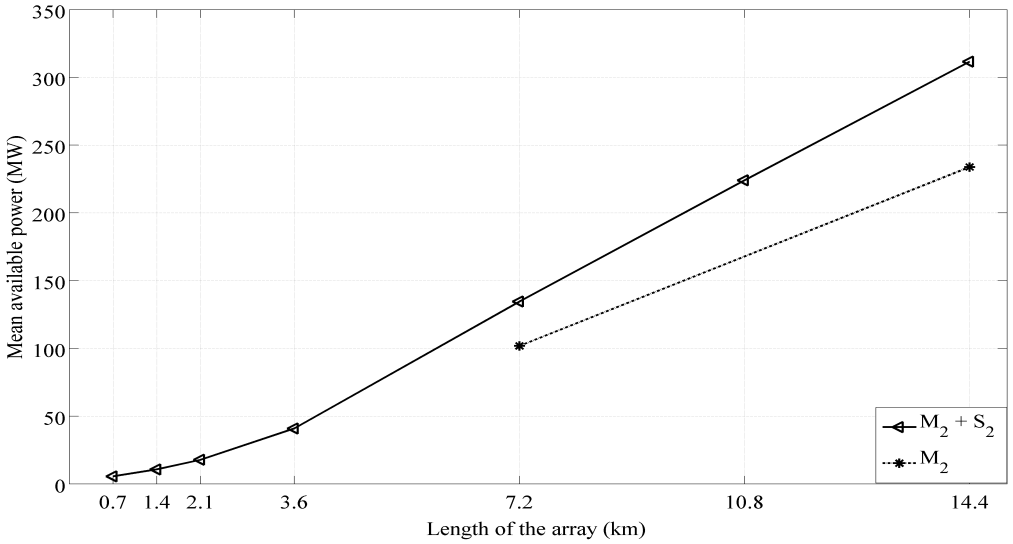

Figure 6.14 – Mean available power extracted by the turbines over a number of different array lengths across the Bristol Channel.

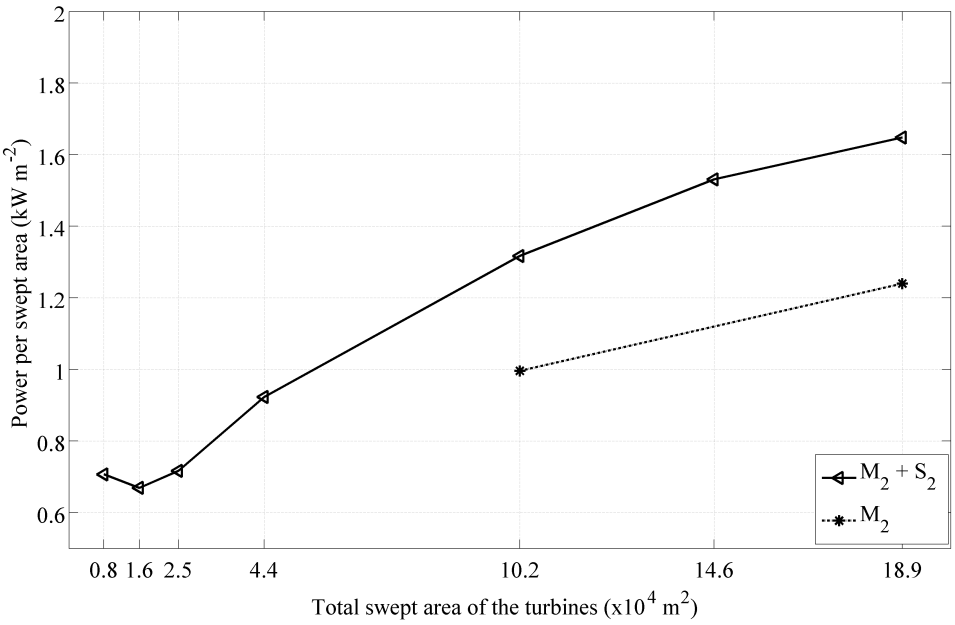

Figure 6.15 – Time averaged power per swept area as a function of total swept area of the turbines for a high blockage case (B=0.5).

Figure 6.14 also shows that including S_2 tidal constituent in the simulations increases the maximum average available power by 25%. This increment in available power by S_2 constituent is also seen in the power per swept area plotted in Figure 6.15. In Figure 6.15, there is a loss in power per swept area parameter when the array is extended from 720 m to 1440 m. The exact reason for this loss in still unknown, however it is assumed that at this point, as the local bathymetric depth is too shallow ($h_{average} \cong 20$ m), the energy loss due to bed friction overweighs the thrust applied to the flow by the array, which reduces the available power to the turbines. However, Figure 6.14 and Figure 6.15 both show that connecting the arrays in parallel is advantageous in terms of extracting the available power and it is better to encourage parallel configurations in the Bristol Channel region.

Series Configuration

For arrays connected in series, the maximum available power is reduced, mostly when the turbines apply a high drag to the flow ($B = 0.5$). For a low blockage case ($B = 0.1$), the economic gain factor (explained in Chapter 5) shows there is no significant energy loss due to the interaction of the turbine arrays. However, as the blockage is increased, and hence the total drag applied to the flow is increased, a reduction in the available power is observed. The economic gain factor presented in Table 6.8 shows that when $B = 0.5$, for a two-row array (R1-BCL30), the associated energy loss is approximately 20%, and it is about 30% for a three-row array (R1-BCL304). When two-row arrays are considered, it is observed that deployment of the arrays further apart from each other results in a slight recovery in available power. An example of this behaviour is given by R1-BCL30 (series combination of R1-BCL3 and R1-BCL0) and R1-BCL34 (series combination of R1-BCL3 and R1-BCL4) array configurations. For R1-BCL30, the distance between the arrays is 2.5 km and the maximum available power is 161.7 MW for a blockage ratio of 0.5 (see Table 6.8). As the distance between the arrays is doubled as in R1-BCL34 array configuration, there is a 10.7 MW increment in the available power. However, it is seen that there is always a reduction in the available power when the arrays are deployed in series (Vennell, 2011). As explained by Vennell (2011), the arrays deployed in series interact with each other. The interaction occurs, as tuning of any array in the series configuration will increase the total thrust applied to the

flow, which results in a reduction in the flow passing through the arrays. Hence, the amount of power that is available to all turbines is decreased.

Array	Blockage	Optimum α_4	$P_{available}$ (MW)	$\Sigma P_{available}$ (MW)	Economic Gain
R1-BCL30	0.1	0.35	18	18.3	0.984
	0.3	0.39	74.2	80.8	0.918
	0.5	0.47	161.7	197.5	0.818
R1-BCL34	0.1	0.35	17.9	18.2	0.984
	0.3	0.38	75.9	80.1	0.948
	0.5	0.46	172.4	196.2	0.879
R1-BCL304	0.1	0.36	26	26.9	0.967
	0.3	0.40	103.4	119	0.869
	0.5	0.50	214.1	291.9	0.734
R2-BCL30	0.1	0.36	16	16.4	0.976
	0.3	0.39	64.6	71.6	0.903
	0.5	0.49	135.8	171.2	0.793
R2-BCL34	0.1	0.35	15.6	15.9	0.981
	0.3	0.39	64.8	68.8	0.941
	0.5	0.48	141.6	163.9	0.864
R2-BCL304	0.1	0.35	23.1	24	0.963
	0.3	0.41	89.1	104.5	0.853
	0.5	0.52	176.1	250.7	0.702

Table 6.8 - Power values for different blockage ratios at optimum wake velocity coefficients for array connections in series.

When high thrust is applied to the flow (i.e. $B = 0.5$), the reduction in the available power is at a maximum (see Table 6.8). In this respect, the optimum α_4 values are increased in order to compensate possible flow diversion, which limits the available power to the arrays. These findings are consistent with the Anglesey Skerries analysis.

6.4. Effects of Tidal Turbine Arrays on the Local Flow Field

The change in the local velocity flow field of the Bristol Channel system will be discussed in this section. The analysis conducted herein coincides with the analysis presented in the Anglesey Skerries (see Section 5.4.).

The naturally occurring flow in the Bristol Channel is almost rectilinear, flowing towards the head of the Channel during a flood tide, and out again in an ebb tide. Figure 6.16 illustrates the natural velocity flow field in the Bristol Channel during an ebb tide.

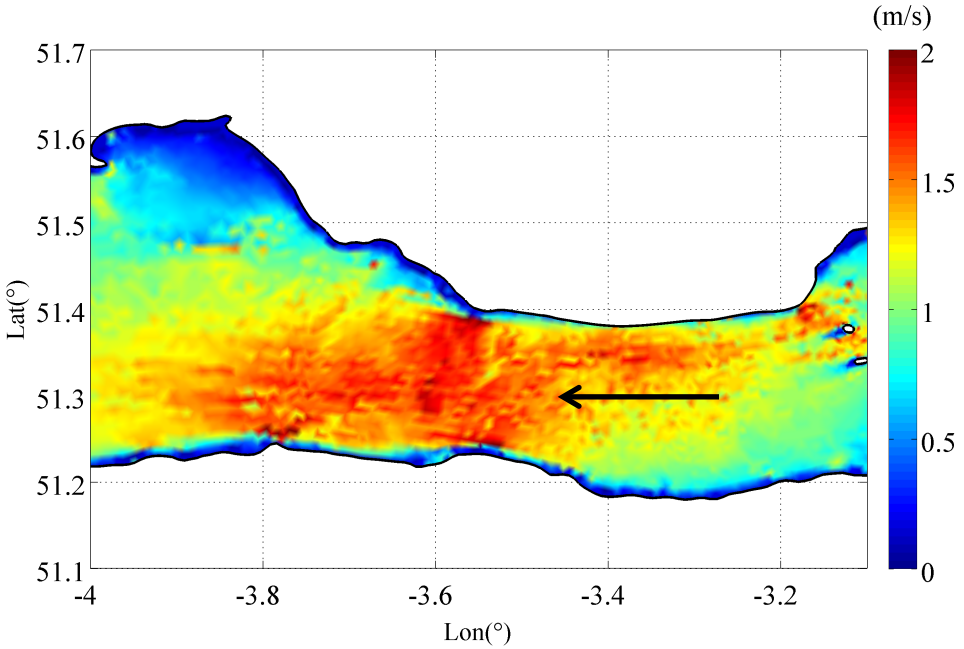

Figure 6.16 – Natural velocity flow field of the Bristol Channel. The arrow indicates the flow direction.

Installation of tidal turbine devices will inevitably alter the flow field. The analysis conducted in Chapter 5 shows that the flow bypasses the turbine arrays at the ends of the arrays, however the bypass flow is asymmetric and changes with respect to the array configurations. To analyse the change in the flow field, two array configurations are considered in the Bristol Channel for a high blockage case (B = 0.5). The local flow fields during an ebb tide due to a parallel (BCL3) and a series array operation (R1-BCL304) are illustrated in Figure 6.17 and Figure 6.18 respectively. Both figures indicate an accelerated flow around the edges of the turbine arrays. This result is consistent with the Anglesey Skerries analysis and indicates that the flow diverts due to the thrust applied to the flow by the arrays.

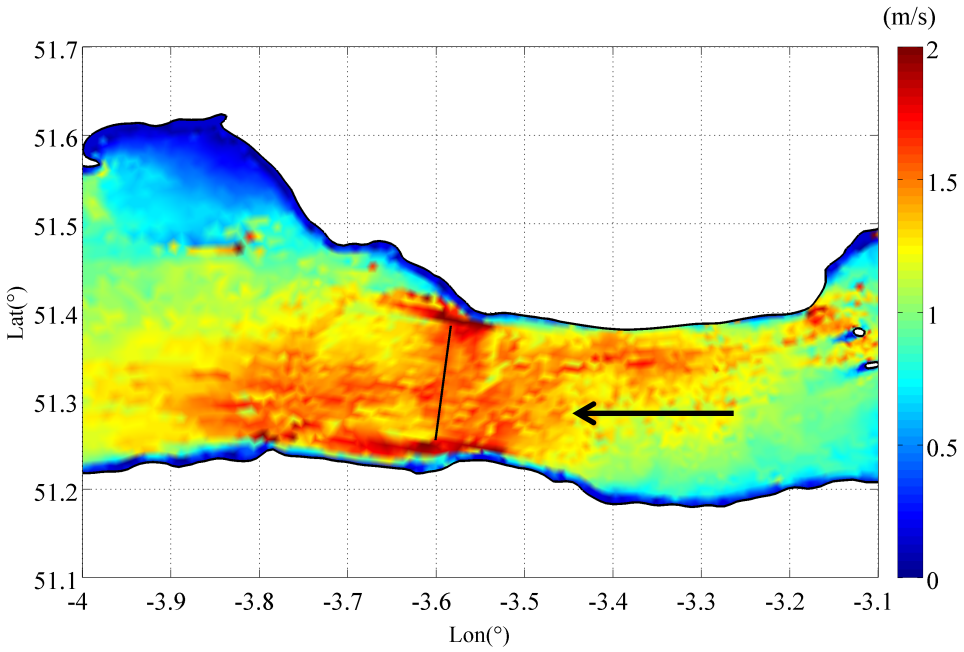

Figure 6.17 – Local velocity flow field of the Bristol Channel when BCL3 parallel array is operating. The arrow indicates the flow direction.

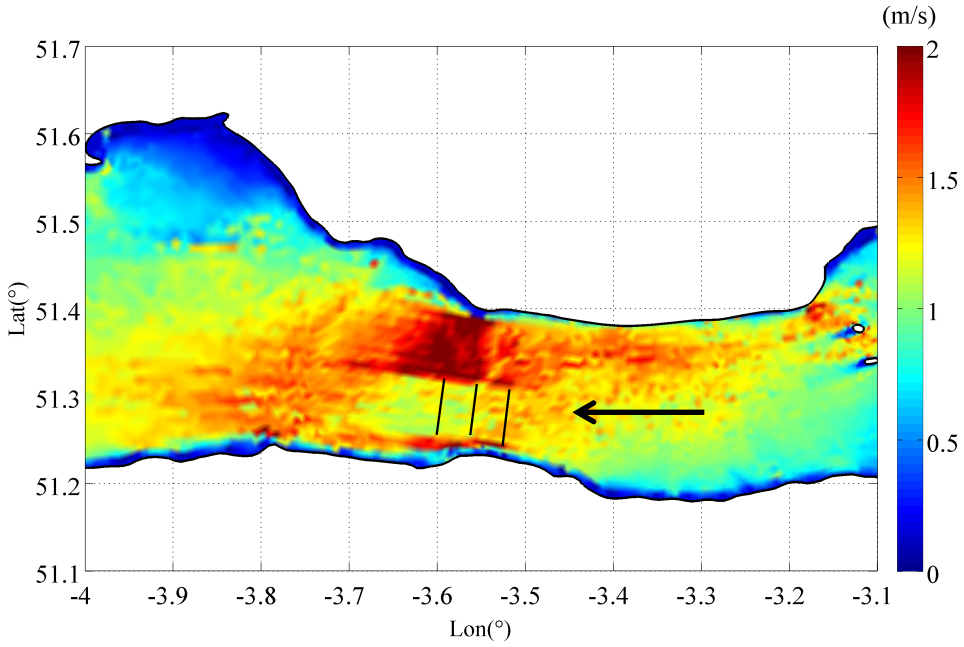

Figure 6.18 – The local velocity flow field when R1-BCL3, R1-BCL0 and R1-BCL4 arrays are installed in the Bristol Channel. The arrow indicates the flow direction.

The changes in the flow fields are illustrated in Figure 6.19 and Figure 6.20 respectively for the parallel and series array deployments.

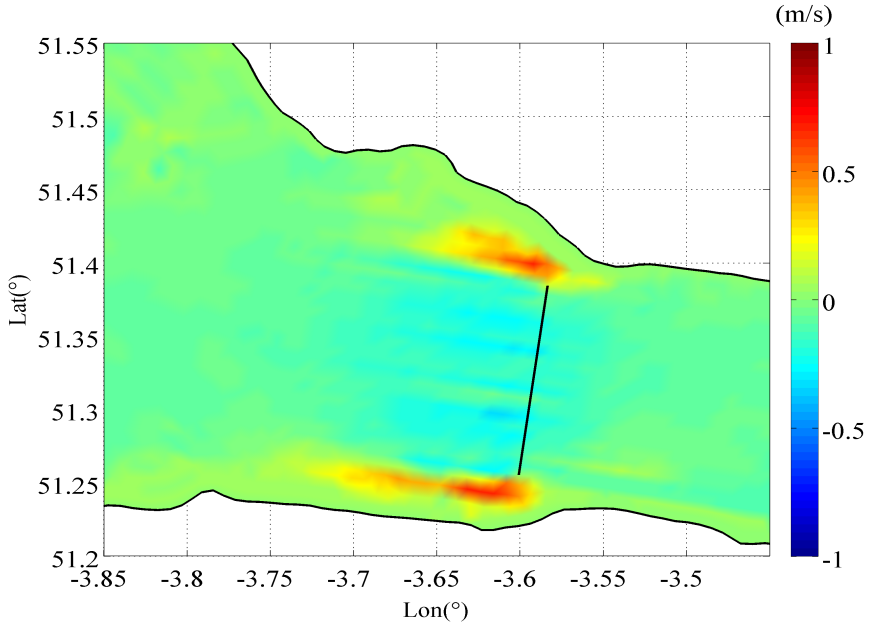

Figure 6.19 – Change in the velocity flow field when parallel BCL3 array is installed in the Bristol Channel.

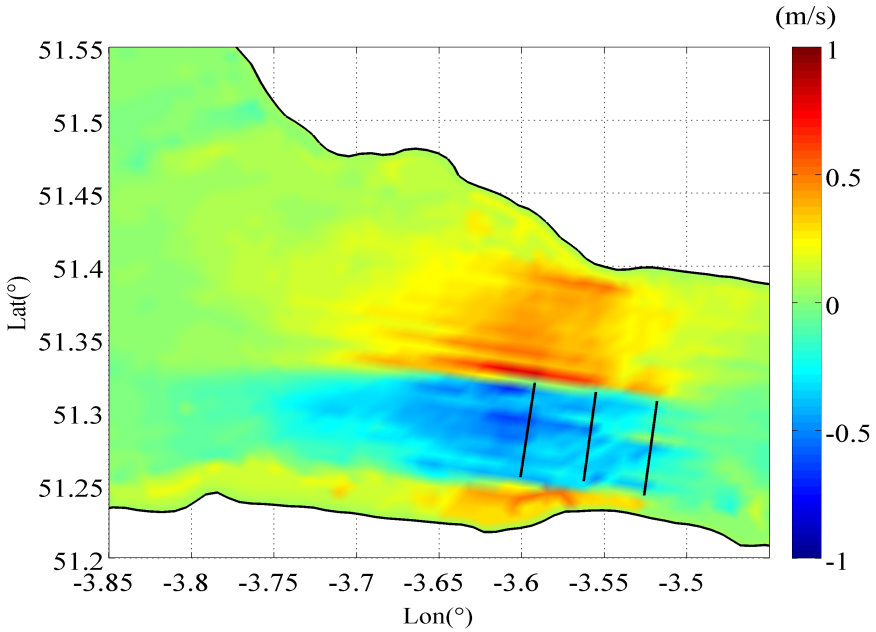

Figure 6.20 – Change in the velocity flow field when R1-BCL3, R1-BCL0 and R1-BCL4 arrays are installed in series in the Bristol Channel.

The bypass flow speed increases by approximately 1 m/s on both sides of the parallel array (Figure 6.19). The flow speed decreases by approximately 0.3 m/s on the downstream of the array due to energy extraction. Regarding the series configuration, Figure 6.20 shows that the bypass flow speed increases by ~1 m/s towards to the right hand side of the arrays (considering the direction of the ebb tide). The flow passing the turbine arras slows down as

expected. Especially for a series array deployment, the flow diversion indicates that the available power is restricted with respect to the thrust applied on the flow.

6.5. Conclusions

The circulation in the Bristol Channel is driven by the tidal movements. The semi-diurnal tides observed in the Bristol Channel are one of the largest in the world with a mean tidal range of 12.2 m at spring tides. There are two main mechanisms that play a role in the amplification of tides in the area. One of these is acknowledged as the quarter-wave length resonance of the Channel with the Atlantic tidal wave; and the other is the funnelling of the waves at the upper reaches of the Bristol Channel due to its wedge-shaped geometry and shallow bathymetry. This chapter introduced a preliminary study to further investigate the resonance occurring in the Bristol Channel.

The response curve is computed by exciting the model using a range of artificially altered M_2 forcing frequencies. The original model (DG-ADCIRC-WD) encountered numerical instabilities due to the interaction of ingoing and reflected waves at the open boundaries when forcing the model with low forcing frequencies ($\omega/\omega_{M2} < 1$). Therefore, the study has been conducted by using a larger model, which includes the English Channel and extends beyond the North Channel towards the Scottish Isles of Tiree and Coll including the north-west coasts of the Northern Ireland.

The study shows that the quarter-wavelength resonant period of the Bristol Channel is between 10.3 – 11.3 hours, which is close to the semi-diurnal tidal band. This result agrees well with the previous studies that focus on the resonance occurring in the Celtic Sea. The resonance curve obtained in the study presented in Section 6.1.2 suggests that there is a couple resonance occurring in the Bristol Channel, one is induced from the outer Channel (Celtic Sea) and the other is the resonant response of the Bristol Channel itself.

A parametric study is also conducted to analyse the importance of the turbine operating conditions, array locations and connectivity on the available power output. It is seen that BCL3, BCL0 and BCL4 arrays, which are located between Minehead and west of Barry (Aberthaw-Wales), operate more effectively when compared to the other array configurations. It is believed that this is mainly due to the local fast flows increasing the available power of

the system. Regarding the connectivity of the arrays, it is seen that extending the length of the array (parallel configuration) is more effective in terms of extracting available energy than connecting arrays in series, especially for high blockage cases. The closure problem introduced in Section 6.3.2 supports this conclusion. For a high blockage case, the upper bound of the mean available power is approximately 240 MW for BCL3 parallel array configuration. This value is reduced to 214 MW when the most effective series configuration is considered (R1-BCL304 for $B = 0.5$). The additional rows of turbines increase the available power, however a reduction in the overall available power occurs due to the altered flow regime in the entire Channel.

When the change in the flow field is considered, as the proposed tidal arrays act as an additional resistance, the flow diverts at the ends of the arrays (see Section 6.4). The example case studies discussed in Section 6.4 consider a very high blockage ($B = 0.5$), which means a high thrust is applied to the flow. In this case, the flow is reduced due to the increased array thrust. The flow tends to divert around the edges of the array (i.e. bypassing the arrays). Regarding the reduction in the flow passing through the arrays, the power that is available to the arrays is decreased. These results are coherent with the analysis conducted for the Anglesey Skerries introduced in Chapter 5.

Chapter 7

Interaction of Tidal Stream Energy Sites

This chapter investigates energy and flow interactions that could occur between two or more tidal farms deployed in the vicinity of each other at selected sites off Anglesey and in the Bristol Channel. The interactions are determined using the discontinuous Galerkin ADCIRC finite element shallow water model (Kubatko *et al.*, 2006a) with linear momentum actuator disk theory (following Houlsby *et al.*, 2008) used to evaluate the head loss due to the turbines which is treated within ADCIRC as a line momentum sink (Serhadlıoğlu *et al.*, 2013; Draper *et al.*, 2013). In evaluating the head loss, three parameters are utilised: the blockage ratio, a wake velocity coefficient and the upstream flow conditions prescribed by the Froude number. This approach acts essentially as a link between device-scale analysis and basin-scale analysis, and has already been used in Chapter 5 and Chapter 6 to study the effects of tidal array deployments in different tidal basins. This chapter extends the analysis to consider interactions between tidal farms when they are deployed within the same tidal basin. Section 7.1 summarises the different scales involved in tidal energy analysis. Section 7.2 presents the results obtained for different configurations of tidal farm sited off the coast of Anglesey, and interprets the interactions in terms of the maximum available power and changes to the tidal hydrodynamics of the basin. Section 7.3 presents a similar analysis conducted for tidal farms in the Bristol Channel. Section 7.4 presents a combined analysis of operating the arrays proposed at the Anglesey and the Bristol Channel sites. Section 7.5 concludes the discussions and lists the major findings

7.1. Introduction

Estimation of the maximum power available to tidal arrays involves analyses at different scales. Detailed experimental measurements and 3-D CFD computational analyses of the fluid-structure interaction of one or more turbines at device-scale are being undertaken (see e.g. Mycek *et al.*, 2013; Myers *et al.*, 2011). Provided the CFD mesh resolution resolves properly the wake downstream of the tidal turbines, such models can be used to simulate the

dynamically changing localised flow field as the flow passes through and around the turbine during the tidal cycle (Vogel *et al*., 2013). Once validated against experimental data, device-scale analysis is very useful in individual turbine design. However, although accurate, device-scale modelling is computationally very expensive, and it is not yet feasible to extend the approach to tidal farms at basin-scale. Instead, array-scale analysis is required for multiple devices in order to estimate the optimum extraction of tidal stream power noting energy, economic, and environmental constraints (see e.g. Vogel *et al.*, 2013). So far, it is explained that the turbines act as an additional resistance to the flow, which ultimately changes the flow regime and hence has an adverse effect on the available power. At basin-scale, the presence of tidal farms causes a feedback effect between the total mass flux passing through the arrays and the tidal hydrodynamics of the basin system. This effect may be estimated by means of a two-dimensional depth-averaged shallow water model where it is assumed the tides are long waves, and the domain is predominantly horizontal (Draper *et al.*, 2010). In basin-scale models, the tidal arrays can be represented by means of an additional localised drag force (see e.g. Sutherland *et al*., 2007). However, use of an enhanced drag force can lead to errors in predicting the available power to the turbines (Vogel *et al.*, 2013; Draper, 2011), and hinders the analysis of array interactions within a given site. Herein, the approach taken to basin-scale resource estimation (and assessment of tidal farm interactions) is based on linear momentum actuator disk theory (Houlsby *et al.*, 2008) whereby the energy extracted by the turbines is estimated using the momentum equations and the resulting head loss represented as a momentum sink in the shallow water equations (Draper *et al.*, 2010; Adcock *et al.*, 2013).

The remainder of this chapter examines the effects of placing more than one tidal farm at different tidal sites: off Anglesey (a headland), in the Bristol Channel (an oscillating bay), and simultaneously both off Anglesey and in the Bristol Channel.

Figure 7.1 shows contours of the undisturbed kinetic energy flux densities off Anglesey, where candidate sites for tidal turbine farms would appear to be off the western headland at Holyhead and between the northwest headland and the Skerries island and beyond. Figure 7.2 presents the undisturbed kinetic energy flux densities for the Bristol Channel, where locations favourable for tidal farm deployment appear to be near Lundy island, Ilfracombe, and along the main channel.

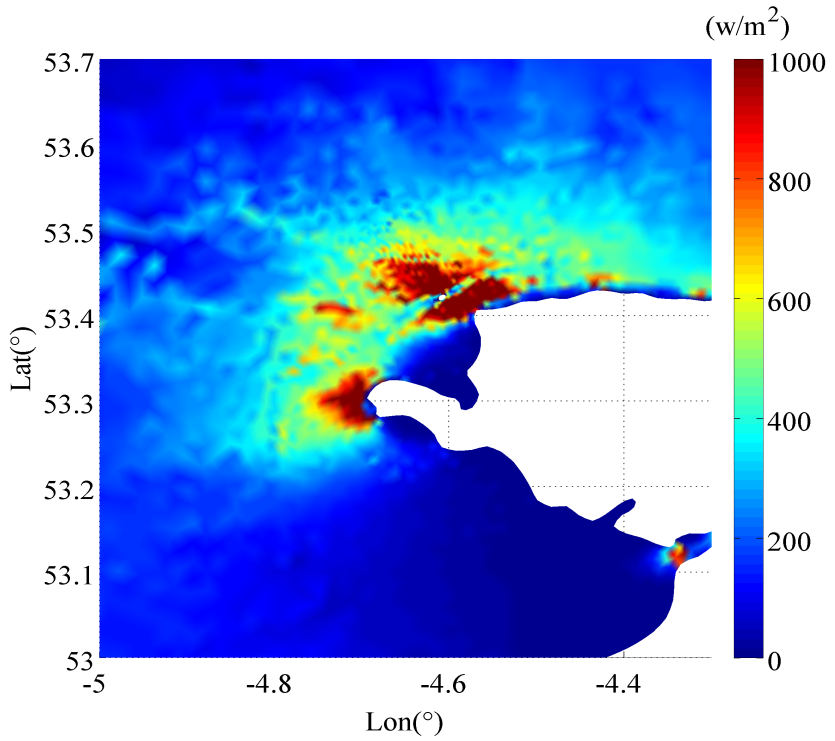

Figure 7.1 – Undisturbed kinetic energy density map for the coastal waters off Anglesey

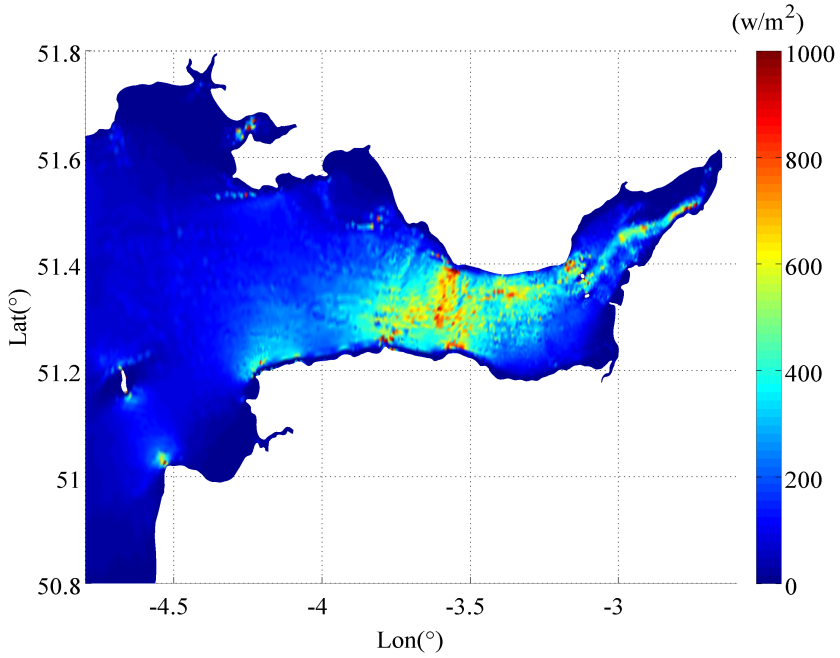

Figure 7.2 – Undisturbed kinetic energy density map for the Bristol Channel

Table 7.1 lists the estimated values of kinetic energy flux density at the various candidate locations. Table 7.2 lists the case studies that were selected to investigate deployment of tidal arrays at different locations in the vicinity of Anglesey and in the Bristol Channel.

Site	Location	Coordinates	Undisturbed kinetic energy flux density, ρ_{KE} (W/m^2)
Anglesey	Holyhead (HH)	53°18'10"N 4°45'58"W	720
	Skerries – Offshore (SO)	53°26'37"N 4°39'23"W	680
	Skerries - Strait (SS)	53°24'52"N 4°35'14"W	1460
Bristol Channel	Lundy (LU)	51°5'26"N 4°35'79"W	175
	Ilfracombe (IL)	51°14'43"N 4°14'42"W	300
	Channel (BC)	51°17'46"N 3°30'10"W	500

Table 7.1 Locations where high tidal currents are observed off Anglesey and in the Bristol Channel.

Region	Case Study Area
Anglesey	Holyhead and Skerries (Offshore)
	Holyhead and Skerries (Strait)
	Skerries (Offshore) and Skerries (Strait)
	Holyhead, Skerries (Offshore) and Skerries (Strait)
Bristol Channel	Lundy and Ilfracombe
	Lundy and Channel
	Ilfracombe and Channel
	Lundy, Ilfracombe and Channel

Table 7.2 Case study locations and proposed array configurations.

The analysis follows the same approach as taken in Chapters 5 and 6. Here, it is intended to examine the extent of the disturbance to the local hydrodynamics caused by the presence of the turbine arrays. In each simulation, the effect of the turbine array is represented using linear momentum actuator disk theory for a high blockage ratio ($B = 0.5$) and the computed optimum wake velocity coefficient. The analysis conducted in this chapter considers a spring tide. The forcing harmonics are the dominant semidiurnal M_2 and S_2 tides.

The model parameters include the Coriolis force and a constant eddy viscosity term of 3 kg/(s.m) used as in Adcock *et al* (2013). The bed friction coefficient used in the simulations is $c_f = 0.0025$. Sections 7.2 and 7.3 present the results obtained for turbine array deployment in the Anglesey headland region and the Bristol Channel respectively. Section 7.4 considers both

sites together, the aim being to assess whether any significant hydrodynamic interactions could occur as a result of simultaneous deployments at both sites.

7.2. Anglesey

7.2.1. Individual Arrays

Chapter 5 has introduced a parametric study focusing solely on a tidal farm array configuration near the Anglesey Skerries. The present section investigates potential interactions between tidal farm sites located in close vicinity to each other off the Anglesey headland. Figure 7.3 illustrates the locations of the selected tidal farm sites. Following the methodology explained in Chapter 5, a parametric study has been conducted in order to compute the optimum wake velocity coefficient for a high blockage case. Using a fixed blockage ratio ($B = 0.5$) and varying the prescribed wake velocity coefficient (α_4), the optimum wake velocity coefficient is computed by fitting a cubic spline to the averaged available power values obtained from each simulation.

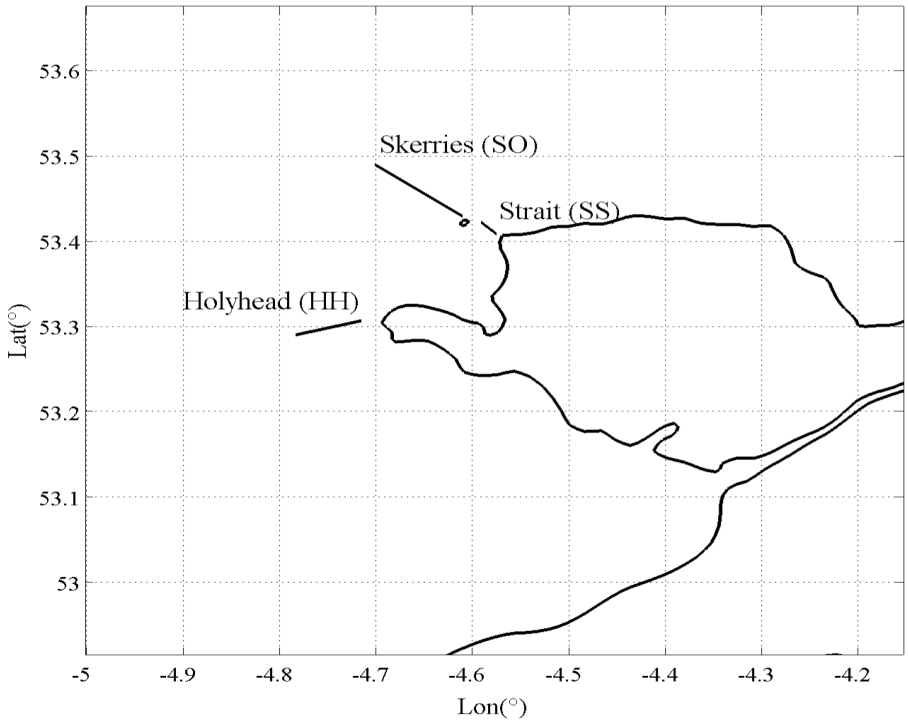

Figure 7.3 – Locations of selected tidal farms off Anglesey headland

Table 7.3 summarises the computed optimum (α_4) values and the corresponding maximum available and extracted power values that are averaged over a spring tide period for each region considered.

Location	Length (km)	Optimum (α_4)	Maximum available power (MW)	Maximum extracted power (MW)
Holyhead (HH)	4.9	0.48	168.3	275.9
Skerries - Offshore (SO)	9.1	0.46	385.8	658.1
Skerries - Strait (SS)	1.8	0.55	86	127.7

Table 7.3 Optimum wake velocity coefficients of the arrays located at different sites off Anglesey. The maximum available and extracted power values are also given.

The change in the local hydrodynamics is estimated by considering the semidiurnal M_2 and S_2 harmonics. Figure 7.4 shows selected stations where changes in harmonic constituents are computed. Stations S1, S2 and S3 are chosen to evaluate changes to the far field owing to the energy extraction from the different sites, whereas S4 is selected to compare changes to the hydrodynamics near the coast of Anglesey headland. The remaining observation points are selected in order to examine the effects upstream and downstream of each tidal farm.

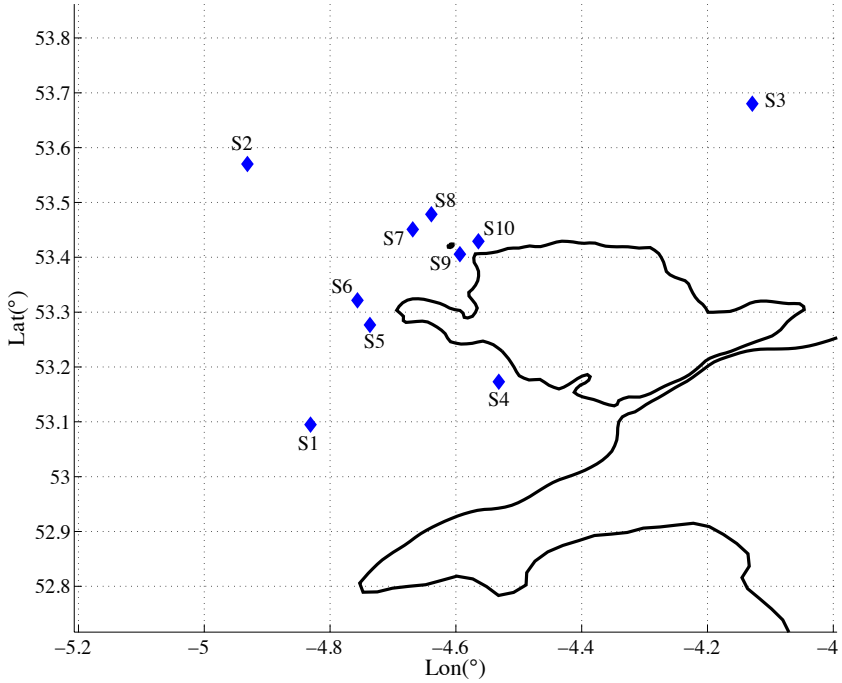

Figure 7.4 – Locations of the stations off Anglesey, selected for comparison

Table 7.4 and Table 7.5 summarise the harmonic analysis results for the M_2 and S_2 tidal elevations respectively. Table 7.4 shows that the M_2 elevation amplitude changes in the vicinity of the arrays are within 1% for the Holyhead (HH) and Skerries-Strait (SS) cases. This change is slightly higher (2.5 - 3 %) for the Skerries-Offshore (SO) case owing to the higher thrust applied to the flow because of the length of the array. The M_2 phases do not alter significantly due to the presence of the arrays. The maximum change is observed in the

Skerries-Offshore (SO) case, in which high water occurs approximately 5 min earlier (~ 2.6°) than natural, upstream of the array, whereas it is delayed around 2 min at the downstream location. It should be noted that the upstream and downstream locations relative to the arrays are determined with respect to the direction of the flood tide.

Station	Amplitude (m)				Phase (°)			
	Natural	*HH*	*SO*	*SS*	*Natural*	*HH*	*SO*	*SS*
S1	1.44	1.44	1.48	1.44	284	283	283	284
S2	1.88	1.88	1.93	1.88	310	310	309	310
S3	2.54	2.54	2.58	2.54	319	320	319	320
S4	1.60	1.60	1.64	1.59	281	280	281	281
S5	1.70	1.71	1.74	1.70	290	289	289	290
S6	1.77	1.77	1.81	1.77	294	295	294	294
S7	2.02	2.03	2.07	2.03	303	304	301	303
S8	2.08	2.08	2.13	2.08	306	306	307	306
S9	2.04	2.04	2.08	2.03	300	300	299	299
S10	2.12	2.13	2.17	2.14	305	305	305	305

Table 7.4 Amplitude and phase of the M_2 tidal elevations at different observation stations off Anglesey under natural conditions and in the presence of different array configurations. The station readings at the upstream and downstream of the arrays are highlighted in grey.

Station	Amplitude (m)				Phase (°)			
	Natural	*HH*	*SO*	*SS*	*Natural*	*HH*	*SO*	*SS*
S1	0.52	0.52	0.53	0.52	313	313	313	313
S2	0.58	0.57	0.58	0.57	340	340	339	340
S3	0.73	0.72	0.73	0.72	354	355	354	355
S4	0.57	0.57	0.57	0.56	311	311	311	311
S5	0.57	0.58	0.58	0.57	320	318	319	320
S6	0.58	0.57	0.59	0.58	324	325	324	324
S7	0.63	0.63	0.64	0.63	334	335	331	334
S8	0.63	0.63	0.63	0.63	337	338	339	337
S9	0.63	0.63	0.63	0.63	331	331	331	330
S10	0.64	0.64	0.64	0.64	337	337	337	338

Table 7.5 Amplitude and phase of the S_2 tidal elevations at different observation stations off Anglesey under natural conditions and in the presence of different array configurations. The station readings at the upstream and downstream of the arrays are highlighted in grey.

The change in the semidiurnal solar harmonic (S_2), due to the presence of arrays, is insignificant. Table 7.5 summarises the predicted S_2 elevation amplitudes and phases at different observation stations. The amplitudes differ by approximately 0.01 m. Across the

turbine arrays, the phases change by 5° at the Skerries-Offshore (SO) case. However, for other case studies the average difference is approximately 2°.

Table 7.6, Table 7.7, Table 7.8 and Table 7.9 present the change in the M_2 and S_2 tidal currents due to the presence of the individual tidal arrays. From Table 7.6, it can be seen that the M_2 tidal current magnitudes are not changed greatly at the offshore stations S1, S2 and S3. However, in the vicinity of the arrays, the velocity magnitudes decrease considerably. For the Holyhead (HH) array, the M_2 velocity magnitude decreases by 13% upstream and 9% on the downstream of the array. The estimated velocity magnitude changes for the Skerries-Offshore (SO) array is 16% upstream and 11% downstream. The maximum difference is observed for the Skerries-Strait (SS) array. The upstream M_2 velocity magnitude is altered by ~25% upstream and by ~20% downstream of the array.

Station	U_{mag} (m/s)				φ_{mag} (°)			
	Natural	*HH*	*SO*	*SS*	*Natural*	*HH*	*SO*	*SS*
S1	0.82	0.82	0.81	0.82	228	228	228	228
S2	0.96	0.97	0.98	0.97	239	240	241	240
S3	0.82	0.82	0.81	0.82	240	241	240	241
S4	0.39	0.38	0.40	0.39	229	226	229	230
S5	1.47	1.28	1.44	1.46	226	219	226	226
S6	1.28	1.16	1.22	1.26	227	217	225	227
S7	1.48	1.47	1.25	1.50	230	230	221	230
S8	1.47	1.47	1.31	1.49	232	232	223	232
S9	2.17	2.16	2.28	1.65	206	206	213	204
S10	2.02	2.01	2.05	1.60	217	217	219	214

Table 7.6 Amplitude and phase of the M_2 tidal current at different observation stations in the Irish Sea off Anglesey under natural conditions and in the presence of different array configurations. The station readings at the upstream and downstream of the arrays are highlighted in grey.

The M_2 velocity phase lags show that for Skerries-Offshore (SO) and Holyhead (HH) arrays, fastest currents occur approximately 20 min earlier than natural case. This change is less significant at the Skerries-Strait (SS) array, where the currents reach their maximum speed 5 min earlier than the natural case. The Skerries-Offshore (SO) array affects the tides reaching the strait between Anglesey Skerries and the headland. From Table 7.6, the M_2 phase lag difference observed in the stations S9 and S10 indicate that the fastest currents are

delayed. This delay is approximately 15 min at the station S9. However at S10, the fastest currents are delayed by 5 min.

Station	Eccentricity				Inclination (°)			
	Nat	*HH*	*SO*	*SS*	*Nat*	*HH*	*SO*	*SS*
S1	0.097	0.124	0.098	0.098	83	84	83	83
S2	-0.101	-0.107	-0.091	-0.100	44	44	44	44
S3	-0.032	-0.031	-0.039	-0.033	3	3	2	3
S4	0.117	0.115	0.101	0.119	116	115	118	116
S5	0.038	0.011	0.037	0.037	105	106	105	105
S6	0.080	0.108	0.088	0.090	76	73	76	77
S7	-0.040	-0.059	-0.079	-0.048	38	37	39	38
S8	-0.030	-0.041	-0.013	-0.033	28	27	26	28
S9	-0.082	-0.083	-0.069	-0.099	51	51	51	54
S10	-0.001	-0.010	0.002	0.021	31	31	31	28

Table 7.7 Eccentricity and inclination of the M_2 currents at different observation stations in the Irish Sea off Anglesey under normal conditions and in the presence of different array configurations. The station readings at the upstream and downstream of the arrays are highlighted in grey.

The eccentricity and inclination (Table 7.7) values indicate the impact on the tidal ellipses, which express a rectilinear flow when eccentricity is equal to 0 and a circular flow when equal to 1. For far-field observation stations, considering that the semi-major axis values do not change significantly, the observed change in eccentricity relates to the change in semi-minor axis. Noting the results obtained for these far-field stations, it appears the presence of HH array has an impact on the tidal ellipse structure in the incoming tide from the western Irish Sea. The presence of the Skerries-Offshore (SO) array has a similar impact on the tidal ellipse structure observed in the western Irish Sea. The case study concerning the operation of the Skerries-Strait (SS) array indicates that the ellipse structure is changing in the Anglesey Skerries offshore site as well as in the strait. This result implies that the change in the hydrodynamics is limited within the vicinity of the array and is also influenced by the coastal characteristics of the site.

A similar analysis has been conducted for S_2 tidal currents. Table 7.8 shows the maximum current magnitudes and phase lags at different observation stations around Irish Sea, which are computed for conditions when there is no array operating (Natural) and when there are arrays present (HH, SO and SS). The table shows that the far-field stations are not affected by

the existence of the arrays. However, the current magnitudes decrease both upstream and downstream of the arrays. The change is about 20% at the HH and SO arrays, and 30% at the SS array. The reason for this considerable difference is primarily due to flow diversion. The phase lags indicate a maximum of 30 minutes delay for the S_2 tidal currents to reach their maximum at the vicinity of the arrays.

Station	U_{mag} (m/s)				φ_{mag} (°)			
	Nat	*HH*	*SO*	*SS*	*Nat*	*HH*	*SO*	*SS*
S1	0.24	0.24	0.24	0.24	264	264	264	264
S2	0.28	0.28	0.28	0.28	278	280	281	280
S3	0.25	0.24	0.24	0.24	280	280	279	280
S4	0.12	0.11	0.12	0.12	261	257	260	261
S5	0.48	0.36	0.47	0.47	259	251	257	259
S6	0.38	0.33	0.38	0.38	264	248	257	263
S7	0.45	0.44	0.35	0.45	266	266	254	266
S8	0.45	0.44	0.37	0.45	268	268	256	268
S9	0.61	0.60	0.60	0.41	234	232	242	231
S10	0.59	0.57	0.57	0.42	248	247	251	244

Table 7.8 Amplitude and phase of the S_2 tidal current at different observation stations in the Irish Sea off Anglesey under natural conditions and in the presence of different array configurations. The station readings at the upstream and downstream of the arrays are highlighted in grey.

Station	Eccentricity				Inclination (°)			
	Natural	*HH*	*SO*	*SS*	*Natural*	*HH*	*SO*	*SS*
S1	0.126	0.175	0.133	0.130	82	82	82	82
S2	-0.054	-0.069	-0.053	-0.060	42	42	43	42
S3	-0.030	-0.024	-0.039	-0.026	2	2	1	2
S4	0.161	0.125	0.146	0.166	115	115	116	114
S5	0.063	0.035	0.053	0.064	103	105	104	104
S6	0.112	0.164	0.106	0.119	79	73	78	80
S7	-0.019	-0.077	-0.071	-0.048	37	37	39	38
S8	0.006	-0.033	-0.003	-0.013	27	27	26	27
S9	-0.083	-0.093	-0.057	-0.119	47	48	48	52
S10	0.064	0.028	0.019	0.053	29	31	32	29

Table 7.9 Eccentricity and inclination of the S_2 currents at different observation stations in the Irish Sea off Anglesey under natural conditions and in the presence of various array configurations. The station readings at the upstream and downstream of the arrays are highlighted in grey.

Table 7.9 lists the eccentricity and inclination values for S_2 tidal current ellipses. According to Table 7.9, the existence of the SS array mainly affects the local flow towards offshore of Anglesey Skerries (again due to flow diversion). A similar behaviour is observed when the SO array operates. In this case, the far-field observation stations do not show any significant changes in the current eccentricities. However, operating HH array affects the overall flow regime. When the effect of all individual arrays is concerned, it is observed that for station S8, the presence of arrays changes the direction of the S_2 tidal ellipse from anti-clockwise to clockwise. Table 7.9 also shows that operating the tidal arrays individually do not cause any significant effect on the current inclinations.

7.2.2. Analysis of Multiple Array Deployments

This section considers the effect of installing multiple turbine arrays within the Anglesey basin. The array configurations studied in this section are:

1. Holyhead and Skerries-Offshore (HH + SO),
2. Holyhead and Skerries-Strait (HH + SS),
3. Skerries-Offshore and Skerries-Strait (SO + SS) and,
4. Holyhead, Skerries-Offshore and Skerries-Strait (HH + SO + SS).

Regarding the power that is available to the arrays, Chapter 5 and Chapter 6 previously concluded that arrays connected in parallel interact constructively, and those in series interact destructively. For a spring tide, a similar analysis has been conducted to evaluate the total available power from the site for each array configuration. The simulations use the optimum wake velocity coefficients presented in Table 7.3. The local blockage ratio is set to 0.5 and the model is forced with the dominant semi-diurnal M_2 and S_2 constituents. Table 7.10 shows the simulated available power output (P_{avail}) and the arithmetic sum of the available power outputs (ΣP_{avail}) for each array combination. From Table 7.10, it is evident that when Holyhead (HH) array is operating along with other arrays, there is no significant change in the power extracted by the either turbine arrays. However, operation of Skerries-Offshore (SO) array together with the Skerries-Strait (SS) array corresponds to operating arrays connected in parallel, thus increasing the local blockage, which increases the available power. The arithmetic sum of the available power of SO and SS arrays that operate in isolation is 471.8 MW, whereas the simulated available power is 515.4 MW. There is a 44.2 MW (8.5%)

increase of the available power in this configuration due to parallel operation. For Case Study 4, when all the arrays are operating together, the enhancement over the sum of the individual arrays is only 28.1 MW, as compared to the 44.1 MW increase when SS and SO are operated together. The decrement of 16.1 MW is attributed to the destructive interference of the HH array acting in series with the other two arrays. Interestingly, this decrement is significantly higher than that observed when combining HH + SS or HH + SO. This is attributed (qualitatively) to the fact that it is only when SS and SO are both operated that there is any effective barrier in series with HH.

Case Study	Array Combinations	P_{avail} (MW)	$\sum P_{avail}$ (MW)
1	HH + SO	553.3	554.1
2	HH + SS	254	254.3
3	SO + SS	515.4	471.8
4	HH + SO + SS	668.4	640.1

Table 7.10 Comparison of the estimated (P_{avail}) and calculated (ΣP_{avail}) available power output for each test case studied for Anglesey region.

The local hydrodynamics of the system is examined by focusing on the M_2 tidal harmonic constituent. Figure 7.5 illustrates the change in the M_2 elevation amplitudes case by case. Here, Case 1 considers the joint operation of the Holyhead (HH) and Skerries-Offshore (SO) arrays; Figure 7.5(a) shows that the M_2 tidal amplitudes are increased by an average of 1.5 cm at the upstream of the HH array (regarding the direction of the flood tide). This is expected as the tidal devices are acting as an additional resistance to the flow, which causes the flow to build up in front of the devices. Due to the energy extraction, there is a head drop observed across the array. The total head drop across the array is approximately for the operation of HH array. As for the SO array, the flow tends to divert towards the northern edge of the array. The diversion of the flow reduces the mass flux entering the array closer to the Skerries, thus reducing the M_2 tidal elevations over that region.

Figure 7.5(b) shows the M_2 elevation amplitude change for the Holyhead (HH) and Skerries-Strait (SS) arrays. The Holyhead (HH) array behaves in a similar manner as in Figure 7.5(a). For the SS array, it is evident that the amplitudes are decreased at the upstream side

(regarding the direction of the flood tide) of the array due to the flow diversion. During the ebb tide, the amplitudes are increased in front of the array owing to the increased resistance. The head drop across the SS array is approximately 2 cm in average. Figure 7.5(c) and Figure 7.5(d) reveal that the arrays act individually and do not interact significantly as far as M_2 elevation amplitudes are concerned. The arrays behave in a similar manner for each case study.

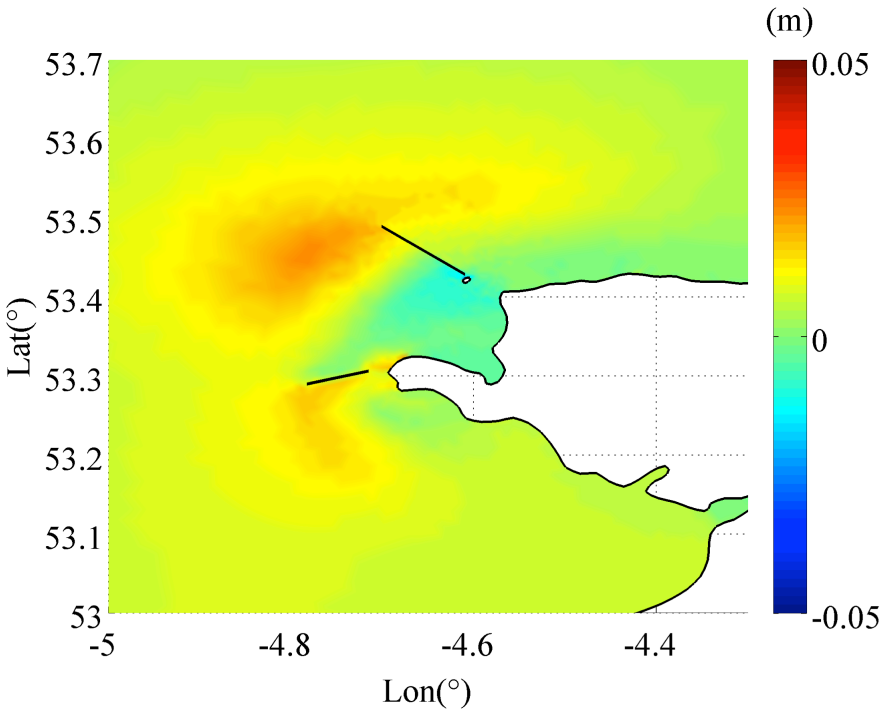

a) HH and SO arrays

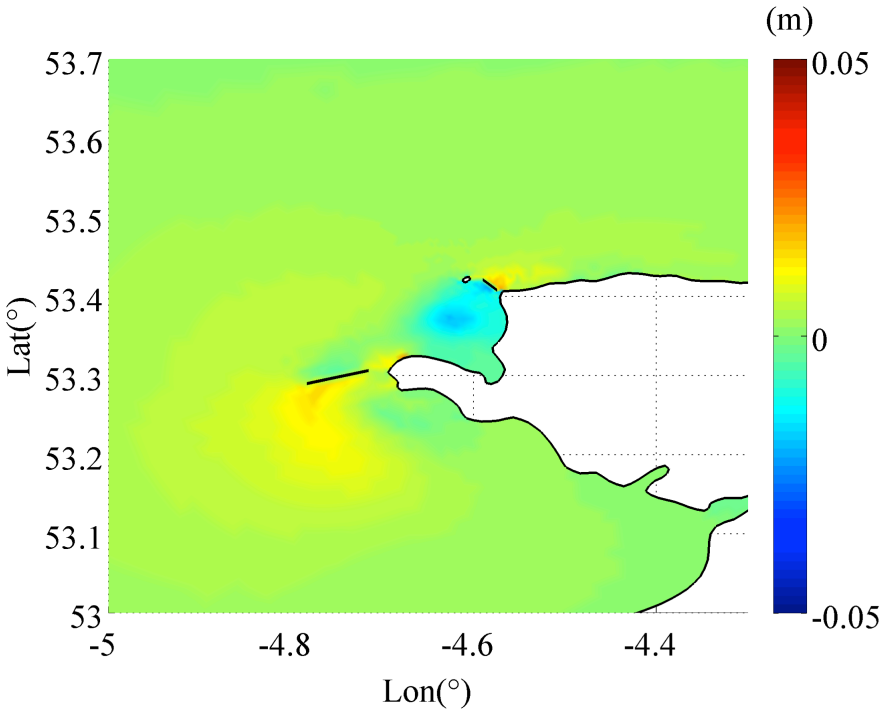

b) HH and SS arrays

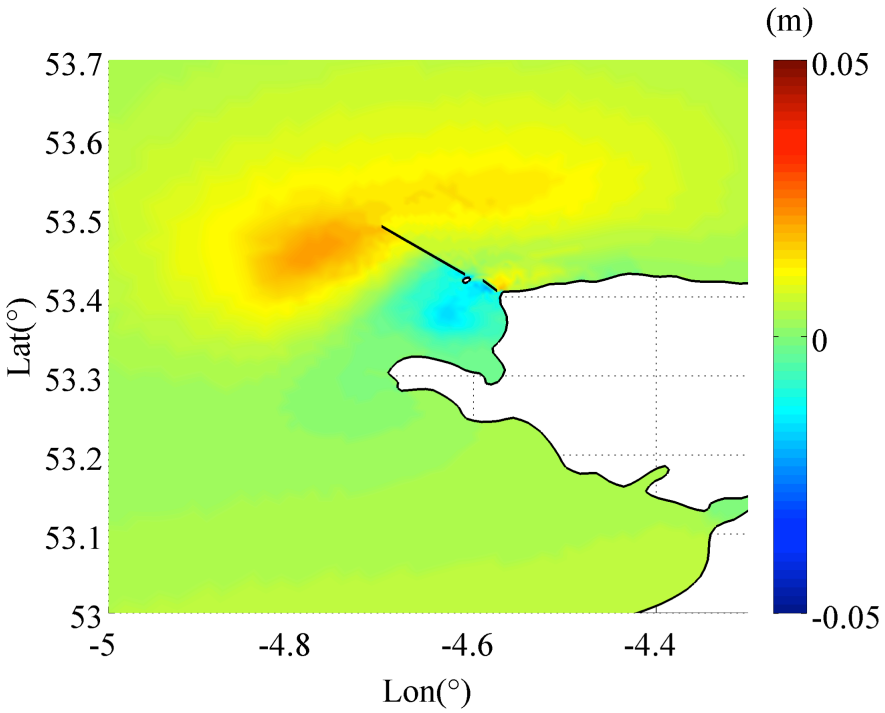

c) SO and SS arrays

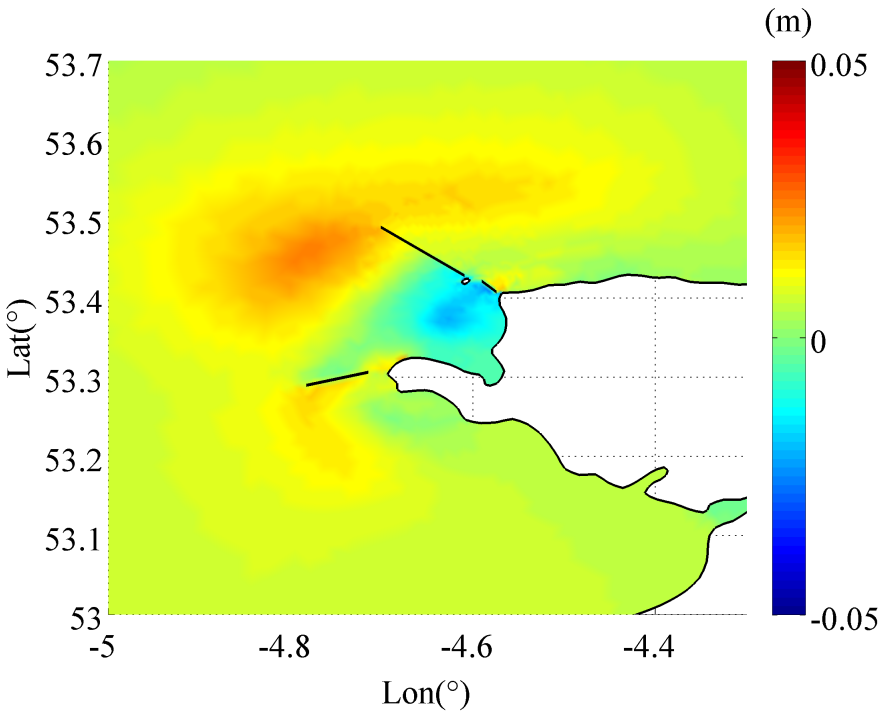

d) HH, SO and SS arrays

Figure 7.5 – M_2 amplitude change from natural conditions off Anglesey due to the presence of different array configurations

Table 7.6 shows that significant changes occur in the M_2 current amplitudes in the vicinity of the arrays. Figure 7.6 illustrates the changes in the M_2 current amplitudes, which are calculated for each case study. Bearing in mind that the tides are bidirectional, reductions in

the current amplitudes at both sides of the arrays are to be expected. For each case study, Figure 7.6 illustrates that the by-pass flow increases at the ends of the arrays. Due to the irregular bathymetry, the velocity magnitudes exhibit strong variations near the arrays.

Figure 7.6(a) shows that the presence of the HH + SO arrays cause the flow to divert both further offshore and towards the strait between the Skerries and the Anglesey headland. Figure 7.6(b) illustrates the array configuration for HH and SS. It is seen that the flow is diverted primarily further offshore, increasing the M_2 velocity magnitude at the Anglesey Skerries site by 0.1 m/s. Figure 7.6(c) shows that SO + SS increases the by-pass flow approximately by 0.5 m/s at the north end of the SO array. This increment decreases radially as the bathymetry of the site changes. The flow velocity is decreased more at the shallower ends of the arrays. Lastly, Figure 7.6(d) illustrates the M_2 velocity magnitude change for when all the arrays are operating together. The presence of HH array in this configuration contributes negatively as it enhances the flow diversion before the flow reaches the SO + SS arrays. However, as the arrays are far away from each other, the disturbance to the flow caused by HH array is relatively small. The analyses conducted in this section confirm that the presence of tidal array in a partially blocked flow enhances the bypass flow.

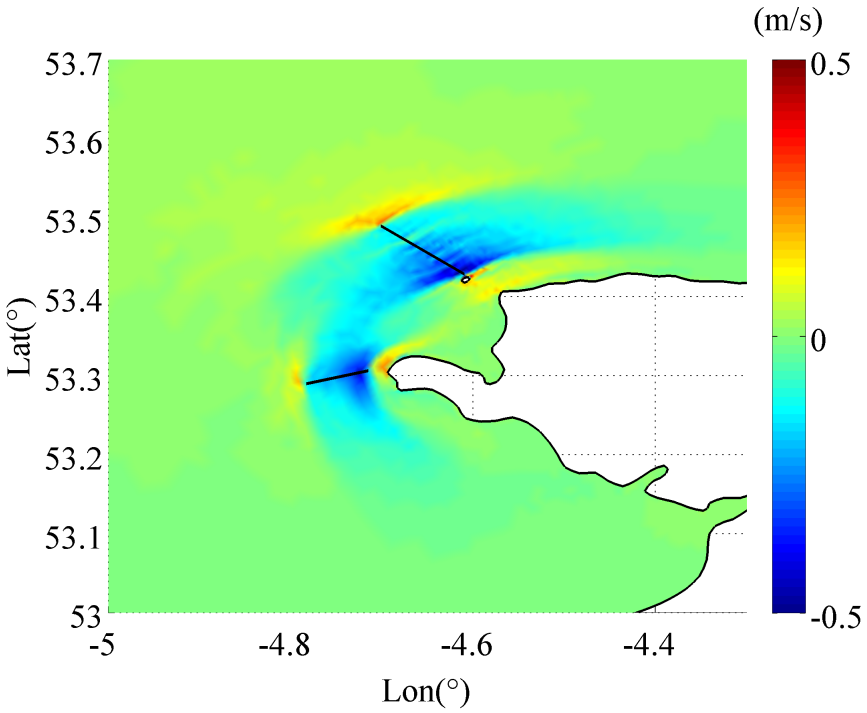

a) HH and SO arrays

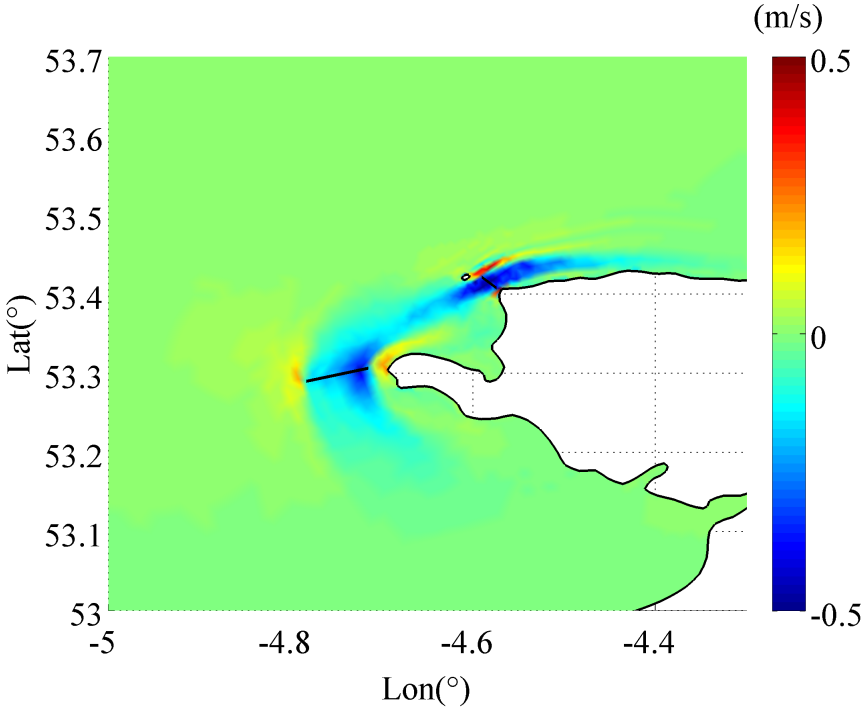

b) HH and SS arrays

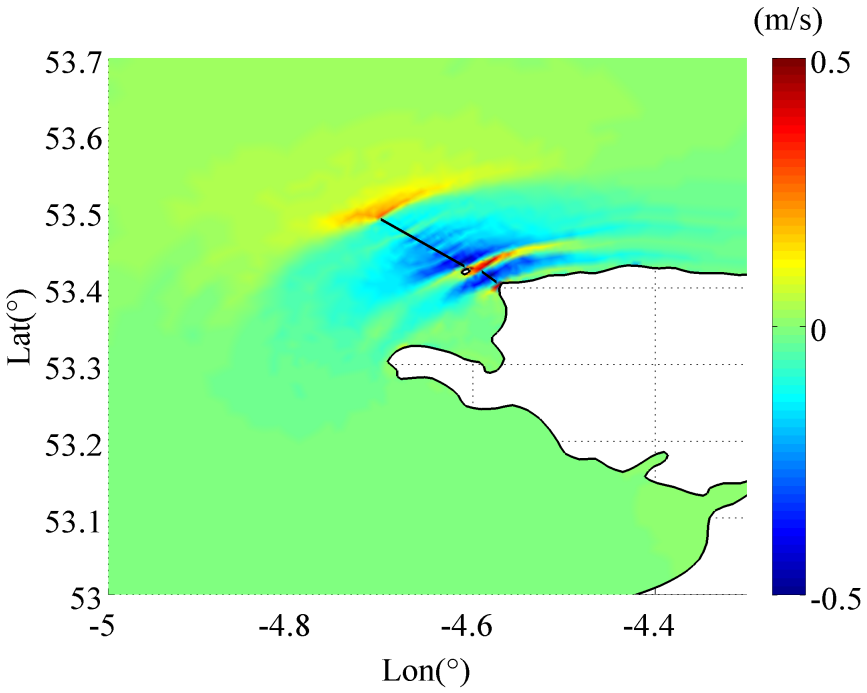

c) SO and SS arrays

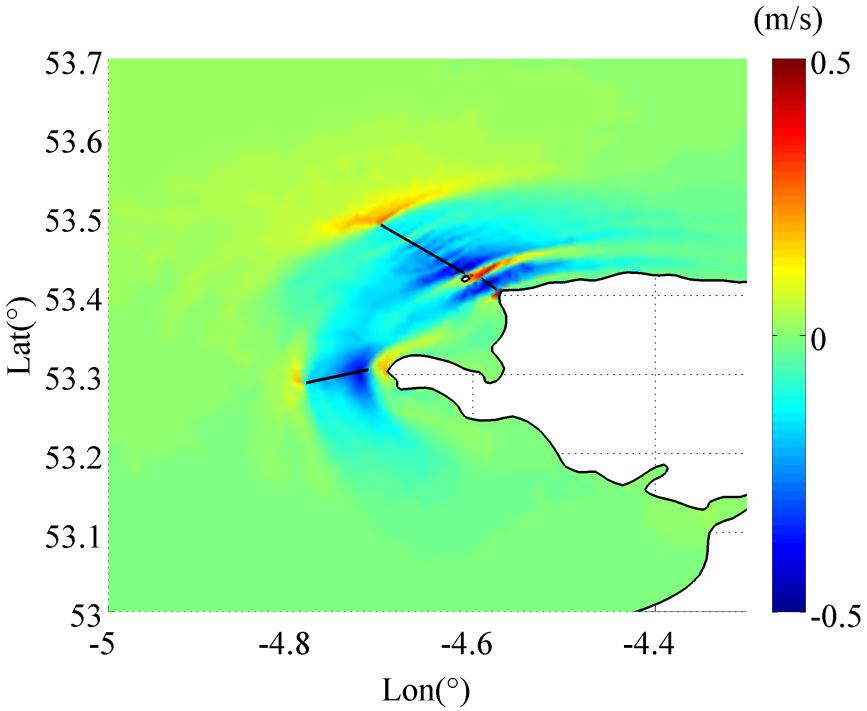

d) HH, SO and SS arrays

Figure 7.6 – M_2 current speed change from natural conditions off Anglesey due to the presence of different array configurations.

7.3. Bristol Channel

7.3.1. Individual Arrays

This section considers individual array deployment in the Bristol Channel and presents results from a very similar analysis as that conducted for off the Anglesey. Figure 7.7 depicts the following selected sites for turbine arrays in the Bristol Channel:

1. Lundy Array: Flow passing between an island and a headland,
2. Ilfracombe Array: Flow passing a headland and,
3. Channel Array: Flow in an oscillating bay.

A set of simulations has been prepared for each array in order to determine its optimum wake velocity coefficients (α_4) that maximises the available power. The simulations consider a fixed blockage ratio ($B = 0.5$) where the α_4 values are varied. The model is forced with the dominant semi-diurnal tidal constituents M_2 and S_2. The time-varying power output is averaged over a spring tide. The averaged available power values are then fitted to a spline to calculate the maximum available power (Adcock *et al.*, 2013).

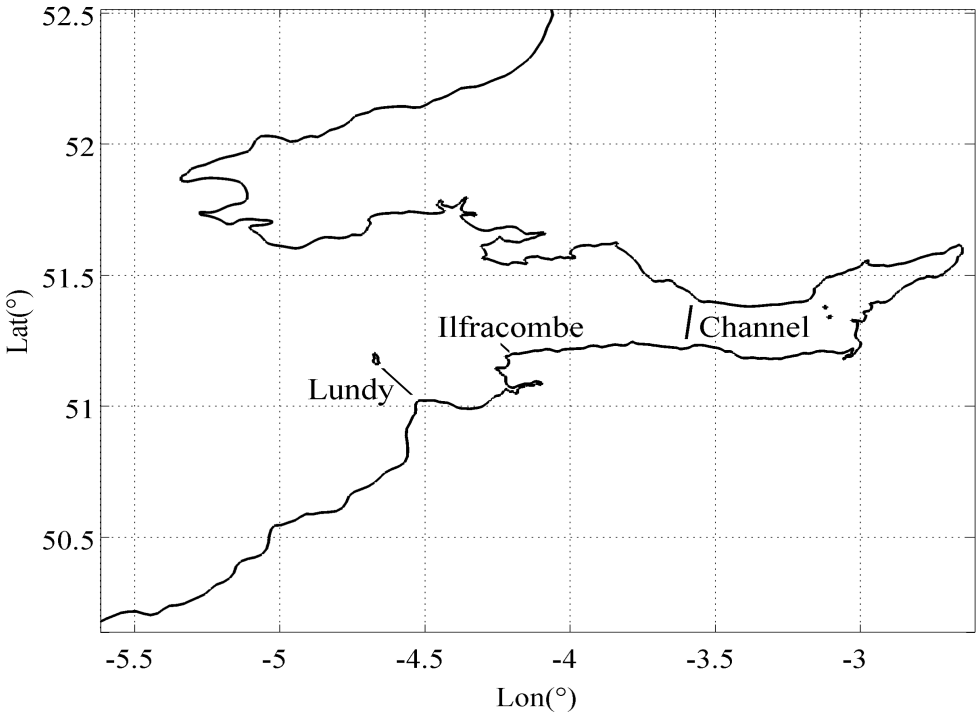

Figure 7.7 – Locations of selected tidal turbine arrays in the Bristol Channel.

Table 7.11 lists the optimum wake velocity coefficients and corresponding maximum available power values for the selected tidal turbine arrays in the Bristol Channel.

Location	Length (km)	Optimum α_4	Maximum available power (MW)	Maximum extracted power (MW)
Lundy (LU)	13.2	0.40	162.7	315
Ilfracombe (IL)	4	0.47	47.8	80.4
Channel (CH)	14.4	0.44	308.4	549.8

Table 7.11 Optimum wake velocity coefficients for tidal turbine arrays located at different sites in the Bristol Channel. Maximum available and extracted power values are also given.

Several comparison stations are chosen (see Figure 7.8) in order to evaluate changes to the tidal system at locations in the Celtic Sea, and the outer and inner Bristol Channel. As explained in Chapter 6, the Bristol Channel system is well known for its resonance characteristics. The purpose of this section is to understand how the system responds in the case of deployment of arrays at different sites in the Bristol Channel.

Table 7.12 and Table 7.13 present the M_2 and S_2 tidal elevation amplitudes and phase lags computed at the stations in case of natural conditions (no tidal array deployments) and in cases of various array installed at different sites listed in Table 7.11. The results show that M_2 and S_2 tidal elevation amplitudes are not affected significantly when arrays located on Lundy (LU) or Ilfracombe (IL) operate. The deployment of Channel (CH) array, however, causes a reduction in the semi-diurnal M_2 and S_2 tidal elevations. The observed change in the outer Channel (Figure 7.8.a) and mid-Channel regions (Figure 7.8.b) are approximately 3 to 5 cm for M_2 tidal constituent (Table 7.12). The CH array is located at the inner Channel and the results show that across the array, the M_2 tidal elevations are decreased by 8 cm. Within the Severn Estuary, the M_2 elevations are approximately 10 cm less than the natural case. Similarly, Table 7.13 shows that the S_2 tidal elevations are reduced by 5 cm throughout the Severn when the CH array is operating.

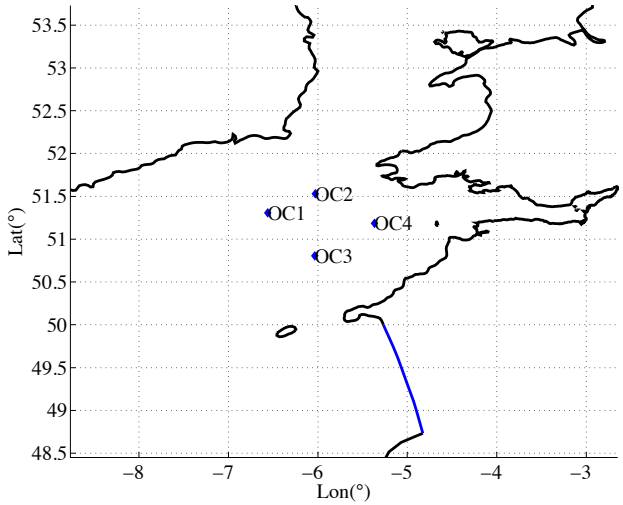

a) Outher Channel

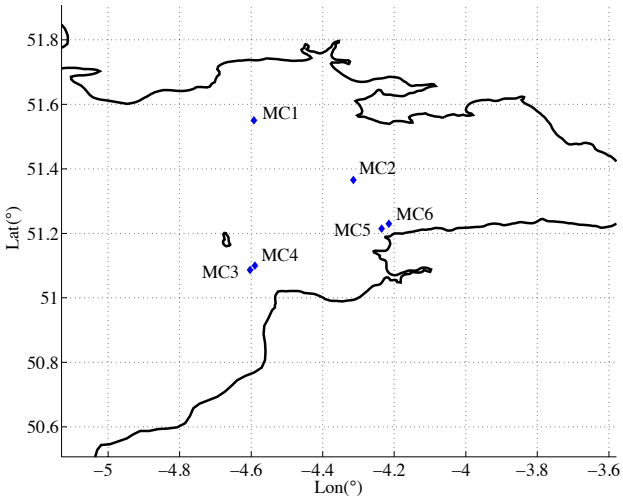

b) Mid-Channel

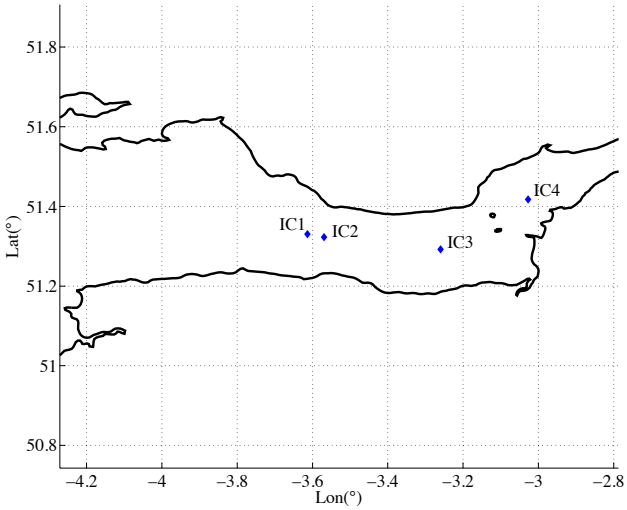

c) Inner Channel

Figure 7.8 – Locations of stations in the Bristol Channel, selected for comparison purposes

The M_2 phase lags (Table 7.12) indicate insignificant changes within the flow field while either Lundy (LU) array or the Ilfracombe (IL) array is operating. The maximum phase difference is observed when the Channel (CH) array is operating. However, the change in the phase lag is only 3°, which implies that high tides are delayed by approximately 6 min immediately east of the array.

Station	Amplitude (m)				Phase (°)			
	Natural	*LU*	*IL*	*CH*	*Natural*	*LU*	*IL*	*CH*
OC1	1.61	1.60	1.61	1.58	155	155	155	155
OC2	1.62	1.62	1.62	1.59	165	165	165	165
OC3	1.91	1.91	1.91	1.89	150	150	150	150
OC4	2.14	2.13	2.14	2.11	162	162	162	162
MC1	2.72	2.71	2.72	2.68	173	174	173	173
MC2	2.92	2.91	2.92	2.87	171	171	171	171
MC3	2.64	2.65	2.64	2.61	162	161	162	162
MC4	2.65	2.65	2.65	2.62	163	164	162	163
MC5	2.96	2.95	2.96	2.92	166	167	166	167
MC6	2.99	2.98	2.99	2.95	167	168	168	167
IC1	3.64	3.63	3.64	3.56	180	181	181	180
IC2	3.66	3.65	3.67	3.58	181	181	181	184
IC3	4.08	4.08	4.09	3.98	187	187	187	189
IC4	4.40	4.41	4.43	4.31	192	193	193	194

Table 7.12 Amplitude and phase of the M_2 tidal elevations at observation stations in the Bristol Channel and Celtic Sea under natural conditions and in the presence of different array configurations. The station readings at the upstream and downstream of the arrays are highlighted in grey.

Table 7.13 shows that the Celtic Sea – Bristol Channel system behaves in a similar manner regarding the S_2 tidal phase lags. The high tides are delayed by 8 minutes east of the Channel (CH) array. However, there are no significant effects observed in the presence of LU and IL arrays. The change in the currents is examined by considering the M_2 and S_2 tidal constituents. Table 7.14 lists the M_2 current magnitude and phase lags computed at the observation stations for natural case study as well as in the presence of the arrays. Table 7.15 presents the corresponding M_2 current eccentricities and inclinations.

Station	Amplitude (m)				Phase (°)			
	Nat	*LU*	*IL*	*CH*	*Nat*	*LU*	*IL*	*CH*
OC1	0.51	0.51	0.51	0.51	205	204	205	204
OC2	0.54	0.54	0.54	0.54	216	216	216	216
OC3	0.62	0.63	0.63	0.62	198	198	198	197
OC4	0.71	0.72	0.72	0.71	211	211	211	211
MC1	0.89	0.89	0.90	0.89	222	223	222	222
MC2	0.95	0.95	0.95	0.94	220	221	221	220
MC3	0.88	0.89	0.88	0.87	211	210	211	210
MC4	0.88	0.87	0.88	0.88	211	213	211	211
MC5	0.97	0.96	0.97	0.96	216	217	216	216
MC6	0.97	0.97	0.97	0.97	217	218	218	217
IC1	1.10	1.09	1.10	1.08	234	235	235	233
IC2	1.11	1.10	1.10	1.05	235	236	236	239
IC3	1.18	1.18	1.19	1.13	244	245	245	247
IC4	1.24	1.24	1.25	1.19	252	253	253	255

Table 7.13 Amplitude and phase of the S_2 tidal elevations at observation stations in the Bristol Channel and Celtic Sea under natural conditions and in the presence of different array configurations. The station readings at the upstream and downstream of the arrays are highlighted in grey.

Table 7.14 indicates that the Lundy (LU) array causes a slight reduction in the M_2 velocity magnitudes at stations OC1 and OC3 but a small increase at stations OC2 and OC4. The stations just before and after the LU array (MC3 and MC4) show that, due to the energy extraction, the M_2 velocity magnitudes are decreased by approximately 4%. It is also seen that the M_2 current velocities are delayed approximately by 2 minutes within the inner Channel. The inner Channel (Severn Estuary) site is not affected greatly due to the presence of the LU array. The M_2 phase lags are similar to that of the natural case for the outer stations when LU is operating. However, when the current reaches the LU array, the MC3 and MC4 station readings show that the maximum velocities occur approximately 15 minutes earlier than natural. The stations located far east of the LU array indicate that the maximum velocities are observed at similar times to that of the natural case. Operating LU array shows local effect on the M_2 current velocities.

Operation of the Ilfracombe (IL) array causes minor changes in M_2 velocity magnitudes until the flow reaches the array. Stations upstream and downstream of the IL array (MC5 and MC6) show that the M_2 velocity magnitude reduces by 11%. The stations located at the inner

Channel region show that the velocity magnitudes are slightly increased when compared to the naturally occurring velocities. The M_2 phase lags indicate that the maximum currents are observed 12-14 min earlier than the natural case at stations MC5 and MC6 that are located either side of the IL array. However, there is no other change observed at other stations by means of the times when fast currents occur.

Station	U_{mag} (m/s)				φ_{mag} (°)			
	Natural	*LU*	*IL*	*CH*	*Natural*	*LU*	*IL*	*CH*
OC1	0.3118	0.3108	0.3110	0.3147	153	153	153	155
OC2	0.4950	0.4967	0.4968	0.5033	202	203	203	202
OC3	0.3781	0.3762	0.3770	0.3734	114	114	114	115
OC4	0.4994	0.5008	0.4993	0.4920	90	90	90	90
MC1	0.5976	0.5999	0.6010	0.5805	83	85	84	83
MC2	0.8703	0.8690	0.8791	0.8385	94	94	95	95
MC3	0.8401	0.8086	0.8389	0.8185	101	93	101	102
MC4	0.8434	0.8056	0.8431	0.8221	101	93	101	102
MC5	1.2418	1.2291	1.0968	1.2258	90	89	84	90
MC6	1.1469	1.1395	1.0120	1.1255	92	91	85	93
IC1	1.4932	1.4960	1.5004	1.3353	282	282	282	281
IC2	1.4366	1.4378	1.4420	1.2946	282	282	282	281
IC3	1.1471	1.1438	1.1472	1.1008	103	103	103	104
IC4	1.1518	1.1551	1.1589	1.1111	114	114	114	115

Table 7.14 Amplitude and phase of the computed M_2 tidal current at different observation stations in the Bristol Channel and Celtic Sea under natural conditions and in presence of different array configuration. The station readings at the upstream and downstream of the arrays are highlighted in grey.

Comparing the results obtained when the Channel (CH) array is operating to the naturally occurring M_2 tidal currents, it is seen that the system responds differently to the previous arrays discussed. Bearing in mind that the M_2 elevations also decrease at the Severn Estuary when the CH array is operating, it is believed that the system is moving away from resonant frequency. The reduction in the M_2 velocity magnitudes is approximately 10% at the upstream and downstream of the array (station IC1 and IC2). Maximum M_2 currents occur at the same times in the tidal cycle as for the undisturbed flow conditions. Although, there is a significant impact on the response of the Bristol Channel system by operating the CH array, this does not affect the timing of the fastest currents.

Station	Eccentricity				Inclination (°)			
	Nat	*LU*	*IL*	*CH*	*Nat*	*LU*	*IL*	*CH*
OC1	0.3461	0.3457	0.3462	0.3332	40	40	40	41
OC2	0.2934	0.2917	0.2918	0.2805	80	80	80	80
OC3	0.2333	0.2357	0.2338	0.2429	34	34	34	35
OC4	0.5635	0.5732	0.5631	0.5871	6	6	6	6
MC1	0.0901	0.0787	0.0884	0.0924	14	15	15	15
MC2	0.0613	0.0458	0.0586	0.0636	12	12	12	12
MC3	0.0943	0.0826	0.0950	0.0965	33	33	34	34
MC4	0.0956	0.0774	0.0965	0.0970	33	33	34	34
MC5	0.0137	0.0075	-0.0205	0.0073	31	31	31	32
MC6	0.0124	0.0074	0.0140	0.0138	23	22	22	24
IC1	0.0108	0.0114	0.0112	0.0278	174	174	174	175
IC2	0.0111	0.0118	0.0115	0.0200	173	173	173	173
IC3	-0.0151	-0.0147	-0.0146	-0.0134	8	8	8	8
IC4	0.0388	0.0373	0.0374	0.0360	59	59	59	59

Table 7.15 Eccentricity and inclination of predicted M_2 currents at different observation stations in the Celtic Sea and Bristol Channel under natural conditions and in presence of various array configurations. The station readings at the upstream and downstream of the arrays are highlighted in grey.

Table 7.15 shows the M_2 current ellipse parameters at the observation stations for different cases. From the table, it is seen that installing the LU array alters the ellipse structure very mildly at the Celtic Sea front. The eccentricity is decreased at stations located in the mid-Channel region. The flow is still rectilinear. The ellipse structure is changed at the immediate upstream and downstream of the LU array. When the IL array is in operation, the system responds in a similar manner as in described for the LU array. The eccentricity changes significantly at MC5, which is located at the upstream of the array (with respect to the direction of the flood tide) indicating that the M_2 ellipse is changing direction from anti-clockwise to clockwise. However, towards the east of the array, the ellipse structure does not change significantly. When the CH array is in operation, the change in the eccentricity varies throughout the Celtic Sea – Bristol Channel system. There is a slight decrease in eccentricity observed at the outer Channel stations OC1 and OC2, whereas the eccentricity tends to increase slightly until the flow reaches the Ilfracombe headland. The eccentricity is doubled at the inner Channel stations IC1 and IC2, which are located at the upstream and downstream of the array.

Table 7.16 and Table 7.17 present the S_2 tidal current characteristics of magnitude, phase lag, eccentricity and inclination.

Station	U_{mag} (m/s)				φ_{mag} (°)			
	Nat	*LU*	*IL*	*CH*	*Nat*	*LU*	*IL*	*CH*
OC1	0.1416	0.1396	0.1399	0.1394	188	187	187	188
OC2	0.1761	0.1729	0.1732	0.1739	229	230	230	229
OC3	0.1545	0.1540	0.1543	0.1529	162	161	161	161
OC4	0.1771	0.1781	0.1772	0.1746	151	152	151	151
MC1	0.1780	0.1768	0.1782	0.1708	136	140	138	136
MC2	0.2750	0.2732	0.2785	0.2617	149	150	151	150
MC3	0.2967	0.2878	0.2963	0.2887	154	142	154	154
MC4	0.2960	0.2847	0.2956	0.2877	154	143	154	155
MC5	0.4095	0.4034	0.3400	0.4014	138	138	132	138
MC6	0.3734	0.3674	0.3036	0.3636	140	141	133	142
IC1	0.4507	0.4513	0.4533	0.3896	338	339	339	339
IC2	0.4368	0.4352	0.4373	0.3676	338	339	339	340
IC3	0.3265	0.3229	0.3243	0.3056	162	163	162	164
IC4	0.3432	0.3426	0.3438	0.3274	173	175	175	176

Table 7.16 Amplitude and phase of the S_2 tidal current at different observation stations in the Bristol Channel and Celtic Sea under natural conditions and in presence of different array configuration. The station readings at the upstream and downstream of the arrays are highlighted in grey.

Table 7.16 shows that operating tidal arrays cause a small reduction in the S_2 velocity magnitudes at the outer Channel stations. Similarly to M_2 tidal current analysis, S_2 velocity magnitudes are decreased at the observation stations in the vicinity of the arrays. Maximum change in the velocity magnitudes is observed when Ilfracombe (IL) array is operating. The S_2 velocity magnitudes are reduced by approximately 18%. This is again because the flow is partially blocked which forces it to divert around the edges of the array and, also reduces the mass flux passing through the array. Operating the Channel (CH) array reduces the S_2 velocity magnitudes across the Celtic Sea and Bristol Channel area. The maximum reduction is approximately 15%, which is observed at stations located upstream and downstream of the array. The S_2 velocity phase changes are similar to the M_2 velocity phase changes. The maximum S_2 tidal currents are observed approximately 20 min earlier than the natural case when Lundy (LU) array is operating. As far as the Ilfracombe (IL) array is concerned, the

maximum S_2 currents occur 12 min prior to the natural case. The effect of Channel (CH) array to the S_2 phase lags is insignificant.

Station	Eccentricity				Inclination (°)			
	Nat	*LU*	*IL*	*CH*	*Nat*	*LU*	*IL*	*CH*
OC1	0.2014	0.2020	0.2023	0.2009	35	34	34	35
OC2	0.3488	0.3553	0.3561	0.3457	71	71	71	71
OC3	0.1579	0.1567	0.1549	0.1585	36	36	36	37
OC4	0.5321	0.5412	0.5296	0.5442	23	24	23	24
MC1	0.0897	0.0771	0.0983	0.1062	18	19	18	19
MC2	0.0298	-0.0015	0.0237	0.0316	15	14	15	15
MC3	0.0739	0.0632	0.0832	0.0831	35	35	36	36
MC4	0.0798	0.0777	0.0881	0.0867	36	35	36	36
MC5	-0.0294	-0.0304	-0.0400	-0.0087	31	31	32	32
MC6	-0.0174	-0.0205	-00075	-0.0012	23	23	23	24
IC1	0.0184	0.0067	0.0058	0.0413	175	175	175	175
IC2	0.0143	0.0028	0.0028	0.0383	174	173	173	173
IC3	0.0292	0.0257	0.0267	0.0306	8	8	8	8
IC4	0.0276	0.0213	0.0225	0.0194	59	59	59	60

Table 7.17 Eccentricity and inclination of the computed S_2 tidal current at different observation stations in the Bristol Channel and Celtic Sea under natural conditions and in the presence of various array configurations. The station readings at the upstream and downstream of the arrays are highlighted in grey.

Table 7.17 presents the characteristic parameters of the S_2 tidal currents. Table 7.17 shows that the effect of deployment of arrays seen at the outer Channel site is small when the S_2 tidal current ellipse structure is concerned. When the LU array is operating, the eccentricity of S_2 currents decreases at the stations in the vicinity of the array location, as well as the stations located in the Severn Estuary. The ellipse size is reduced throughout the Bristol Channel area. Similarly, the eccentricity decreases within the Bristol Channel site when Ilfracombe (IL) array is operating. As discussed earlier on M_2 current analysis, the eccentricity of S_2 current ellipses increase when Chanel array (CH) is in operation.

In terms of change in inclination, the operation of arrays shows no significant change to this parameter. This implies that the angle between the semi-major axis relative to the horizontal velocity axis does not change due to the energy extraction.

7.3.2. Analysis of Multiple Array Deployments

This section considers the effect of installing multiple arrays within the Bristol Channel site. The array configurations studied in this section are:

1. Lundy and Ilfracombe (LU + IL),
2. Lundy and Channel (LU + CH),
3. Ilfracombe and Channel (IL + CH) and,
4. Lundy, Ilfracombe and Channel (LU + IL + CH).

The simulations are designed by operating each array using the optimum wake velocity coefficients. Table 7.18 compares the maximum available power outputs that are averaged over a spring tide for each case study with the arithmetic sum of the individual maximum power available to the arrays in isolation. From Table 7.18, it is seen that the Lundy (LU) and Ilfracombe (IL) arrays do not interact with each other significantly in terms of available power. However, operating the Channel (CH) array in combination with other arrays, improves the performance of the CH array. This unexpected result (given that the CH array is in series with the other sites) is mainly due to the slight rise in the head at the upstream of the CH array caused by operation of other arrays. As the mass flux passing through the CH array is increased, the available power to that array is increased as well.

Case Study	Array Combinations	P_{avail} (MW)	$\sum P_{avail}$ (MW)
1	LU + IL	213.6	210.5
2	LU + CH	503.9	474.3
3	IL + CH	391.3	359.4
4	LU + IL + CH	546.7	522.1

Table 7.18 Comparison between the estimated (P_{avail}) and calculated (ΣP_{avail}) available power output averaged over a spring period for each multiple array case in the Bristol Channel.

The change in the flow field is evaluated in terms of the M_2 tidal elevations and M_2 tidal current magnitudes. Figure 7.9 shows the change in M_2 tidal elevations when multiple arrays are operating using the configurations presented in Table 7.18. Case study 1 considers the joint deployment of Lundy and Ilfracombe arrays. Figure 7.9(a) illustrates that the M_2 surface elevations are increased by 5 cm towards the Celtic Sea. However, the elevations are

decreased by an average of 1.5 cm at the Channel side of the basin. The abrupt changes in elevation observed in Swansea Bay are an artefact of the wetting and drying algorithm in the numerical model, and so are treated as spurious.

It was found in Section 6.3.1 that the presence of the CH array leads to a considerable change to the M_2 elevation from Minehead towards the tip of the Bristol Channel. The array effectively decreases the length of the Bristol Channel basin, and so it is assumed that the response of the system shifts away from the resonance frequency. This implies a reduction in observed water surface elevations. Joint operation of the LU and CH arrays (Figure 7.9.b) also results in a similar reduction in observed water surface elevations at the downstream entrance to the Bristol Channel. However, the LU + CH configuration causes a small increase (~1 cm) in M_2 elevation immediately in front of the CH array. Figure 7.9 (c) and Figure 7.9 (d) show that the system responds in a similar manner in the Bristol Channel site as CH array is being operated. However, the figures also show that inclusion of either IL or LU array (or even a combination of both arrays) do not cause a significant hydrodynamic interaction with the CH array.

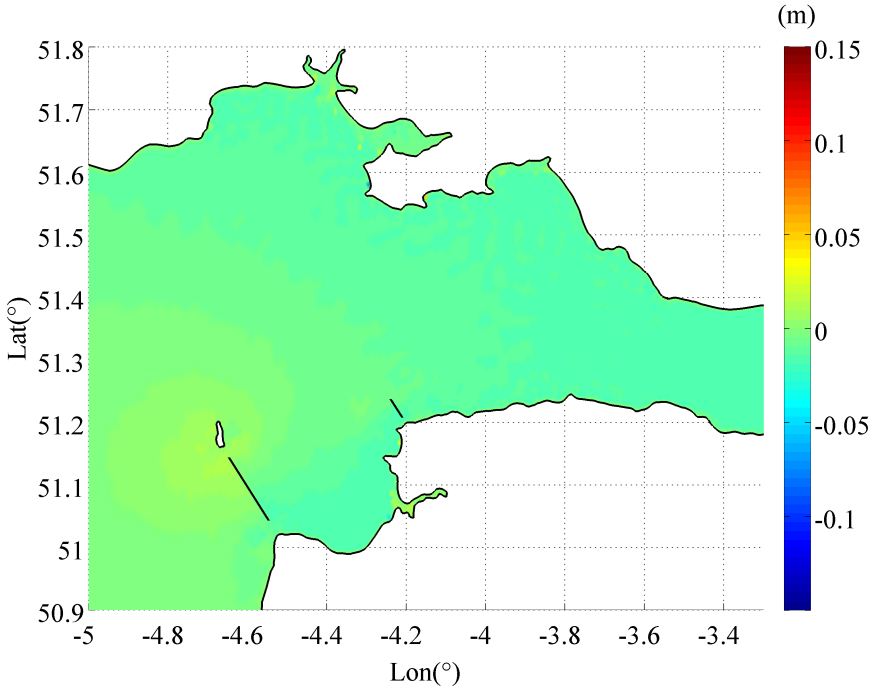

a) LU and IL arrays

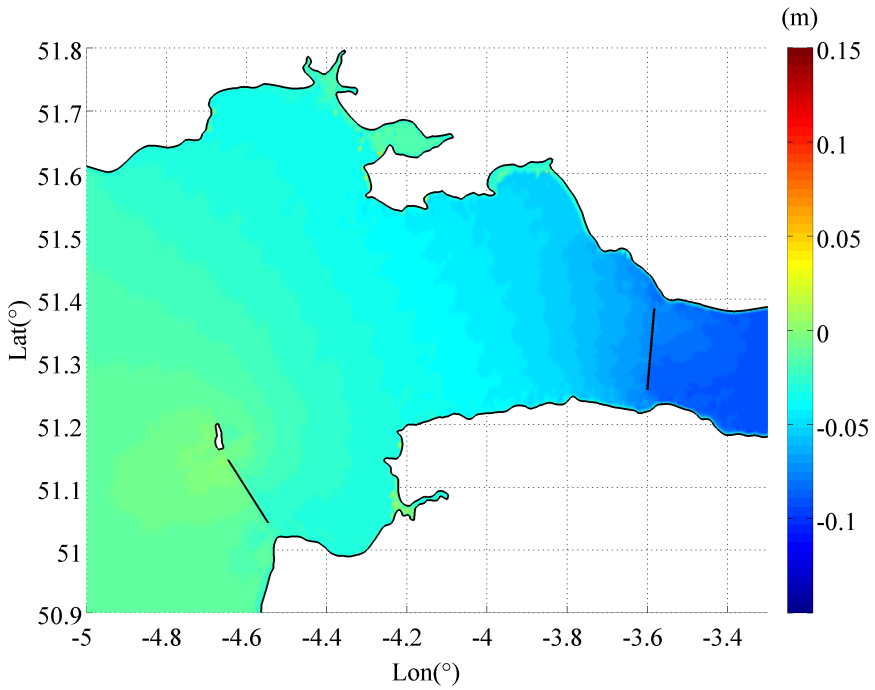

b) LU and CH arrays

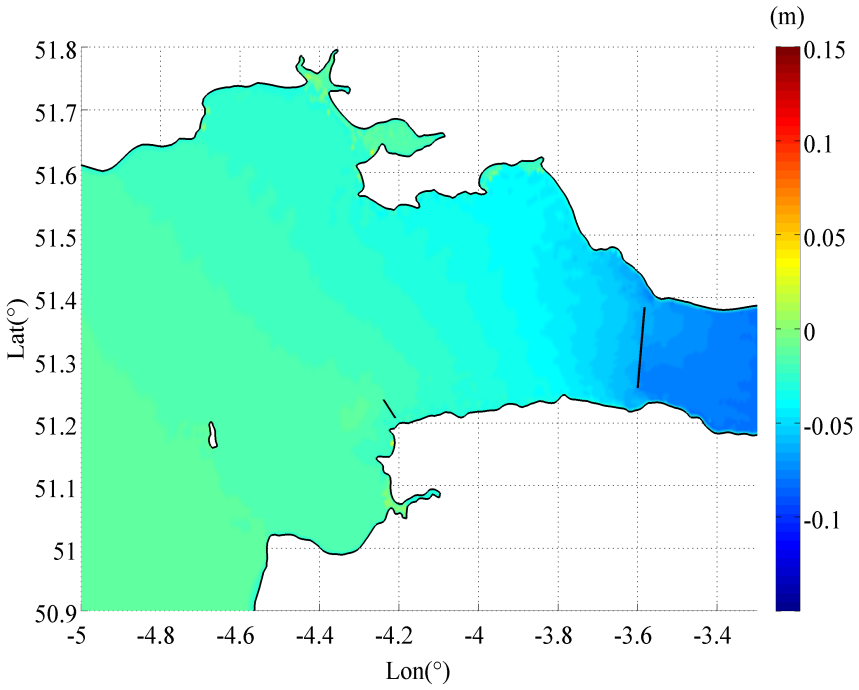

c) IL and CH arrays

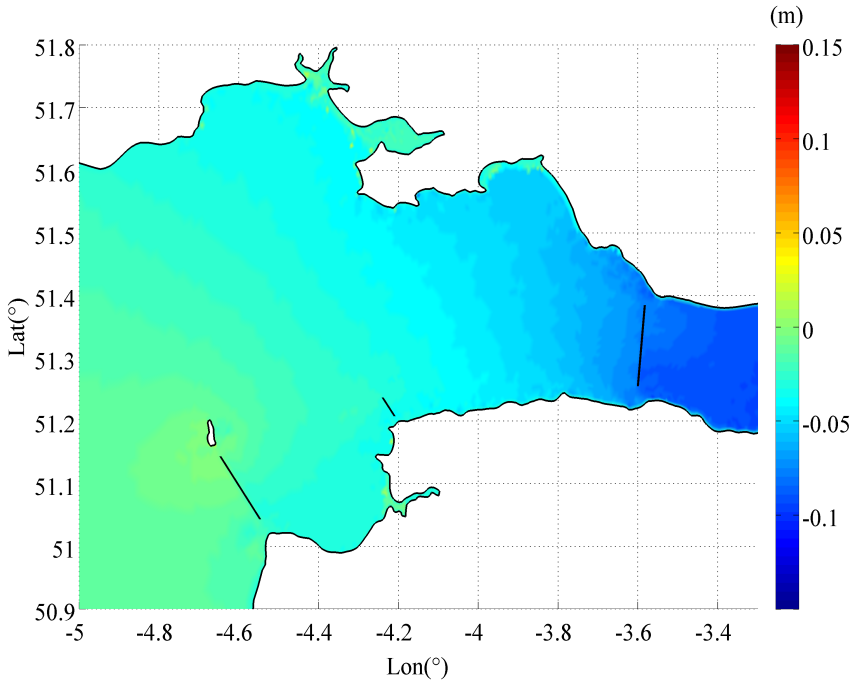

d) LU, IL and CH arrays

Figure 7.9 – M_2 amplitude change in presence of different array configurations

Figure 7.10 plots the system response to the presence of different array configurations with respect to the M_2 tidal current changes. From the figure, it is seen that the flow accelerates at the edges of the arrays due to the flow diversion. Figure 7.10(a) illustrates the combination of Lundy (LU) and Ilfracombe (IL) arrays. From this figure, it is seen that the flow is diverted to

the north of Lundy Island as the LU array is operating. The presence of IL array also contributes into this diversion. Figure 7.10(b) shows the array configuration of Lundy (LU) and Channel (CH) arrays. From the figure, there is not a direct interaction between arrays by means of change in the M_2 current velocities. For both arrays, the by-pass flow is accelerated due to the thrust applied by the turbines. Comparing Figure 7.10(a) and Figure 7.10(b), it is seen that LU and IL arrays do interact in terms of the velocities as the fast flow is further delivered towards the Welsh coasts. Figure 7.10(c) presents the results obtained for operating Ilfracombe (IL) array with the Channel (CH) array. Even though the arrays are closer to each other when compared to the array combination discussed in Figure 7.10(b), there is no evident hydrodynamic interaction observed. Figure 7.10(d) shows the change in M_2 velocity magnitudes when all three arrays are operating together. This figure also confirms that the by-pass flow is accelerated at the ends of the arrays, but there is no significant interaction between the arrays in terms of tidal hydrodynamics of the system.

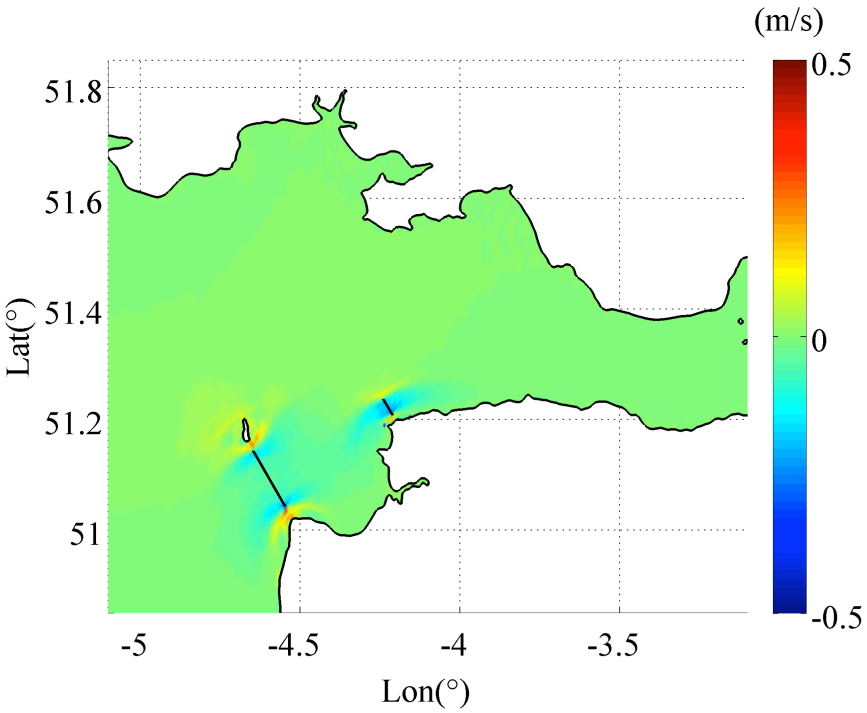

a) LU and IL arrays

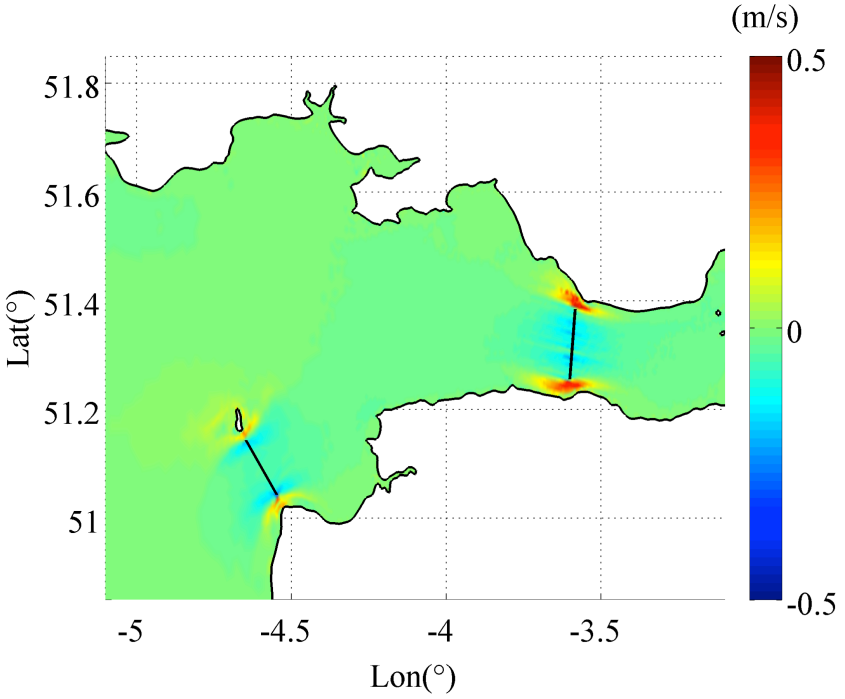

b) LU and CH arrays

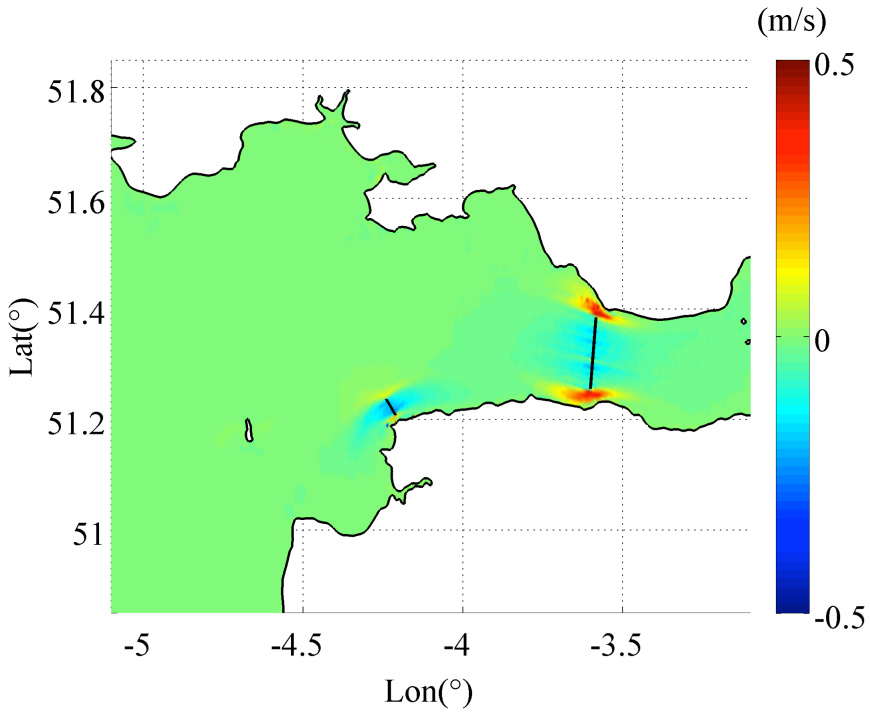

c) IL and CH arrays

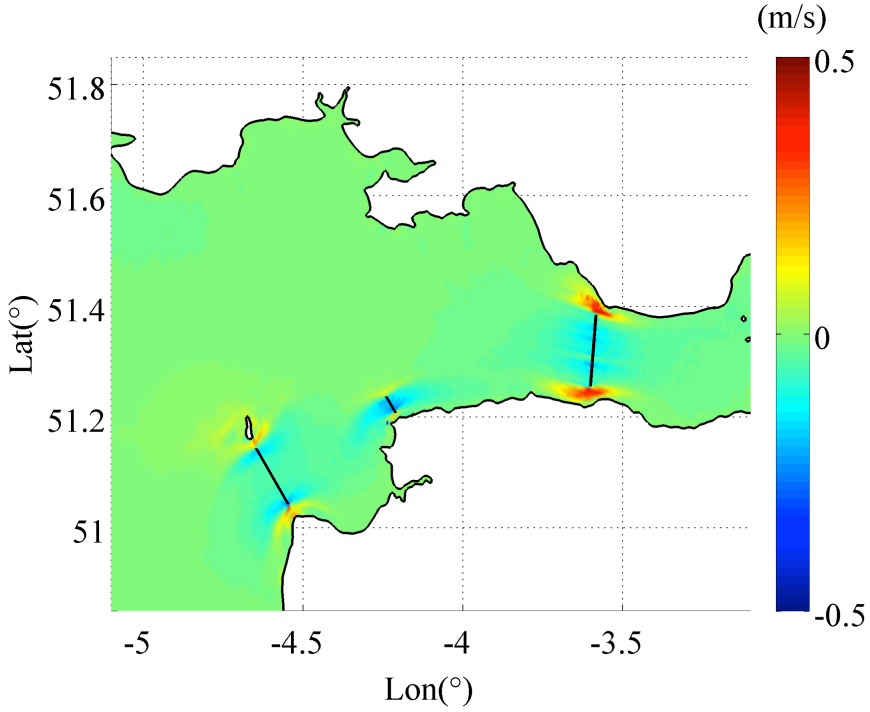

d) LU, IL and CH arrays

Figure 7.10 – M_2 current change in presence of different array configurations

7.4. Anglesey and the Bristol Chanel

Previous sections consider the analyses regarding the power available to the turbines and the hydrodynamic effect of extracting energy from the tidal stream off Anglesey and in the

Bristol Channel. These sites are geographically close to each other, thus there may be hydrodynamic interactions in the case of operating tidal farms at both these sites.

In order to investigate longer distance interaction effects, an additional test case has been prepared which considers operating all of the 6 arrays together. The model parameters are the same as in the previous analyses. The arrays are defined by the computed optimum wake velocity coefficients. This test case also considers a high blockage ratio to be applied to the flow (B = 0.5). Table 7.19 summarises the arrays and the optimum wake velocity coefficients used in the simulation. Table 7.19 also shows the power available to the three arrays deployed at each of the main sites averaged over a spring tidal period. Table 7.19 illustrates that the simulated total available power is trivially different from the sum of the three arrays operated at Anglesey and in the Bristol Channel independently: in other words the analysis indicates no significant long distance interaction between tidal farms.

Array	Optimum α_4	Individual Array P_{avail} (MW)	Simulated P_{avail} (MW) for 3 array cases	$\sum P_{avail}$ (MW)	Simulated P_{avail} (MW)
Holyhead	0.48	168.3	668.4	1162.2	1212.9
Skerries-Offshore	0.46	385.8			
Skerries-Strait	0.55	86.0			
Lundy	0.40	162.7	546.7		
Ilfracombe	0.47	47.8			
Channel	0.40	311.6			

Table 7.19 Summary of the power available to the turbine arrays located off Anglesey and in the Bristol Channel.

Considering the change in the tidal dynamics of the system, the M_2 tidal elevations show a similar change when compared to the results presented in the previous sections. As for the M_2 currents (see Figure 7.11), the far-field velocities change approximately by 0.05 – 0.1 m/s. However, this change does not affect the sites directly. Thus, it is concluded that there is no significant hydrodynamic interaction between Anglesey and the Bristol Channel sites.

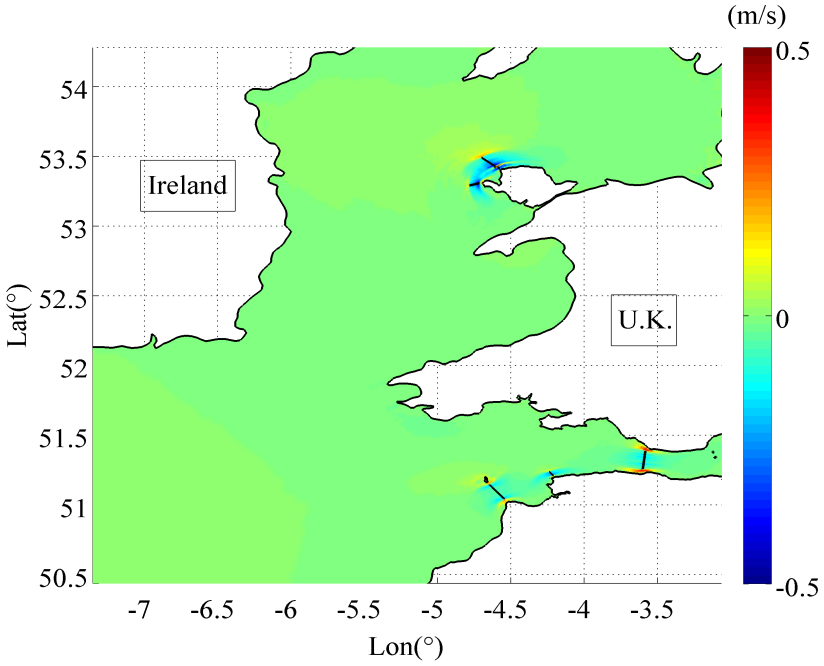

Figure 7.11 – Change in the M_2 tidal current within the Irish Sea, Celtic Sea and the Bristol Channel in case of operating all arrays considered.

7.5. Conclusions

This chapter examines the basin-scale environmental changes that occur when large arrays of tidal stream turbines are operating in selected tidal basins. For the analysis, two sites are chosen; the Anglesey headland and the Bristol Channel. A combined analysis of these sites is also conducted to evaluate the possible hydrodynamic interaction between proposed tidal array sites.

The presence of tidal turbines causes a reduction in the flow through the turbine array relative to the case wherein there were no turbines present. It is seen that, if the turbine array extend across an entire channel (see e.g. the Bristol Channel analysis) then the thrust applied to the flow causes reduced flow velocities primarily in the vicinity of the array. In the case of a partially blocked flow as studied in the Anglesey Skerries case, there will be a fast bypass flow around the ends of the turbine array. This in turn, results in a reduced mass flux passing through the turbine arrays, which limits the available power to the turbines.

The changes to the tidal dynamics are geographically contained to the near vicinity of the turbine array. Hence, there is virtually no hydrodynamic interaction between the turbine arrays installed at the Anglesey and the Bristol Channel.

Overall, at peak available energy extraction, there would be a measurable change in the tidal dynamics, which may lead to a significant environmental impact. Assessing this impact is beyond the scope of this thesis. However, taking these effects into account is important when designing a tidal turbine farm, as there may need to be a compromise between the change to the tidal dynamics of the site and the amount of power to be generated.

Chapter 8

Conclusions and Recommendations

Tidal stream power offers considerable promise as a renewable energy resource, given increasing worldwide energy demand and environmental concerns regarding fossil fuels. This thesis has considered a resource assessment of selected tidal sites around the UK in order to estimate an upper limit to the available power at each site and simulate the consequent hydrodynamic changes due to the presence of tidal turbines. Following the approach taken by Draper *et al*. (2010) and Draper (2011), a line sink of momentum was embedded in a selected numerical solver in order to represent the effects of tidal turbine fences. The momentum sink across the turbines was determined as a head drop using Linear Momentum Actuator Disk Theory (LMADT) extended to include wake mixing effects (Houlsby *et al*. 2008). Incorporation of the head loss from LMADT into the numerical model by inserting a momentum sink is more accurate than alternative techniques based on increased bed stress in estimating the power potential of a site. Moreover, the LMADT solution enabled a distinction to be made between the power available to the turbine devices and the total power that is extracted from the current, which includes the mixing losses. This method was applied to assess the tidal stream power potential at selected sites near the Anglesey Skerries and in the Bristol Channel. The following sections summarise the main conclusions derived from the modelling techniques and results. Section 8.4 proposes topics for future research. Finally, Section 8.5 provides a brief summary of the work conducted in this thesis.

8.1. Numerical Model

The two-dimensional Shallow Water Equations (SWEs) were used to model the ocean tides. The selected numerical solver (DG-ADCIRC) used discontinuous Galerkin Finite Element Method (DG-FEM) to solve the SWEs. A series of idealised tests was employed to verify DG-ADCIRC code, including uniform flow in an open channel, laminar flow past a sidewall expansion, Coriolis advection of a Gaussian hump, and still water in a basin with

non-uniform fixed bed topography. The DG-ADCIRC hydrodynamic solver provided satisfactory results when compared against analytical solutions.

The DG-ADCIRC hydrodynamic solver was then modified to incorporate a line sink of momentum due to the presence of the conceptual tidal turbine arrays. The associated momentum sink was computed using a sub-grid model based on Linear Momentum Actuator Disk Theory (LMADT). As mentioned above, LMADT was used to approximate the local flow-field in the presence of tidal turbines, and provided an accurate representation of the flow velocity at the turbines for evaluating the available power. For prescribed turbine operating conditions (known blockage ratio and wake velocity coefficient) and the upstream flow conditions, LMADT provided the head drop and flow velocity across the turbines. The derivation of LMADT for open channel flow with a free surface and downstream mixing allowed the efficiency of the turbines to be described as the ratio of the extracted power by the turbines to the total power removed from the tidal stream. A variety of turbine operating conditions were examined as a part of the parametric study. It should be noted that use of a high blockage ratio with an optimum wake velocity coefficient leads to higher power extraction from the stream. However, this has a limit. Increasing the blockage ratio while using an optimum wake velocity coefficient results in critical bypass flow. In this case, the solution of the quartic equation in β_4 (equation 3.9) becomes physically inadmissible. Due to the excessive energy extraction, the head drop across the turbine becomes too large resulting in very low downstream depths. This implies that the energy can only be conserved in the bypass flow, which eventually becomes critical (Draper, 2011). Provided this situation does not arise, it is reasonable to represent tidal turbines using LMADT as a head loss momentum sink in the numerical model.

This study aimed to estimate the maximum power that can be extracted by tidal turbine arrays and assess the far-field effects of energy extraction in the designated areas around the UK. In this respect, a calibrated numerical model has been developed, which is validated against field measurements. The development of the model involved constructing two unstructured finite element models, one with and one without the inter-tidal zones around the Bristol Channel and the Welsh coasts. The numerical models consider the south-west coasts of the UK including the Irish Sea and the Celtic Sea. The southern open boundary extended

beyond the European continental shelf in order to model accurately the quarter-wavelength resonance occurring in the Bristol Channel. The models were forced using the dominant semi-diurnal M_2 and S_2 tidal components.

The inter-tidal zones around the Bristol Channel and the Welsh coasts were omitted in the simpler model (DG-ADCIRC), whereas these regions were included in the more complex model (DG-ADCIRC-WD). The aim of constructing two models was to assess the impact of including the inter-tidal zones in the domain – which required a wetting and drying treatment within the simulation – on the model accuracy. The model validation study was undertaken for both models using field data. The DG-ARCIRC model predictions were found to agree well with the observations, especially with respect to water surface elevation time series and harmonic analysis results. Less good agreement was obtained between predicted and measured currents. There are several reasons for the discrepancies. Firstly, a relatively large bed friction coefficient was used in the DG-ARCIRC model to obtain a stable solution. This in turn resulted in predictions of slower currents. Secondly, comparisons with current measurements are intrinsically more difficult because of uncertainties related to the observations. The current measurements were derived from recordings of the direction and magnitude of the currents, and so even a small error in direction would have caused a large error in the magnitude of the velocity components.

The DG-ARCIRC-WD model included the intertidal zones, which used a wetting and drying treatment to handle the moving boundary problem. It was found that the DG-ARCIRC-WD model reproduced more accurately the tidal hydrodynamics observed in the Bristol Channel. Use of a smaller bed friction coefficient in the computation provided closer agreement between predictions and measurements of water elevations and currents.

8.2. Power Assessment

This thesis aimed to assess an upper limit for the tidal stream resources of the Anglesey Skerries and the Bristol Channel. Both analyses indicated that parallel configurations perform better then arrays deployed in series. With this in mind, the parametric studies conducted on the Anglesey Skerries and the Bristol Channel showed that the maximum mean available power values are 301.2 MW and 233.9 MW respectively for the array configurations considered. These upper limits consider only the power that is extracted from the M_2 tides.

The parametric studies showed that the amount of power that can be extracted by the turbines is limited due to the geometry of the tidal basin, the location of the turbine arrays, the array configurations, the turbine operating conditions and more importantly the hydrodynamic disturbance within the tidal system. The results demonstrate that locations with high natural kinetic energy fluxes are sensible options for tidal array deployments. In terms of operating conditions, it was found that increasing the blockage increases the available power given that an optimum wake velocity coefficient is used. However, with a high induction factor, setting the blockage too high would choke the flow, which inevitably means that no power can be extracted from the current. Increasing the blockage results in increasing the thrust applied to the flow, which causes the flow to bypass the array. Regarding the array configuration, it was found that extending the length of the array (parallel) is more advantageous than deploying multiple arrays in series, especially when working with high blockage ratios.

The geometry of the tidal basin is also important. The analysis conducted on the Anglesey Skerries, which is a headland site, showed that the available power is restricted mainly by the bypass flow. The model simulations also indicated that more power can be extracted by turbine arrays when placed closer to the Skerries. The bypass flow is dependent on the array configuration and is higher on the ocean side when the arrays are deployed in series. The Bristol Channel analysis showed that the best performing arrays of those considered were located between Aberthaw and Wales. The closure problem indicated how the available energy improves by extending the length of the array, which agrees well with Draper *et al*. (2013), Vennell (2012) and Vennell (2011).

8.3. Local Hydrodynamics

To examine and quantify the disturbance caused by turbine arrays to the local hydrodynamics, this thesis considered the change in the M_2 tides (see Chapter 7). In both tidal site studies, it was found that neither the amplitude nor the phase of the M_2 constituent changed significantly, even at maximum power extraction. For the Anglesey Skerries headland site, the hydrodynamic changes were mainly confined to the vicinity of the tidal array. In the Bristol Channel analysis, it was, however, observed that the M_2 elevation amplitude decreased by approximately 10 cm throughout the region between the arrays and the mouth of the Channel. The Bristol Channel site is particularly sensitive to tidal resonance,

and so is very susceptible to perturbation. Deployment of tidal arrays would inevitably lead to interference with the natural resonance of the system.

Chapter 7 presented a unique analysis of the large-scale hydrodynamic changes that can occur when all the proposed arrays in the Anglesey and the Bristol Channel are operating. The analysis revealed that no significant far-field effects resulted from the simultaneous operation of multiple arrays located at the various tidal sites considered.

8.4. Future Research

8.4.1. Comparisons with the Increased Bed-Friction Approach

Several approaches are presently used in practice to represent the hydrodynamic effect of tidal array deployments in two-dimensional shallow water solvers. A commonly used method is to smear the drag applied by the turbines over an area within the computational domain by increasing the bed friction coefficients of given nodes. The main advantages of this approach are that it requires no modifications to the source code and is easy to implement in the selected numerical code (DG-ADCIRC). However, as Draper *et al* (2010) discuss, the drag coefficient included in the model is not associated with a particular turbine design and does not include the effect of array configuration (i.e. parallel or series) in the flow domain. The method provides a theoretical amount of power that can be extracted from the stream, which includes the energy that is lost through wake mixing. Vogel *et al* (2013) also discuss these disadvantages of the method and identify that the power that can be usefully extracted from a site is dependent on the flow velocity at the turbines and the total mass flux entering the flow. In this respect, Vogel et al highlight that the accurate flow velocities at the turbines cannot be captured by smearing the drag over an element.

An approximation to the local flow field is possible by employing an analytical solution such as the linear momentum actuator disk theory discussed in this thesis. This approach is embedded to the two-dimensional depth-averaged model following Draper (2011) by incorporating a line sink of momentum in the computations. The main advantage of this method is that it enables a distinction to be made between the power that is solely extracted by the turbines to the total power that is removed from the tidal stream. Using this method provides more accurate assumptions on the local flow velocity at the turbines, which in turn ensures accuracy in the power output estimations. Representing turbines as a discontinuity in

the computations enables to capture the flow diversion due to the additional resistance applied to the flow by the turbine arrays, which effectively includes the effects of deploying tidal arrays to the far-field hydrodynamics. However, as discussed previously, LMADT sub-grid model does not account for vertical velocity changes due to the power extraction, thus the effect turbines to the flow field are not represented accurately. Additionally, the method does not account for electrical and mechanical losses, which results in overestimations in drawing an upper bound for the available power at a site.

It should also be noted that it is still unknown which method performs better in terms of accurately estimating the power that is available to the turbines. To address this issue, Draper *et al* (2013) conducted a study to evaluate the performance of using a line sink of momentum approach in modelling the flow conditions around a tidal fence placed at an idealised headland by comparing their numerical results with large-scale laboratory experimental results. Comparisons between the two sets of results show that the numerical model using a line-sink of momentum approach estimate the thrust applied by the turbine fence reasonably accurately, although this study was limited to a single row of turbines.

The line sink of momentum approach embedded in the DG-ADCIRC assumes that the upstream flow conditions, the blockage ratio and also the thrust applied to the flow are known. The thrust is calculated within the code by using the prescribed wake velocity coefficient, which enables the resultant equation set to be in the order of a cubic. It is possible to include a subroutine in the DG-ADCIRC code to evaluate the upstream and downstream flow conditions as a user-defined drag coefficient approach to extract a similar amount of power from the tidal current. However, LMADT solution is still needed to evaluate the ratio of the power that is extracted solely by the turbines.

8.4.2. Response Curve of the Severn Estuary/Bristol Channel System

The Severn Estuary/Bristol Channel system is a dynamically complex system, which is well known for its quarter-wavelength resonance. The analysis conducted on the Bristol Channel in Chapter 6 aimed to explain this observed resonant response in the system, however, the complexity of the system merits further investigation. This further analysis could address the following points:

- Explaining the importance of the model boundaries on the observed response of the system,
- Investigating the possibility of a coupled Celtic Sea – Bristol Channel resonance observed within the system and,
- Understanding the global effects of extracting energy from the Bristol Channel.

8.4.3. Environmental Impact of Energy Extraction

At peak available energy extraction, there is a measureable change in the tidal dynamics, which could lead to significant environmental impacts. It is important that the decision to deploy tidal turbines includes environmental impact assessment in addition to economic and social assessments. Draper *et al.* (2013) and Kadiri *et al.* (2012) have pointed out that the geometry of the basin plays a major role in tidal hydrodynamics that affect the regional environment. For an idealised headland, Draper *et al.* (2013) state that inserting tidal arrays would increase the mean bed shear stress, which inevitably increases the transport of suspended sediments and pollutants. The water quality would also be affected by the increased amounts of suspended sediments and pollutants. As suggested by Ahmadian and Falconer (2012) further studies are needed to evaluate the environmental effect of tidal array deployments.

The numerical solver used in this study (DG-ADCIRC) is coupled with a sediment transport model, thus it is feasible to investigate the sedimentation in a tidal system. However, care must be taken to conduct an analysis using both the sediment transportation and a line sink of momentum routines, as there may be instabilities related to coding structures. In order to evaluate the change in the water quality, the DG-ADCIRC source code must be modified to include a water quality model coupled within the hydrodynamic solver. To the author's knowledge, no attempt has been made so far to include this feature in the DG-ADCIRC code.

8.4.4. Severn Tidal Barrage Analysis

This thesis aimed to draw an upper limit to the maximum available power that may be extracted from the fast tidal currents occurring at the Bristol Channel and the Anglesey Skerries sites. However, historically the Bristol Channel was considered as a site to construct a tidal barrage. According to the DECC (2010) report, the UK Government still considers this scheme to be viable in the future. Although, previous studies determined the tidal range

resource of the Bristol Channel, it is unclear how much power can be generated by a Severn tidal barrage in accordance with tidal arrays deployed in the Bristol Channel. Research undertaken by Xia *et al.* (2012) considers the magnitude of the annual energy output of a proposed barrage across the Severn Estuary. In the analysis, Xia *et al.* used a theoretical and a numerical method separately to compute the annual tidal energy output from a barrage. The numerical model was modified to include a routine to estimate this power output from the barrage. A similar modification is required in the DG-ADCIRC code to represent a tidal barrage in the computations. The DG-ADCIRC code originally has the capability to model internal barriers, such as levees, or raised roads, within the computational domain (Dawson *et al.*, 2011). In the model, the effects of these structures to the local flow field are included by manipulating the numerical flux terms. To account for a tidal barrage, the subroutine associated with the internal barrier calculations need to be altered to account for the operating mode of the barrage. The modification to the original DG-ADCIRC source code is expected to be minimal to incorporate the effect of tidal barrages in the computations. With this modification, it will be possible to analyse the performance of a proposed tidal array when a tidal barrage is operating simultaneously at this designated tidal site.

8.5. Summary

This study considered evaluating the maximum amount of power that can be generated from tidal currents, while assessing the far-field effects of such energy extraction. A two-dimensional hydrodynamic solver, DG-ADCIRC, which is based on a discontinuous Galerkin finite element method, has been employed to conduct the analyses. The DG-ADCIRC has been verified against several benchmark tests. The DG-ADCIRC solver is then modified to include a line sink of momentum to incorporate the effects of deploying conceptual tidal turbine arrays in a basin. The tidal turbines were parameterised using a sub-grid model using Linear Momentum Actuator Disk Theory (LMADT). A validated and calibrated numerical model of the south-west coasts of the UK including the Irish Sea and the Celtic Sea has been constructed to model the naturally occurring tides. The constructed model has then been used to conduct parametric studies to evaluate the importance of tidal array locations, configurations and operating conditions on the available power at the Anglesey Skerries and the Bristol Channel. It is found that connecting the arrays in parallel (i.e. extending the length

of the turbine array) is more advantageous than series array deployments, especially when using a high blockage ratio.

For Anglesey Skerries site, it was found that the turbines closer to the Skerries is more effective in delivering power. The analysis also showed that, especially when high thrust is applied to the flow, connecting the arrays in parallel rather than in series is more effective. The ASA1+ASA2 parallel array configuration delivers a maximum average available power of 301.2 MW for a high blockage case. However, for a four-row series connection (ASA2+ASB2+ASC2+ASD2) the available power is only 257 MW.

For Bristol Channel site, a similar parametric study has been conducted. Consistent with the Anglesey Skerries outcomes, it is found that parallel arrays perform better in the Bristol Channel area when compared to series array deployments. Using a high blockage case, the maximum averaged available power delivered by the parallel BCL3 array is 233.9 MW, whereas this value is only 214.1 MW for the series R1-BCL304 array connection.

The study also examined the potential tidal farm interactions by deploying several tidal arrays at both Anglesey Skerries and the Bristol Channel. The study concluded that energy extraction from the currents affects the flow field in the vicinity of the turbines significantly, however, at a larger scale these effects are ceased.

Appendix 1

Linear Momentum Actuator Disk Theory Applied on an Open-Channel Flow

Linear momentum actuator disk theory (LMADT) is an extension to actuator disk theory (ADT), proposed by Froude (1889), which provides a one-dimensional analysis of the steady flow field around a ship propeller. ADT approximates the propeller as an infinitely thin disk that shows no resistance to air passing through it, under incompressible flow assumptions (Horlock, 1978). In the analysis, the thrust on a real propeller is replaced by the uniform normal pressure distribution on the actuator disk (Van Kuik, 2007). Lanchester (1915) and Betz (1920) independently applied actuator disk theory to assess the performance of wind turbines, and defined an upper limit of kinetic energy that can be converted to usable power (Bergey, 1979). In their studies, Lanchester and Betz showed that the power available to the turbine cannot exceed 16/27 of the total upstream kinetic energy flux passing through the actuator disk. This upper limit is called the Lanchester-Betz limit, and it has been used to design wind turbines over many years. The derivation of the limit can be obtained through mass and momentum conservation laws, and by applying the Bernoulli relations to the fluid passing through the turbine (see Figure 1). The momentum change is used to evaluate the thrust applied on the disk. The turbine power is then estimated by multiplying the calculated thrust by the velocity at the disk. The Lanchester-Betz limit is obtained by dividing the turbine power by the power of the unconstrained uniform flow passing through the turbine area (Gorban *et al.*, 2001). However, in reality, the efficiency of the designed turbines cannot reach the Lanchester-Betz limit, mainly due to wake formation, mechanical inefficiencies, and aerodynamic drag (Draper, 2011).

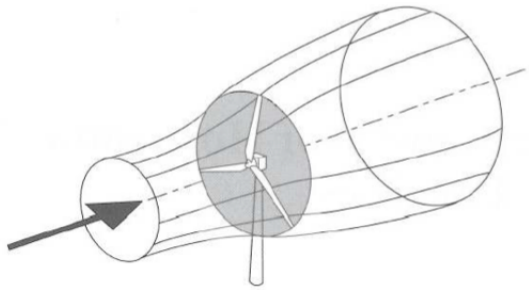

Figure 1 - Flow field around a wind turbine represented as a stream tube (Burton *et al*., 2001).

The successful utilization of wind as a renewable energy source has encouraged engineers to apply LMADT to the analogous design of tidal turbines. However, standard LMADT assumes unbounded flow conditions, and hence is not applicable to tidal turbine design in a straightforward way. Bryden *et al.* (2007) explain that the standard Betz model is derived assuming that the flow is incompressible and unconstrained, meaning that the boundaries are sufficiently far away from the turbines. However, in open channel flow, the flow is constrained by the seabed and the free surface, which influences the behaviour of the downstream flow. Furthermore, the operating fluid (water) must be treated as heavy, as there are important gravitational effects, which do not feature in the original analysis.

Application of LMADT to open channel flow has been documented in many studies involving both analytical and numerical models, which were summarised in Chapter 1 (Karsten *et al.*, 2013; Vogel, 2012; Draper, 2011; Whelan *et al.*, 2009; Garrett and Cummins, 2005). Of these studies, Whelan *et al.* (2009) introduced a variable free surface in their model, which considers finite upstream Froude numbers. A similar approach was undertaken by Houlsby *et al.* (2008) in order to include downstream mixing, as the flow is not uniform after passing through the turbine. Houlsby *et al*. (2008) approximated open channel flow by a combination of both volume (Garrett and Cummins, 2005), and pressure-constrained model, which is valid under the following assumptions (Draper, 2011):

- Uniform upstream flow of constant velocity u, depth h, in a channel of width b,
- Actuator disks represent turbines with blockage ratio ($B = A/hb$) that accounts for the effective cross-section of the channel hb,
- The flow is inviscid, and
- Pressures in the upstream and mixing regions are hydrostatic (see Figure 2).

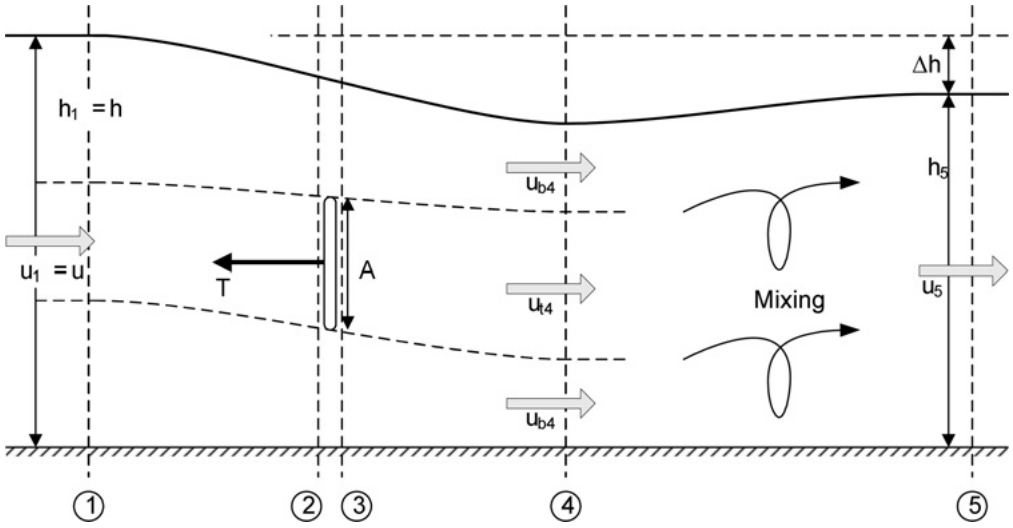

Figure 2 - An actuator disk placed in an open channel flow with a free water surface (figure taken from Draper *et al.*, 2010).

The analysis conducted by Houlsby *et al*. has two parts. In the first part, expressions for thrust and power are derived using the Bernoulli equation in accordance with mass and momentum conservation laws. In the second part, the contribution of downstream mixing is investigated in determining the turbine efficiency.

The flow field is indicated as in Figure 2 for an open channel flow with a free surface elevation. The flow field is divided into several stations for the analysis. At stations 1, 4, and 5, it is assumed that the pressure is hydrostatic. In the analysis, the upstream uniform flow is denoted as u, the turbine velocities at stations 2 and 4 are $u_{t2} = \alpha_2 u$ and $u_{t4} = \alpha_4 u$ respectively, where α_2 is the turbine velocity coefficient and α_4 is the wake velocity coefficient. Considering that the bypass flow velocity coefficient is β_4, the bypass flow velocity can then be computed by the relation, $u_{b4} = \beta_4 u$.

In Figure 2, T represents the thrust applied to the fluid by the turbine with a swept area of A, and a blockage ratio of B and Δh is the associated head difference with respect to the energy that is extracted from the flow (Draper *et al.*, 2010; Houlsby *et al.*, 2008).

The first part of the analysis begins with the determination of T. In this respect, the Bernouilli equation is firstly applied to the bypass flow between stations 1 and 4,

$$h + \frac{u^2}{2g} = h_4 + \frac{u^2 \beta_4^2}{2g}, \qquad 1$$

and secondly on each side of the turbine flow (stations 2 and 3),

$$h + \frac{u^2}{2g} = h_{2t} + \frac{u^2\alpha_2^2}{2g}, \tag{2}$$

$$h_{3t} + \frac{u^2\alpha_2^2}{2g} = h_4 + \frac{u^2\alpha_4^2}{2g}. \tag{3}$$

Combining equations 2 and 3 provides a relation for the head drop across the turbine,

$$h_{2t} - h_{3t} = \frac{u^2}{2g}(\beta_4^2 - \alpha_4^2). \tag{4}$$

The head drop can be related back to the thrust applied on the flow by the turbine by,

$$\frac{u^2}{2g}(\beta_4^2 - \alpha_4^2) = \frac{T}{\rho g B b h}. \tag{5}$$

where ρ is the density of the fluid and g is the gravitational acceleration. The thrust applied to the flow can also be obtained by the momentum equation applied across stations 1 and 4,

$$\frac{1}{2}\rho g b(h^2 - h_4^2) - T = \rho u^2 b h B\alpha_2(\alpha_4 - 1) + \rho u^2 b h(1 - B\alpha_2)(\beta_4 - 1)\,. \tag{6}$$

Substituting equation 5 into equation 6 to eliminate T, the momentum equation becomes,

$$\begin{aligned}\frac{1}{2}g(h^2 - h_4^2) - Bh\frac{u^2}{2}(\beta_4^2 - \alpha_4^2) \\ = u^2 hB\alpha_2(\alpha_4 - 1) + u^2 h(1 - B\alpha_2)(\beta_4 - 1)\,.\end{aligned} \tag{7}$$

Lastly, applying the continuity equation between stations 1 and 4 provides,

$$h_4 = Bh\frac{\alpha_2}{\alpha_4} + h\frac{(1 - B\alpha_2)}{\beta_4}, \tag{8}$$

which can be reorganised to give,

$$\alpha_2 = \frac{\alpha_4\big(h(1 - \beta_4) + \beta_4(h - h_4)\big)}{Bh(\alpha_4 - \beta_4)}. \tag{9}$$

Rearranging equation 9 by using equations 1, 7, and 8 provides the constant pressure-volume boundary derivation of the LMADT (Houlsby *et al.*, 2008),

$$\alpha_2 = \frac{2(\beta_4 + \alpha_4) - \dfrac{(\beta_4 - 1)^3}{B\beta_4(\beta_4 - \alpha_4)}}{4 + \dfrac{\beta_4^2 - 1}{\alpha_4\beta_4}}. \tag{10}$$

Equation 10 provides a relation of the flow velocities across the turbine, which accounts for the effect of the bypass flow and can be solved once B and β_4 are prescribed, while defining either α_2 or α_4. Solution of equation 10 is of importance for calculating the thrust applied and power extracted by the turbine. Considering that the bypass flow velocity will change with respect to the variable upstream Froude (Fr) number, β_4 needs to be calculated for varying upstream flow conditions. The relation for β_4 is,

$$\frac{Fr^2}{2}\beta_4^4 + 2\alpha_4 Fr^2\beta_4^3 - (2 - 2B + Fr^2)\beta_4^2 - (4\alpha_4 + 2\alpha_4 Fr^2 - 4)\beta_4 + \left(\frac{Fr^2}{2} + 4\alpha_4 - 2B\alpha_4^2 - 2\right) = 0\,. \tag{11}$$

Equation 11 is quartic in bypass velocity coefficient β_4, and can be solved for defined blockage ratio B, upstream Froude number Fr, and wake velocity coefficient α_4. However, when the bypass flow becomes critical, equation 11 becomes physically inadmissible (Draper, 2011; Whelan *et al.*, 2009; Houlsby *et al.*, 2008).

When the roots are real, it is possible to calculate the thrust applied to the flow and the associated power extracted by the turbines (Houlsby *et al.*, 2008),

$$T = \frac{1}{2}\rho u^2 Bbh(\beta_4^2 - \alpha_4^2) = \frac{1}{2}\rho u^2 BbhC_T, \tag{12}$$

$$P = \alpha_2 uT = \frac{1}{2}\rho u^3 Bbh\alpha_2(\beta_4^2 - \alpha_4^2) = \frac{1}{2}\rho u^3 BbhC_P, \tag{13}$$

where C_T and C_P indicate the thrust and power coefficients respectively. In equation 12, the thrust coefficient is defined as $C_T = \beta_4^2 - \alpha_4^2$. Similarly the power coefficient in equation 13 is defined as, $C_P = \alpha_2 C_T = \alpha_2(\beta_4^2 - \alpha_4^2)$.

The second part of the analysis indicates the effect of downstream mixing in the efficiency of power extraction. Taking into account the downstream mixing and applying momentum conservation between stations 1 and 5 provides,

$$\frac{1}{2}\rho gb(h^2 - (h - \Delta h)^2) - T = \rho bhu\left(\frac{uh}{h - \Delta h} - u\right). \tag{14}$$

Substituting the thrust from equation 5 into equation 14, and rearranging gives,

$$\frac{1}{2}\left(\frac{\Delta h}{h}\right)^3 - \frac{3}{2}\left(\frac{\Delta h}{h}\right)^2 + \left(1 - Fr^2 + \frac{C_T BFr^2}{2}\right)\frac{\Delta h}{h} - \frac{C_T BFr^2}{2} = 0. \tag{15}$$

Equation 15 is a cubic expression, which defines the relative head drop ($\Delta h/h = (h - h_5)/h$) when the turbine operating conditions (B and α_4) are defined for prescribed flow conditions (upstream Fr).

It is important to highlight one important result from the analysis made by Houlsby *et al*. (2008) and Draper (2011), which is that the actuator disk is removing potential energy from the flow rather than the kinetic energy, which is observed as a relative head difference across the turbine. To conserve mass, at the downstream of the turbine, the velocity of the flow accelerates to compensate for the head drop. This result is in contradiction with the classical LMADT applied to the wind turbines, in which the turbines extract kinetic energy of the flow thus causing a reduction in the immediate downstream flow velocity (Draper, 2011).

For zero-Froude number flow, equation 15 provides a relation in terms of relative head drop, which determines the total amount of power that is extracted from the turbine. Under the assumption of the inviscid flow, the turbine efficiency (η) is then defined as the ratio of the power extracted by the turbine to the total power loss from the tidal stream (Draper, 2011),

$$\eta = \frac{P_{turbine}}{P_{turbine} + P_{wake}}. \qquad 16$$

The power extracted by the turbines ($P_{turbine}$) is given by equation 13, and the power lost in the wake (P_{wake}) is provided by Houlsby *et al*. (2008). Using these relations and substituting them in equation 16 provides the turbine efficiency as,

$$\eta = \frac{P_{turbine}}{\rho g u b h \Delta h}\left(1 - Fr^2 \frac{1 - \frac{1}{2}\left(\frac{\Delta h}{h}\right)}{\left(1 - \frac{\Delta h}{h}\right)^2}\right)^{-1}. \qquad 17$$

One of the conclusions Draper (2011) derives from equation 17 is that the efficiency converges to α_2 when the upstream Froude number converges to zero, noting that $P = \alpha_2 u T$. Draper (2011) notes that this result holds true for the volume-constrained flow analysis of Garrett and Cummins (2007). Draper (2011) derives the efficiency for arbitrary Froude number flows as,

$$\eta = \alpha_2 \frac{(1 - \Delta h/2h) - Fr^2(\Delta h/h)^{-1}}{1 - Fr^2(1 - \Delta h/2h)(1 - \Delta h/h)^{-2}}. \qquad 18$$

When the upstream Froude number and the associated head difference are very small, such as the tidal flows, the efficiency reduces to (Draper, 2011),

$$\eta \approx \alpha_2 \left(1 - \frac{\Delta h}{2h}\right). \qquad 19$$

Equation 19 indicates that the efficiency is maximised when α_2 converges to 1, while $\Delta h/h$ converges to zero. This implies no energy extraction, which in turn shows that the efficiency of a turbine should not be taken as an optimisation parameter (Draper *et al.*, 2013; Draper, 2011; Houlsby *et al.*, 2008). However, for flow conditions when the Froude number and downstream depth change are given, the efficiency increases with increasing turbine velocity coefficient α_2, which is in relation with the blockage ratio, B. This implies that with increasing the blockage ratio, the power efficiency might be improved when the upstream Froude number of the flow and downstream depth change are fixed, while keeping α_2 and B in an optimum range so that the bypass flow will not become critical (Draper *et al.*, 2013; Draper *et al.*, 2010). These results are the conclusions highlighted by Draper *et al.* (2010), which are supported by several parameter studies for optimising these values to obtain high efficiency for idealised cases.

Bibliography

Abbott, M.B. and Minns, A.W. (1979) *Computational Hydraulics*, Ashgate Publishing Co., Brookfield, Ct. Great Britain.

ABPmer, MET, Garrard Hassan, and Proudman Oceanographic Laboratory (2004) Atlas of UK Marine Renewable Energy Resources.

Adcock, T.A.A., Borthwick, A.G.L. and Houlsby, G.T. (2011) The open boundary problem in modelling tidal energy extraction, 9th EWTEC, Southampton, U.K.

Adcock, T.A.A. Draper, S., Houlsby, G.T., Borthwick, A.G. and Serhadlıoğlu, S. (2013) The available power from tidal stream turbines in the Pentland Firth, *Proceedings of the Royal Society A: Mathematical, Physical and Engineering Science,* **469**: 2157.

Adcock, T.A.A. and Draper, S. (2014) Power extraction from tidal channels – multiple tidal constituents, compound tides and overtides, *Renewable Energy*, accepted.

Admiralty Charts (2006) North coast of Scotland pilot. N.P. 52. Hydrographic office, Taunton.

Ahmadian, R. and Falconer, R.A. (2012), Assessment of array shape of tidal stream turbines on hydro-environmental impacts and power output, *Renewable Energy*, **44**: 318-327.

Ahmadian, R., Falconer, R. and Bockelmann-Evans, B. (2012) Far-field modelling of the hydro-environmental impact of tidal stream turbines, *Renewable Energy*, **38**: 107-116.

Aizinger, V. and Dawson, C. A. (2002) A discontinuous Galerkin method for two-dimensional flow and transport in shallow water, *Advances in Water Resources*, **25**: 67-84.

Armaly, B.F., Durst, F., Pereira, J.C.F. and Schonung, B. (1983) Experimental and theoretical investigation of backward-facing step flow, *Journal of Fluid Mechanics*, **127**: 473-496.

Baker, C. (1991) Tidal power, *Energy Policy*, **19**(8): 792-797.

Bayliss, A. and Turkel, E. (1980) Radiation boundary conditions for wave-like equations, *Communications on Pure and Applied Mathematics*, **33**: 707-725.

Bergey, K.T. (1979) The Lanchester-Betz limit, *Journal of Energy*, **3**: 382-384.

Bermudez, A. and Vazquez, M.E. (1994) Upwind methods for hyperbolic conservation laws with source terms, *Computer Fluids*, **23**(8): 1049-1071.

Betz, A. (1920) Das Maximum der Theoretisch Moglichen Ausnutzung des Windes durch Windmotoren, *Zeitschrift für das gesamte Turbinenwesen*, **26**: 307-309.

Black and Veatch (2005) Phase II UK tidal stream energy resource assessment, Technical Report, London: Black & Veatch Corporation.

Blanchfield, J., Garrett, C., Wild, P. and Rowe, A. (2008) The extractable power from a channel linking a bay to the open channel, *Proc. IMechE Part A: J. Power Energy*, **222**: 289-297.

Blunden, L.S., and Bahaj, A.S. (2007) Tidal energy resource assessment for tidal stream generators, *IMechE Part A: J. Power and Energy*, **221**: 137-146.

Bondi, H. (1981) Tidal power from the Severn Estuary, Department of Energy, Technical Report 46.

Bowden, K.F. (1955) Physical oceanography of the Irish Sea, *MAFF Fish. Invest. Ser. II*, **18**(8): 67p. H.M.S.O., London, UK.

Bowers, D.G. and Al-Barakati, A. (1997) Tidal rectification on drying estuarine sandbanks, *Estuaries*, **20**(3): 559-568.

Boyle G. (2004) *Renewable energy power for a sustainable future*, 2nd ed. Berlin: Oxford University Press.

Brufau, P., Vazquez-Cendon, M.E. and García-Navarro, P. (2002) A numerical model for the flooding and drying of irregular domains, *International Journal for Numerical Methods in Fluids*, **39**: 247-275.

Bryden, I.G., Grinsted, T. and Melville, G.T. (2004) Assessing the potential of a simple tidal channel to deliver useful energy, *Applied Ocean Research*, **26**(5): 198–204.

Bryden, I.G. and Couch, S.J. (2006) ME1 – marine energy extraction: tidal resource analysis, *Renewable Energy*, **31**: 133-139.

Bryden, I.G. and Couch, S.J. (2007) How much energy can be extracted from moving water with a free surface: A question of importance in the field of tidal current energy?, *Renewable Energy*, **32**(11): 1961-1966.

Bryden, I.G., Couch, S.J., Owen, A., and Melville, G. (2007) Tidal current resource assessment, *Proc. IMech*, **221**: 125-135.

Bunya, S., Kubatko, E.J., Westerink, J.J. and Dawson, C. (2009) A wetting and drying treatment for the Runge-Kutta discontinuous Galerkin solution to the shallow water equations, *Comput. Methods Appl. Mech. Engrg.*, **198**: 1548-1562.

Burton, T., Sharpe, D., Jenkins, N. and Bossanyi, E. (2001) *Wind Energy Handbook*, John Wiley & Sons Ltd, West Sussex, U.K.

Cartwright, D.E. (1993) Theory of ocean tides with application to altimetry, *Satellite Altimetry in Geodesy and Oceanography*, **50**: 100-141.

Chow, V.T. (1959) *Open Channel Hydraulics*, McGraw-Hill Book Co., New York, USA.

Clarke, F.J.P. (1982) Severn Barrage schemes from 1849 onwards, *Severn Barrage*, Institution of Civil Engineers, Thomas Telford, London, UK.

Cockburn, B. and Shu C.W. (1998) TVB Runge-Kutta local projection discontinuous Galerkin finite element method for conservation laws V: multi-dimensional systems, *Journal of Computational Physics*, **141**: 199-224.

Cockburn, B and Shu C.W. (2000) *Runge-Kutta discontinuous Galerkin methods for convection-dominated problems*, ICASE Report No. 2000-46, ICASE NASA Langley Research Centre, Hampton, Virginia, USA.

Crickmore, M.J. (1982) Data collection – tides, tidal currents, suspended sediment, Institution of Civil Engineers, Thomas Telford, London, UK.

Davies, A.M., and Jones, J.E. (1992) A three dimensional model of the M2, S2, N2, K1 and O1 tides in the Celtic and Irish Seas, *Prog. Oceanog.*, **29**: 197-234.

Dawson, C., Kubatko, E.J., Westerink, J.J., Trahan, C., Mirabito, C., Michoski, C. and Panda, N. (2011) Discontinuous Galerkin methods for modeling hurricane storm surge, *Advances in Water Resources*, **34**(9): 1165-1176.

DECC (2010) Marine Energy Action Plan 2010, London: Department of Energy and Climate Change, UK.

Defant, A. (1961) *Physical Oceanography, Volume 2*, Pergamon Press, New York, USA.

Denham, M.K. and Patrick, M.A. (1974) *Laminar flow over a downstream-facing step in a two-dimensional flow channel*, Chemical Engineering Research and Desing, **52a**: 361-367.

Denny, E. (2009) The economics of tidal energy, *Energy Policy*, **37**(5): 1914-1924.

Divett, T., Vennell, R. and Stevens, C. (2013) Optimisation of multiple turbine arrays in a channel with tidally reversing flow by numerical modelling with adaptive mesh, *Phil. Trans. Royal Society A*, **371**(1985): 20120251.

Doodson, A.T. (1921) The Harmonic Development of the Tide-Generating Potential. *Proceedings of the Royal Society of London, Series A*, **100**: 305-329.

Draper, S. (2011) *Tidal Stream Energy Extraction in Coastal Basins*, DPhil Thesis University of Oxford, U.K.

Draper, S., Houlsby, G.T., Oldfield, M.L.G. and Borthwick, A.G.L. (2010) Modelling tidal energy extraction in a depth-averaged coastal domain, *IET Renew. Power Gener.*, **4**: 545-554.

Draper, S., Borthwick, A.G.L. and Houlsby, G.T. (2013) Energy potential of a tidal fence deployed near a coastal headland, *Philosophical Transactions of the Royal Society A: Mathematical, Physical and Engineering Sciences*, **371**(1985): 20120176.

DTI Atlas of UK Marine Renewable Energy Resources (2008) ABPmer. Technical Report No. R.1106, Department of Trade and Industry.

Dubiner, M. (1998) Spectral methods on triangles and other domains, *Journal of Scientific Computing*, **6**: 345-390.

Ern, A., Piperno, S. and Djadel, K. (2008) A well-balanced Runge-Kutta discontinuous Galerkin method for the shallow-water equations with flooding and drying, *International Journal for Numerical Methods in Fluids*, **58**: 1-25.

Eskilsson, C., and Sherwin, S.J. (2000) A triangular spectral/hp discontinuous Galerkin method for modelling 2D shallow water equations, *International Journal for Numerical Methods in Fluids*, **201**: 1-28.

Eskilsson, C., and Sherwin, S.J. (2005) Discontinuous Galerkin spectral/hp element modelling of dispersive shallow water systems, *Journal of Scientific Computing*, **22**: 269-288.

European Union Energy Directive 2009/28/EC (2009) available at, http://eurlex.europa.eu/LexUriServ/LexUriServ.do?uri=OJ:L:2009:140:FULL:EN:PDF

Falconer, R. A. (1993) *An introduction to nearly horizontal flows. In Coastal, Estuarial and Harbour Engineers' Reference Book* (Abbott, M. B. & Price, W. A., eds). E & FNSpon Ltd., London, pp.736.

Ferrer, E. (2012) *A high order discontinuous Galerkin-Fourier incompressible 3D Navier-Stokes solver with rotating sliding meshes for simulating cross-flow turbines*, DPhil Thesis University of Oxford, U.K.

Flather, R.A. (1972) Analytical and numerical studies in the theory of tides and storm surges, Ph.D. Thesis, University of Liverpool.

Flather, R.A. (1976) A tidal model of the North-West European Continental Shelf, *Mem. Soc. R. Sci. Liege, Ser. 6*, **10**: 141-164.

Fleming, C.F., McIntosh, S.C. and Willden, R.H.J. (2013) Tidal turbine performance in sheared flow, Proc. 10th European Wave and Tidal Energy Conference, Aalborg, Denmark.

Fong, S.W. and Heaps, N.S. (1978) Note on quarter-wave tidal resonance on the Bristol Channel, Institute of Oceanographic Science Report No. 63.

Foundation for Water Research (1993) A framework for marine and estuarine model specification in the UK, Report No. FR0374, pp: 58.

Fraenkel, P. (2002) Power from marine currents, *Proceedings of the Institution of Mechanical Engineers, Part A: Journal of Power and Energy*, **216**(1): 1-14.

Fraenkel, P.L. (2007) Marine current turbines: pioneering the development of marine kinetic energy converters, *P. Mech. Eng. A: J. Pow.,* **221**: 159-169.

Froude, R. (1889) On the part played in propulsion by differences of fluid pressure, *Transactions of the Institute of Naval Architects*, **30**: 390-405.

García-Navarro, P., Brufau, P., Burguete, J. and Murillo, J. (2008) The shallow water equations: An example of hyperbolic system, *Monografias de la Real Acadeia de Ciencias de Zaragoza*, **31**: 89-119.

Garrett, C. and Cummins, P. (2005) The power potential of tidal currents in channels, *Proc. R. Soc. A*, **461**(2060): 2563-2572.

Garrett, C. and Cummins, P. (2007) The efficiency of a turbine in a tidal channel, *Journal of Fluid Mechanics*, **588**: 243-251.

Garrett, C. and Cummins, P. (2008) Limits to tidal current power, *Renewable Energy*, **33**(11): 2485-2490.

Garrett, C.J.R. and Maas, L.R.M. (1993) Tides and their effects, *Oceanus*, **36**(1): 27-37.

Giles, J., Godfrey, I., Bryden, I., Myers, L., O'Nians, J., Bahaj, A. and Griffiths, J. (2010) An innovative tidal fence development for the Severn Estuary, UK, 3rd International Conference on Ocean Energy, Bilbao, Spain.

Giraldo, F. X., and Warburton, T. (2008) A high-order triangular discontinuous Galerkin oceanic shallow water model, *International Journal for Numerical Methods in Fluids*, **56**: 899-925.

Godin, G. (1983) On the predictability of currents, *Int. Hydrogr. Rev.*, **60**: 119-126.

Google image (2012) accessed on 14th March 2012.

Gorban, A.N., Goriov, A.M. and Silantyev, V.M. (2001) Limits of the turbine efficiency for free fluid flow, *Journal of Energy Resources Technology*, **123**: 311-317.

Gross, R. (2004) Technologies and innovation for system change in the UK: status, prospects and system requirements of some leading renewable energy options, *Energy Policy*, **32**(17): 1905-1919.

Harris, E.L., Falconer, R.A. and Lin, B. (2004) Modelling hydroenvironmental and health risk assessment parameters along the South Wales Coast, *Journal of Environmental Management*, **73**: 61-70.

Heaps, N.S. (1965) Storm surges on a continental shelf, *Phil. Trans. R. Soc. A*, **257**: 351-383.

Heath, R.A. (1981) Resonant period and Q of the Celtic Sea and Bristol Channel, *Estuarine, Coastal and Shelf Science*, **12**: 291-301.

Hesthaven, J.S. and Warburton, T. (2008) *Nodal discontinuous Galerkin methods, algorithms, analysis, and applications*, Springer, New York, USA.

Hirsch, C. (1988) *Numerical computation of internal and external flows, Vol.1*, John Wiley & Sons, New York, N.Y.

Horlock, J.J. (1978) *Actuator disk theory – discontinuities in thermo-fluid dynamics*, McGraw-Hill International Book Co., New York.

Houlsby, G.T., Draper, S., and Oldfield, M.L.G. (2008) *Application of Linear Momentum Actuator Disc Theory to Open Channel Flow,* Technical Report, Department of Engineering Science, University of Oxford, U.K.

Houston, P., Senior, B., and Süli, E. (2002) hp-Discontinuous Galerkin finite element methods for hyperbolic problems: error analysis and adaptivity, *International Journal for Numerical Methods in Fluids*, **40**: 153-169.

Howarth, M.J. (1984) *Currents in the Eastern Irish Sea*, Oceanography and Marine Biology An Annual Review, **22**, p: 2-47, Aberdeen University Press.

International Energy Agency (2007) World Energy Outlook 2007.

Kadiri, M., Ahmadian, R., Bockelmann-Evans, B., Rauen, W. and Falconer, R. (2012) A review of the potential water quality impacts of tidal renewable energy systems, *Renewable and Sustainable Energy Reviews*, **16**(1): 329-341.

Kalenauskas, (2010) Energy Conversion Lecture Notes: Wind Energy, Michigan Technical University.

Karniadakis, G. E., and Sherwin, S. (2005) *Spectral/hp Element Methods for Computational Fluid Dynamics*, 2nd Edition, Oxford Science Publications, U.K.

Karsten, R.H., McMillan, J.M., Lickley, M.J. and Haynes, R.D. (2008) Assessment of tidal current energy in the Minas Passage, Bay of Fundy, *Proceedings of the Institution of Mechanical Engineers, Part A: Journal of Power and Energy*, **225**(5): 493-507.

Karsten, R.H., Swan, A. and Culina, J. (2013) Assessment of arrays of in-stream tidal turbines in the Bay of Fundy, *Philosophical Transactions of the Royal Society A: Mathematical, Physical and Engineering Sciences*, **371**(1985): 20120189.

Kubatko, E.J., Westerink, J.J., and Dawson, C. (2006a) hp Discontinuous Galerkin methods for advection dominated problems in shallow water flow, *Comput. Methods Appl. Mech. Engrg.*, **196**: 437-451.

Kubatko, E.J., Westerink, J.J., and Dawson, C. (2006b) An unstructured grid morphodynamic model with a discontinuous Galerkin method for bed evolution, *Ocean Modelling*, **15**: 71-89.

Kubatko, E., Dawson, C., and Westerink, J.J. (2008) Time step restrictions for Runge-Kutta discontinuous Galerkin methods on triangular grids, *Journal of Computational Physics*, **227**: 9697-9710.

Kubatko, E.J., Bunya, S., Dawson, C., Westerink, J.J. and Mirabito, C. (2009) A performance comparison of continuous and discontinuous finite element shallow water models, *Journal of Scientific Computing*, **40**(1-3): 315-339.

Lamb, H. (1932) *Hydrodynamics*, 6th Edition, Cambridge University Press, UK.

Lanchester, F. (1915) A contribution to the theory of propulsion and the screw propeller, *Transactions of the Institute of Naval Architects*, **57**: 98-116.

Le Méhauté (1976) *An introduction to hydrodynamics and water waves*, Springer, New York.

Le Provost, C. (1991) *Generation of overtides and compound tides*, In Tidal Hydrodynamics, ed. B. B. Parker. John Wiley and Son.

Le Provost, C., Genco, M. L. and Lyard, F. (1995) Modeling and predicting tides over the World Ocean, Quantitative Skill Assessment for Coastal Ocean Models, *Coastal and Estuarine Studies*, **47**: 175-201.

LeVeque, R. J. (2002) *Finite Volume Methods for Hyperbolic Problems*, First edition, Cambridge University Press, Cambridge, U.K.

Li, H., and Liu, R.X. (2001) The discontinuous Galerkin finite element method for the 2D shallow water equations, *Mathematics and Computers in Simulation*, **56**: 171-184.

Lisitzin, E. (1957) The tidal cycle of 18.6 years in the oceans, *Journal du Conseil*, **22**(2): 147-151.

MacKay, D. (2007) Under-estimation of the UK tidal resource, Technical Report, Cavendish Laboratory, University of Cambridge.

McAdam, R. (2011) Studies into the Technical Feasibility of the Transverse Horizontal Axis Water Turbine, DPhil Thesis University of Oxford, U.K.

McAdam, R.A., Houlsby, G.T. and Oldfield, M.L.G. (2012) Experimental results from 1/20th scale model tests of the Transverse Horizontal Axis Water Turbine, Oxford Tidal Energy Workshop 2012 Proceedings.

McAdam, R.A., Houlsby, G.T. and Oldfield, M.L.G. (2013) Experimental measurements of the hydrodynamic performance and structural loading of the Transverse Horizontal Axis Water Turbine: Part 1, *Renewable Energy*, **59**: 105-114.

Marine Current Turbine Ltd, Tidal Turbine Array at Anglesey Skerries, http://www.marineturbines.com/3/news/article/44/marine_current_turbines_kicks_off_first_tidal_array_for_wales accessed on 17 February 2014

Mignone, A., and Bodo, G. (2005) An HLLC Riemann solver for relativistic flows – I. Hydrodynamics, *Mon. Not. R. Astron. Soc.*, **364**: 126-136.

Militello, A. and Zundel, A.K. (1999) Surface-water modeling system tidal constituents toolbox for ADCIRC, *Coastal Engineering Technical Note CETN IV-21*, U.S. Army Engineer Research and Development Center, Vicksburg, MS.

Minesto Deep Green Technology, http://www.minesto.com/deepgreentechnology/index.html, accessed on 21 February, 2014.

Monahan, D. (2008), Application of the General Bathymetric Chart of the Oceans (GEBCO) Digital Atlas in the delineation of continental shelves under Article 76, *Journal of Ocean Technology*, **3**: 24-29.

Mycek, P., Gaurier, B., Germain, G., Pinon, G. and Rivoalen, E. (2013) Numerical and Experimental Study of the Interaction Between Two Marine Current Turbines, *International Journal of Marine Energy*, **1**: 70-83.

Myers, L.E., Keogh, B. and Bahaj, A.S. (2011) Layout Optimisation of 1st-Generation Tidal Energy Arrays, 9th European Wave and Tidal Energy Conference, Southampton, UK.

Nadaoka, K., and Yagi, H. (1998) Shallow-water turbulence modelling and horizontal large-eddy computation of river flow, *J. Hydraul. Eng.*, **124**: 493-500.

NASA, TOPEX/Poseidon Revealing Hidden Tidal Energy, 2006.

Neill, S.P., Litt, E.J., Couch, S.J. and Davies, A.G. (2009) The impact of tidal stream turbines on large-scale sediment dynamics, *Renewable Energy*, **34**: 2803-2812.

Nishino, T., and Willden, R.H.J. (2012a) Effects of 3-D channel blockage and turbulent wake mixing on the limit of power extraction by tidal turbines, *International Journal of Heat and Fluid Flow*, **35**: 123-135.

Nishino, T., and Willden, R.H.J. (2012b) The efficiency of an array of tidal turbines partially blocking a wide channel, *Journal of Fluid Mechanics*, **708**: 596-606.

O'Leary, R.A. and Mueller, T.J. (1969) *Correlation of physical and numerical experiments for incompressible laminar separated flows*, Technical Report, Notre Dame University Ind. Coll. of Engineering.

O'Rourke, F., Boyle, F. and Reynolds, A. (2010) Tidal Energy Update 2009, *Applied Energy*, **87**: 398-409.

O'Rourke, F., Boyle, F. and Reynolds, A. (2009) Renewable energy resources and technologies applicable to Ireland, *Renewable and Sustainable Energy Review*, **13**(8): 1975-1984.

Owen, A. (1980) The tidal regime of the Bristol Channel: a numerical modelling approach, *Geophys. J. R. Astr. Soc.*, **62**: 59-75.

Pawlowicz, R., Beardsley, B., Lentz, S. (2002) Classical tidal harmonic analysis including error estimates in MATLAB using T_TIDE, *Computers & Geosciences*, **28**(8): 929-937

Percy, J.A. (1996) *Dykes, damns and dynamos: The impact of coastal structures*, Clean Annapolis River Project, **5**: 1-5.

Platzman, G.W., Curtis, G.A., Hansen, K.S. and Slater, R.D. (1981) Normal modes of the world ocean. Part II: Description of modes in the period range 8 to 80 hours, *Journal of Physical Oceanography*, **11**: 579-603.

Prandle, D. (1980) Modelling of tidal barrier schemes: an analysis of the open-boundary problem by reference to AC circuit theory, *Estuarine and Coastal Marine Science*, **11**: 53-71.

Prandle, D. (1984) Simple theory for designing tidal power schemes, *Adv. Water Resour*, 7(1): 21-27.

Proudman, J. (1953) *Dynamical Oceanography*, London: Methuen and Co., UK.

Pugh, D.T. (1981) Tidal amphidrome movement and energy dissipation in the Irish Sea, *Geophysical Journal of the Royal Astronomical Society*, **67**: 515-527.

Pugh, D.T. (1987) *Tides, Surges and Mean Sea-Level*, John Wiley and Sons, Chichester, UK.

Pulse Tidal Hydrofoil, http://pulsetidal.com/our-technology.html, accessed on 21 February 2014.

Radford, P.J. (1982) *The effects of a barrage on water quality in Severn Barrage*, p: 203-216, Institution of Civil Engineers, Thomas Telford, London, UK.

Rainey, R.C.T. (2009) The optimum position for a tidal power barrage in the Severn Estuary, *Journal of Fluid Mechanics*, **636**: 497-507.

Rankine, W. (1865) On the mechanical properties of propellers, *Transactions of the Institute of Naval Architects*, **6**: 13-30.

Redfield, A.C. (1980) *The tides of the waters of New England and New York*, Woods Hole: Woods Hole Oceanographic Institution.

Roache, P.J. (1997) Quantification of uncertainty in computational fluid dynamics, *Annu. Rev. Fluid Mech.*, **29**, p: 123-160.

Robinson, I.S. (1978) Tidal response of a wedge-shaped estuary to the installation of a tidal power barrage: a simplified analytical approach, *Proc. Instn. Civ. Engrs., Part 2*, **65**: 773-790.

Robinson, I.S. (1979) The tidal dynamics of the Irish and Celtic Seas, *Geophysical Journal of the Royal Astronomical Society*, **56**(1), p: 159-197.

Robinson, I.S. (1980) Tides in the Bristol Channel – an analytical wedge model with friction, *Geophys. J. R. Astr. Soc.*, **62**: 77-95.

Rodi, W. (1993) *Turbulence Models and Their Application in Hydraulics: A State-of-the Art Review*, IAHR Monograph Balkema, The Netherlands, 104 pages.

Rodi, W., Constantinescu, G. and Stoesser, T. (2013) *Large-Eddy Simulation in Hydraulics*, CRC Press/Balkema, Taylor & Francis Group, Leiden, The Netherlands, ISBN 978-1-138-00024-7.

Roe, P.L. (1981) Approximate Riemann solvers, parameter vectors and difference schemes, *J. Comp. Phys.*, **43**: 357-372.

Rogers, B.D. (2001) *Refined localised modelling of coastal flow features using adaptive quadtree grids*, DPhil thesis University of Oxford.

Schlichting, H. (1968) *Boundary Layer Theory*, McGraw-Hill, New York, U.S.A.

Schluntz, J. and Willden, R.H.J. (2013) The effect of rotor design on the power output of closely packed tidal turbines, Proc. 10th European Wave and Tidal Energy Conference, Aalborg, Denmark.

Serhadlıoğlu, S., Adcock, T.A.A., Houlsby, G.T., Draper, S. and Borthwick, A.G.L. (2013) Tidal stream energy resource assessment of the Anglesey Skerries, *International Journal of Marine Energy*, **3**: 98-111.

Shu, C.W. (1987) TVB uniformly high-order schemes for conservation laws, *Math. Comput.*, **49**: 105-121.

Shu, C.W. (2003) High order finite difference and finite volume WENO schemes and discontinuous Galerkin methods for CFD, *Int. J. of Comp. Fluid Dynamics*, **17**(2): 107-118.

Sod, G. (1978) A survey of several finite difference methods for systems of nonlinear hyperbolic conservation laws, *J. Comp. Phys.*, **27**: 1-31.

Soulsby, R. (1998) *Dynamics of Marine Sands*. Thomas Telford.

Stansby, P.K. (2006) Limitations of depth-averaged modelling for shallow wakes, *ASCE J. Hydraulic Engineering*, **132**(7): 737-740.

Stansby, P.K., and Lloyd, P.M. (2001) Wake formation around islands in oscillatory laminar shallow-water flows. Part 2. Three-dimensional boundary-layer modelling, *Journal of Fluid Mechanics*, **429**: 239-254.

Stephenson, G. (1970) *An introduction to partial differential equations for science students*, Longman Group Ltd., 2nd Edition, Great Britain.

Stommel, H. (1948) The westward intensification of wind-driven ocean currents, *Transactions, American Geo- physical Union*, **29**(2): 202-206.

Sutherland, G., Foreman, M., and Garrett, C. (2007) Tidal current energy assessment for Johnstone Strait, Vancouver Island, *Proc. IMechE Part A: J. Power and Energy*, **221**: 147-157.

Taylor, G.I. (1921) Tides in the Bristol Channel, *Proc. Camb. Phil. Soc.*, **20**: 320-325.

The University of Oxford Advanced Research Computing (ARC) website, http://www.arc.ox.ac.uk/content/services, *accessed on* 6th July 2014.

Toro, E. F. (1997) *Riemann Solvers and Numerical Methods for Fluid Dynamics: A Practical Introduction*, Springer-Verlag, Berlin.

Toro, E. F. (2001) *Shock-capturing methods for free-surface shallow flows*, Wiley, U.K.

Tu, S., and Aliabadi, S. 2005, A Slope Limiting Procedure in Discontinuous Galerkin Finite Element Method for Gasdynamics Application, International Journal of Numerical Analysis and Modeling, **2**(2): 163-178.

Uncles, R.J. (1981) A numerical simulation of the vertical and horizontal M_2 Tide in the Bristol Channel and comparisons with observed data, *Limnology and Oceanography*, **26**: 571-577.

Uncles, R.J. (1983) Hydrodynamics of the Bristol Channel, *Marine Pollution Bulletin*, **15**(2): 47-53.

US, NREL (2005) Climate change technology program, technology options: for the near and long term, DOE/PI-0002.

Walkington, I. and Burrows, R. (2009) Modelling tidal stream power potential, *Applied Ocean Research*, **31**(4): 239-245.

Webb, D.J. (1976) Patterns in the Equilibrium Tide and the observed tide, *Australian Journal of Marine and Freshwater Research*, **27**: 617-632.

Weiyan, T. (1992) *Shallow water hydrodynamics*, Elsevier Oceanography Series, Water & Power Press, Beijing, China.

Westerink, J.J., Luettich, Jr.R.A. and Muccino, C. (1994) Modeling tides in the western North Atlantic using unstructured graded grids, *Tellus A*, **46**(2): 178-199.

Whelan, J., Graham, J. and Peiro, J. (2009) A free-surface and blockage correction for tidal turbines, *Journal of Fluid Mechanics*, **624**: 281-291.

Van Kuik, G.A.M. (2007) The Lancester-Betz-Joukowsky Limit, *Wind Energy*, **10**: 289-291.

Vennell, R. (2010) Tuning turbines in a tidal channel, *Journal of Fluid Mechanics*, **663**: 253-267.

Vennell, R. (2011) Tuning tidal turbines in-concert to maximise farm efficiency, *Journal of Fluid Mechanics*, **671**: 587-604.

Vennell, R. (2012) Realizing the potential of tidal currents and the efficiency of turbine farms in a channel, *Renewable Energy*, **47**: 95-102.

Verkley, W.T.M. (1990) Notes and correspondence on beta-plane approximation, *Journal of Atmospheric Sciences*, **47**(20): 2453-246.

Vogel, C.R., Houlsby, G.T., and Willden, R.H.J. (2014) On the extractable power of an array of turbines partially spanning a wide channel with a free surface, *Journal of Fluid Mechanics*, To be submitted.

Vogel, C. R., Willden, R.H.J., and Houlsby, G.T. (2013) A correction for depth-averaged simulations of tidal turbine arrays, 10th European Wave and Tidal Energy Conference, Aalborg, Denmark.

Vogel, C.R. (2012) Globalising Tidal Power Generation – Second Generation Tidal Energy, Transfer Report, University of Oxford, UK.

Vreugdenhil, C.B. (1994) *Numerical methods for shallow-water flow*, Kluwer Academic Publisher, the Netherlands.

Xia, J., Falconer, R.A., Lin, B. and Tan, G. (2012) Estimation of annual energy output from a tidal barrage using two different methods, *Applied Energy*, **93**: 327-336.

Xia, J., Falconer, R.A. and Lin, B. (2010a) Hydrodynamic impact of a tidal barrage in the Severn Estuary, UK, *Renewable Energy*, **35**:1455-1468.

Xia, J., Falconer, R.A. and Lin, B. (2010b) Impact of different operating modes for a Severn Barrage on the tidal power and flood inundation in the Severn Estuary, UK, *Applied Energy*, **87**: 2374-2391.

Xia, J., Falconer, R.A. and Lin, B. (2010c) Numerical model assessment of tidal stream energy resources in the Severn Esturary, UK, *Proceedings of the Institution of Mechanical Engineers Part A: Journal of Power and Energy*, **224**(7): 969-983.

Yates, N., Walkington, I., Burrows, R. and Wolf, J. (2013) Appraising the extractable tidal energy resource of the UK's western coastal waters, *Phil. Trans. R. Soc. A*, **371**: 20120181.

Zhou, J., Pan, S. and Falconer, R.A. (2014) Effects of open boundary location on the far-field hydrodynamics of a Severn Barrage, *Ocean Modelling*, **73**: 19-29.

Zienkiewicz, O. C., and Taylor, R. L. (2005) *The finite element method for solid and structural mechanics*, Elsevier Butterworth-Heinemann, 6th edition, Oxford, UK.